Spatial Modulation Spectroscopy Of Single Nano-Objects In A Liquid Environment For Biosensing Applications

Jan-Michael Rye

N° d'ordre NNT : 2017LYSE1053

THÈSE DE DOCTORAT DE L'UNIVERSITÉ DE LYON
opérée au sein de
l'Université Claude Bernard Lyon 1

École Doctorale ED52
Physique et Astrophysique

Discipline : Physique

Soutenue publiquement le 16/03/2017, par :
Jan-Michael Rye

Spatial Modulation Spectroscopy Of Single Nano-Objects In A Liquid Environment For Biosensing Applications

---

Devant le jury composé de :

Renaud Bachelot, Pr., HDR, Université Technologique de Troyes	Président, Rapporteur
Agnès Maître, Pr., HDR, Université Pierre et Marie Curie	Rapporteuse
Valérie Halté-Filippi, MCF, HDR, Université de Strasbourg	Examinatrice
Alice Berthelot, MCF, Université Claude Bernard Lyon 1	Examinatrice
Pierre Billaud, MCF, Université Paris-Sud	Examinateur, invité
Emmanuel Cottancin, Pr., HDR, Université Claude Bernard Lyon 1	Directeur de thèse
Christophe Bonnet, MCF, Université Claude Bernard Lyon 1	Co-directeur de thèse
Frédéric Lerouge, MCF, HDR, Université Claude Bernard Lyon 1	Co-directeur de thèse, invité

UNIVERSITE CLAUDE BERNARD - LYON 1

Président de l'Université	**M. le Professeur Frédéric FLEURY**
Président du Conseil Académique	M. le Professeur Hamda BEN HADID
Vice-président du Conseil d'Administration	M. le Professeur Didier REVEL
Vice-président du Conseil Formation et Vie Universitaire	M. le Professeur Philippe CHEVALIER
Vice-président de la Commission Recherche	M. Fabrice VALLÉE
Directeur Général des Services	M. Alain HELLEU

COMPOSANTES SANTE

Faculté de Médecine Lyon Est – Claude Bernard	Directeur : M. le Professeur J. ETIENNE
Faculté de Médecine et de Maïeutique Lyon Sud – Charles Mérieux	Directeur : Mme la Professeure C. BURILLON
Faculté d'Odontologie	Directeur : M. le Professeur D. BOURGEOIS
Institut des Sciences Pharmaceutiques et Biologiques	Directeur : Mme la Professeure C. VINCIGUERRA
Institut des Sciences et Techniques de la Réadaptation	Directeur : M. X. PERROT
Département de formation et Centre de Recherche en Biologie Humaine	Directeur : Mme la Professeure A-M. SCHOTT

COMPOSANTES ET DEPARTEMENTS DE SCIENCES ET TECHNOLOGIE

Faculté des Sciences et Technologies	Directeur : M. F. DE MARCHI
Département Biologie	Directeur : M. le Professeur F. THEVENARD
Département Chimie Biochimie	Directeur : Mme C. FELIX
Département GEP	Directeur : M. Hassan HAMMOURI
Département Informatique	Directeur : M. le Professeur S. AKKOUCHE
Département Mathématiques	Directeur : M. le Professeur G. TOMANOV
Département Mécanique	Directeur : M. le Professeur H. BEN HADID
Département Physique	Directeur : M. le Professeur J-C PLENET
UFR Sciences et Techniques des Activités Physiques et Sportives	Directeur : M. Y.VANPOULLE
Observatoire des Sciences de l'Univers de Lyon	Directeur : M. B. GUIDERDONI
Polytech Lyon	Directeur : M. le Professeur E.PERRIN
Ecole Supérieure de Chimie Physique Electronique	Directeur : M. G. PIGNAULT
Institut Universitaire de Technologie de Lyon 1	Directeur : M. le Professeur C. VITON
Ecole Supérieure du Professorat et de l'Education	Directeur : M. le Professeur A. MOUGNIOTTE
Institut de Science Financière et d'Assurances	Directeur : M. N. LEBOISNE

Spatial Modulation Spectroscopy Of Single Nano-Objects In A Liquid Environment For Biosensing Applications

Advances in the development of rapid, accurate and highly sensitive methods for detecting target analytes in solution will provide crucial tools for research and applications in medicine and molecular biology. One of the currently most promising approaches is the development of nanosensors based on the localized surface plasmon resonance (LSPR) of noble metal nano-objects (MNOs), which is an optical response that depends on their size, shape, composition and local environment. The ability to measure the modification of the reponse of a single MNO in the presence of a target analyte would allow each object to act as an independent probe with increased sensitivity as the signal would be isolated from the averaging effects of ensemble measurements. Furthermore it would allow the development of micrometric, functionalized multiprobe samples for multitarget label-free assays.

In this work, a novel experimental setup based on the spatial modulation spectroscopy (SMS) technique has been developed to measure the optical response of individual nano-objects in a liquid environment. In parallel, a new technique has also been developed to elaborate stable probes for measurements with the new setup, with a focus on gold bipyramids due to numerous qualities that make them excellent candidates for biosensing probes. The setup has been used to measure the response of individual objects in environments of different real refractive indices and the detected changes have been shown to be in good agreement with theoretical calculations. Numerical studies have also been performed to investigate the influence on the optical response of numerous factors encountered in the studied systems.

Keywords: single nano-object, optical response, noble metals, localized surface plasmon resonance (LSPR), spatial modulation spectroscopy (SMS), bipyramid, biosensing

Spectroscopie À Modulation Spatiale De Nano-Objets Uniques En Milieu Liquide Pour Des Applications En Biosensing

Le développement de méthodes rapides, précises et ultra-sensibles pour la détection d'analytes cibles en solution est crucial pour la recherche et les applications potentielles en médecine ou biologie moléculaire. Une approche très prometteuse consiste à développer des nano-capteurs à partir de nano-objets métalliques (NOM) qui présentent une résonance d'extinction dans leur réponse optique. Cette résonance nommée résonance de plasmon de surface localisée (RPSL) peut être ajustée spectralement en jouant sur la nature, la morphologie et l'environnement du NOM. Mesurer des modifications sur la RPSL de nano-objets individuels en présence d'analytes cibles doit permettre de s'affranchir des effets de moyennes dans les mesures d'ensemble. De plus, cela ouvre la voie vers le développement d'échantillons micrométriques pour des tests multicibles sans étiquette ("label-free").

Dans ce travail, on a développé un nouveau dispositif expérimental basé sur la technique de spectroscopie à modulation spatiale (SMS) permettant de sonder la réponse optique de NOM individuels en milieu liquide. En parallèle des méthodes de synthèse ont été mises au point pour obtenir des échantillons sondes stables permettant des mesures sur NOM unique, en particulier sur des bipyramides d'or qui présentent de nombreuses propriétés intrinsèques faisant d'elles de bonnes candidates pour le "biosensing". Des mesures experimentales ont été réalisées dans des environnements d'indice variable et les changements détectés sont en bon accord avec les simulations théoriques. De plus, nous montrons dans ce travail que les NOM ont une réponse stable dans le temps et sont réutilisables. Par ailleurs, de nombreuses études théoriques ont été réalisées pour comprendre l'influence des nombreux paramètres agissant sur la réponse optique des systèmes étudiés.

Mots-clés: nano-objet unique, réponse optique, métaux nobles, résonance de plasmon de surface localisée (RPSL), spectroscopie à modulation spatiale (SMS), bipyramide, biosensing

Host Laboratories

Clusters and Nanostructures group
Institute of Light and Matter (ILM)
CNRS UMR 5306
Université Claude Bernard Lyon 1 (UCBL)
Université de Lyon
Bâtiment Kastler, 10 rue Ada Byron
69622 Villeurbanne CEDEX, France

Functional Materials and Photonics group
Laboratoire de Chimie (LC)
CNRS UMR 5182
École Normale Supérieure (ENS) de Lyon
Université de Lyon
46, allée d'Italie
69364 Lyon CEDEX 07, France

Financial Support

This work was supported by the LABEX iMUST (ANR-10-LABX-0064) of Université de Lyon, within the program "Investissements d'Avenir" (ANR-11-IDEX-0007) operated by the French National Research Agency (ANR).

Résumé Substantiel En Langue Française

Introduction

Le manuscrit commence par une brève introduction aux nanotechnologies et leur développement au cours des dernières décennies montrant que c'est un domaine de recherche très actif et prometteur. En particulier, les avancements à venir en nanotechnologies devraient trouver des applications importantes dans les domaines de la médecine et la biologie moléculaire, aussi bien dans la recherche fondamentale que dans des applications cliniques et commerciales. Une attention particulière est portée au potentiel de développer le "biosensing", i.e. la détection des analytes biologiques, ce qui est le but ultime de ce travail.

Les principales approches sont présentées avant de discuter des techniques visant à exploiter le phénomène de résonance de plasmon de surface localisée (RPSL). Ce phénomène, brièvement introduit ici et développé en détails dans le premier chapitre, se manifeste dans les nanoparticules (NPs) de métaux nobles et dépend, entre autres, de l'environnement proche de la NP. Si on peut mesurer ce phénomène sur une NP individuelle, on pourra l'exploiter comme sonde pour le "biosensing". Une technique pour mesurer une telle réponse est la spectroscopie à modulation spatiales (SMS), qui jusqu'à maintenant était limitée à des mesures dans l'air. Le but des applications de ce travail de thèse était de développer un tel dispositif en milieu liquide pour des applications de biosensing.

1: Réponse Optique Des Nanoparticules D'Or Individuelles

À partir de la structure électronique des atomes individuels, ce chapitre montre d'abord l'origine de la structure de bandes dans les métaux nobles. Le modèle de Drude est ensuite présenté pour fournir un aperçu des propriétés diélectriques intrinsèques de ces métaux. Ensuite on considère la réponse optique des NPs individuelles de métaux nobles. L'absorption, la diffusion et l'extinction sont définies avant de montrer comment ces phénomènes peuvent être modélisés tout d'abord dans l'approximation quasi-statique puis par la théorie de Mie.

La deuxième partie du chapitre présente les résultats des études numériques effectuées avec la théorie de Mie généralisée et le méthode des éléments finis, ainsi que quelques rappels sur les autres techniques possibles. Les premières études considèrent l'influence du substrat, du mouillage et des faibles déformations sur la réponse optique d'une sphère et démontrent que le modèle d'un indice de réfraction effectif suffit dans certains cas à reproduire la réponse optique d'un "vrai" système en masquant la complexité de ces différents facteurs. Pour explorer plus loin les effets de facettage, des études avec des cubes sont ensuite présentées.

2: Spectroscopie À Modulation Spatiale Dans Un Milieu Liquide

La spectroscopie à modulation spatiale (SMS) est une technique pour mesurer la réponse optique d'une NP individuelle jusqu'à quelques dizaines de nanomètres. Un des défis principaux de cette thèse a été de développer un tel dispositif SMS en milieu liquide. Ce chapitre présente d'abord les principes de la SMS. Les éléments centraux d'un dispositif de SMS sont ensuite détaillés pour faire le lien entre le théorie et les mesures en pratique. La procédure d'acquisition des cartographies pour localiser des NPs sur un échantillon et des mesures de spectres d'extinction des NPs ainsi localisées sont aussi présentés.

Le chapitre décrit ensuite les adaptations d'un dispositif SMS à des mesures en milieu liquide. Cette partie présente la mise en place d'un nouveau porte-échantillon avec une cellule fluidique ainsi que l'utilisation des objectifs adaptés pour faire des mesures avec ce porte-échantillon. Un miroir oscillant a aussi été mis en place pour assurer la modulation spatiale au cas où le poids de la cellule empêcherait l'oscillation suffisante de la platine qui la porte. Pour piloter le dispositif, un logiciel très adaptable a été développé en LabVIEW avec des capacités importantes d'automatisation.

On clôt ce chapitre avec la présentation des nombreux tests et contrôles pour assurer que ces modifications n'affectent pas les mesure SMS avec ce dispositif et que les résultats obtenus sont comparables avec un dispositif "classique". Des courbes des calibrations sont calculées et utilisées pour mesurer des sections d'extinction absolues des NPs individuelles. Ces mesures sont comparées avec des valeurs théoriques obtenues par modélisation avec le méthode des éléments finis (FEM) et cette comparaison démontre que les valeurs expérimentales sont en bon accord avec les valeurs théoriques.

3: Bipyramides D'Or Comme Biocapteurs

Les différents critères pour sélectionner une sonde pour réaliser du biosensing sont présentés ainsi qu'un aperçu des sondes utilisées actuellement en recherche. Plusieurs caractéristiques des bipyramides (BPs) d'or qui sont prometteuses pour faire des biocapteurs sont présentées. Elles ont motivé le choix des BPs comme sonde dans ce travail. Ces propriétés sont ensuite illustrées plus en détail par des simulations numériques avant de présenter leur synthèse chimique.

Les difficultés initiales de la préparation des échantillons de BPs stables et optiquement utilisables sont brièvement présentées avant de discuter le développement d'une nouvelle technique pour produire des échantillons stables par silanisation. Ensuite les résultats d'essais avec des échantillons de sphères silanisées ont montré que la silanisation n'entrave pas les mesures de la SMS.

Dans une première série d'expériences avec des échantillons de BPs silanisées, le nouveau

dispositif de SMS en milieu liquide a été utilisé pour détecter le changement d'indice optique de différents milieux (eau, glycérol et des mélanges eau-glycérol) en observant le décalage du pic plasmonique de la RPSL des NPs individuelles. Cette détection a été faite avec succès dans un régime statique en immergeant l'échantillon dans des solutions différentes et même en dynamique en laissant le glycérol diffuser dans l'eau.

Ensuite des études pour vérifier la stabilité et la robustesse de ces échantillons sont présentées. Les objets précédemment étudiés ont été réétudiés dans l'air peu après les études en liquide puis après plusieurs mois à l'air. Les résultats montrent que les échantillons peuvent être réutilisés même après de longues périodes de stockage.

Mesures De Retrodiffusion

Dans ce mini-chapitre de perspectives, on présente quelques résultats de travaux annexes menés pendant les années de thèse visant à mesurer la rétrodiffusion d'une NP individuelle en exploitant encore la modulation spatiale. Les bases théoriques sont brièvement présentées, montrant que les signaux en rétrodiffusion sont sensibles au déphasage se produisant à la RPSL. Nous montrons que la dépendance du signal avec l'environnement est plus sensible que les mesures en extinction. Quelques premiers essais sont présentés avec des différents résultats. Certains valident le principe de la mesure mais d'autres démontrent la difficulté de maîtriser la géométrie locale pour exploiter ce phénomène.

Conclusion et Perspectifs

On a montré dans ce travail comment un nouveau dispositif de SMS en milieu liquide a été développé et un protocole pour élaborer des échantillons de NPs d'or anisotropes stables et robustes pour ce dispositif. La détection des changements d'indice de réfraction dans des milieux liquides ont été démontré avec succès et les échantillons restent stables même après plusieurs mois.

Des essais de biosensing avec des échantillons fonctionnalisés sont prévus pour sonder des analytes cibles. Des modifications sont aussi prévues pour faire des mesures en dynamique en temps réel ainsi que de poursuivre les mesures en rétrodiffusion. Différentes sondes comme les échantillons lithographiés et les dimères de nanocubes sont aussi envisagées, avec l'objectif à long terme de faire des échantillons "multiplexés", c.a.d. composés de plusieurs sondes différemment fonctionnalisées pour détecter plusieurs analytes en parallèle.

Remerciements

Je tiens à remercier en premier lieu mes trois directeurs de thèse Emmanuel Cottancin, Christophe Bonnet et Frédéric Lerouge qui m'ont donné cette opportunité et qui m'ont suivi de près pendant ces années. Merci de m'avoir laissé assez de liberté pour me perdre de temps en temps et de toujours avoir été là pour me réorienter quand il le fallait.

Je remercie aussi Agnès Maître, Renaud Bachelot, Valérie Halté-Fillipi, Alice Berthelot et Pierre Billaud d'avoir accepté de participer à mon jury et de s'être intéressés à mon travail. Merci aussi pour toutes vos remarques et corrections après la soutenance, en particulier à Pierre qui a pris le temps de me transmettre ses nombreuses notes par courriel.

Avec mes directeurs je remercie également tous les autres membres, anciens et nouveaux, de l'équipe Agrégats et Nanostructures (AgNano) de l'ILM qui m'ont accompagné et guidé tout au long de cette thèse: Michel Pellarin, Jean Lermé, Alexis Mosset, Marie-Ange Lebeault, Michel Broyer, Jean-Louis Vialle, Matthias Hillenkamp, Sylvain Hermelin et Julien Laverdant. Merci de toujours avoir pris de temps pour répondre à mes nombreuses questions avec pédagogie et patience et merci aussi pour votre convivialité qui a rendu ce passage dans l'équipe très agréable.

Pendant ces trois ans j'ai eu la chance de partager un bureau luxueux[1] avec mes co-thésards d'AgNano, Nicolas Troc et Julien Ramade. Merci pour toutes les blagues stupides, les innombrables rounds de Slingshot, l'émerveillement de la quantité de sel qui peut être supporté par un corps humaine, les encouragements et les moments de décontraction en dehors du bureau.

Y por supuesto agradezco Pablo pour su apoyo inquebrantable y omnipresente que ha creado un ambiente agradable durante estos tres años.

Merci à Christophe Moulin et le centre NanOpTec, Alain Bourgey, Cécile Jamois, Xavier Jaurand et le CTμ, et Christian Clavier pour leur contributions qui m'ont permis d'avancer mon travail. Merci également au Labex iMUST[2] qui m'a permis de réaliser cette thèse pluridisciplinaire en collaboration entre deux groupes, de présenter mon travail à de nombreuses conférences, et de me former à COMSOL et au MEB.

Je tiens aussi à remercier l'administration de l'ILM, de l'école PHAST et de la DRED, en particulier Dominique Farjot, Véronique Chavret, Françoise Champion, Delphine Kervella, Sylvie Flores, Fabienne Macro, Sad Mezzour et Francisco Pinto.

[1] Avec le fameux canapé et mini-frigo.

[2] Ce travail a été réalisé grâce au soutien financier du LABEX iMUST (ANR-10-LABX-0064) de l'Université de Lyon, dans le cadre du programme "Investissements d'Avenir" (ANR-11-IDEX-0007) géré par l'Agence Nationale de la Recherche (ANR).

Je suis passé par plusieurs portes pour arriver ici en thèse, ce qui n'aurait pas été possible sans ceux qui me les ont ouvertes. Je remercie ainsi Christophe Dujardin de m'avoir accepté dans l'école PHAST, Stéphane Parola de m'avoir accepté dans son équipe, et Dany Davesne de m'avoir accepté en licence de physique quand je suis arrivé à Lyon.

Merci aussi à Estelle Salmon qui m'a beaucoup aidé avec toutes les démarches après mon accident de trajet en début de deuxième année.

Enfin et surtout je tiens à remercier Amélie de tout mon cœur, pour sa compréhension, son soutien, son amour et sa patience surhumaine. Sans toi je n'y serais pas arrivé.

Contents

Introduction

In 1959, Richard Feynman gave a now famous lecture at a meeting of the American Physical Society entitled "There is Plenty of Room at the Bottom" in which he discussed the possibilities and challenges of what we today call nanotechnology. One of the ideas evoked during this lecture was to write an entire encyclopaedia on the head of a pin. 31 years later, 2 scientists would succeed in individually arranging 35 xenon atoms on a nickel surface to spell out "IBM"[1]. Advances in nanomanipulation have continued and today we can fit an entire encyclopedia on a thumb drive, but writing it out in words on the head of a pin remains impractical if not impossible.

Feynman stressed the word *plenty* in the title of the lecture and this has proven to be true. Research on all levels from the micrometric down to the Ångström scale remains intense and our ability to manipulate single atoms in one system does not yet enable us to build molecules or nanometric structures atom by atom in another. The nanoworld is complex and bizarre with different properties emerging at different scales, which all present their own unique challenges. One of the first lessons of any introductory course in nanoscience is that as the length scale L of a system is reduced, surface effects scale as L^2 while volumetric effects scale as L^3, so the former become dominant at smaller sizes. If we continue on to even smaller systems, we reach the limits of the quasi-continuity of macroscale systems and we are confronted with discretization and quantum effects. Just as a puddle and a drop of water exhibit different properties, so too do a gold nanoparticle (NP) of 100 nm and one of 2 nm. The study of each is complementary and equally necessary.

This complementarity extends across different fields at all scales. Scientific research in one field continually builds on previous work in both its own and others. For example, the nanoscale IBM logo was made possible by the invention of the scanning tunneling microscope (STM) 8 years earlier[2], which, along with the related invention of the atomic force microscope (AFM)[3], opened up the doors for nanoscale manipulation in the decades that followed[4]. These inventions would not have been possible without advances in other fields such as materials science and electrical engineering. It is often the case that a breakthrough in one field will suddenly open entirely new avenues in others.

There are several important examples of this in the field of medicine. The discovery of X-rays in 1895 by the physicist Wilhelm Röntgen, for which he won the first Nobel Prize in

Physics in 1901, heralded a revolution in medical diagnostics. In the century since the first medical radiographs, many great strides have been made in medical imaging technology due to progress in other fields. A culmination of advances in multiple fields over the seven decades after the discovery of X-rays led to the first commercial computed tomography (CT) scanners in the 1970s, for which an electrical engineer and a physicist would share the Nobel Prize in Medicine in 1979[5]. Also building upon decades of previous work in nuclear magnetic resonance (NMR), magnetic resonance imaging (MRI) was invented in 1971[6] by a chemist and refined a few years later by a physicist[7]. They too would share the Nobel Prize in Physiology or Medicine in 2003.

Continuing this strong connection to other fields, the next revolutionary advances in medicine are expected to come from nanotechnology[8], which will have direct impact through applications such as the development of targeted drug design and delivery, in-vivo imaging with theranostic[3] agents and point of care analyses via lab-on-a-chip (LOC) devices[9–13], but also indirect impact through the development of novel methodology in the fields that underpin it, such as molecular diagnostics and systems biology, paving the way to greater insights, new applications and personalized medicine[14–17].

While each of these areas faces its own specific challenges, there are several that are shared between them. One of these is the rapid and reliable label-free[4] detection of biomolecular analytes, which has a wide range of applications from the discovery of viruses and antibodies in serum analysis in a clinical setting to the identification and quantification of proteins involved in a given signaling pathway in proteomics research. Due to this vast potential, the development of novel biomolecular sensors ("biosensors") is a key area of current research and many different approaches are currently under investigation [18–39], with several focused on the ultimate goal of detecting single label-free molecules [23, 25, 28, 40–48].

One of the more promising approaches that has received considerable attention in recent years is the use of plasmonic probes for biosensing [19, 22–24, 27, 29–31, 36, 40, 42, 44, 48]. A plasmonic probe is a metallic nano-object (MNO) that exhibits a phenomenon known as localized surface plasmon resonance (LSPR)[5], which manifests in the near-ultraviolet (NUV) to near-infrared (NIR) range of the optical response of the object[6]. LSPR is affected by the local environment around the MNO and so the presence of an analyte will modify its optical response. If this modification can be measured then the analyte can be detected. The sensitivity of a biosensor therefore depends crucially on both the induced

[3] "Theranostic" is a portmanteau of "therapeutic" and "diagnostic" and is used to describe agents that fulfill both purposes simultaneously.

[4] "Label-free" indicates that the target analyte is not modified prior to the detection assay, for example through the integration of radioactive isotopes or fluorescent markers. Such modifications are only possible after manipulation of the analyte, and they often fundamentally change the analyte's nature.

[5] LSPR will be described in detail in chapter 1.

[6] We will show that the spectral position of the LSPR of certain MNOs can be controlled through synthesis parameters, which allows one to e.g. tailor the LSPR to the transparent therapeutic window of biological tissues.

change in the probe's optical response and the ability to measure it.

The aim of the present work has been to develop both a highly sensitive setup to measure the optical response of plasmonic nanoprobes in a liquid environment, and to develop suitable probes for use with this setup for biosensing applications. It has been undertaken as a collaboration between the Clusters and Nanostructures group at the Institute of Light and Matter (ILM) of Université Claude Bernard Lyon 1 (UCBL), who are physicists specializing in the theory and measurement of plasmonic NPs, and the Functional Materials and Photonics group at the Laboratoire de Chimie (LC) of École Normale Supérieure de Lyon (ENS de Lyon), who are chemists with expertise in the design and synthesis of plasmonic NPs.

Because plasmonic biosensors rely on changes in the optical response of MNOs to indicate the presence of target analytes, it is necessary to understand the nature of this response and how it is influenced by various factors such as the size, shape and composition of the MNO and its environment. The underlying theory will therefore be introduced in chapter 1, where it will be shown that the electronic structure of MNOs along with confinement effects ultimately leads to the phenomenon known as LSPR, which may be exploited for sensing applications. We will see how this may be modeled numerically and we will present the results of a numerical investigation into the influence of various factors on LSPR, such as the shape of the object, the presence of a substrate and wetting effects.

Once we have an understanding of the change in the optical response induced by an analyte, we require a way to measure it. Several methods will be briefly discussed in chapter 2 before presenting a detailed overview of spatial modulation spectroscopy (SMS), which is a technique that can be used to measure the optical response of individual nano-objects. This will be followed by a presentation of our work to adapt a SMS setup to measure the optical response of nano-objects in a liquid environment for biosensing applications. This is necessary because most biological reactions are aqueous. The chapter will conclude with the results of initial tests showing that the new setup is able to correctly measure the response of individual MNOs in both air and a liquid environment, and thus the changes between them.

In chapter 3 we will consider the requirements of suitable probes and samples for use with this setup, with an aim towards biosensing applications. We will discuss some of the different probes used in the literature and how they are evaluated. Gold bipyramids (BPs) will be introduced and shown to be promising candidates for biosensing applications. We will discuss their synthesis and how we may vary different parameters to tailor their LSPR for sensing applications. This will be followed by a presentation of a novel protocol to produce stable plasmonic probe samples for SMS measurements in a liquid environment. The chapter will conclude with several studies of different samples produced with this protocol to test their sensitivity and stability. These will show that the protocol is able to produce robust samples that can be used to detect small changes in the refractive index (RI) of a liquid medium via shifts in the LSPR peak of individual NPs.

Finally, we will briefly discuss some initial work that was undertaken in an attempt to exploit interferometric backscattering to increase the sensitivity of plasmonic probes via phase shifts. Some promising preliminary results will be presented along with the basic theory of these measurements.

References

[1] D. M. Eigler and E. K. Schweizer. Positioning single atoms with a scanning tunnelling microscope. *Nature*, 344(6266):524–526, April 1990. ISSN 0028-0836. doi:10.1038/344524a0.

[2] G. Binnig, H. Rohrer, C. Gerber, and E. Weibel. Surface Studies by Scanning Tunneling Microscopy. *Physical Review Letters*, 49(1):57–61, July 1982. doi:10.1103/PhysRevLett.49.57.

[3] G. Binnig, C. F. Quate, and C. Gerber. Atomic Force Microscope. *Physical Review Letters*, 56(9):930–933, March 1986. doi:10.1103/PhysRevLett.56.930.

[4] C. Gerber and H. P. Lang. How the doors to the nanoworld were opened. *Nature Nanotechnology*, 1(1):3–5, October 2006. ISSN 1748-3387. doi:10.1038/nnano.2006.70.

[5] A. G. Filler. The History, Development and Impact of Computed Imaging in Neurological Diagnosis and Neurosurgery: CT, MRI, and DTI. *The Internet Journal of Neurosurgery*, 7(1), December 2009.

[6] P. C. Lauterbur. Image Formation by Induced Local Interactions: Examples Employing Nuclear Magnetic Resonance. *Nature*, 242(5394):190–191, March 1973. ISSN 0028-0836. doi:10.1038/242190a0.

[7] P. Mansfield and P. K. Grannell. "Diffraction" and microscopy in solids and liquids by NMR. *Physical Review B*, 12(9):3618–3634, November 1975. doi:10.1103/PhysRevB.12.3618.

[8] K. Riehemann, S. W. Schneider, T. A. Luger, B. Godin, M. Ferrari, and H. Fuchs. Nanomedicine—Challenge and Perspectives. *Angewandte Chemie International Edition*, 48(5):872–897, January 2009. ISSN 1521-3773. doi:10.1002/anie.200802585.

[9] O. M. Koo, I. Rubinstein, and H. Onyuksel. Role of nanotechnology in targeted drug delivery and imaging: a concise review. *Nanomedicine: Nanotechnology, Biology and Medicine*, 1(3):193–212, September 2005. ISSN 15499634. doi:10.1016/j.nano.2005.06.004.

[10] S. M. Janib, A. S. Moses, and J. A. MacKay. Imaging and drug delivery using theranostic nanoparticles. *Advanced Drug Delivery Reviews*, 62(11):1052–1063, August 2010. ISSN 0169-409X. doi:10.1016/j.addr.2010.08.004.

[11] P. S. Dittrich and A. Manz. Lab-on-a-chip: microfluidics in drug discovery. *Nature Reviews Drug Discovery*, 5(3):210–218, March 2006. ISSN 1474-1776. doi:10.1038/nrd1985.

[12] C. D. Chin, V. Linder, and S. K. Sia. Lab-on-a-chip devices for global health: Past studies and future opportunities. 7(1):41–57, December 2006. ISSN 1473-0189. doi:10.1039/B611455E.

[13] P. Couvreur and C. Vauthier. Nanotechnology: Intelligent Design to Treat Complex Disease. *Pharmaceutical Research*, 23(7):1417–1450, June 2006. ISSN 0724-8741, 1573-904X. doi:10.1007/s11095-006-0284-8.

[14] A. D. Weston and L. Hood. Systems Biology, Proteomics, and the Future of Health Care: Toward Predictive, Preventative, and Personalized Medicine. *Journal of Proteome Research*, 3(2):179–196, April 2004. ISSN 1535-3893. doi:10.1021/pr0499693.

[15] L. Hood, J. R. Heath, M. E. Phelps, and B. Lin. Systems Biology and New Technologies Enable Predictive and Preventative Medicine. *Science*, 306(5696):640–643, October 2004. ISSN 0036-8075, 1095-9203. doi:10.1126/science.1104635.

[16] L. Hood and S. H. Friend. Predictive, personalized, preventive, participatory (P4) cancer medicine. *Nature Reviews Clinical Oncology*, 8(3):184–187, March 2011. ISSN 1759-4774, 1759-4782. doi:10.1038/nrclinonc.2010.227.

[17] S. B. Shinde, C. B. Fernandes, and V. B. Patravale. Recent trends in in-vitro nanodiagnostics for detection of pathogens. *Journal of Controlled Release*, 159(2):164–180, April 2012. ISSN 0168-3659. doi:10.1016/j.jconrel.2011.11.033.

[18] A. Campion and P. Kambhampati. Surface-enhanced Raman scattering. *Chemical Society Reviews*, 27(4):241, 1998. ISSN 0306-0012, 1460-4744. doi:10.1039/a827241z.

[19] K. Aslan, J. R. Lakowicz, and C. D. Geddes. Plasmon light scattering in biology and medicine: new sensing approaches, visions and perspectives. *Current Opinion in Chemical Biology*, 9(5):538–544, October 2005. ISSN 1367-5931. doi:10.1016/j.cbpa.2005.08.021.

[20] J. Wang. Carbon-Nanotube Based Electrochemical Biosensors: A Review. *Electroanalysis*, 17(1):7–14, January 2005. ISSN 1521-4109. doi:10.1002/elan.200403113.

[21] K. E. Sapsford, T. Pons, I. L. Medintz, and H. Mattoussi. Biosensing with Luminescent Semiconductor Quantum Dots. *Sensors*, 6(8):925–953, August 2006. doi:10.3390/s6080925.

[22] K. A. Willets and R. P. Van Duyne. Localized Surface Plasmon Resonance Spectroscopy and Sensing. *Annual Review of Physical Chemistry*, 58(1):267–297, May 2007. ISSN 0066-426X, 1545-1593. doi:10.1146/annurev.physchem.58.032806.104607.

[23] J. N. Anker, W. P. Hall, O. Lyandres, N. C. Shah, J. Zhao, and R. P. Van Duyne. Biosensing with plasmonic nanosensors. *Nature Materials*, 7(6):442–453, June 2008. ISSN 1476-1122. doi:10.1038/nmat2162.

[24] M. E. Stewart, C. R. Anderton, L. B. Thompson, J. Maria, S. K. Gray, J. A. Rogers, and R. G. Nuzzo. Nanostructured Plasmonic Sensors. *Chemical Reviews*, 108(2):494–521, February 2008. ISSN 0009-2665, 1520-6890. doi:10.1021/cr068126n.

[25] F. Vollmer and S. Arnold. Whispering-gallery-mode biosensing: label-free detection down to single molecules. *Nature Methods*, 5(7):591–596, July 2008. ISSN 1548-7091, 1548-7105. doi:10.1038/nmeth.1221.

[26] B. Sepúlveda, P. C. Angelomé, L. M. Lechuga, and L. M. Liz-Marzán. LSPR-based nanobiosensors. *Nano Today*, 4(3):244–251, June 2009. ISSN 1748-0132. doi:10.1016/j.nantod.2009.04.001.

[27] A. Biswas, T. Wang, and A. S. Biris. Single metal nanoparticle spectroscopy: optical characterization of individual nanosystems for biomedical applications. *Nanoscale*, 2(9):1560, 2010. ISSN 2040-3364, 2040-3372. doi:10.1039/c0nr00133c.

[28] D.-K. Lim, K.-S. Jeon, H. M. Kim, J.-M. Nam, and Y. D. Suh. Nanogap-engineerable Raman-active nanodumbbells for single-molecule detection. *Nature Materials*, 9(1): 60–67, January 2010. ISSN 1476-1122. doi:10.1038/nmat2596.

[29] K. M. Mayer and J. H. Hafner. Localized Surface Plasmon Resonance Sensors. *Chemical Reviews*, 111(6):3828–3857, June 2011. ISSN 0009-2665. doi:10.1021/cr100313v.

[30] T. Sannomiya and J. Voeroes. Single plasmonic nanoparticles for biosensing. *Trends in Biotechnology*, 29(7):343–351, July 2011. ISSN 0167-7799. doi:10.1016/j.tibtech.2011.03.003. WOS:000292675700005.

[31] S. Zeng, K.-T. Yong, I. Roy, X.-Q. Dinh, X. Yu, and F. Luan. A Review on Functionalized Gold Nanoparticles for Biosensing Applications. *Plasmonics*, 6(3):491–506, September 2011. ISSN 1557-1955, 1557-1963. doi:10.1007/s11468-011-9228-1.

[32] S. Arnold, V. R. Dantham, C. Barbre, B. A. Garetz, and X. Fan. Periodic plasmonic enhancing epitopes on a whispering gallery mode biosensor. *Optics Express*, 20(24): 26147–26159, November 2012. doi:10.1364/OE.20.026147.

[33] F.-G. Banica. *Chemical sensors and biosensors: fundamentals and applications*. John Wiley & Sons Inc., Chichester, West Sussex, U.K., 2012. ISBN 978-1-118-35416-2 978-1-118-35425-4 978-1-118-35423-0. OCLC: 808366382.

[34] L. Dykman and N. Khlebtsov. Gold nanoparticles in biomedical applications: recent advances and perspectives. *Chem. Soc. Rev.*, 41(6):2256–2282, 2012. ISSN 0306-0012, 1460-4744. doi:10.1039/C1CS15166E.

[35] F. Vollmer and L. Yang. Review Label-free detection with high-Q microcavities: a review of biosensing mechanisms for integrated devices. *Nanophotonics*, 1(3-4), January 2012. ISSN 2192-8614, 2192-8606. doi:10.1515/nanoph-2012-0021.

[36] E. Ringe, B. Sharma, A.-I. Henry, L. D. Marks, and R. P. Van Duyne. Single nanoparticle plasmonics. *Physical Chemistry Chemical Physics*, 15(12):4110, 2013. ISSN 1463-9076, 1463-9084. doi:10.1039/c3cp44574g.

[37] M. Holzinger, A. Le Goff, and S. Cosnier. Nanomaterials for biosensing applications: a review. *Frontiers in Chemistry*, 2, August 2014. ISSN 2296-2646. doi:10.3389/fchem.2014.00063.

[38] S. Schlücker. Surface-Enhanced Raman Spectroscopy: Concepts and Chemical Applications. *Angewandte Chemie International Edition*, 53(19):4756–4795, May 2014. ISSN 1521-3773. doi:10.1002/anie.201205748.

[39] H. Peng, H. Tang, and J. Jiang. Recent progress in gold nanoparticle-based biosensing and cellular imaging. *Science China-Chemistry*, 59(7):783–793, July 2016. ISSN 1674-7291. doi:10.1007/s11426-016-5570-7. WOS:000379509500002.

[40] K. M. Mayer, F. Hao, S. Lee, P. Nordlander, and J. H. Hafner. A single molecule immunoassay by localized surface plasmon resonance. *Nanotechnology*, 21(25):255503, June 2010. ISSN 0957-4484. doi:10.1088/0957-4484/21/25/255503.

[41] S. I. Shopova, R. Rajmangal, S. Holler, and S. Arnold. Plasmonic enhancement of a whispering-gallery-mode biosensor for single nanoparticle detection. *Applied Physics Letters*, 98(24):243104–243104–3, June 2011. ISSN 00036951. doi:doi:10.1063/1.3599584.

[42] I. Ament, J. Prasad, A. Henkel, S. Schmachtel, and C. Sönnichsen. Single Unlabeled

Protein Detection on Individual Plasmonic Nanoparticles. *Nano Letters*, 12(2):1092–1095, February 2012. ISSN 1530-6984, 1530-6992. doi:10.1021/nl204496g.

[43] V. R. Dantham, S. Holler, V. Kolchenko, Z. Wan, and S. Arnold. Taking whispering gallery-mode single virus detection and sizing to the limit. *Applied Physics Letters*, 101(4):043704–043704–4, July 2012. ISSN 00036951. doi:doi:10.1063/1.4739473.

[44] P. Zijlstra, P. M. R. Paulo, and M. Orrit. Optical detection of single non-absorbing molecules using the surface plasmon resonance of a gold nanorod. *Nature nanotechnology*, 7(6):379–382, June 2012. ISSN 1748-3395. doi:10.1038/nnano.2012.51.

[45] V. G. Kravets, F. Schedin, R. Jalil, L. Britnell, R. V. Gorbachev, D. Ansell, B. Thackray, K. S. Novoselov, A. K. Geim, A. V. Kabashin, and A. N. Grigorenko. Singular phase nano-optics in plasmonic metamaterials for label-free single-molecule detection. *Nature Materials*, 12(4):304–309, April 2013. ISSN 1476-1122. doi:10.1038/nmat3537.

[46] M. Piliarik and V. Sandoghdar. Direct optical sensing of single unlabelled proteins and super-resolution imaging of their binding sites. *Nature Communications*, 5, July 2014. ISSN 2041-1723. doi:10.1038/ncomms5495.

[47] M. A. Beuwer, M. W. J. Prins, and P. Zijlstra. Stochastic Protein Interactions Monitored by Hundreds of Single-Molecule Plasmonic Biosensors. *Nano Letters*, 15(5):3507–3511, May 2015. ISSN 1530-6984, 1530-6992. doi:10.1021/acs.nanolett.5b00872.

[48] S. M. E. Peters, M. A. Verheijen, M. W. J. Prins, and P. Zijlstra. Strong reduction of spectral heterogeneity in gold bipyramids for single-particle and single-molecule plasmon sensing. *Nanotechnology*, 27(2):024001, January 2016. ISSN 0957-4484, 1361-6528. doi:10.1088/0957-4484/27/2/024001.

Chapter 1

Optical Response Of Single Gold Nanoparticles: From Basic Theory To A Numerical Investigation

Contents

Introduction

As the ultimate goal of this work is to exploit the optical response of individual gold nano-objects for sensing applications, it is necessary to begin with an exposition of the origin of this response. This chapter begins with a basic description of the electron configuration of the noble metals, with a focus on gold. This configuration will be shown to lead to the electronic band structure that determines the optical response of bulk metal. From there, the optical response of individual noble metallic nano-objects (MNOs) will be considered, in which confinement effects lead to distinctive optical spectra through the phenomenon of localized surface plasmon resonance (LSPR). The quasi-static approximation and Mie theory will be discussed to introduce the basic theory of LSPR.

To investigate how the size, shape and environment of a gold nano-object affect its optical response, we will then turn to numerical simulations. The currently most common numerical methods will be briefly discussed before focusing on generalized Mie theory (GMT) and finite element method (FEM) calculations which have been used in this work[1]. The results of a numerical investigation of the influence of sample substrate, wetting, surfactant films and shape will then be presented and discussed in order to understand the optical response of a real sample prepared by deposition of gold nano-objects on a glass substrate. We will show how these effects may be accounted for in a simple way under some circumstances while allowing the effects of a selected factor to be studied. This is important for the intended sensing applications where the local environment of the probe is often not fully known.

[1] A general note about calculations and analysis in this work: Generalized Mie theory (GMT) calculations[1–3] were performed with unpublished scripts developed by Jean Lermé. Finite element method (FEM) calculations were performed with COMSOL Multiphysics® v. 5.1[4]. The refractive index (RI) values of gold from Johnson and Christy [5] were used in all calculations. Data processing, analysis and visualization were performed with Python using the NumPy/SciPy and Matplotlib modules[6–9]. For a comparison of available RI values, see Billaud [10].

1.1 Intrinsic Optical Response of Noble Metals

To understand the optical response of a single noble MNOs, one must first understand the intrinsic optical response of the metal itself. We therefore begin with a discussion of the electronic structure of the noble metals, which underlies this response. We will show how this structure arises from the electron configuration of individual atoms and consider various optical phenomena that emerge as a consequence. This will lay the groundwork for section 1.2, which will explore how the intrinsic response is modified by size effects to yield the characteristic response of single MNOs.

1.1.1 Electronic Structure

On a basic level, light interacts with matter through the absorption and emission of photons[11, 12], during which the energy of the photon, $h\nu$ is transferred to or from the material via the excitation or relaxation of an electron. When an electron absorbs a photon, it moves to an orbital which differs in energy from the previous orbital by $h\nu$. In the case of emission, the opposite occurs. The optical response of a material is therefore determined by its electrons and orbitals.

The electrons present in a material depend on the electron configurations of the individual atoms that comprise it. The orbitals that exist in the material depend on this configuration too, but also on the way the atoms in the material are arranged and how they interact. This varies widely between different types of materials. In the case of metals, with which we concern ourselves here, the so-called conduction electrons occupy delocalized orbitals that extend throughout the bulk of the material and confer particular properties.

Here we will focus on the electronic structure of a subclass of metals, namely the noble metals. In particular, due to their optical properties in the visible and near-visible range, we will be primarily interested in those of group 11 of the periodic table: copper, silver and gold. The MNOs used in this work have been made of gold so special attention will be paid to it.

Noble Metal	Electronic Configuration
Cu	**[Ar]** $3d^{10}4s^{1}$
Ag	**[Kr]** $4d^{10}5s^{1}$
Au	**[Xe]** $4f^{14}5d^{10}6s^{1}$

Table 1.1: Electronic configuration of the noble metal atoms.[12]

Table 1.1 presents the electronic structure of atomic copper, silver and gold. These three metals each contains a filled (n-1)d shell and a single electron in the ns shell. As atoms are brought together, their outer orbitals overlap and hybridize to form discrete energy levels, the number of which is proportional to the number of atoms brought together, as shown in figure 1.1. While these energy levels remain discrete, the energy difference between them gradually decreases as more atoms are added and they eventually form an effective continuum known as an energy band.[11–13]

Figure 1.1: Principle of orbital hybridization in the noble metals: equivalent orbitals combine to form non-degenerate orbitals of different energy levels. As the number of atoms increases, the distance between these levels decreases until the discrete orbitals form an effective continuum.

Figure 1.2 shows a simplified schematic of the bands that result from the outer electrons of the noble metals. As the ns band widens, it overlaps both energetically and spatially with the widening np band and hybridizes with it to form a single n(sp) band. This n(sp) band is the energetically highest occupied in the resulting crystal at 0 K. It is only partially filled because it arises from the half-filled ns orbital and the 3 empty np orbitals of each atom and thus acts as a conduction band in which the occupying electrons may move almost freely throughout the crystal. Their dispersion relation is consequently parabolic:

$$E(\vec{k}) = \frac{\hbar^2 \vec{k}^2}{2m^*} \tag{1.1}$$

where m^* is the effective mass of the electron. In the case of gold, $m^* \approx m_e$[5]. The energy of the highest occupied orbital in this band is thus the Fermi energy, E_F, which corresponds to the chemical potential at 0 K. In this band, photons may be absorbed over an effectively continuous range as long as the new energy level remains within the band. Such transitions are called intraband transitions and they will be the most interesting in the work that follows because they mediate the optical response in the visible and near-IR range[14].

Below the n(sp) band lies the (n-1)d band, which emerges from the the (n-1)d atomic orbitals. Although this band may overlap energetically with the n(sp) band, they do not hybridize and thus remain separate. The (n-1)d band is of lower energy and completely filled so no intraband transitions are possible. A sufficiently energetic photon, however, may excite an electron from the (n-1)d band to an empty orbital in the n(sp) band via a so-called interband transition if the energy of the photon exceeds the interband energy

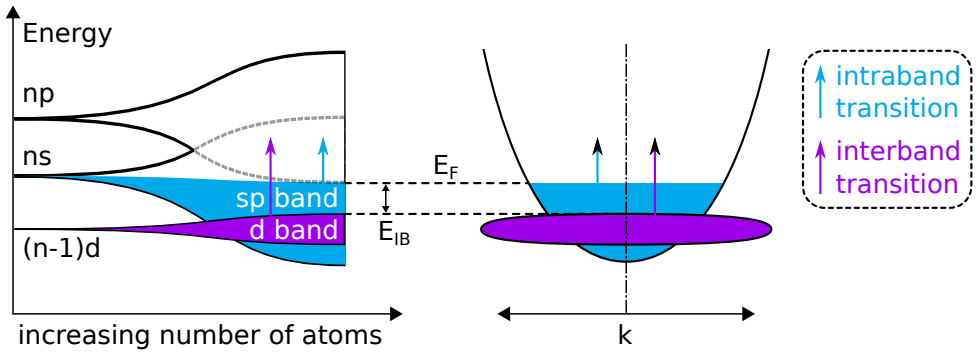

Figure 1.2: Simplified schematic diagram of the band structure and associated dispersion relation of the noble metals. As the solid forms, the separate atomic orbitals coalesce into band structures with effectively continuous energy levels that may overlap to form larger bands as in the case of the ns and np orbitals[11–14]. The band occupancy is represented at 0 K.

threshold, E_{IB}, which is the difference in energy between the Fermi energy and the energy of the highest occupied orbital in the (n-1)d band. For gold and copper, E_{IB} is around 1.9 eV (650 nm) and thus within the visible spectrum whereas for silver it lies in the UV range around 4 eV (310 nm)[5, 14]. Strictly speaking, E_{IB} depends on the orientation of the crystal lattice in monocrystalline structures, and it is minimum at the point X of the Brillouin zone in gold[15], for example. In polycrystalline structures, E_{IB} is effectively averaged over different orientations. We shall see in the following sections how these interband and intraband transitions determine the optical response of a metallic nano-object.

1.1.2 Drude Model

The Drude model[12] provides a basis for understanding the collective electronic behavior under electromagnetic (EM) excitation in the case of simple, non-magnetic metals. In a first approximation, we may consider the conduction electrons of the n(sp) band as quasi-free and non-relativisitic[2]. A single electron that undergoes collisions at an average rate of γ_0 under an oscillating electric field $\vec{E}_0 \exp(-i\omega t)$ obeys the equation of motion

$$m_e \frac{\mathrm{d}^2\vec{r}}{\mathrm{d}t^2} = -e\vec{E}_0 \exp(-i\omega t) - m_e\gamma_0 \frac{\mathrm{d}\vec{r}}{\mathrm{d}t} \tag{1.2}$$

where m_e is the mass of the electron, e is the elementary charge, $\vec{E}_0$ and ω are the strength and angular frequency of the incident field, respectively, and $\vec{r}$ is the position of

[2]The electrons are not subject to magnetic forces or the electric fields of other electrons.

the electron.

For a driven oscillation of angular frequency ω, the steady-state solution takes the form $\vec{r} = \vec{C}\exp(-i\omega t)$ which, solving for $\vec{C}$, yields

$$\vec{C} = \frac{e\vec{E}_0}{m_e\omega(\omega + i\gamma_0)} \tag{1.3}$$

The dipole moment introduced by the displacement of each quasi-free electron is $\vec{p} = -e\vec{r}$ and thus the polarization vector of the material is given by

$$\vec{P}(\omega) = -N_e e\vec{r} = \frac{-N_e e^2}{m_e\omega(\omega + i\gamma_0)}\vec{E}_0\exp(-i\omega t) \tag{1.4}$$

where N_e is the number of electrons per unit volume (e.g. $5.90 \times 10^{28}\,\mathrm{m}^{-3}$ for gold[16]). If we introduce the plasma angular frequency[17]

$$\omega_\mathrm{p} = \sqrt{\frac{N_e e^2}{m_e\varepsilon_0}} \tag{1.5}$$

we may rewrite (1.4) as

$$\vec{P}(\omega, t) = \frac{-\varepsilon_0\omega_\mathrm{p}^2}{\omega(\omega + i\gamma_0)}\vec{E}_0\exp(-i\omega t) = \frac{-\varepsilon_0\omega_\mathrm{p}^2}{\omega(\omega + i\gamma_0)}E(\vec{\omega}, t) \tag{1.6}$$

Recalling the basic definitions of polarization and electric displacement in a linear, isotropic medium[18–21]

$$\vec{P} = \varepsilon_0\chi_\mathrm{e}\vec{E} \tag{1.7}$$

$$\vec{D} = \varepsilon_0\vec{E} + \vec{P} = \varepsilon_0(1 + \chi_\mathrm{e})\vec{E} = \varepsilon_0\varepsilon_\mathrm{r}\vec{E} \tag{1.8}$$

we identify the Drude electric susceptibility, $\chi_\mathrm{e}^\mathrm{D}$, in (1.4) as

$$\chi_\mathrm{e}^\mathrm{D} = \frac{-\omega_\mathrm{p}^2}{\omega(\omega + i\gamma_0)} \tag{1.9}$$

and thus the Drude relative permittivity, $\varepsilon_{\mathrm{r}}^{\mathrm{D}}$, as

$$\varepsilon_{\mathrm{r}}^{\mathrm{D}}(\omega) = 1 - \frac{\omega_{\mathrm{p}}^2}{\omega(\omega + i\gamma_0)} \tag{1.10}$$

Finally, we identify the real and the imaginary components of $\varepsilon_{\mathrm{r}}^{\mathrm{D}}$:

$$\varepsilon_{\mathrm{r},1}^{\mathrm{D}}(\omega) = 1 - \frac{\omega_{\mathrm{p}}^2}{\omega^2 + \gamma_0^2} \approx 1 - \frac{\omega_{\mathrm{p}}^2}{\omega^2} \quad (\text{if } \gamma_0 \ll \omega) \tag{1.11}$$

$$\varepsilon_{\mathrm{r},2}^{\mathrm{D}}(\omega) = \frac{\omega_{\mathrm{p}}^2\gamma_0}{\omega\left(\omega^2 + \gamma_0^2\right)} \approx \frac{\omega_{\mathrm{p}}^2}{\omega^3}\gamma_0 \quad (\text{if } \gamma_0 \ll \omega) \tag{1.12}$$

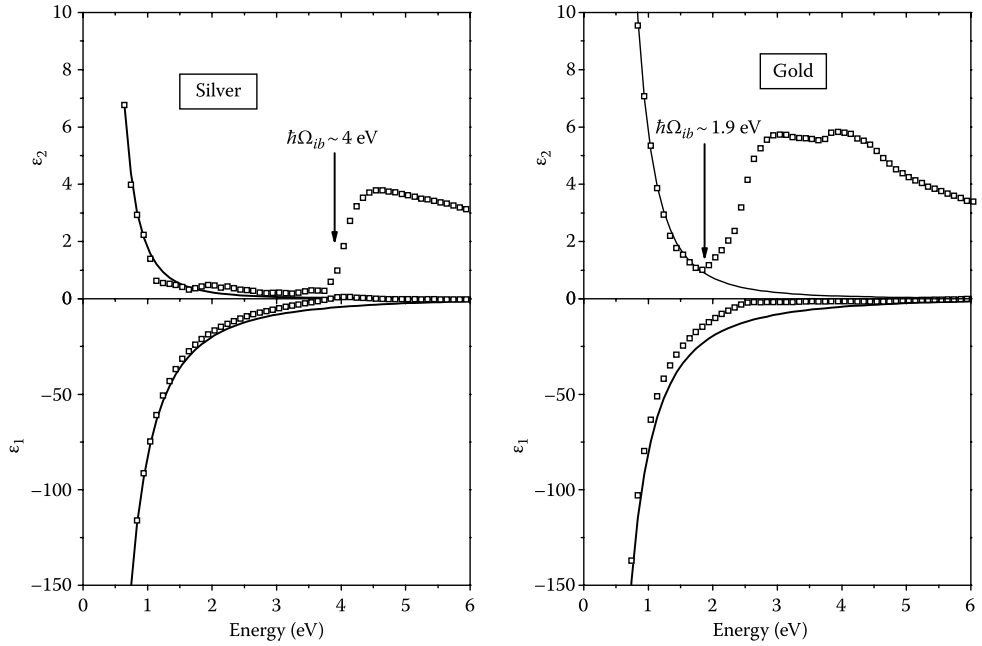

Figure 1.3: The real (ε_1) and imaginary (ε_2) parts of the relative permittivity of silver (left) and gold (right). Comparison of the values calculated by the Drude model (solid lines) to the experimental values of Johnson and Christy [5]. Image source: Cottancin et al. [14].

For metals, approximation of $\gamma_0 \ll \omega$ is valid in the near-UV to near-IR range[14, 22]. Figure 1.3 compares the relative permittivities calculated by the Drude model to those measured by Johnson and Christy [5] for silver and gold. The values are in relatively good agreement in the lower-energy range but the imaginary component diverges considerably towards higher energies due to the interband transitions from the (n-1)d band discussed previously in section 1.1.1. The real component is also affected because of its connection

to the imaginary component via the Kramers-Kronig relations[3][12, 14]. We must take this into account in the relative permittivity with the additional term $\chi_{\mathrm{e}}^{\mathrm{IB}}(\omega)$:

$$\varepsilon_{\mathrm{r}}(\omega) = 1 + \chi_{\mathrm{e}}^{\mathrm{D}}(\omega) + \chi_{\mathrm{e}}^{\mathrm{IB}}(\omega) = \varepsilon_{\mathrm{r}}^{\mathrm{D}}(\omega) + \varepsilon_{\mathrm{r}}^{\mathrm{IB}}(\omega) - 1 \tag{1.13}$$

This additional term may be calculated via e.g. thermomodulation theory[23] or Lindhard theory[12], or determined from experimental measurements[24].

1.1.2.1 Modification Of The Dielectric Function In A Confined System

In the previous derivations, γ_0 represents an intrinsic average collision rate of electrons in the bulk metal. When dealing with nano-objects we must also conceptually account for "collisions" with the surface of the object to obtain a modified collision rate:

$$\gamma(L) = \gamma_0 + g\frac{v_{\mathrm{F}}}{L} \tag{1.14}$$

where L is a characteristic dimension of the nano-object, v_{F} is the Fermi velocity and g is a phenomenological parameter that is often of the order of unity[22, 25–27]. If we replace γ_0 above with $\gamma(L)$ while still accepting that $\gamma(L) \ll \omega$, we see that the surface collisions modify the imaginary part of the Drude relative permittivity (1.12) and, if $\gamma(L) \ll \omega$, the relative permittivity becomes

$$\varepsilon_{\mathrm{r}}(\omega, L) = \varepsilon_{\mathrm{r}}(\omega, \infty) + i\frac{\omega_{\mathrm{p}}^2}{\omega^3} g \frac{v_{\mathrm{F}}}{L} \tag{1.15}$$

The size effect on the imaginary part of ε_{r} is thus inversely proportional to the characteristic dimension of the nano-object. For L above approximately 10 nm, this modification is negligible and $\gamma(L) \approx \gamma_0$.

1.2 Optical Response Of Single Noble Metal Nano-objects

Now that we have considered the optical response of bulk noble metals, we may turn to study the single noble MNOs. We will begin with an overview of the phenomena

[3]These relationships are due to mathematical restrictions of causality in the time domain.

of absorption, scattering and extinction. From there we will move on to the quasi-static approximation and show how this gives rise to the phenomenon of LSPR. We will consider small spheres and ellipsoids in this approximation before continuing to Mie theory to model larger spheres.

1.2.1 Absorption, Scattering and Extinction

Let us consider a MNO that is irradiated by an incident plane wave of the form

$$\vec{E}_{\text{inc}}(\vec{r},t) = \vec{E}_0 \exp\left(i\left(\vec{k}\cdot\vec{r} - \omega t\right)\right) \tag{1.16}$$

as depicted in figure 1.4. If the object is in a non-absorbing, non-magnetic medium of RI $n = \sqrt{\varepsilon_{\text{m}}}$ then the average incident irradiance I_{inc} is

$$I_{\text{inc}} = \frac{1}{2}\varepsilon_0 n c E_0^2 \tag{1.17}$$

were c is the velocity of light in a vacuum. Some of the light interacts with the object and transfers energy to it. This energy is either scattered (i.e. re-emitted as radiation) or absorbed and dissipated. We denote the scattered power P_{sca} and absorbed power P_{abs}. Their sum is the total power "lost" by the incident irradiation and is therefore called the "extinction". We therefore define the extinguished power as $P_{\text{ext}} = P_{\text{sca}} + P_{\text{abs}}$.

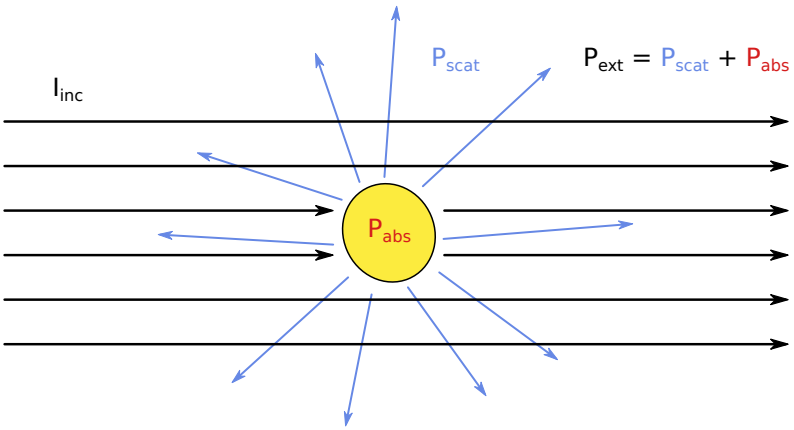

Figure 1.4: Schematic diagram of absorption and scattering of a nanoparticle under exposure to incident radiation.

For irradiances that do not induce non-linear effects, P_{abs} and P_{sca} and thus P_{ext} are proportional to I_{inc} and we may therefore define optical cross-sections for a given object

as the ratio between these values:

$$\sigma_{\text{abs}} = \frac{P_{\text{abs}}}{I_{\text{inc}}} \tag{1.18}$$

$$\sigma_{\text{sca}} = \frac{P_{\text{sca}}}{I_{\text{inc}}} \tag{1.19}$$

$$\sigma_{\text{ext}} = \frac{P_{\text{ext}}}{I_{\text{inc}}} = \frac{P_{\text{abs}} + P_{\text{sca}}}{I_{\text{inc}}} = \sigma_{\text{abs}} + \sigma_{\text{sca}} \tag{1.20}$$

It should be noted here that although σ_{abs}, σ_{sca} and σ_{ext} have the units of area, they do not represent real geometric cross-sections. As a conceptual aid, they may be thought of as the cross-section of an idealized perfectly absorbing or perfectly scattering material, respectively, but they are really just proportionality coefficients.

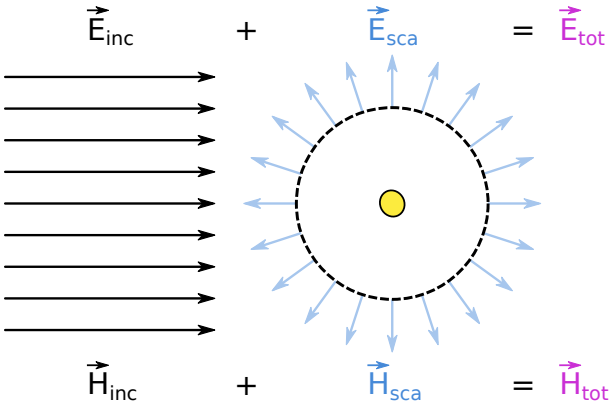

Figure 1.5: The total far-field around a NP is the sum of the incident and scattered field. These may be used to compute the total energy flux over an imaginary surface far away from the NP.

We may derive expressions for these cross-sections by considering the EM fields around a nanoparticle (NP) in a non-absorbing medium[19] (figure 1.5). The total electric field is the sum of the incident and scattered electric fields and an equivalent relationship holds for the total magnetic field:

$$\vec{E}_{\text{tot}} = \vec{E}_{\text{inc}} + \vec{E}_{\text{sca}} \tag{1.21}$$

$$\vec{H}_{\text{tot}} = \vec{H}_{\text{inc}} + \vec{H}_{\text{sca}} \tag{1.22}$$

The EM energy flux through an arbitrary surface A is $P = \iint_A \left\langle \vec{S}_{\text{tot}} \right\rangle \cdot \vec{n}\, \mathrm{d}A$ where $\vec{n}$ is the

surface normal vector in the direction to be calculated and $\left\langle \vec{S}_{\text{tot}} \right\rangle$ is the time-averaged Poynting vector of the total field:

$$\begin{aligned}
\left\langle \vec{S}_{\text{tot}} \right\rangle &= \frac{1}{2}\,\text{Re}\Big(\vec{E}_{\text{tot}} \times \vec{H}^{*}_{\text{tot}}\Big) \\
&= \frac{1}{2}\,\text{Re}\Big(\Big(\vec{E}_{\text{inc}} + \vec{E}_{\text{sca}}\Big) \times \Big(\vec{H}_{\text{inc}} + \vec{H}_{\text{sca}}\Big)^{*}\Big) \\
&= \frac{1}{2}\,\text{Re}\Big(\vec{E}_{\text{inc}} \times \vec{H}^{*}_{\text{inc}}\Big) + \frac{1}{2}\,\text{Re}\Big(\vec{E}_{\text{sca}} \times \vec{H}^{*}_{\text{sca}}\Big) + \frac{1}{2}\,\text{Re}\Big(\vec{E}_{\text{inc}} \times \vec{H}^{*}_{\text{sca}} + \vec{E}_{\text{sca}} \times \vec{H}^{*}_{\text{inc}}\Big) \\
&= \left\langle \vec{S}_{\text{inc}} \right\rangle + \left\langle \vec{S}_{\text{sca}} \right\rangle + \left\langle \vec{S}_{\text{ext}} \right\rangle
\end{aligned} \tag{1.23}$$

where we have introduced the Poynting vectors of the incident field ($\left\langle \vec{S}_{\text{inc}} \right\rangle$) and the scattered field ($\left\langle \vec{S}_{\text{sca}} \right\rangle$), along with an interaction term that we will treat as Poynting vector ($\left\langle \vec{S}_{\text{ext}} \right\rangle$).

Because the medium is non-absorbing, the net energy inward through an imaginary surface around the object will be equal to the absorption and thus by (1.23) we have:

$$\begin{aligned}
P_{\text{abs}} &= \iint_A \left\langle \vec{S}_{\text{tot}} \right\rangle \cdot \vec{n}\,\mathrm{d}A \\
&= \iint_A \left\langle \vec{S}_{\text{inc}} \right\rangle \cdot \vec{n}\,\mathrm{d}A + \iint_A \left\langle \vec{S}_{\text{sca}} \right\rangle \cdot \vec{n}\,\mathrm{d}A + \iint_A \left\langle \vec{S}_{\text{ext}} \right\rangle \cdot \vec{n}\,\mathrm{d}A \\
&= 0 - P_{\text{sca}} + \iint_A \left\langle \vec{S}_{\text{ext}} \right\rangle \cdot \vec{n}\,\mathrm{d}A
\end{aligned} \tag{1.24}$$

where $\iint_A \left\langle \vec{S}_{\text{inc}} \right\rangle \cdot \vec{n}\,\mathrm{d}A$ vanishes identically. The sign of P_{sca} is negative because the scattered power, which is a positive quantity, is defined as the power radiated outward from the NP. By definition, $P_{\text{ext}} = P_{\text{abs}} + P_{\text{sca}}$ and so we identify P_{ext}:

$$P_{\text{ext}} = \iint_A \left\langle \vec{S}_{\text{ext}} \right\rangle \cdot \vec{n}\,\mathrm{d}A \tag{1.25}$$

where $\vec{n}$ is the inward-facing normal vector. By (1.23), we see that the extinction is formally due to interference between the incident and the scattered fields in the classical

EM model.

For an incident electric field polarized along $\hat{e}_x$, general expressions can be derived for the cross-sections[19]

$$\sigma_{\text{ext}} = \frac{4\pi}{k^2}\,\text{Re}\left(\left(\vec{X}\cdot\hat{e}_x\right)_{\theta=0}\right) \tag{1.26}$$

$$\sigma_{\text{sca}} = \iint_{4\Omega}\frac{\left|\vec{X}\right|^2}{k^2}\,\text{d}\Omega \tag{1.27}$$

where $\vec{X}$ is the vector scattering amplitude. The absorption cross-section may be determined from (1.26) and (1.27) as $\sigma_{\text{abs}} = \sigma_{\text{ext}} - \sigma_{\text{sca}}$.

1.2.2 Quasi-Static Approximation: Localized Surface Plasmon Resonance

The optical response of a metal confined at the nanoscale leads to the emergence of novel properties such as the localized surface plasmon resonance (LSPR). In this section we will show how the quasi-static approximation can be used to model the optical response of small metal spheres and ellipsoids and we will see, in a simple way, how the phenomenon of LSPR can occur. We begin by considering the case of spheres.

1.2.2.1 Spheres

To derive expressions for the optical cross-sections, consider what occurs when a spherical MNO of relative permittivity ε_{r} is irradiated with a plane wave as depicted in figure 1.6. If the radius of the object is much smaller than the incident wavelength ($R \ll \lambda$), the object experiences an effectively uniform oscillating field throughout its volume. Within this field, the electrons oscillate collectively about the crystal lattice and the object may be approximated as an oscillating dipole.

By solving Maxwell's equations for an incident field $\vec{E}_{\text{inc}}(t)$ inside and outside of the object embedded in a non-absorbing medium of relative permittivity ε_{m}, an expression for the internal field of a spherical MNO of radius R can be derived[14]:

$$\vec{E}_{\text{NP}}(\omega,t) = 3\frac{\varepsilon_{\text{m}}}{\varepsilon_{\text{r}}(\omega)+2\varepsilon_{\text{m}}}\vec{E}_{\text{inc}}(t) \tag{1.28}$$

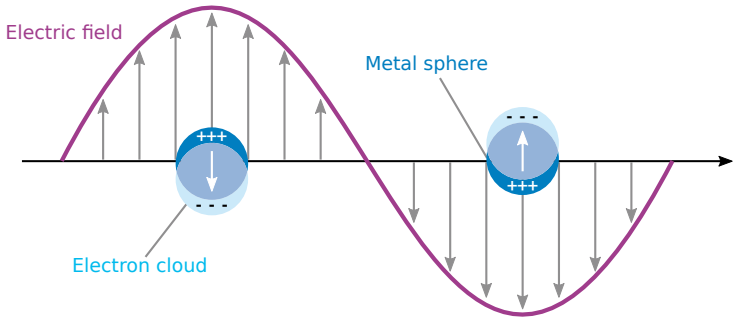

Figure 1.6: Schematic overview of localized surface plasmon resonance in a spherical NP exposed to an EM plane wave. When the size of the NP is much less than the wavelength, the NP experiences an effectively uniform field which drives the oscillation. This is the quasi-static approximation. Source: adaptation of a figure from Willets and Van Duyne [28]

The dipole moment $\vec{p}$ of the fictitious point dipole is then

$$\vec{p}(\omega,t) = \left(\frac{4}{3}\pi R^3\right)\varepsilon_0\varepsilon_\mathrm{m}3\left(\frac{\varepsilon_\mathrm{r}-\varepsilon_\mathrm{m}}{\varepsilon_\mathrm{r}+2\varepsilon_\mathrm{m}}\right)\vec{E}_\mathrm{inc}(t) = \alpha(\omega)\vec{E}_\mathrm{inc}(t) \tag{1.29}$$

where $\alpha(\omega)$ is the dynamic polarizability of the MNO. The external near field is the sum of the incident field $\vec{E}_\mathrm{inc}$ and the field produced by the point dipole $\vec{p}$. The imaginary part of the polarizability accounts for energy absorption within the object via the expression $\frac{1}{2}E_0^2\omega\,\mathrm{Im}(\alpha)$, from which we may calculate σ_abs[14]:

$$\sigma_\mathrm{abs}(\omega) = \frac{9\omega\varepsilon_\mathrm{m}^{3/2}}{c}V\frac{\varepsilon_{\mathrm{r},2}(\omega)}{\left(\varepsilon_{\mathrm{r},1}(\omega)+2\varepsilon_\mathrm{m}\right)^2+\varepsilon_{\mathrm{r},2}(\omega)^2} \tag{1.30}$$

where V is the volume of the object and $\varepsilon_{\mathrm{r},1}$ and $\varepsilon_{\mathrm{r},2}$ are the real and imaginary components of the relative permittivity. As the dipole oscillates under the incident irradiation, it will created a scattered far field described by[19]

$$\vec{E}_\mathrm{sca} = \frac{\exp(ikr)}{-ikr}\frac{ik^3}{4\pi\varepsilon_\mathrm{m}}\hat{e}_r\times(\hat{e}_r\times\vec{p}) \tag{1.31}$$

From this expression, it is possible to determine the interference with the incident field $\vec{E}_\mathrm{inc}$ and derive expressions via (1.27) and (1.26) for σ_sca and σ_ext[14, 19], respectively, as functions of the angular frequency or the wavelength:

$$\begin{aligned}\sigma_{\mathrm{sca}}(\omega) &= \frac{3\omega^4\varepsilon_{\mathrm{m}}^2}{2\pi c^4}V^2\frac{\left(\varepsilon_{\mathrm{r},1}(\omega)-\varepsilon_{\mathrm{m}}\right)^2+\varepsilon_{\mathrm{r},2}(\omega)^2}{\left(\varepsilon_{\mathrm{r},1}(\omega)+2\varepsilon_{\mathrm{m}}\right)^2+\varepsilon_{\mathrm{r},2}(\omega)^2} \\ \sigma_{\mathrm{sca}}(\lambda) &= \frac{24\pi^3\varepsilon_{\mathrm{m}}^2}{\lambda^4}V^2\frac{\left(\varepsilon_{\mathrm{r},1}(\lambda)-\varepsilon_{\mathrm{m}}\right)^2+\varepsilon_{\mathrm{r},2}(\lambda)^2}{\left(\varepsilon_{\mathrm{r},1}(\lambda)+2\varepsilon_{\mathrm{m}}\right)^2+\varepsilon_{\mathrm{r},2}(\lambda)^2}\end{aligned} \tag{1.32}$$

$$\begin{aligned}\sigma_{\mathrm{ext}}(\omega) \approx \sigma_{\mathrm{abs}}(\omega) &\approx \frac{9\omega\varepsilon_{\mathrm{m}}^{3/2}}{c}V\frac{\varepsilon_{\mathrm{r},2}(\omega)}{\left(\varepsilon_{\mathrm{r},1}(\omega)+2\varepsilon_{\mathrm{m}}\right)^2+\varepsilon_{\mathrm{r},2}(\omega)^2} \\ \sigma_{\mathrm{ext}}(\lambda) \approx \sigma_{\mathrm{abs}}(\lambda) &\approx \frac{18\pi\varepsilon_{\mathrm{m}}^{3/2}}{\lambda}V\frac{\varepsilon_{\mathrm{r},2}(\lambda)}{\left(\varepsilon_{\mathrm{r},1}(\lambda)+2\varepsilon_{\mathrm{m}}\right)^2+\varepsilon_{\mathrm{r},2}(\lambda)^2}\end{aligned} \tag{1.33}$$

The scattering cross-section is proportional to the square of the volume and inversely proportional to the fourth power of the wavelength, which corresponds to the Rayleigh scattering. For a spherical NP of fixed radius R, $\frac{\sigma_{\mathrm{sca}}}{\sigma_{\mathrm{ext}}} \propto \frac{R^3}{\lambda^3}$. Consequently, it is clear that within the quasi-static approximation ($R \ll \lambda$), the extinction is dominated by absorption.

The expressions for the cross-sections given by (1.30), (1.32) and (1.33) show that they will be enhanced when the term in the denominator tends towards zero. Recalling the expressions (1.11) and (1.12) derived within the Drude model for the relative permittivity under the approximation $\gamma(L) \ll \omega$, along with the modification (1.13), we see that this will occur when $\varepsilon_{\mathrm{r},1}(\omega) + 2\varepsilon_{\mathrm{m}}$ is minimized. For metals in which $\varepsilon_{\mathrm{r},1} < 0$, this value may approach zero at the angular frequency ω_{lspr} that satisfies

$$\omega_{\mathrm{lspr}} \approx \frac{\omega_{\mathrm{p}}}{\sqrt{\varepsilon_{\mathrm{r},1}^{\mathrm{IB}}(\omega)+2\varepsilon_{\mathrm{m}}}} \tag{1.34}$$

When the angular frequency of the incident field is ω_{lspr}, the collective oscillation of the conduction electrons exhibit resonance. This is the phenomenon known as localized surface plasmon resonance (LSPR) that appears in optical spectra. Examples are presented in figure 1.7 for silver and gold spheres with a radius of 5 nm. In the case of the silver NP, a strong and narrow peak appears around 350 nm. In the case of the gold NP, the peak appears around 510 nm and is much weaker. The interband transitions are visible to the left of the LSPR peak for gold and these serve to damp the resonance.

We note that the expressions for the cross-sections only account for size effects through a

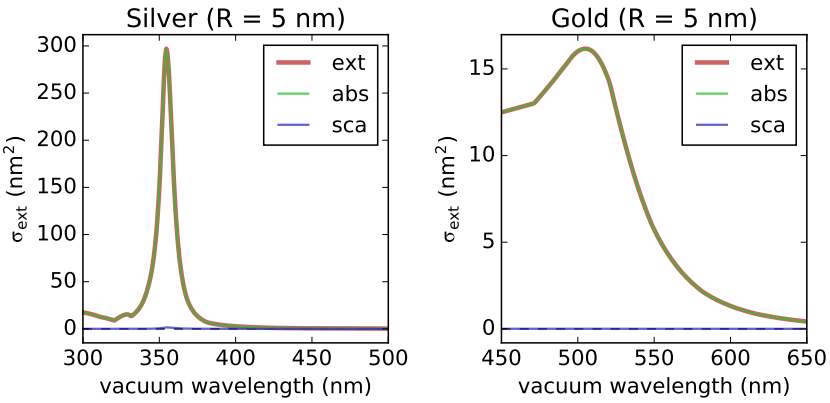

Figure 1.7: Extinction, absorption and scattering cross-sections of a silver and a gold sphere of radius 5 nm in air ($n = 1$). For small sizes, the scattering is negligible.

constant of proportionality (V for σ_{abs} and σ_{ext} and V^2 for σ_{sca}). Nevertheless, size effects may be included through modification of the dielectric function $\varepsilon_{\text{r}}(\omega, L)$: (1.15).

1.2.2.2 Ellipsoids

The scattering and extinction cross-sections of ellipsoidal NPs of small size (compared to the wavelength), subjected to an incident field polarized along one of its principal axes, can be calculated analytically in the quasi-static approximation[14, 19]. The extinction cross-section, which is approximately equal to the absorption cross-section, for each axis i is given by

$$\sigma_{\text{ext},i}(\lambda) \approx \sigma_{\text{abs},i}(\lambda) = \frac{2\pi\varepsilon_{\text{m}}^{3/2}}{\lambda}\frac{V}{L_i^2}\frac{\varepsilon_{\text{r},2}(\lambda)}{\left(\varepsilon_{\text{r},1}(\lambda) + \varepsilon_{\text{m}}\frac{1-L_i}{L_i}\right)^2 + \varepsilon_{\text{r},2}(\lambda)^2} \tag{1.35}$$

where $V = \frac{4}{3}\pi abc$ is the volume of the ellipsoid with semi-axes a, b and c and L_i is a geometrical factor given by

$$L_i = \frac{abc}{2}\int_0^\infty \frac{\mathrm{d}u}{\left(u + l_i^2\right)\sqrt{(u+a^2)^2(u+b^2)^2(u+c^2)^2}} \tag{1.36}$$

where l_i denotes the semi-axis a, b or c along which the incident field $\vec{E}_{\text{inc}}$ is polarized. $L_a + L_b + L_c = 1$ so for the case of a sphere, $L_a = L_b = L_c = 1/3$.

In a first approximation, the resonance condition for excitation along the axis i is $L_i\varepsilon_{\mathrm{r},1}(\lambda)+(1-L_i)\varepsilon_{\mathrm{m}}=0$. This condition will be different for axes of different length. Consequently, up to 3 resonances may be exhibited when $\vec{E}_{\mathrm{inc}}$ is not polarized along a principle axis. For axes of equal length, the resonance will be degenerate. If all three are equal, the case of the sphere is recovered.

Figure 1.8 shows the optical response along the long and short axes of an oblate ($a < b = c$) spheroid with a volume equivalent to a sphere of radius 5 nm. As the aspect ratio $ar = b/a$ increases, the LSPR response due to an electric field polarized along the long axis red-shifts and increases as it escapes the damping induced by the coupling with the interband transitions. The opposite occurs for polarization along the short axis. These tendencies are general and will be seen later for larger NPs.

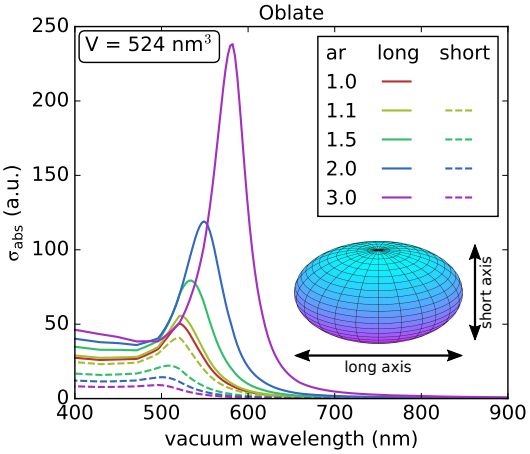

Figure 1.8: Absorption spectra in water ($n = 1.33$) of gold spheroids of different aspect ratio $ar = b/a$ with constant volume equivalent to a sphere of radius 5 nm. For each ar, the spectrum is shown for light polarized along both the long and the short axis.

1.2.3 Mie Theory

The preceding discussion has focused on the quasi-static approximation in which the dimension of the MNO is significantly shorter than the wavelength of the incident field along the direction of propagation. This approximation treats the field as uniform throughout the object and thus considers only the dipolar modes of excitation where the electrons oscillate collectively.

If the object's dimensions are comparable to the wavelength, the object experiences an increasingly heterogeneous field that may induce higher-order resonance modes such as the quadripolar mode shown in figure 1.9. The excitation of these modes is not exclusive and

multiple modes may be excited simultaneously to different degrees for a given wavelength. The quasi-static approximation is thus no longer valid for larger objects and a different approach is required.

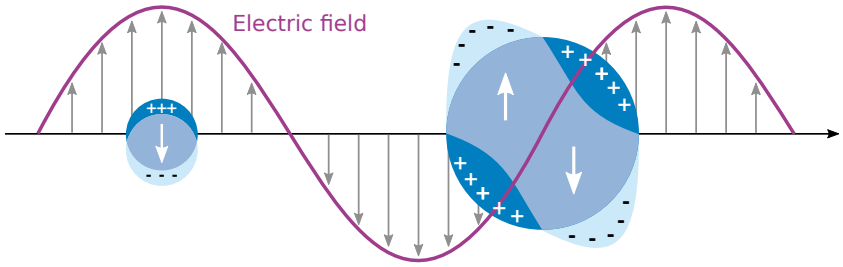

Figure 1.9: Schematic overview of dipolar and quadripolar modes of a nanoparticle under incident radiation. When the dimension of the object is of the same order or greater than the wavelength, the quasi-static approximation is no longer valid and higher-order modes are excited, such as the quadripolar mode represented on the right. Note that the figure is only schematic and not an accurate representation of electron distribution.

The optical response of spherical[4] objects of arbitrary size can be calculated using Mie theory[19, 33–35], which uses multipolar developments of the fields to derive analytical equations for the object's cross-sections. In a homogeneous, non-absorbing medium, the resulting $\vec{E}$ and $\vec{H}$ fields are solenoidal ($\vec{\nabla}\cdot\vec{\Psi} = 0$) and satisfy the Helmholtz wave equation ($\nabla^2\vec{\Psi} + k^2\vec{\Psi} = 0$). They also preserve the tangential components of the vector fields across surface boundaries in accordance with Maxwell's equations. Within the framework of Mie theory, solutions to these equations are expressed as linear combinations of the vector spherical harmonics (VSH) $\left\{\vec{M}_{nm}, \vec{N}_{nm}\right\}$[14, 19, 34–36] where the integer indices ($n, m \in \mathbb{Z},\ n \geq 1,\ -n \leq m \leq n$) determine the form of each VSH function. These functions form an orthonormal basis that can be used to develop the incident, internal and scattered fields to an arbitrary order.

Using the notation conventions of Bohren and Huffman [19], the following expressions may be derived for σ_{ext} and σ_{sca} by calculating the energy flux over an imaginary surface that encloses the NP:

[4]Extensions of the theory exist to treat infinite cylinders[29] and spheroids[30–32]. While both provide analytical insights into the absorption and scattering of these shapes, they are of limited practical use. The former is restricted to unphysical systems of infinite circular cylinders while the latter suffers from computational complexity. Neither will be used in this work.

$$\begin{aligned}\sigma_{\text{ext}} &= \frac{1}{2I_{\text{inc}}} \iint_A \text{Re}\left(\vec{E}_{\text{inc}} \times \vec{H}^*_{\text{sca}} + \vec{E}_{\text{sca}} \times \vec{H}^*_{\text{inc}}\right) \cdot \text{d}\vec{A} \\ &= \frac{1}{I_{\text{inc}}} \iint_A \left\langle \vec{S}_{\text{ext}} \right\rangle \cdot \text{d}\vec{A} \\ &= \frac{2\pi}{k^2} \sum_{n=1}^{\infty} (2n+1)\,\text{Re}(a_n + b_n)\end{aligned} \tag{1.37}$$

$$\begin{aligned}\sigma_{\text{sca}} &= \frac{1}{2I_{\text{inc}}} \iint_A \text{Re}\left(\vec{E}_{\text{sca}} \times \vec{H}^*_{\text{sca}}\right) \cdot \text{d}\vec{A} \\ &= \frac{1}{I_{\text{inc}}} \iint_A \left\langle \vec{S}_{\text{sca}} \right\rangle \cdot \text{d}\vec{A} \\ &= \frac{2\pi}{k^2} \sum_{n=1}^{\infty} (2n+1)\left(|a_n|^2 + |b_n|^2\right)\end{aligned} \tag{1.38}$$

where we have identified $\left\langle \vec{S}_{\text{ext}} \right\rangle$ and $\left\langle \vec{S}_{\text{sca}} \right\rangle$ from (1.23). The expression for a_n and b_n may be found in Bohren and Huffman [19]. It can be shown that the different orders correspond to the order of polarity of different resonant modes, with the first order corresponding to the dipolar mode[19]. The contribution of the dipolar mode may be expanded in a power series in terms of R/λ. When $R/\lambda \ll 1$, all terms beyond the lowest may be discarded to recover the quasi-static approximation.

Figure 1.10 shows the extinction, absorption and scattering cross-sections of 3 gold spheres with radii 5 nm, 25 nm and 50 nm calculated with Mie theory. As the radius increases, scattering, which initially scales as V^2, begins to contribute significantly to the extinction and causes the extinction to red-shift.

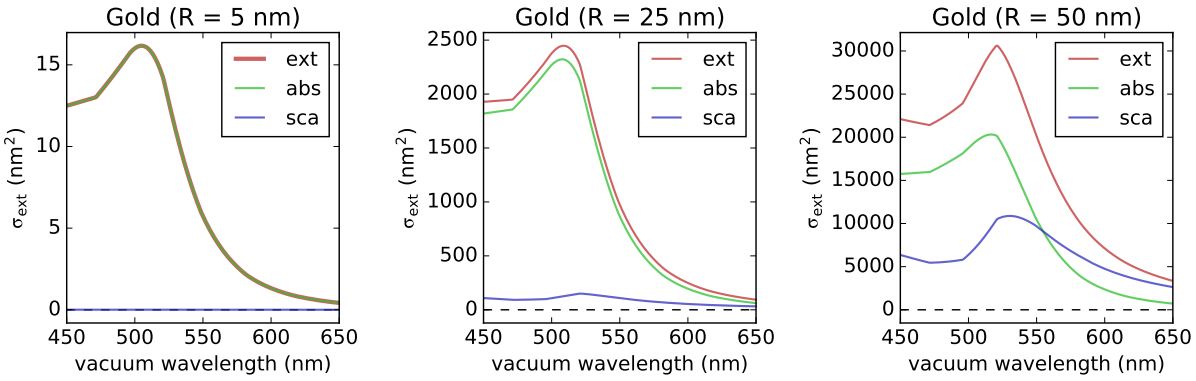

Figure 1.10: Extinction, absorption and scattering cross-sections of golds sphere of radii 5 nm, 25 nm and 50 nm in air ($n = 1$). [GMT calculations]

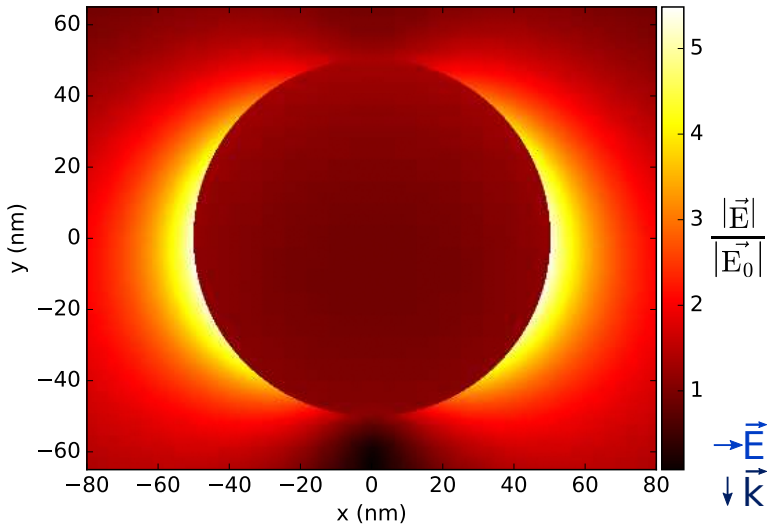

Figure 1.11: The relative enhancement of the electric field around a gold nanosphere of radius 50 nm at LSPR in air. The field is enhanced at the poles along the axis of oscillation.

Mie theory can be used to calculate the exact EM field around a spherical object. The field intensity at 525 nm around a gold sphere of radius 50 nm is presented in figure 1.11. Here we see the so-called "hot-spots" where the electric field is strongly enhanced outside of the object along the axis of polarization. This enhancement is common to plasmonic NPs of all shapes and it makes the LSPR sensitive to the dielectric environment around the NP[37–40]. As we shall see, this sensitivity and how it can be exploited lie at the core of this work.

Now that we have explored the origin of the LSPR, we will investigate various factors that may affect it through a numerical study. To do so, numerical methods to calculate the optical response of objects beyond spheres and ellipsoids will be presented. For further development of the theory of the absorption and scattering of light by MNOs, the interested reader is referred to the original article by Mie [33] and works such as Bohren and Huffman [19], van de Hulst [34], Mishchenko et al. [41], Mishchenko et al. [35], Cottancin et al. [14] and Fox [17],

1.3 Investigation Of Environment And Shape Effects: A Numerical Study

With an understanding of the optical response of MNOs, we now wish to investigate various effects that we may expect to see when studying real systems of objects deposited

on a glass substrate. As we shall see in section 2, our experimental technique measures the extinction cross-section so we shall mostly limit our considerations to σ_{ext} here except in those cases where σ_{abs} and σ_{sca} may provide critical insights into the behavior of the system.

We begin with a brief overview of the methods available for numerical simulations of plasmonic NPs.

1.3.1 Numerical Methods

The previous analytical models are insightful but limited in their direct applicability to real systems. The samples in this work are fabricated by the deposition of chemically synthesized MNOs on glass substrates. The resulting systems include dielectric interfaces, surface wetting effects, surfactant films, impurities, etc. To begin to deal with this complexity, computer simulations are necessary and so in this section we will give an overview of the most common numerical methods currently used to model plasmonic NPs.

We will begin with generalized Mie theory (GMT) calculations, which are analytical and able to yield exact solutions but are limited in the geometries that can be modeled. We will then present a very brief overview of the currently most common numerical methods for simulating more complex shapes and systems along with an explanation of the choice to use the finite element method (FEM) to simulate systems in this work. The accuracy of FEM calculations will then be confirmed through comparison to analytical GMT calculations.

1.3.1.1 Generalized Mie Theory

The Mie theory of section 1.2.3 is analytical and can be used to calculate the absorption, scattering and extinction cross-sections of MNOs with arbitrary precision, but it is limited to spherical objects in homogeneous media. Generalized Mie theory (GMT) is an extension of Mie theory that is able to handle additional cases through further development of the spherical harmonic expansion technique of standard Mie theory. It can be used to simulate multi-layered spherical objects such as core-shell systems, an arbitrary number of interacting spheres (although the calculations become prohibitively complex as the number of spheres grows), and spherical objects near a dielectric interface. GMT can thus be used to study a system such as a gold nanosphere deposited on a glass substrate with a homogeneous coating of water or surfactant.

The GMT calculations in this work are based on Fucile et al. [42], Wriedt and Doicu [43] and recent work by Lermé et al.[1–3] that provides analytical solutions using the multipolar expansion method to extend GMT to systems of multi-layered spherical objects near

dielectric interfaces between different isotropic, non-absorbing media. In the formalism of this approach, the reflected scattered field and its interactions with the NP are calculated exactly. As a conceptual approximation, this interaction may be modeled as the interaction between the NP and its image below the interface. In the quasi-static approximation, this interaction can be quantified within the plasmon hybridization model[1, 3]. In this case, the key difference from a real dimer model is that the image particle's fictitious surface charge density is locked to that of the real object.

The advantage of GMT calculations is that they are both analytical and very fast with a modern desktop computer. Full extinction, absorption and scattering cross-sections can be calculated to arbitrary precision in just a few seconds. The main limitation is that, like standard Mie theory, it is limited to objects of spherical symmetry. It is therefore necessary to employ other methods to study most real systems that are intractable by GMT.

1.3.1.2 Other Numerical Methods

In order to study objects beyond spheres one must look to numerical approaches. Currently the most common techniques of numerical simulation, in no particular order, are the Transition Matrix "null-field" (T-Matrix) method, the discrete dipole approximation (DDA) method, the finite-difference time-domain (FDTD) method and the finite element method (FEM). A review and comparison of these techniques may be found in Parsons et al. [44].

Briefly, the Transition Matrix "null-field" (T-Matrix) method discretizes the object of interest into a finite number of point sources on its surface that scatter the incident wave. It requires the same order of computation time as GMT (a few milliseconds per frequency point) and is therefore very rapid while supporting a wide range of geometries as well as substrate interaction, but calculations are numerically unstable for certain geometries due to matrix truncation and the accumulation of rounding errors.

The discrete dipole approximation (DDA) method discretizes the same object into a regular 3D array of finite cubic elements where each element is treated as a dipole that is coupled to its nearest neighbors. The induced dipole moment of each element is then calculated and used to determine the scattered field. This method is about an order of magnitude slower than GMT and the T-Matrix method. Although it can be applied to a wide range of geometries, the regularity of the 3D array is not adapted to objects with fine features and it may not converge for objects with high aspect ratios or large refractive indices.

The finite-difference time-domain (FDTD) method discretizes the system to be studied in both time and space and then iteratively steps through time until it converges to a steady-state solution. Although applicable to arbitrary shapes, this method is about

another order of magnitude slower (∼3 hours for a full spectrum) than the DDA method and requires permittivity values not only for the studied frequencies but also for those beyond, which may be empirically unavailable.

Finally, FEM calculations discretize the object's geometry irregularly with finer granularity around edges and curves which permits the study of arbitrary shapes. Helmholtz's equations are then solved in the frequency domain with respect to boundary conditions (continuous tangential components across surfaces and far-field decay). FEM calculations are generally about 3 times slower than the DDA method for simple meshes and considerably slower for more complicated meshes.

Given the intention of the present study to investigate a wide variety of shapes in different environments, along with existing expertise in our group, FEM was selected as the method of numerical computation. Calculations were performed with COMSOL Multiphysics® v. 5.1[4] using the RF module to model 3D systems. All systems were modeled with a spherical environment surrounded by a perfectly matched layer (PML). The model calculates the scattered field from the NP in the presence of an applied background field. The extinction, scattering and absorption cross-sections are calculated by integrating the Poynting vectors described in (1.23) over an imaginary surface that contains the object. The absorption cross-section can also be calculated by integrating the local absorption over the volume of the NP, which gives the same results as integrating the total Poynting vector over the surface or taking the difference $\sigma_{\text{ext}} - \sigma_{\text{sca}}$. For systems without a dielectric interface, the background field is set equal to the field of an incident plane wave. For systems with interfaces, the reflected and transmitted fields are calculated analytically using the Fresnel equations (see section 1.3.2.1). The background field is then set as the sum of the incident and reflected fields in front of the interface and as the transmitted field behind it.

1.3.1.3 Comparison of GMT and FEM Calculations

Before moving on to other shapes, the accuracy of a numerical method should be determined by comparing its results for spherical objects to the values predicted by GMT, which is an analytical method and therefore a standard reference for such comparisons. It has been shown that FEM is able to accurately calculate the absorption, scattering and extinction cross-sections of spherical MNOs in homogeneous media[45, 46]. Here we are interested in exploring the accuracy of FEM calculations that seek to model the optical response of objects near an interface between two media of different real refractive indices.

To do this, we choose to model a system of a gold nanosphere with a radius of 50 nm in air above a glass interface. To fully compare FEM calculations to GMT, we plot σ_{ext}, σ_{abs} and σ_{sca} in figure 1.12. The results are shown to be in good qualitative and quantitative agreement for all three curves. There is a very good match throughout the spectrum and the LSPR peaks are reproduced accurately for all three cross-sections. Nevertheless, a

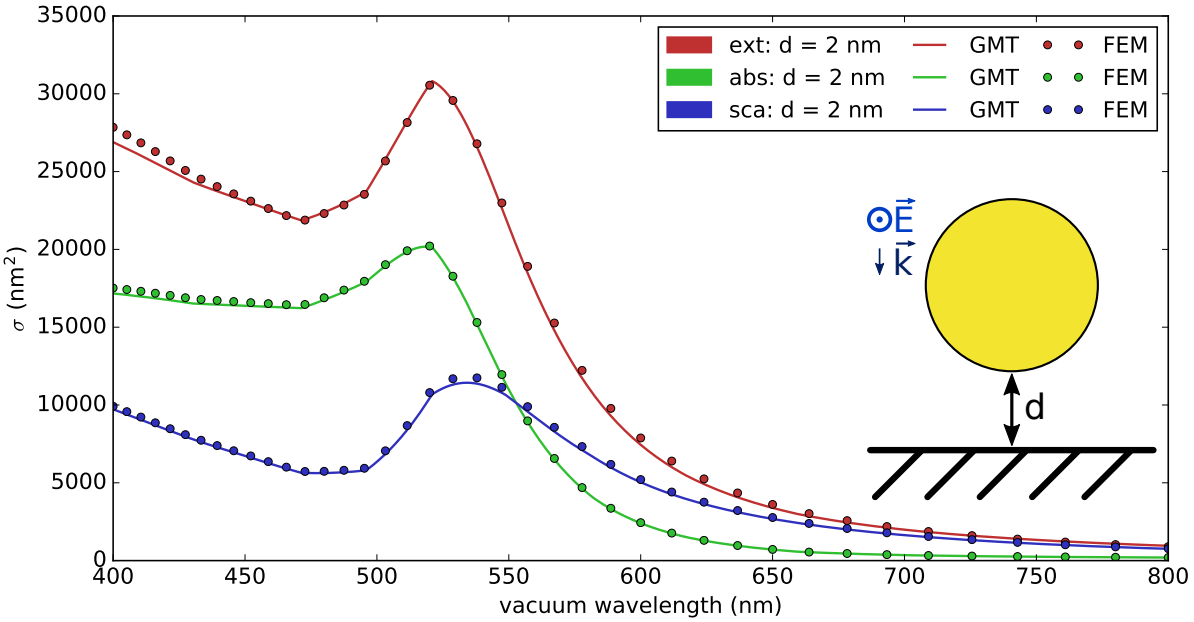

Figure 1.12: Extinction cross-section of a gold sphere ($R = 50\,\text{nm}$) in air ($n = 1$) at $d = 2\,\text{nm}$ from a glass substrate ($n = 1.5$). [GMT and FEM calculations]

discrepancy appears in the interband region around 450 nm and increases with decreasing wavelength, most noticeably in σ_{ext}. The scattering cross-section is also slightly overestimated. Initially this was suspected to be an artifact due to FEM mesh size: the accuracy of the model is expected to depend on the ratio of mesh size to the wavelength. A quick study (figure A.1, appendix A) showed that the further refinement of the mesh sizes had no influence.

Given that this work focuses on LSPR, we may ignore the near-ultraviolet (NUV) discrepancies. The discrepancy in the estimation of the scattering cross-section is also small enough to be negligible. Given the good overall agreement in the region of interest, with correct predictions of the LSPR peak positions (and the extinction peak in particular), we conclude that FEM calculations are sufficiently accurate to model our systems of interest.

1.3.2 Spheres

To study the effects expected in real systems, we begin with the simple case of spheres. In this section we will investigate the influence of the substrate, wetting and surfactants, and shape effects. We will then show that these effects are cumulative under some circumstances.

1.3.2.1 Influence Of A Substrate

The main objects of interest in this work are colloidally synthesized NPs deposited on glass substrates. The presence of a substrate introduces a dielectric interface which will reflect both the incident and scattered field leading to complex interactions. Here we seek to explore the influence of the substrate's presence on the optical response of the NPs.

We begin with the system of the sphere above a substrate shown in figure 1.12, which depicts a gold sphere of radius $R = 50\,\text{nm}$ in air above a glass substrate with a plane wave at 0° incidence. Figure 1.13 shows the results of both GMT and FEM calculations of $\sigma_{\text{ext}} = P_{\text{ext}}/I_{\text{inc}}$, as defined in (1.20), at varying distance d from the surface, where I_{inc} is the irradiance of the incident plane wave.

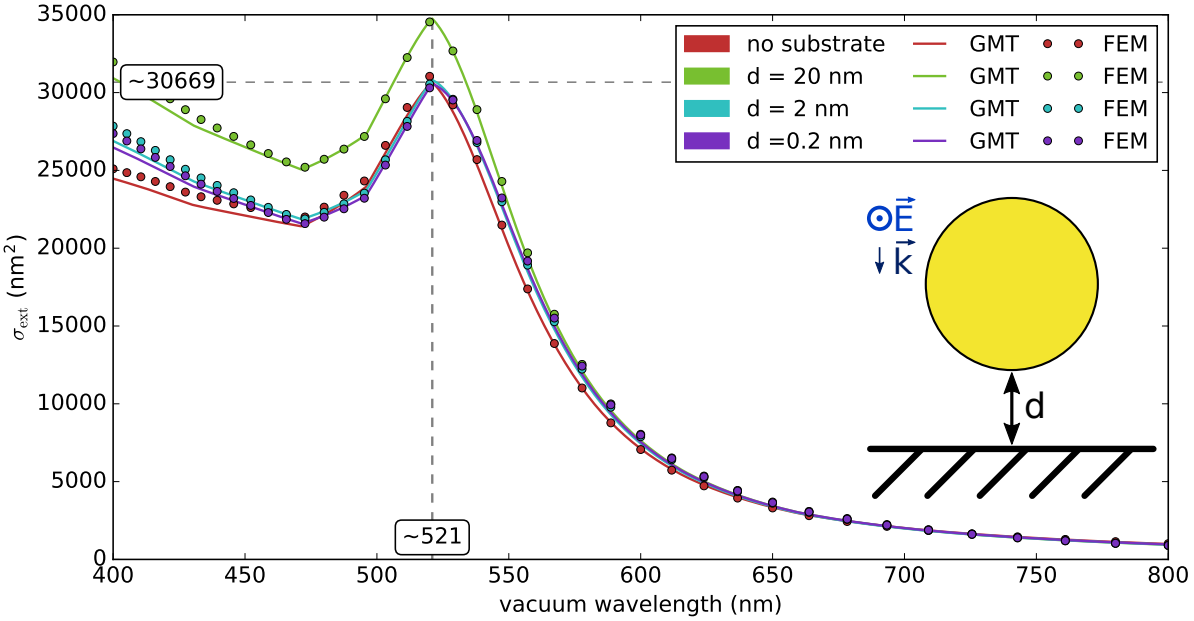

Figure 1.13: Extinction cross-section of a gold sphere ($R = 50\,\text{nm}$) in air ($n = 1$) at varying distance d from a glass substrate ($n = 1.5$). The position of the LSPR peak at $d = \infty$ is marked with dashed lines. [GMT and FEM calculations]

Looking at this figure, we see that the good agreement of both methods found for a single distance in figure 1.12 is also found for other distances. What is initially surprising, however, is that no obvious tendency appears as the object approaches the surface. When the object is 20 nm above the surface, σ_{ext} increases in the interband region and at the LSPR peak around 521 nm but then drops down again when nearing the surface. The interband region also exhibits different slopes at different distances but again with no clear tendency.

In order to compare these spectra and make sense of the underlying optical response when the object approaches the surface, we must consider the field reflected by the interface and how it affects our calculation of σ_{ext}. The interference with the incident field will create zones of greater and lesser average intensity that must be taken into account.

1.3.2.2 Irradiance and Normalization

The reflected field is governed by the Fresnel equations:

$$r_s = \frac{\left(\frac{n_1}{\mu_1}\right)\cos(\theta_1) - \left(\frac{n_2}{\mu_2}\right)\cos(\theta_2)}{\left(\frac{n_1}{\mu_1}\right)\cos(\theta_1) + \left(\frac{n_2}{\mu_2}\right)\cos(\theta_2)} \quad (1.39) \qquad t_s = \frac{2\left(\frac{n_1}{\mu_1}\right)\cos(\theta_1)}{\left(\frac{n_1}{\mu_1}\right)\cos(\theta_1) + \left(\frac{n_2}{\mu_2}\right)\cos(\theta_2)} \quad (1.40)$$

$$r_p = \frac{\left(\frac{n_1}{\mu_1}\right)\cos(\theta_2) - \left(\frac{n_2}{\mu_2}\right)\cos(\theta_1)}{\left(\frac{n_1}{\mu_1}\right)\cos(\theta_2) + \left(\frac{n_2}{\mu_2}\right)\cos(\theta_1)} \quad (1.41) \qquad t_p = \frac{2\left(\frac{n_1}{\mu_1}\right)\cos(\theta_1)}{\left(\frac{n_1}{\mu_1}\right)\cos(\theta_2) + \left(\frac{n_2}{\mu_2}\right)\cos(\theta_1)} \quad (1.42)$$

where r, t, n, μ and θ are the reflection and transmission coefficients, the RI, the permeability and the angle of the beam to the normal, respectively. The subscripts p, s indicate parallel and perpendicular polarization to the plane of incidence and the subscripts 1 and 2 indicate the environment before and after the interface, respectively.

n_{air}	1
$n_{\text{H}_2\text{O}}$	1.33
n_{glass}	1.5

Table 1.2: Refractive indices of air, water and glass used in numerical calculations. The RI of fused quartz is 1.46 at 589 nm whereas that of other glasses is higher[21]. A value of 1.5 was chosen to remain generic and yet different enough from the index of water to elucidate effects in the model systems.

In the present case of normal incidence in non-magnetic media such as air, glass and water, these coefficients reduce to

$$r_s = r_p = r = \frac{n_1 - n_2}{n_1 + n_2} \tag{1.43}$$

$$t_s = t_p = t = \frac{2n_1}{n_1 + n_2} \tag{1.44}$$

where the absence of a plane of incidence removes the distinction between the perpendicular and parallel coefficients. Using the values in table 1.2, for air on glass we have $r = -0.20$ and $t = 0.80$. For an incident plane wave of field strength E_0, the interference creates planar nodes of constructive interference where $E_{\max} = (1 + |r|)E_0 = 1.2E_0$ and planar nodes of destructive interference where $E_{\min} = (1 - |r|)E_0 = 0.8E_0$. The field strength therefore varies by a factor of 40%, which is non-negligible. More importantly, by (1.17), the local irradiance I_{loc} varies by a factor of $|E_{\max}|^2/|E_{\min}|^2 = 1.44/0.64 = 2.25$. Furthermore, as figure 1.14 shows, the distance of these nodes from the interface are static in time but vary for different incident wavelengths.

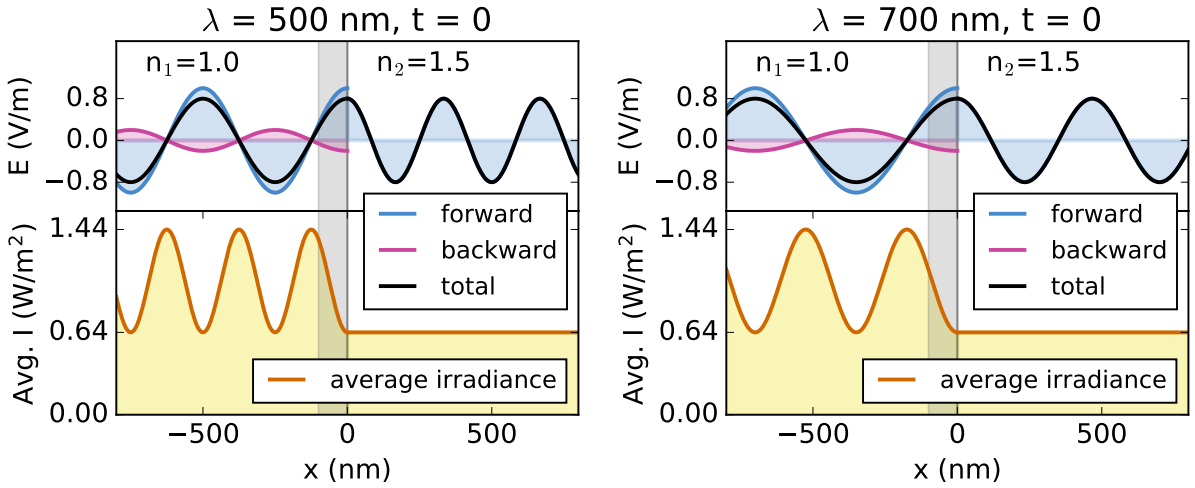

Figure 1.14: Diagram of the incident, reflected and transmitted waves and the average irradiance over time at an air/glass substrate under normal incidence for vacuum wavelengths of 500 nm and 700 nm at $t = 0$. In each subfigure, the real field strengths are shown above and the average irradiance below. The average irradiance is, by definition, constant in time, but varies in space as a function of the incident wavelength. The irradiance of an object near a surface therefore depends both on its distance from the surface and the incident wavelength. The 100 nm zone in front of the surface has been highlighted in grey.

Recalling the definition of σ_{ext} in (1.20) ($\sigma_{\text{ext}} = P_{\text{ext}}/I_{\text{inc}}$), we see that failure to account for the variations in I_{loc} will alter the spectrum of σ_{ext}. In many experimental setups it may be impossible or impractical to determine the true value of I_{loc} but simulations do not share the same limitations. To reduce spectral deformation and permit more meaningful comparisons of spectra for objects at different distances from the surface, one

may therefore define a more appropriate irradiance in different ways. The simplest and most accessible way is to calculate the irradiance using the total field at the height of the object's barycenter above the surface in the absence of the object. For a symmetric object that is much smaller than the wavelength, this will serve as a good average value that approximates the real irradiance on the object. For objects that are asymmetric about a plane parallel to the surface through their barycenter, one may instead calculate an average irradiance using $\left(\iiint_V I(d)\,\mathrm{d}r^3\right)/V$ where $I(d)$ is the irradiance at a distance d from the surface in the absence of the object and V is the volume of the object. Other methods may be used as well, but we shall see that these approximations suffice to reveal general tendencies in the systems considered here.

The application of barycentric normalization to the data presented in figure 1.13 yields figure 1.15. Comparing the two, a clear tendency emerges after normalization. A gradual increase of the interband extinction and the LSPR peak appears as the distance from the surface decreases. The peak is even slightly red-shifted as the object approaches the surface.

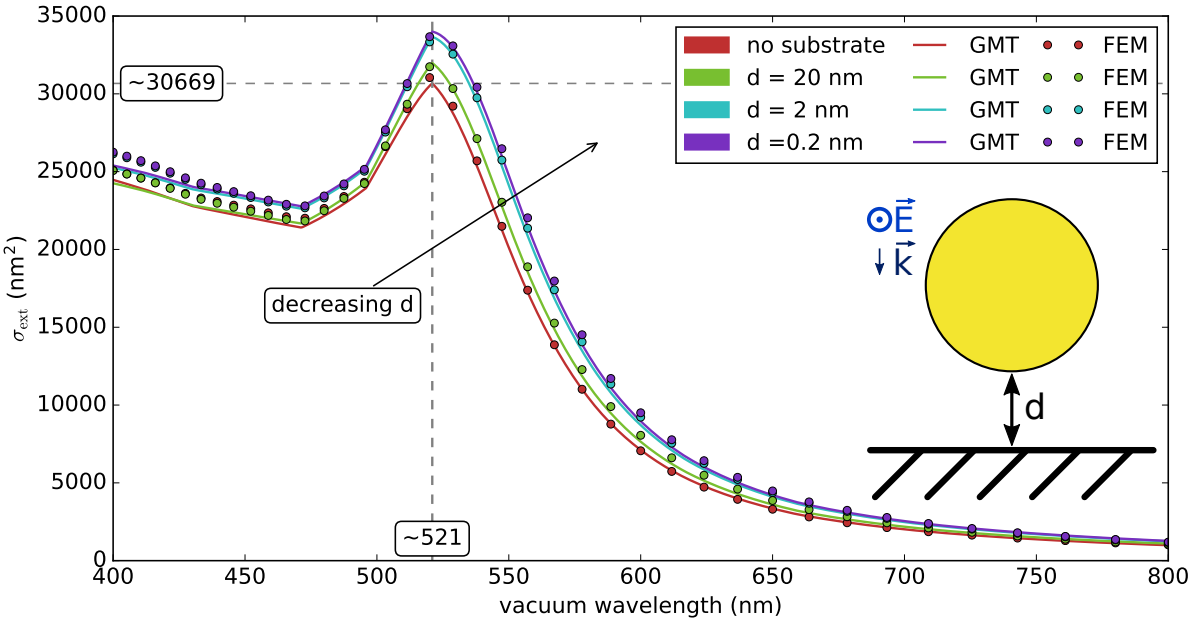

Figure 1.15: Normalized extinction cross-section of a gold sphere ($R = 50\,\mathrm{nm}$) in air ($n = 1$) at varying distance d from a glass substrate ($n = 1.5$). The position of the LSPR peak at $d = \infty$ is marked with dashed lines. The unnormalized values are shown in figure 1.13. [GMT calculations]

This tendency resembles that of an equivalent sphere in a homogeneous environment of increasing real RI n (figure 1.16). To interpret this similarity between these two tendencies and give a physical explanation of the former, we must consider how the object's optical environment changes with distance from the surface. As the object approaches the surface,

the glass substrate occupies a growing proportion of the object's immediate environment and has an increasingly important effect on the object's optical response. The average real RI of the environment will lie between that of the medium ($n = 1$) and the substrate ($n = 1.5$), with the contribution of air being the most important.

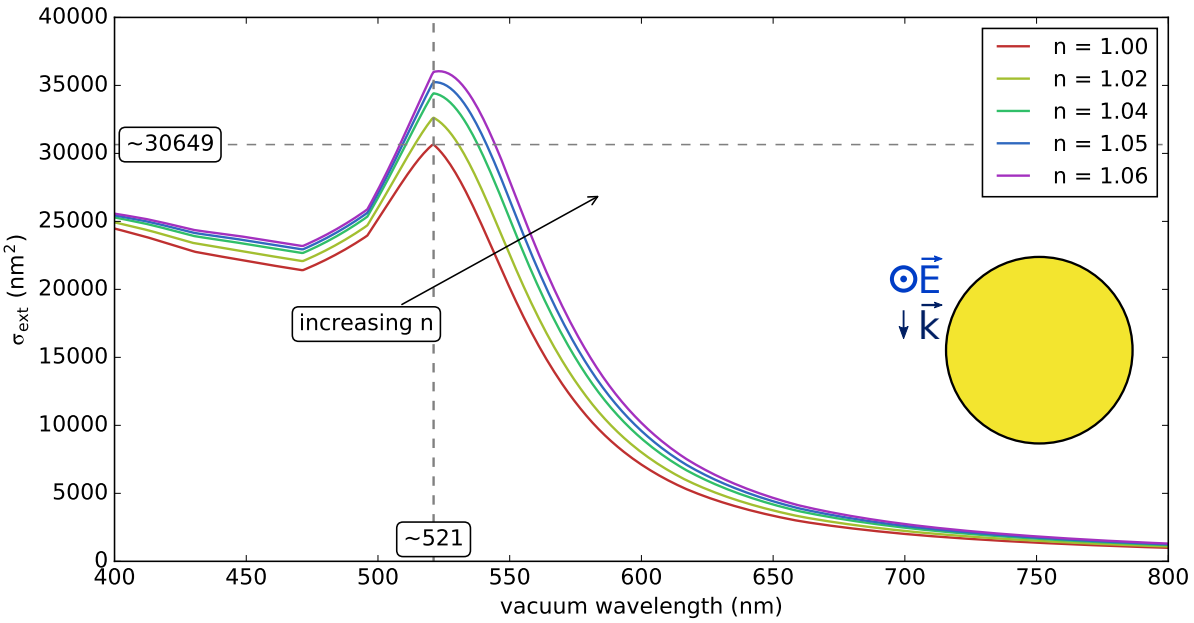

Figure 1.16: Extinction cross-section of a gold sphere ($R = 50\,\text{nm}$) in a homogeneous environment of varying real RI n. [GMT calculations]

The tendencies appear to be congruent, but we may plot the maximum of σ_{ext} against the wavelength at which it occurs for greater clarity. To improve the resolution of the peak positions, we apply cubic interpolation to the discrete numerical data which were calculated with a wavelength step size of 1 nm. The results are shown in figure 1.17, where the increase and slight red shift of the LSPR peak essentially lie along the same apparent curve. The effect of the approaching surface is thus to increase the effective RI n_{eff} around the object as expected, even through the effect is weak for small distances (compare $d = 2\,\text{nm}$ to $0.2\,\text{nm}$).

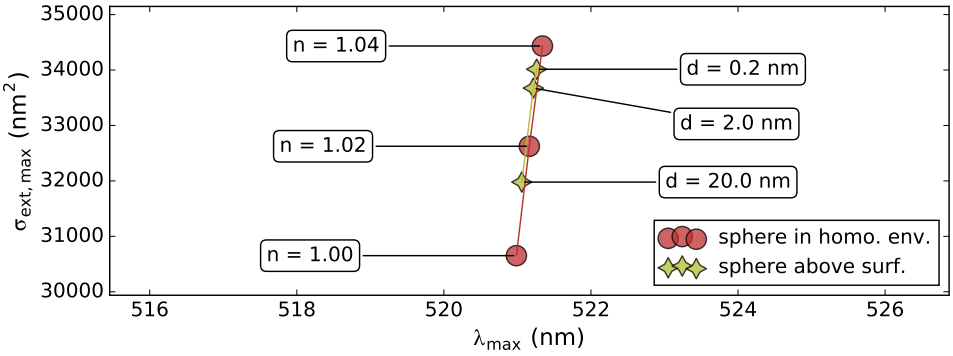

Figure 1.17: Comparison of the LSPR peak maxima of two different systems: a sphere in a homogeneous environment of varying real RI n (figure 1.16) and a sphere at varying distance d above an interface (figure 1.15).

In our group, we have previously compared experimental absolute extinction cross-sections of NPs of known morphology to Mie theory and we have often found that the response of the real NP is similar to that of an ideal NP in a homogeneous environment of real RI $n \approx 1.15$. The effect of the substrate is too weak to account for this observation and so we must explore other factors that can account for these observations.

The influence of these factors on the optical response of a NP will often be compared to the effects of a homogeneous environment of increasing real RI n. It is therefore instructive to examine the evolution of the extinction, absorption and scattering cross-sections of the gold sphere of radius 50 nm used in the previous and following models. The maxima of its three cross-sections are plotted against the wavelength at which they occur for different values of the real RI n in figures 1.18. σ_{max} and λ_{max} are plotted separately against the same values of n in figure 1.19, which also includes a plot of the cross-section values at λ = 425 nm in the interband region.

We note that the extinction and absorption cross sections continue to increase and red-shift with increasing real RI n. The maximum absorption cross-section initially follows the same tendency in both size and spectral position but after $n = 1.17$ the cross-section decreases with increasing n. The spectral position continues the initial red-shift until $n = 1.35$ but then blue-shifts until $n = 1.48$ and then begins to red-shift again. This unique behavior is due to the appearance of higher-energy multipolar modes that come to dominate the absorption response. We shall return to this point later.

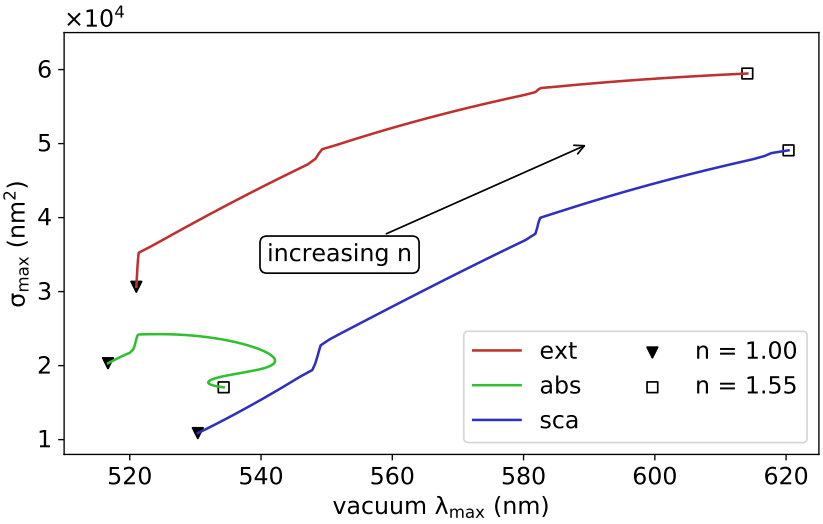

Figure 1.18: Evolution of the maximum extinction, absorption and scattering cross-sections of a gold sphere of radius 50 nm in a homogeneous environment of real RI n from 1.00 to 1.55. [GMT calculations]

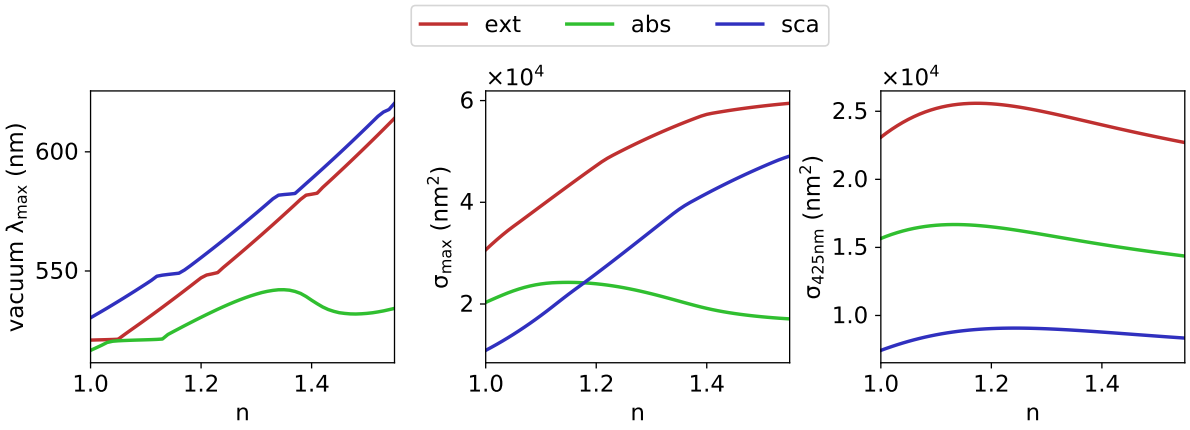

Figure 1.19: The spectral position, maximum value and interband transition intensity at 425 nm of the extinction, absorption and scattering cross-sections of a gold sphere of radius 50 nm vs the real RI n of a homogeneous environment. [GMT calculations]

1.3.2.3 Influence Of Wetting And Surfactants

Samples prepared from solutions of colloidally synthesized nano-objects may fail to completely dry when deposited on a substrate. Water, possibly containing surfactants used to stabilize the nano-objects and other impurities, may remain as a film around the object or between the object and the substrate. Even if the water fully evaporates, it may leave

behind chemical depositions. Here we explore how these different effects may alter the optical response of an object.

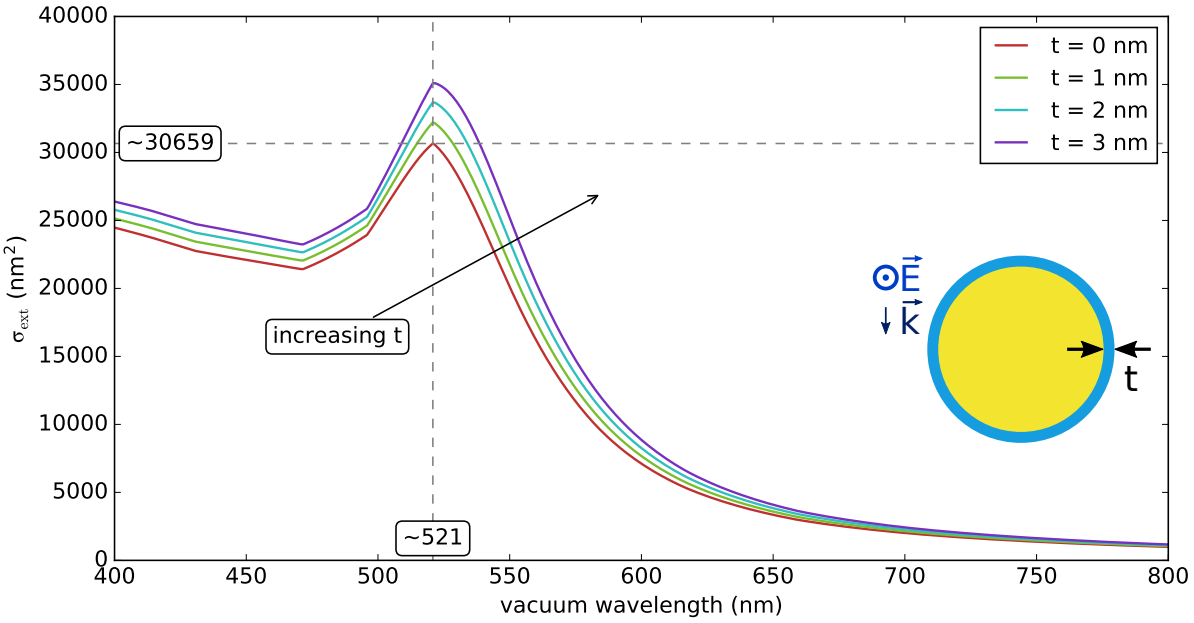

Figure 1.20: Extinction cross-section of a gold sphere ($R = 50\,\text{nm}$) in air ($n = 1$) covered by a shell of water ($n = 1.33$) of varying thickness t. [GMT calculations]

In figure 1.20 we consider the effects of a residual film of water for varying thickness t around a gold nanoparticle of 50 nm as in the previous models. The figure shows that the effects of the film around the object are to increase the LSPR peak with a slight red shift as in the case of increasing n. The interband transitions also slightly increase.

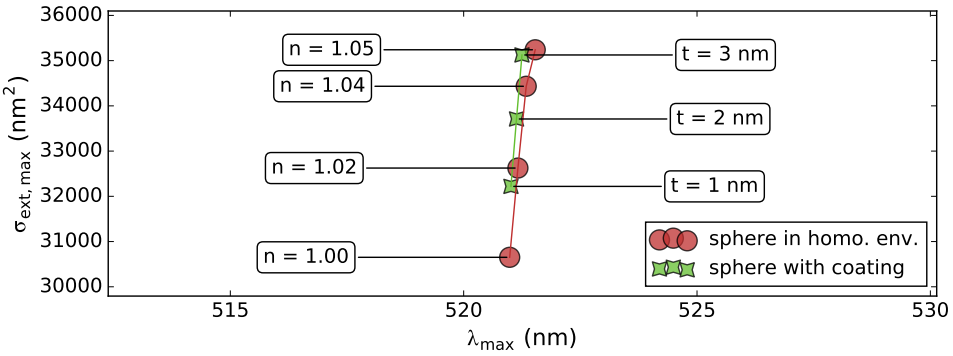

Figure 1.21: Comparison of the LSPR peak maxima of two different systems: a sphere in a homogeneous environment of varying real RI n (figure 1.16) and a sphere with a coating of variable thickness t (figure 1.20).

The results are again compared to those of figure 1.16 via a diagram of $\sigma_{\text{ext,max}}$ vs λ_{max} in figure 1.21, which emphasizes the evolution of the peak. The linear progression may again be interpreted as an increasing n_{eff} as the film grows to occupy more of the environment. For film thicknesses within the expected ranges of a few nanometers, the effect is comparable to that of a changing RI in a homogeneous environment and remains relatively weak.

Another type of wetting may occur when liquid remains on the substrate around the base of the object due to surface tension. To study this effect, we adapt the model of the gold nanosphere of $R = 50\,\text{nm}$ at $d = 2\,\text{nm}$ above a glass substrate. Water of varying height h is added in such a way that the edge of the surface of the water is tangent both to the surface of the nanosphere and the substrate[5]. The results are shown in figure 1.22. When the height of the water reaches the horizontal equator of the object ($h = 52\,\text{nm}$), it occupies a significant portion of the object's environment and the LSPR peak is shifted to the red by over 20 nm with a large increase in intensity and width. There is also a noticeable increase in the interband transition region which may be attributed to the diffusion of the water around the object.

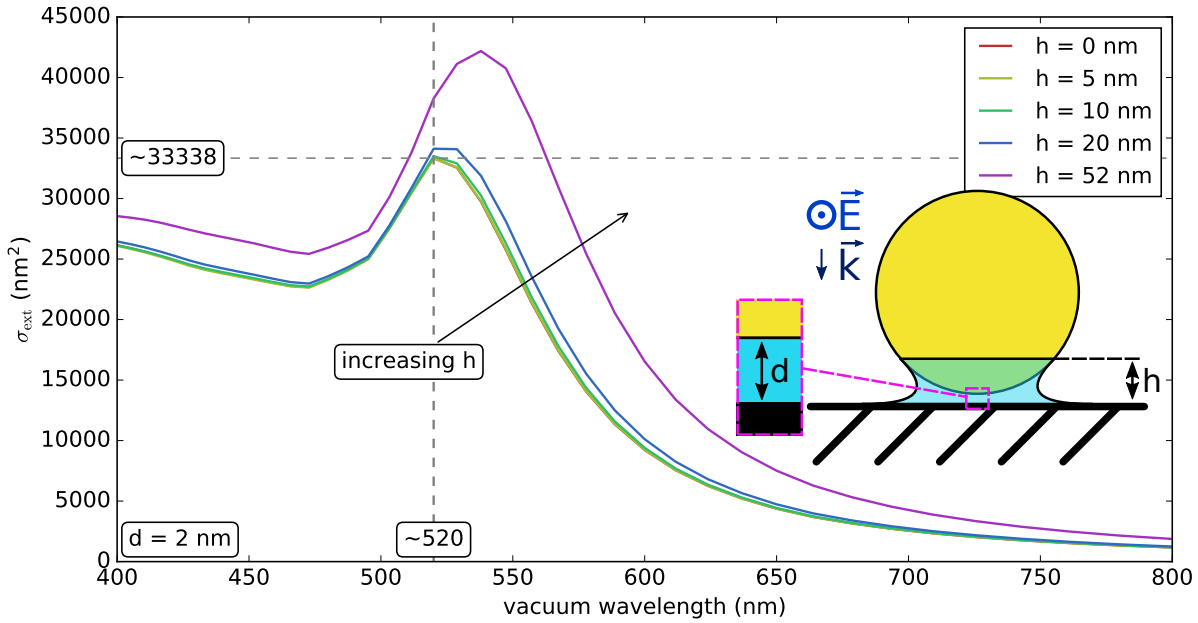

Figure 1.22: Extinction cross-sections of a gold sphere ($R = 50\,\text{nm}$) in air ($n = 1$) at a distance $d = 2\,\text{nm}$ above a glass substrate ($n = 1.5$) with a film of water ($n = 1.33$) of variable height h between the sphere and the surface. [FEM calculations]

Given that these results lie beyond the range of homogeneous indices presented in figure 1.16. we plot additional values of n for the same sphere in a homogeneous environ-

[5]This configuration, while not fully realistic, provides a convenient model for the study.

ment (figure 1.23) to enable comparison. As the value of n increases, the LSPR peak shifts to the red with an increase in intensity and breadth as it escapes the damping of the interband transitions. This trend appears to be the same as the one exhibited by the wetting model which again lends itself to interpretation as an increase in n_{eff}.

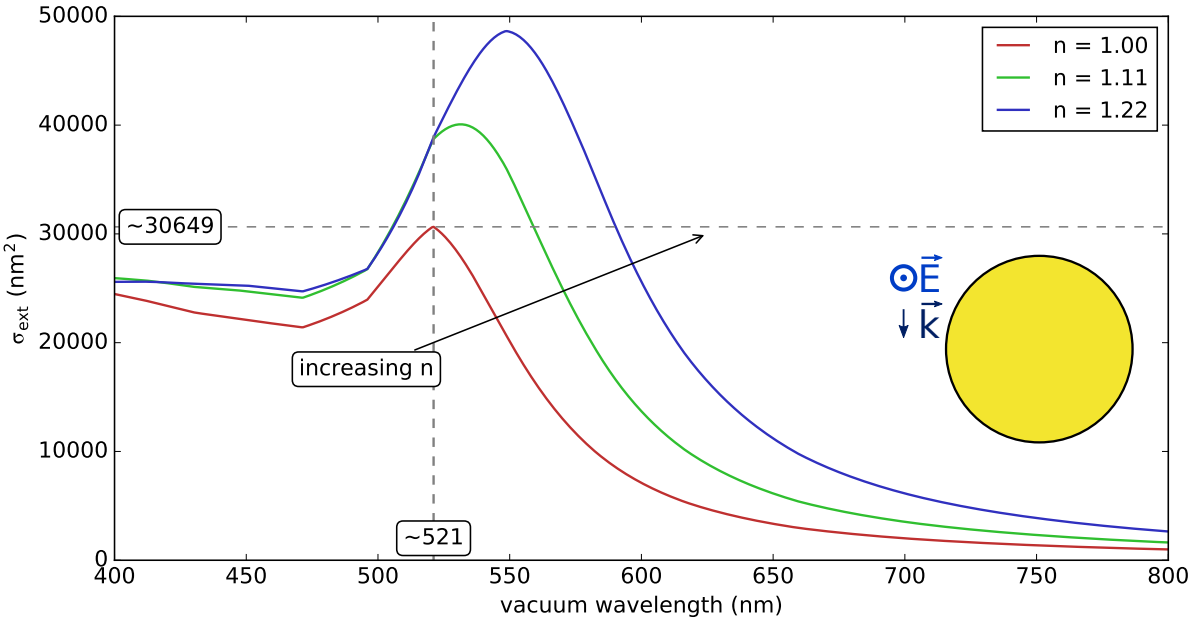

Figure 1.23: Extinction cross-section of a gold sphere ($R = 50\,\text{nm}$) in a homogeneous environment of varying real RI n. [GMT calculations]

This is confirmed by figure 1.24. At first glance it appears that the agreement between lower values of h and n is not as good as in the previous models where there was less red-shift in this region. This is at least in part due to the presence of the substrate which is 2 nm away from the object and thus even at $h = 0$, the starting point is not that of a homogeneous environment of $n = 1$. We shall return to notion of cumulative effects in section 1.3.2.5.

Even with this factor taken into account, the position at $h = 0$ (no wetting) is still slightly lower and red-shifted compared to the previous model (sphere above a surface, figure 1.17), even though the two systems should be equivalent. This discrepancy is likely due to differences in the meshing used by the wetting model. While the study in appendix A shows that refining the meshing further for a given model did not improve the slight discrepancy observed between the GMT and FEM calculations of the previous section, changing the mesh between models can have an effect. The curve traced by varying h runs alongside that of the sphere in a homogeneous environment with relatively good agreement despite the offset. This is similar to the behavior calculated with GMT in figure 1.21 for a sphere with a coating of varying thickness t, albeit with a lower offset. Given how small the discrepancy is and that the current study seeks to elucidate general

tendencies, we choose to ignore it.

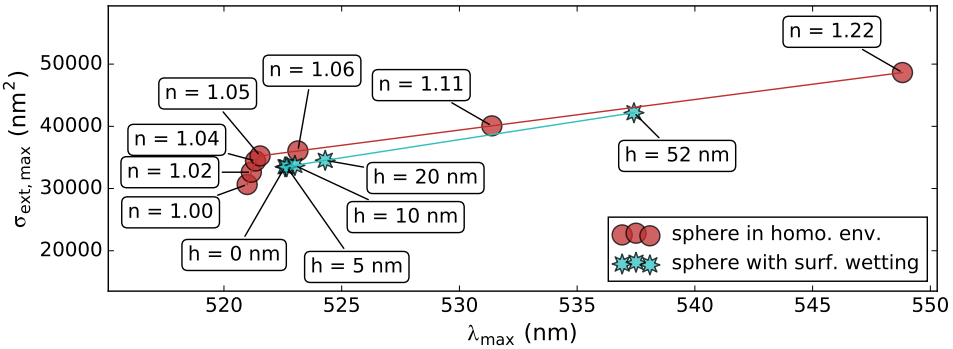

Figure 1.24: Comparison of the LSPR peak maxima of two systems: a sphere in a homogeneous environment of varying real RI n (figures 1.16 and 1.23) and a sphere over an interface with wetting (figure 1.22).

Returning to figure 1.24, we see that just after $n = 1.05$, the slope of $\sigma_{\text{ext,max}}$ vs λ_{max} abruptly changes (see figure 1.18 on page 56 for a plot of $\sigma_{\text{ext,max}}$ vs λ_{max} with greater range and resolution in n.) This new slope coincides quite well with the one traced by increasing h with an offset comparable to that of the point at $h = 0\,\text{nm}$ and the behavior is again interpretable as an increasing n_{eff}, as it was in the case of the surface coating.

1.3.2.4 Faceted Spheres And Ellipsoids

The model system of the perfect gold sphere of $R = 50\,\text{nm}$ studied so far neglects the imperfections of real spherical NPs, which are often faceted as seen in transmission electron microscopy (TEM) images (figure 1.25). In this section we will explore the effects that these imperfections may have.

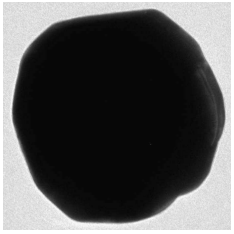

Figure 1.25: TEM image of a gold nanosphere of radius $\sim 40\,\text{nm}$ with visible facets.

To do this, we begin with the same model gold sphere of radius $R = 50\,\text{nm}$. A simple facet may be introduced by removing a slice of a given thickness s from the sphere. This may be done in one of two ways: one which conserves the object's radius but reduces its

volume and one which conserves the volume but increases the radius. If the truncated surface is always perpendicular to $\vec{k}$, the interest of the former is that the dimensions of the two axes in the plane perpendicular to $\vec{k}$ remain unchanged while the interest of the latter is that the mass is conserved and the overall shape is less affected. Both cases are presented in figure 1.26. The facet is oriented perpendicular to $\vec{k}$ so that the aspect ratio ar increases along the direction of $\vec{E}$, with

$$ar = \begin{cases} \dfrac{R}{R - s/2} & \text{if } s \leq R \\ \dfrac{\sqrt{s(2R - s)}}{R - s/2} & \text{if } s > R \end{cases} \tag{1.45}$$

where R is either 50 nm in the constant-radius case or the adjusted radius in the constant volume case. Unrealistically large values of s have been included for the sake of insight into general trends.

For the sphere of constant radius (upper left), the figure shows that as the slice thickness s increases, the LSPR peak red-shifts and initially increases and broadens due to the increasing aspect ratio and decoupling from the interband transitions, but then begins to decrease and narrow. The system with constant volume (middle left) shows the same initial tendencies for small s but the trend continues even for larger s and bears similarities to the sphere in the homogeneous environment of increasing n (figure 1.23). Comparing the two truncated sphere models, the red-shift of the LSPR peak is similar for comparable aspect ratios. Given the decrease in the interband transition region for the sphere of constant radius, it thus seems that the decrease in intensity is primarily due to the significant loss of volume. To verify this, the spectra of the truncated sphere of constant radius have been normalized by the ratio of the volume of the truncated sphere to the volume of the untruncated sphere (V/V_{50}) and plotted in the lower left graph. These spectra exhibit the same tendencies as the truncated sphere of constant volume and appear to exhibit roughly the same dependence on the aspect ratio.

To see if these tendencies are indeed a function of the aspect ratio, we compare the truncated sphere to an oblate ellipsoid of equal volume and aspect ratio $ar = b/a$, where a and b are the short and long semi-axes, respectively. For each system in the left column of figure 1.26, the spectra of the matching ellipsoid are plotted on the right. The ellipsoids are oriented with their short axis parallel to $\vec{k}$ and thus also parallel to the truncated (i.e. the shortened) axis of the sphere.

At first glance, the same general tendencies are apparent for the constant volume system and the matching ellipsoid, although the ellipsoid's red-shift is a little weaker at the highest ar. For the constant radius system without normalization, the initial tendency is the same but diverges as ar increases, where the peak continues to red-shift but decreases in strength for the ellipsoid. This is not surprising because at $ar = 2.50$, the slice thickness

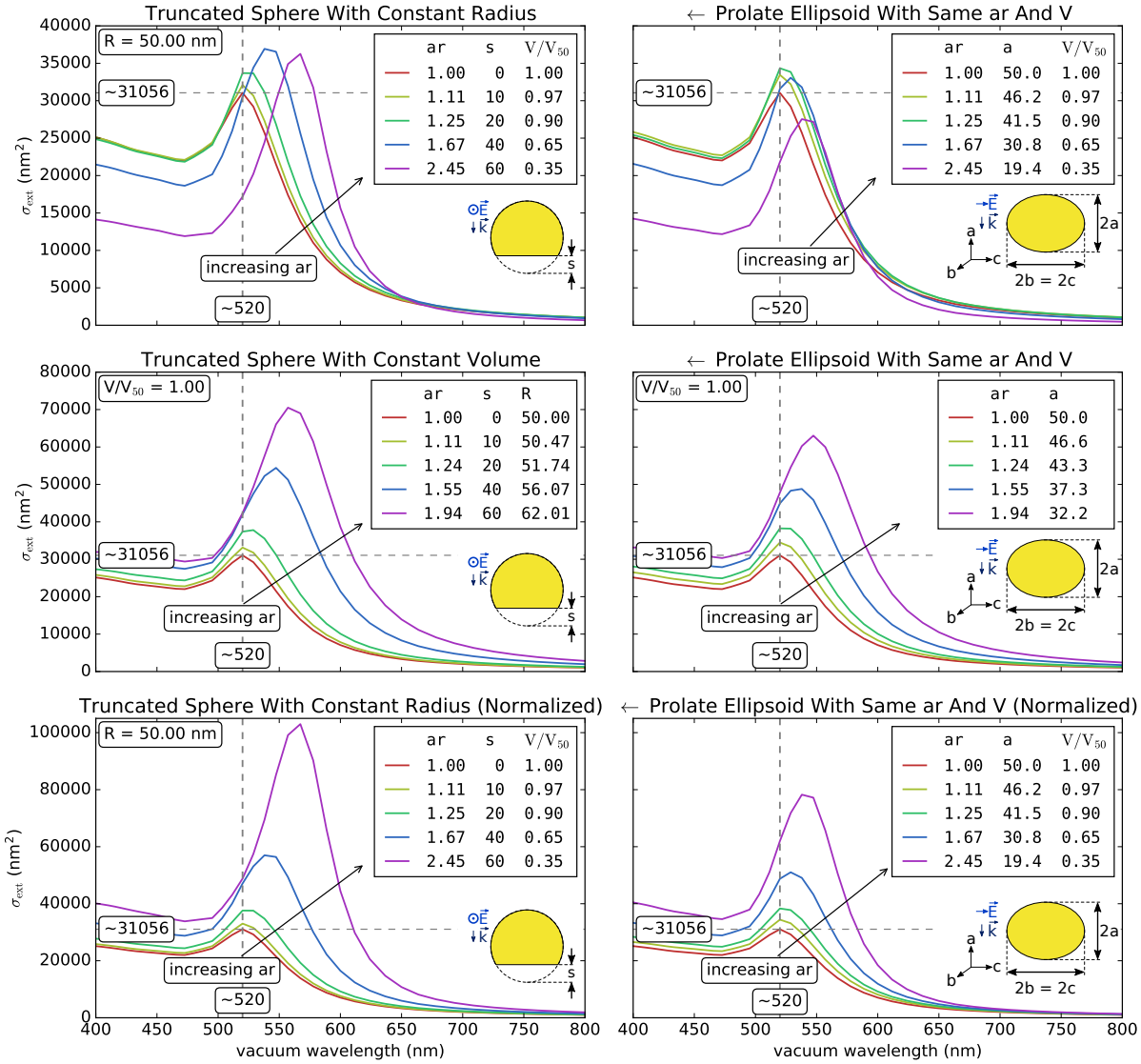

Figure 1.26: Truncated spheres and ellipsoids of equivalent aspect ratio ar and volume V in a homogeneous environment of $n = 1$. The first row shows the spectra of truncated spheres with constant radius $R = 50\,\text{nm}$ formed by removing slices of different thickness s. The second row shows the same with the radius adjusted to preserve the volume equivalent to a sphere of radius 50 nm. The third row shows the first row normalized by the volume fraction V/V_{50}, where V is the volume of the truncated sphere or equivalent ellipsoid and V_{50} is the volume of a sphere of radius 50 nm. [FEM calculations]

s is 60 nm for a constant radius of $R = 50\,\text{nm}$: more than half the sphere has been removed and the resulting shape is thus very different from the ellipsoid, with a large facet and sharp edges. The normalized spectra are nevertheless comparable to the constant volume system and again similar tendencies become evident.

The spectral position of the LSPR as a function of the aspect ratio are compared in figure 1.27. As ar increases, the geometries of the object gradually diverge yet the shift in $\lambda_{\max}$ remains comparable. The slopes of the constant-volume systems are the most similar, which is not surprising as the relative change in shape of the truncated sphere is less than the one in the constant-radius system, which shows a clearer divergence from the matching ellipsoid. This divergence and the offsets between matching systems show that the truncation has an important effect beyond the change in the aspect ratio, even if the aspect ratio is clearly an important parameter.

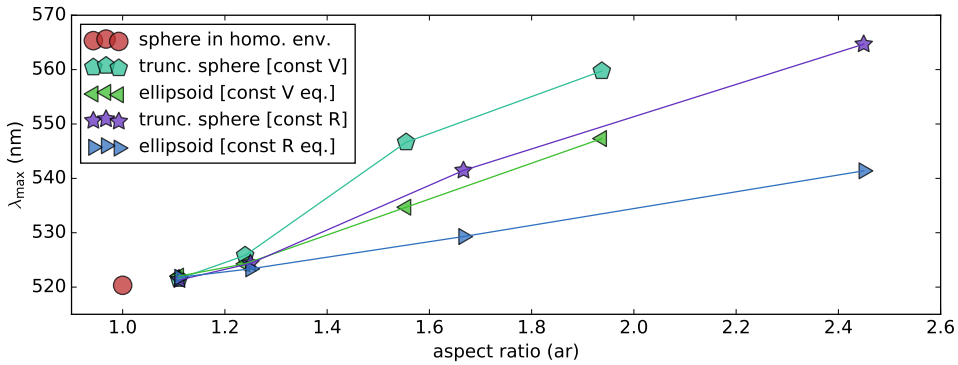

Figure 1.27: Comparison of the LSPR wavelengths of the truncated spheres and ellipsoids (figure 1.26) in a homogeneous environment of $n = 1$ as a function of their aspect ratio ar. [FEM calculations]

This effect is expected to be more important if the facet is brought close to the surface of a substrate. To see if this is so, we simulate spheres of constant radius from which we remove slices of thickness 10 nm and 20 nm, along with their matching ellipsoids, at a distance $d = 2$ nm above a glass substrate. The position of their LSPR is shown in figure 1.28. The objects are oriented as shown with the facets of the truncated spheres lying parallel to the surface. The positions of the LSPR peaks of the same objects in a homogeneous environment of increasing real RI n are also shown in order to see if the influence of the substrate may be interpreted as an increasing n_{eff}.

For both ellipsoids, we see in figure 1.28 that the LSPR peak lies near the curve of the equivalent object in a homogeneous environment, which can therefore be interpreted as an increase in n_{eff}. The value is close to $n = 1.04$, which is in good agreement with the values found for the perfect sphere at the same distance above a substrate (figure 1.17). This is not so for the truncated spheres. First we notice that the response of each object near the surface significantly differs from the same object in a homogeneous environment as compared to the equivalent ellipsoid, and the offset is suggestively similar between the truncated systems. Second, the wavelength shift of the truncated sphere near the surface compared to the equivalent object in a homogeneous environment of $n = 1$ is greater than the equivalent sphere in both cases, significantly so for the $s = 20$ nm, which has a larger surface and sharper edges. This shows that the truncation leads to an intricate interaction

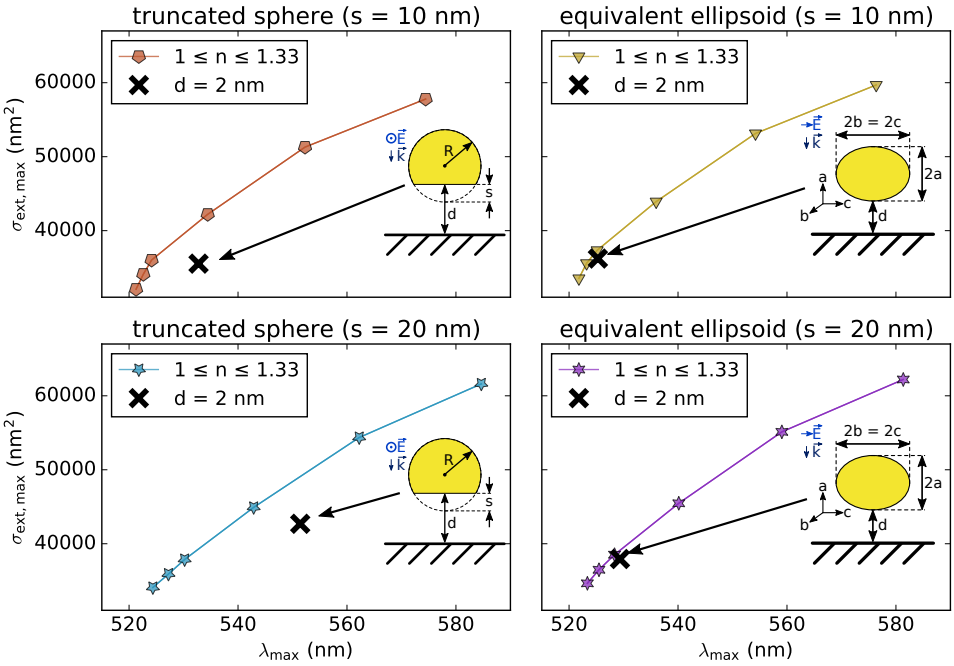

Figure 1.28: Comparison of truncated spheres and ellipsoids of equivalent aspect ratio and volume in air ($n = 1$) at $d = 2\,\text{nm}$ from a glass substrate ($n = 1.5$). The LSPR peaks of the equivalent objects in a homogeneous environment of varying real RI n are shown for comparison.[FEM calculations]

with the surface that cannot be modeled as an object in a homogeneous environment of RI n_{eff}. We shall return to this point in section 1.3.3.

The tendencies observed in figure 1.26 are similar to those observed for the sphere in a homogeneous environment in figures 1.16 and 1.23. As a final comparison to determine if small deformations of a sphere can be treated as an increase in n_{eff}, the LSPR peak positions for small truncations and the equivalent ellipsoids are plotted in figure 1.29 along with the peaks of the 50 nm-radius sphere in a homogeneous environment. For very small deformations, the effect is similar to that of an increasing n_{eff}, which can thus be used to mask the effects of very minor deformations. We note that the response of the truncated sphere of constant radius, the shape of which is deformed the most for a given slice thickness s, is the quickest to deviate, which further highlights the importance of shape effects.

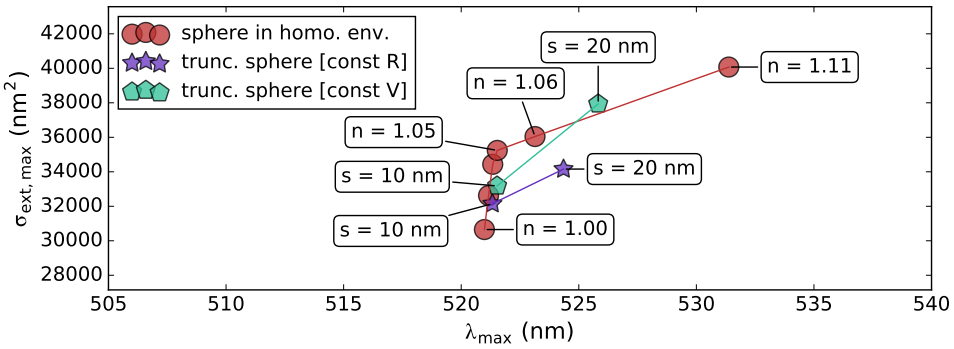

(a) truncated spheres

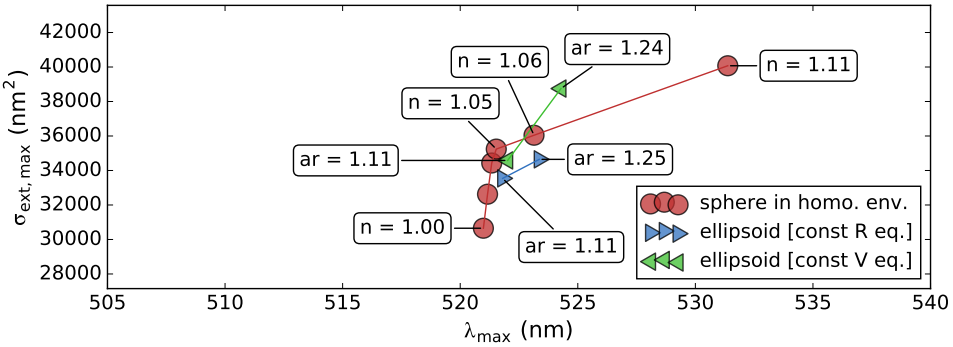

(b) ellipsoids

Figure 1.29: Comparison of the LSPR peak maxima of the truncated spheres and ellipsoids in figure 1.26 to a sphere in a homogeneous environment of increasing real RI n.

1.3.2.5 Cumulative Effects

While discussing the surface wetting simulation (figure 1.24 in section 1.3.2.3), we noted that the wetting model introduced two separate effects, namely the presence of a substrate and the wetting between it and the NP, and the interpretation of the results suggested a cumulative effect of both. In a real system, we may expect multiple effects to be present and it is therefore necessary to investigate their interplay.

To do this, we consider a simple system of a sphere above a glass substrate in air with a layer of water around it (figure 1.30), which gives us two separate parameters: the surface distance d and the coating thickness t. We see that at a each distance, the addition of a coating of 1 nm induces an approximately constant shift in n_{eff}. Likewise, in both the presence or absence of a shell, decreasing d from 40 nm to 2 nm also induces an approximately constant shift. Each effect appears to be independent of and cumulative with the other.

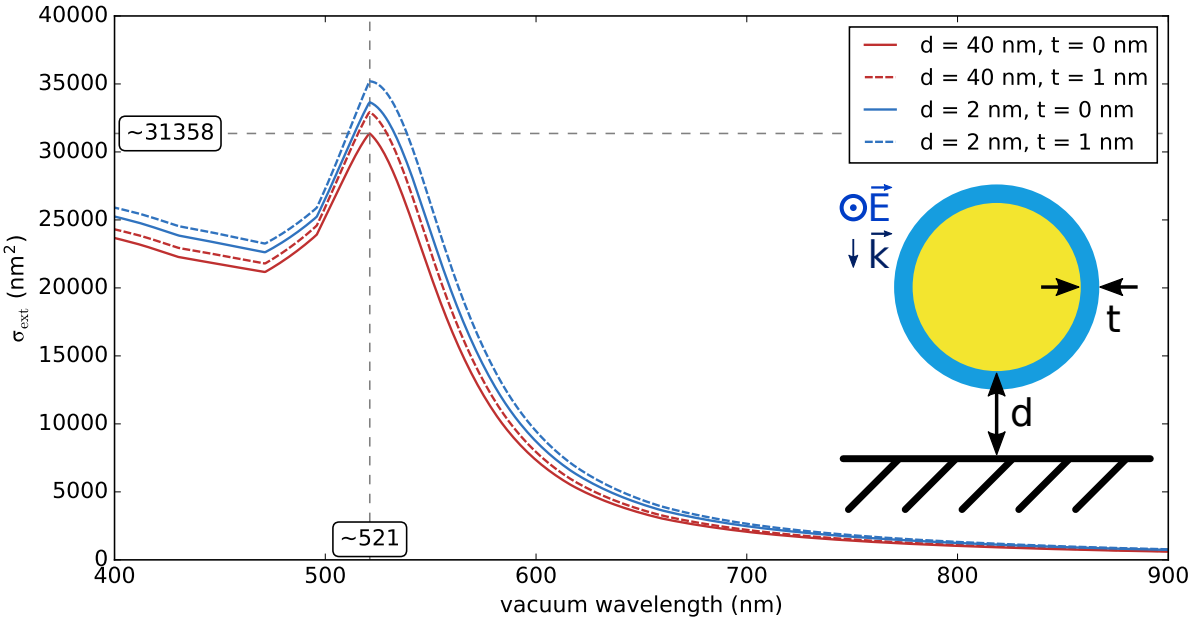

Figure 1.30: Extinction cross-sections of a gold sphere ($R = 50\,\text{nm}$) in air ($n = 1$) with or without a coating of water ($n = 1.33$) of thickness $t = 1\,\text{nm}$ of varying distance d above a glass substrate ($n = 1.5$). See also figures 1.15 and 1.20. [GMT calculations]

For a more precise evaluation, the full σ_{ext} spectrum of this system can be fit to that of a sphere of identical size in a homogeneous environment using the least-squares method to determine n_{eff}. The fit was performed over the range from 400 nm to 900 nm with a resolution of 0.001 RIU (refractive index units) for all combinations of t from 0 nm to 8 nm and d from 40 nm to 2 nm except for those in which $t > d$. The results are shown in figure 1.31 and tabulated in table 1.3.

We see in the figure that the surface is essentially locally linear in both effects and that as each one increases, a proportional and cumulative change is observed. The contour projections clearly show that the effect of one parameter is essentially independent of the other. Checking table 1.3, the difference in n_{eff} between two values of d is largely unaffected by the thickness of the coating. For example, when moving from $d = 10\,\text{nm}$ to $d = 8\,\text{nm}$, n_{eff} increases by a value between 0.02 and 0.03 for all values of t. Similarly, for a change in t, the value of d has little effect. Moving from a thickness of 1 nm to 2 nm induces a change of approximately 0.016 in n_{eff} regardless of the distance.

Although the influence of each step in this example is only affected negligibly by the other parameter, it is not linear within its own parameter. As t increases, $\frac{\partial n_{\text{eff}}}{\partial t}$ decreases (from $\approx 0.016\,\text{nm}^{-1}$ at $t = 0\,\text{nm}$ down to $\approx 0.012\,\text{nm}^{-1}$ at $t = 7\,\text{nm}$). For each additional nm, the added thickness is further away from the object and has less influence on n_{eff}. This is also seen in the decrease of $\frac{\partial n_{\text{eff}}}{\partial d}$ as the object moves away from the surface. Influence

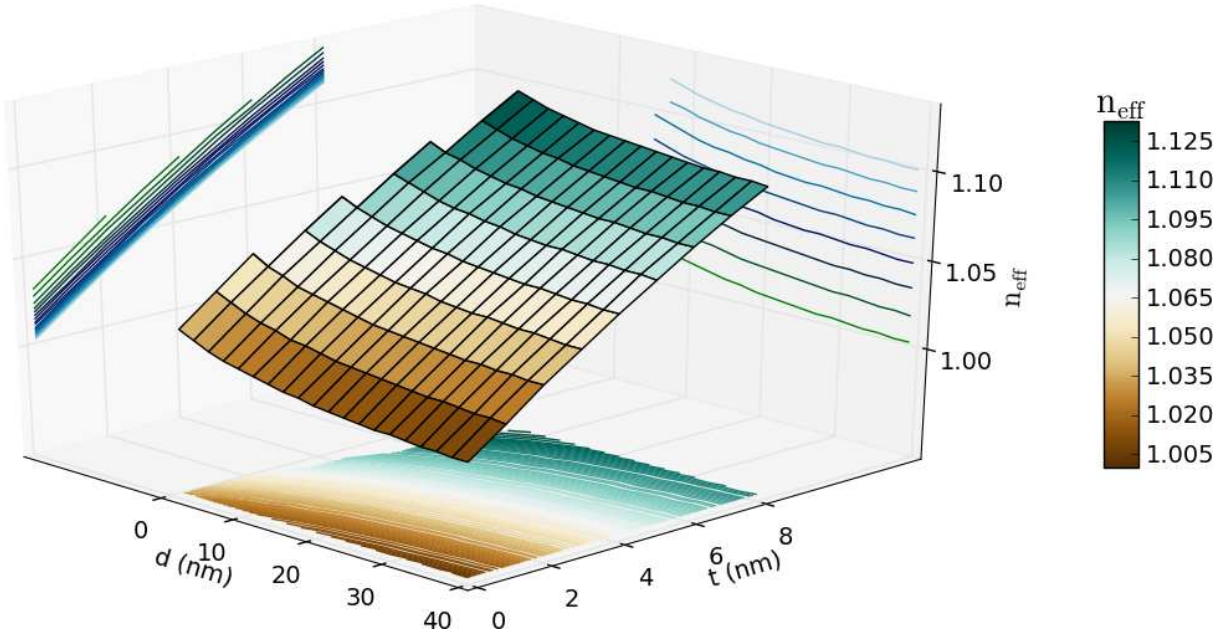

Figure 1.31: Gold sphere of radius $R = 50\,\text{nm}$ in air ($n = 1$) at a distance d above a glass surface ($n = 1.5$) with a coating of variable thickness t of water ($n = 1.33$). The surface shows the values of n_{eff} for varying d and t determined by a least-squares fit of the extinction spectrum to an equivalent sphere in a homogeneous environment. Contour plots are shown for projections along each axis.[GMT calculations]

depends on proximity.

Over longer ranges such as from 40 nm to 8 nm there appears to be a mild effect of the thickness: there is a change of approximately 0.018 RIU over this range at $t = 0\,\text{nm}$ but this increases to 0.021 RIU at $t = 8\,\text{nm}$. Although the medium is non-absorbing, it is scattering and this appears to augment the effect of the surface proximity. While small changes may be nearly linearly cumulative, this shows that the interplay between different effects may be more complicated.

While interesting, a systematic study of the interplay of all of the previously discussed effects is beyond the scope of this work. The goal here is to provide an explanation of the origin of n_{eff} used to interpret and model real systems while masking their inherent complexity. This is necessary because the experimental determination of all possible parameters would be difficult and tedious if not impossible.

		t								
		0 nm	1 nm	2 nm	3 nm	4 nm	5 nm	6 nm	7 nm	8 nm
d	40 nm	1.004	1.019	1.035	1.049	1.063	1.076	1.089	1.101	1.112
	38 nm	1.004	1.020	1.035	1.049	1.063	1.077	1.089	1.101	1.113
	36 nm	1.005	1.020	1.036	1.050	1.064	1.077	1.090	1.102	1.113
	34 nm	1.005	1.021	1.036	1.051	1.064	1.078	1.090	1.102	1.114
	32 nm	1.006	1.022	1.037	1.051	1.065	1.078	1.091	1.103	1.114
	30 nm	1.007	1.022	1.037	1.052	1.066	1.079	1.092	1.104	1.115
	28 nm	1.007	1.023	1.038	1.053	1.066	1.080	1.092	1.104	1.116
	26 nm	1.008	1.024	1.039	1.053	1.067	1.080	1.093	1.105	1.117
	24 nm	1.009	1.025	1.040	1.054	1.068	1.081	1.094	1.106	1.118
	22 nm	1.010	1.026	1.041	1.055	1.069	1.082	1.095	1.107	1.119
	20 nm	1.011	1.027	1.042	1.057	1.070	1.084	1.096	1.108	1.120
	18 nm	1.013	1.028	1.043	1.058	1.072	1.085	1.098	1.110	1.121
	16 nm	1.014	1.030	1.045	1.059	1.073	1.087	1.099	1.111	1.123
	14 nm	1.016	1.032	1.047	1.061	1.075	1.088	1.101	1.113	1.125
	12 nm	1.018	1.033	1.049	1.063	1.077	1.090	1.103	1.115	1.127
	10 nm	1.020	1.036	1.051	1.065	1.079	1.093	1.106	1.118	1.130
	8 nm	1.022	1.038	1.053	1.068	1.082	1.096	1.108	1.121	1.133
	6 nm	1.025	1.041	1.057	1.071	1.085	1.099	1.112		
	4 nm	1.029	1.045	1.060	1.075	1.089				
	2 nm	1.033	1.049	1.065						

Table 1.3: Effective refractive indices n_{eff} for different parameter combinations of the model in figure 1.30 determined by a least-squares fit of σ_{ext} to that of a sphere of 50 nm in a homogeneous environment. t is the thickness of a coating of water with $n = 1.33$. d is the distance to a substrate of glass with $n = 1.5$. Missing values correspond to impossible systems where the coating would be thicker than the distance to the surface. The values are plotted in figure 1.31.

We conclude this section by considering a "real" system that combines the aforementioned effects in order to estimate a reasonable value of n_{eff}. We begin with an imperfect sphere of radius $R = 50.02\,\text{nm}$ with a facet formed by removing a slice of thickness $s = 10\,\text{nm}$, which yields a faceted sphere with a volume equivalent to a perfect sphere of radius 50 nm and thus represents a constant-mass facetting of the latter. This object is place at a distance $d = 2\,\text{nm}$ above a glass substrate of $n = 1.5$ with its facet parallel to the surface. The object is surrounded by a coating of liquid of thickness $t = 2\,\text{nm}$ and which rises to a height of $h = 15\,\text{nm}$ above the surface around the object. The value of n of the liquid is set to 1.35 to represent water residue with molecular impurities. The medium beyond this coating is taken to be air with a RI of 1. A diagram of the system (not to scale) along with the spectra of σ_{ext}, σ_{abs} and σ_{sca} are presented in figure 1.32.

To determine a value of n_{eff} for this system, a model system of a perfect sphere of radius

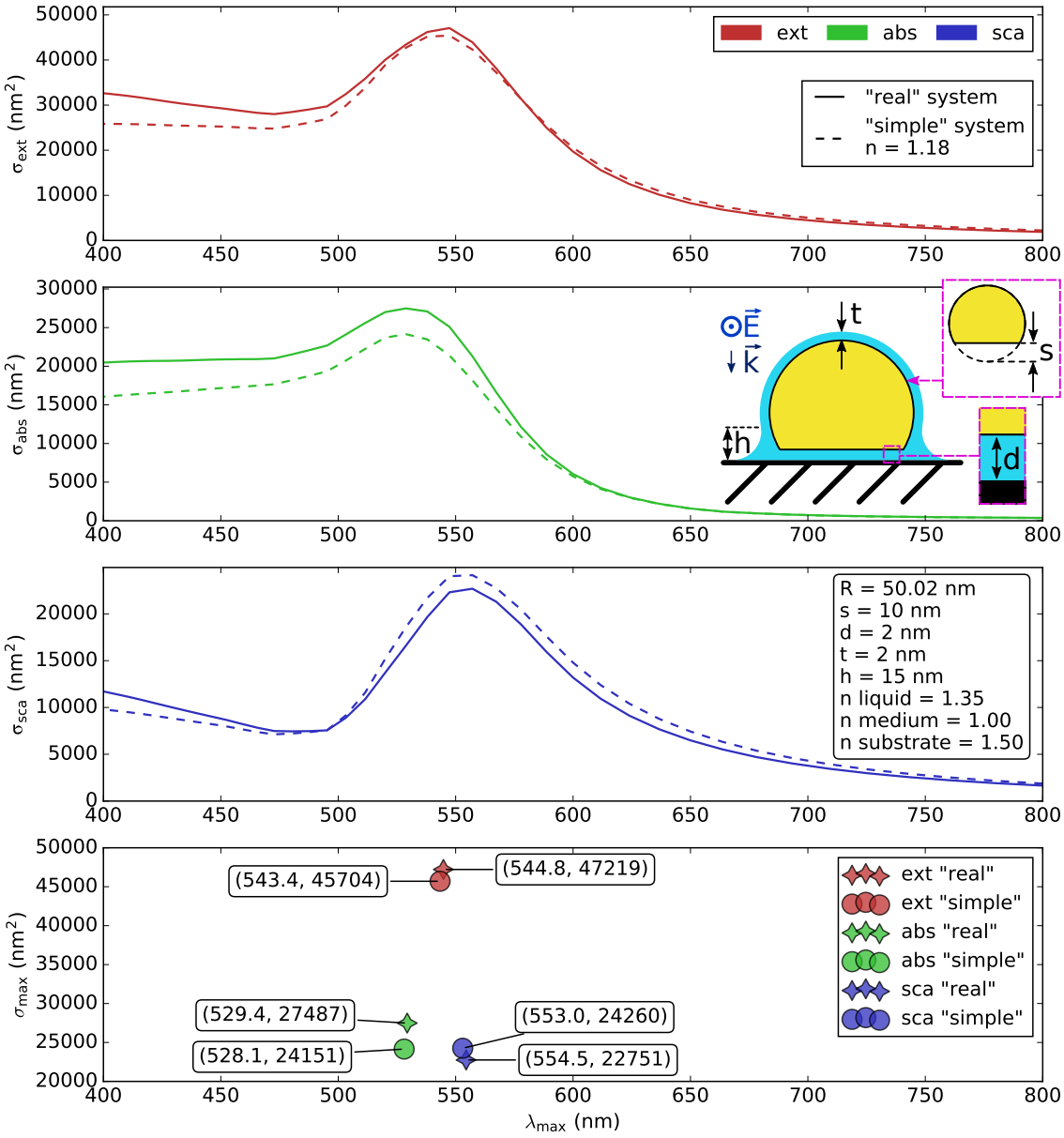

Figure 1.32: Extinction, absorption and scattering cross-sections of a "real" system with several factors influencing n_{eff}. A gold sphere of $R = 50.02\,\text{nm}$ is faceted by removing a slice of thickness $s = 10\,\text{nm}$ which yields an object with a volume equivalent to that of a sphere of radius 50 nm. The object is placed in air ($n = 1$) at a distance $d = 2\,\text{nm}$ from a glass substrate ($n = 1.5$). A liquid residue of $n = 1.35$ coats the object with a thickness $t = 2\,\text{nm}$ and rises around the object to a height of $h = 15\,\text{nm}$. n_{eff} is calculated from the extinction cross-section by a least-squares fit to a "simple" system of a gold sphere of radius $R = 50\,\text{nm}$ in a homogeneous environment of real RI n, which yields $n_{\text{eff}} = 1.18$. The peak positions are plotted and labelled in the final panel for easier comparison. [GMT and FEM calculations]

50 nm has been modelled in a homogeneous environment of varying real RI n. The spectrum of σ_{ext} of this model has then been fit to the spectrum of σ_{ext} presented in the figure by varying n to minimize the least-squares distance between them. This leads to a value of $n_{\text{eff}} = 1.18$. The extinction, absorption and scattering spectra of the homogeneous system of $n = 1.18$ are plotted alongside those of the "real" system for comparison and evaluation of the fit.

The peak positions of the "real" and "simple" systems are plotted at the bottom of the figure, which shows that they are in good but imperfect agreement. The peak absorption is slightly greater for the real system while the scattering is slightly weaker. The peak wavelengths also vary by about 1.5 nm to 1.7 nm. Discrepancies are to be expected as the faceted sphere's response is nontrivially different from that of a perfect sphere as seen in section 1.3.2.4. Nevertheless, there is fairly good agreement considering how different the considered systems are. Fitting against either absorption or scattering instead of the extinction yields the same n_{eff}. This is reassuring and confirms that the concept of n_{eff} is valid for these phenomena considered separately as well. In the next section, we return to shapes for which this simplification is not appropriate.

1.3.3 Cubes

The observations of the truncated spheres seen in section 1.3.2.4 indicate that the presence of a flat surface and edges near a substrate may have an important effect on the response of a NP which defies interpretation via a simplified n_{eff}. Because our group is interested in systems of plasmonic nanocubes[47, 48], which have been shown to exhibit prominent shape effects[39, 48–55], we would like to explore the effects of substrate on cubes in this section. In contrast to spheres, cubes exhibit many resonant eigenmodes which may be indistinguishable in their spectra due to overlapping resonance widths[39, 48, 49, 53–57]. A full exploration of LSPR in cubes requires a detailed description of these modes, which is beyond the scope of this work. We will therefore limit our scope to a cursory qualitative description to gain general insights that will serve use throughout the rest of this work.

As a model we will use a rounded gold cube of length $l = 80.76$ nm and rounding radius $r = 5$ nm. The length has been chosen so that the volume of the object is equivalent to that of a sphere of radius 50 nm as studied in the previous sections. The rounding has been chosen from experimental observations of real cubes.

Figure 1.33 shows the optical response of a rounded cube in a homogeneous environment of varying n. The calculation was performed with the cube oriented as displayed in the diagram. Calculations were also performed with the cube rotated 45° around the axis parallel to $\vec{E}$. This had no significant effect on the calculated spectra (differences of less than 0.1 %) and the results are not shown. As n increases, the LSPR peak increases, broadens and shifts to the red, as it does for the sphere under increasing n (figures 1.16

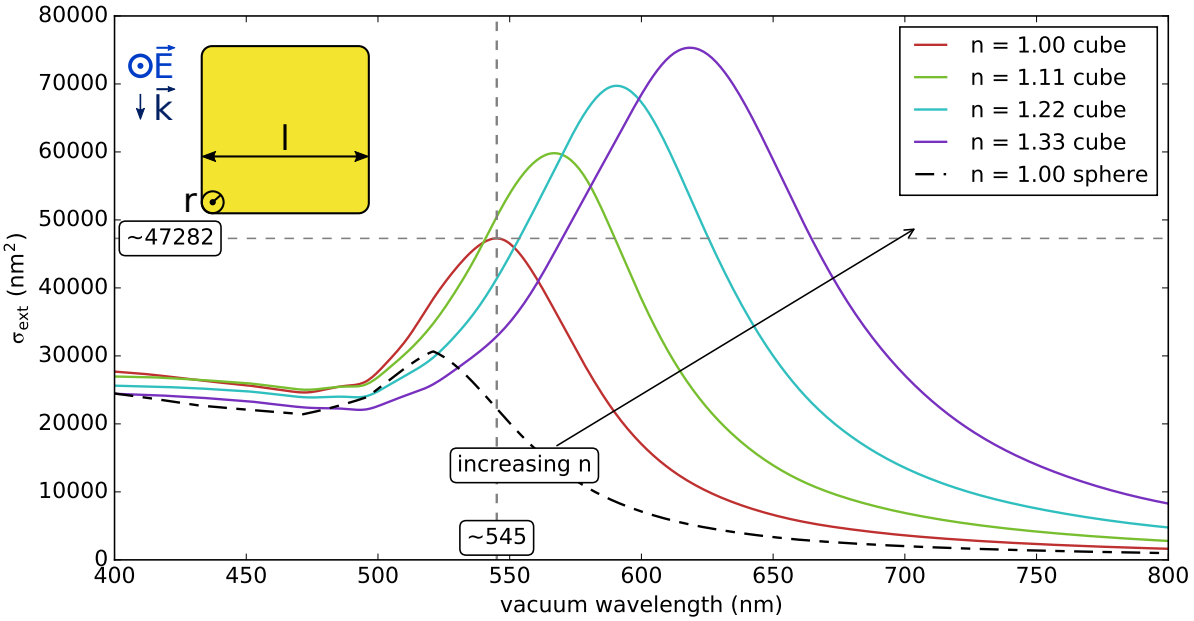

Figure 1.33: Extinction cross-section of a gold cube ($l = 80.76$nm, $r = 5$nm) in a homogeneous environment of varying real RI n. The spectrum of a gold sphere of radius 50 nm and equal volume in a homogeneous environment of real RI n=1 is plotted for reference. [FEM calculations]

and 1.23). The effect of the shape is nevertheless immediately apparent for the LSPR peak at $n = 1$ which is shifted to the red by about 26 nm and increased by about 16 500 nm^2 as compared to the sphere. It also appears to shift more quickly to the red for increasing n.

This observation is confirmed in figure 1.34 where it can be easily seen that a given change of n induces a greater red-shift in $\lambda_{\max}$ for the cube than for the sphere. It is also clear that $\sigma_{\text{ext,max}}$ increases more quickly for the cube as the peak shifts to the red. The optical response of the cube is thus more sensitive to its environment as compared to the sphere.

This conclusion may be tested by returning to a system with a substrate. With the introduction of a surface, the orientation of the cube must be taken into account. Emulating the previous study of the sphere approaching a glass substrate from air, we choose to study 2 different orientations of the cube to the surface.

In the first case, shown in figure 1.35a, one of the cube's faces remains parallel to the surface. As it approaches the substrate we see the same effects as seen in figure 1.33 for an increasing RI and the effect resembles that of increasing n_{eff}. Of note is that the effect is stronger than for the sphere, which supports the conclusion that the response is more sensitive to the environment. In the second case, shown in figure 1.35b, the cube is turned 45° around the axis parallel to $\vec{E}$ so that it approaches the substrate with its edge. Up

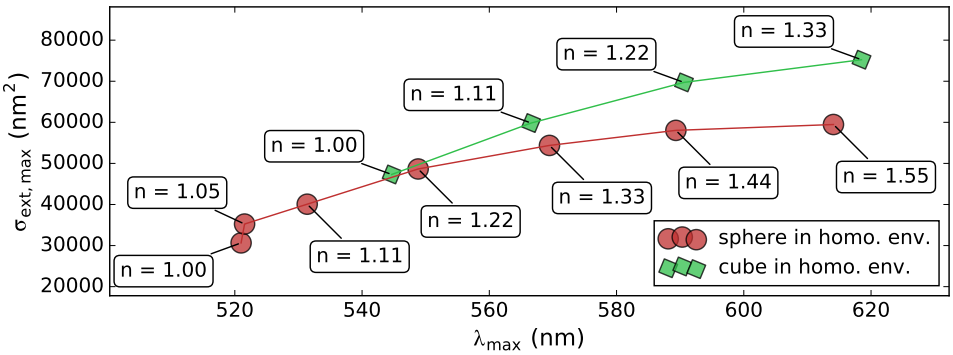

Figure 1.34: Comparison of the LSPR peak maxima of two systems: a sphere in a homogeneous environment of varying real RI n (figures 1.16 and 1.23) and a cube (figure 1.33) in a homogeneous environment of varying real RI n.

to a distance of $d_s = 2\,\text{nm}$ the tendency is again similar but much weaker and then at 0.2 nm the peak broadens further but then unexpectedly decreases.

A comparison of the LSPR peaks of the cubes above the surface to the cube in the homogeneous environment is presented in figure 1.36a. Compared to the case of the sphere (figure 1.17), shifts in λ_{max} for the same surface distances are indeed greater but the cubes' responses deviate significantly from those of the cube in a homogeneous environment of increasing real RI n. The responses of the cubes above the surface seem to gradually fall off the curve followed by cube in the homogeneous environment as the LSPR peak broadens. Both orientations nevertheless exhibit a red-shift of the LSPR peak, with the face-oriented cube showing greater effect. This is expected as the face-oriented cube is overall closer to the surface due to its lower barycenter and greater exposed area at the same distance.

To try to understand these phenomena, we may look at the evolution of the absorption and scattering peaks. In (figure 1.36b), we see that the absorption responses near the surface are significantly different from those of the homogeneous environment. The absorption of the face-oriented cube at very short distances is comparable to a cube in a homogeneous environment of index $n = 1.22$ and indicates that the close proximity of the faces has a strong impact on the absorption. The evolution of the edge-oriented cube is more difficult to interpret. The blue-shift resembles that of a sphere seen in figure 1.18 (page 56). In the case of the sphere, this blue-shift is due to the induction of higher-order modes, which is likely the case here due to the inhomogeneous effects of the surface on the edge-oriented cube[39, 56, 57]. To see if this is the case, we have plotted the absorption cross-sections at $d_s = 0.2\,\text{nm}$ in figure 1.37. Surprisingly, a higher-order mode appears in the spectrum of the face-oriented cube. This mode may be present in the edge-oriented cube as well but it is not evident from the spectrum. This highlights the difficulty in interpreting the optical response. Returning to figure 1.36c, we see that for the scattering of the face-oriented cube

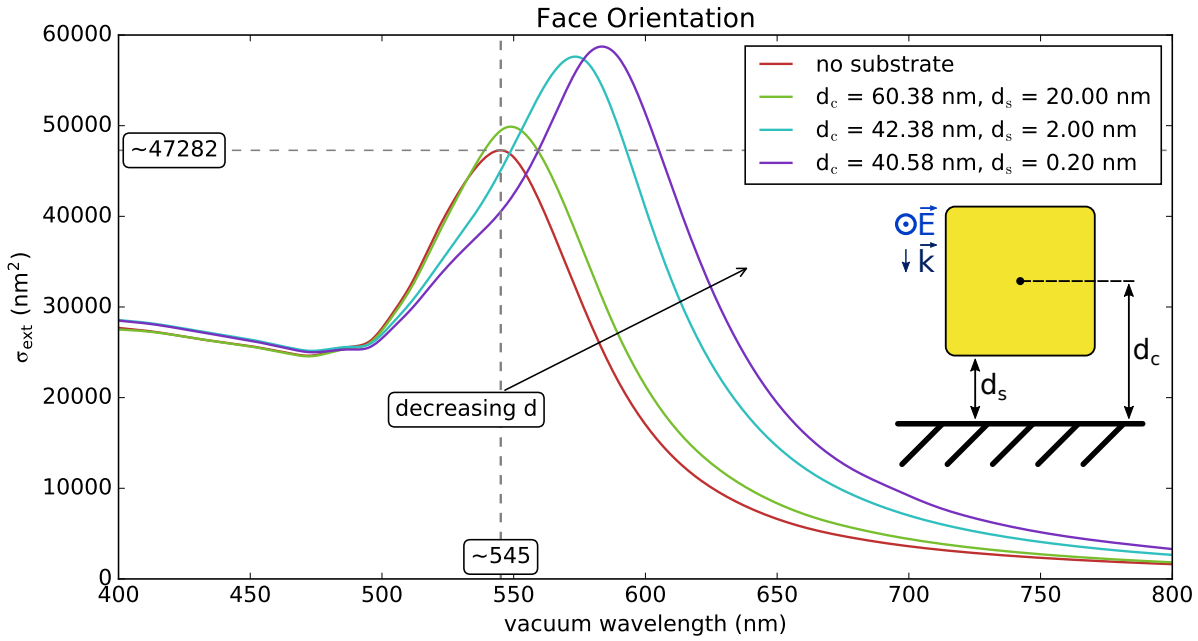

(a)

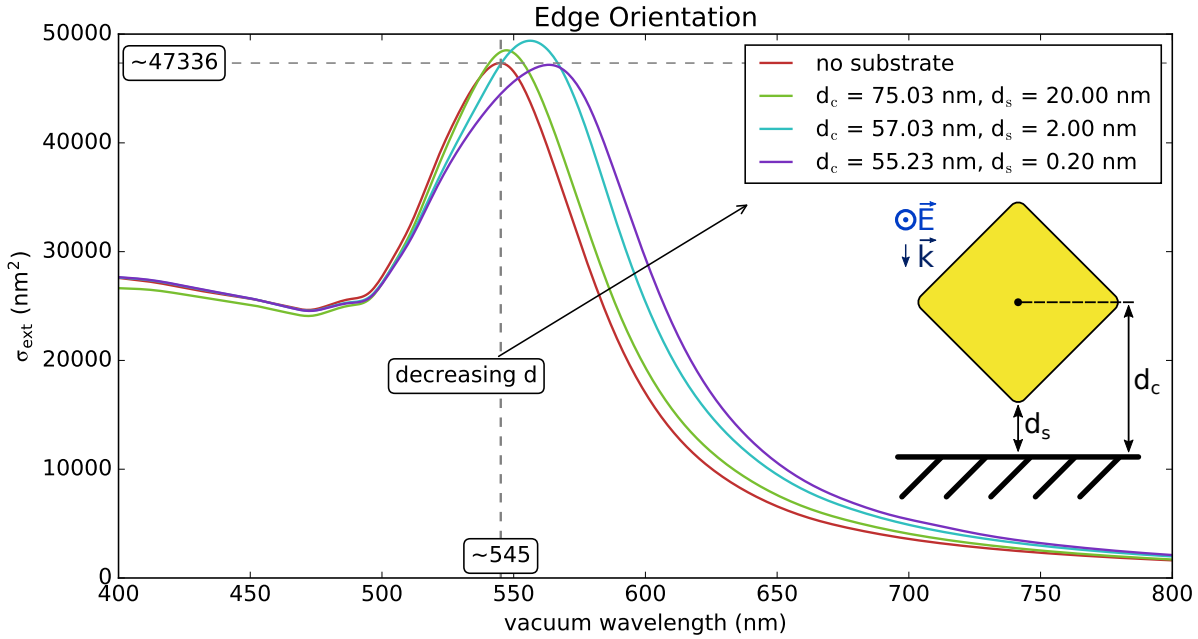

(b)

Figure 1.35: Extinction cross-section of a rounded gold cube ($l = 80.76\,\mathrm{nm}$, $r = 5\,\mathrm{nm}$) in air ($n = 1$) on its face (a) and its edge (b) at varying distance from a glass substrate ($n = 1.5$). d_s: surface-to-surface distance, d_c: cube-barycenter-to-surface distance. [FEM calculations]

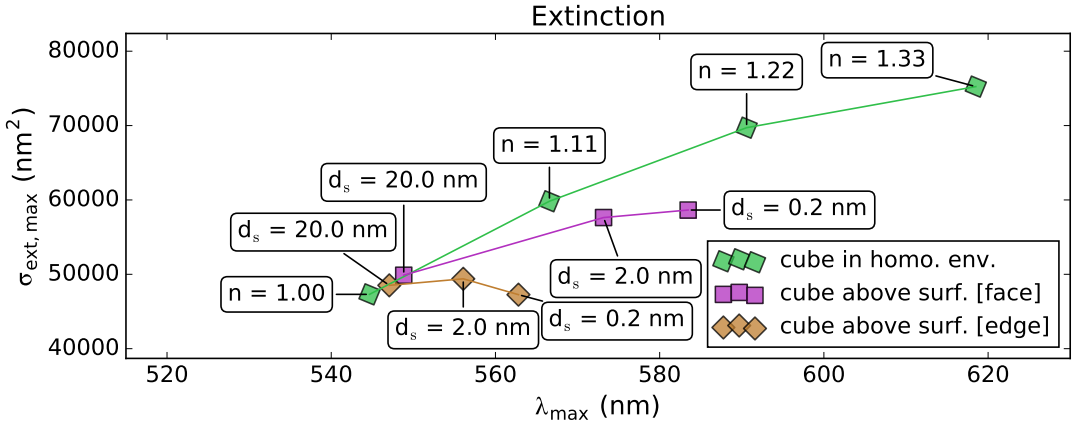

(a)

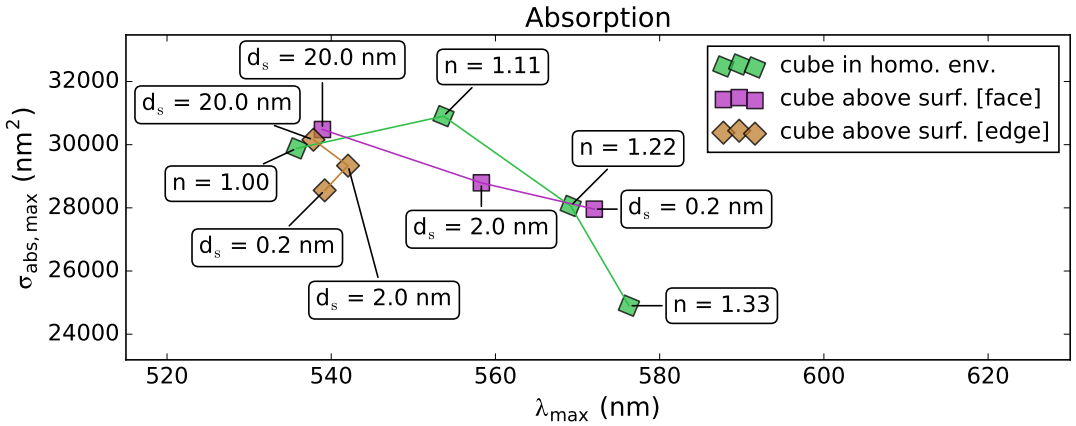

(b)

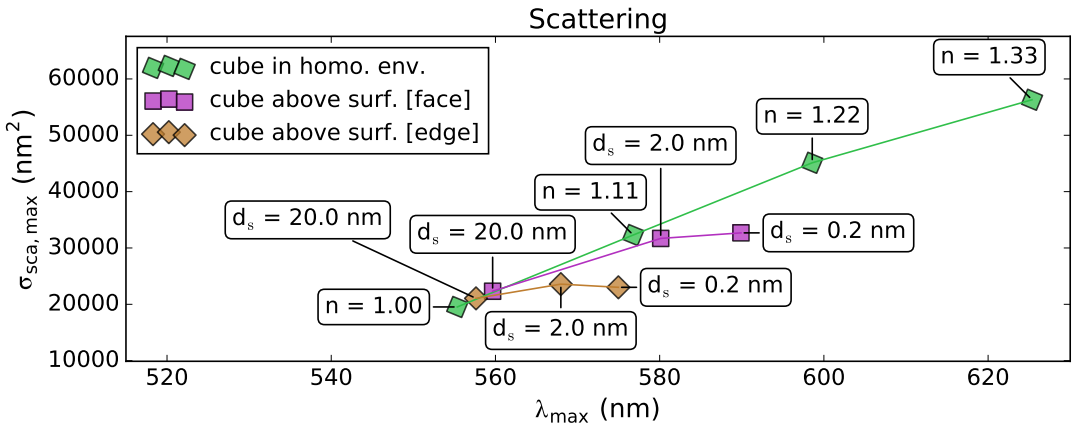

(c)

Figure 1.36: Comparison of the LSPR peak maxima of three systems: a cube in a homogeneous environment of varying real RI n (figure 1.33), a face-oriented cube at varying surface-to-surface distance d_s above a surface (figure 1.35a) and an edge-oriented cube at varying surface-to-surface distance d_s above a surface(figure 1.35b).

is also significantly red-shifted with decreasing distance and initially follows the evolution of the cube in the homogeneous environment. The effect is similar but weaker for the edge-oriented cube. We note that the maximum scattering and maximum absorption of the face-oriented cube at $d_s = 0.2\,\text{nm}$ are only about 15 nm apart while those of the edge-oriented cube are about 35 nm apart, which explains why the latter's peak extinction is lower at this distance.

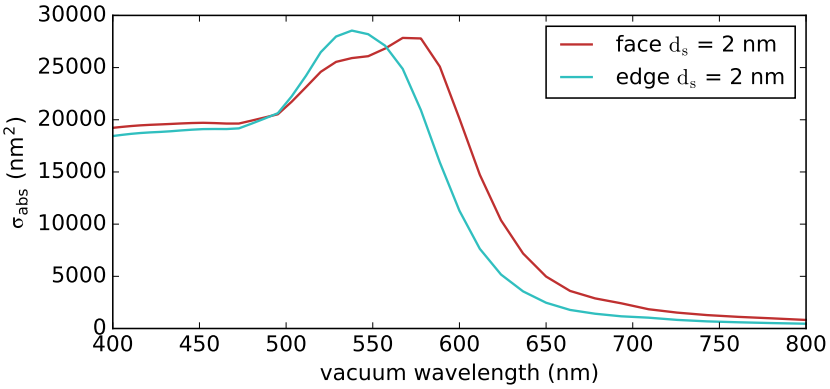

Figure 1.37: Comparison of the absorption cross-sections at $d_s = 0.2\,\text{nm}$ of the edge- and face-oriented cubes in figures 1.35b and 1.35a, respectively. A multipolar mode appears in the face-oriented cube's spectrum as predicted from the interpretation of figure 1.38. [FEM calculations]

We compare σ_{ext} of both cube orientations pairwise at the same surface-to-surface distance d_s in figure 1.38 (which compares the curves in figure 1.35 pairwise) and at the same barycenter-to-surface distance d_c in figure 1.39[6]. The edge-oriented cube is shown at the same distances in both figures. The distance of the face-oriented cube has been adjusted to match either d_c or d_s, depending on which one is being compared. We see that as the cubes approach the surface with the same d_s, the LSPR of the face-oriented cube red-shifts and increases more quickly, as discussed above. If they approach with the same d_c, however, the LSPR of the edge-oriented cube red-shifts more but increases less than that of the face-oriented cube. The relative broadening is also inverted. This is again likely due to the stronger influence of higher-order modes in the edge-oriented cube.

These investigations show that the orientation near the surface is a critical factor in the LSPR response. In each case, we also note that the shift is greater when a larger proportion of mass is in close proximity to the surface.

Finally we compare the face oriented cube to the truncated spheres with s of 10 and 20 nm from section 1.3.2.4 at 20, 2 and 0.2 nm from the surface. The characteristics of the LSPR peaks are plotted in figure 1.40. We see that in each case, the response deviates

[6]For a plot of the optical response of the face-oriented cube with equivalent distances, see figure F.2 on page 242 in the appendix.

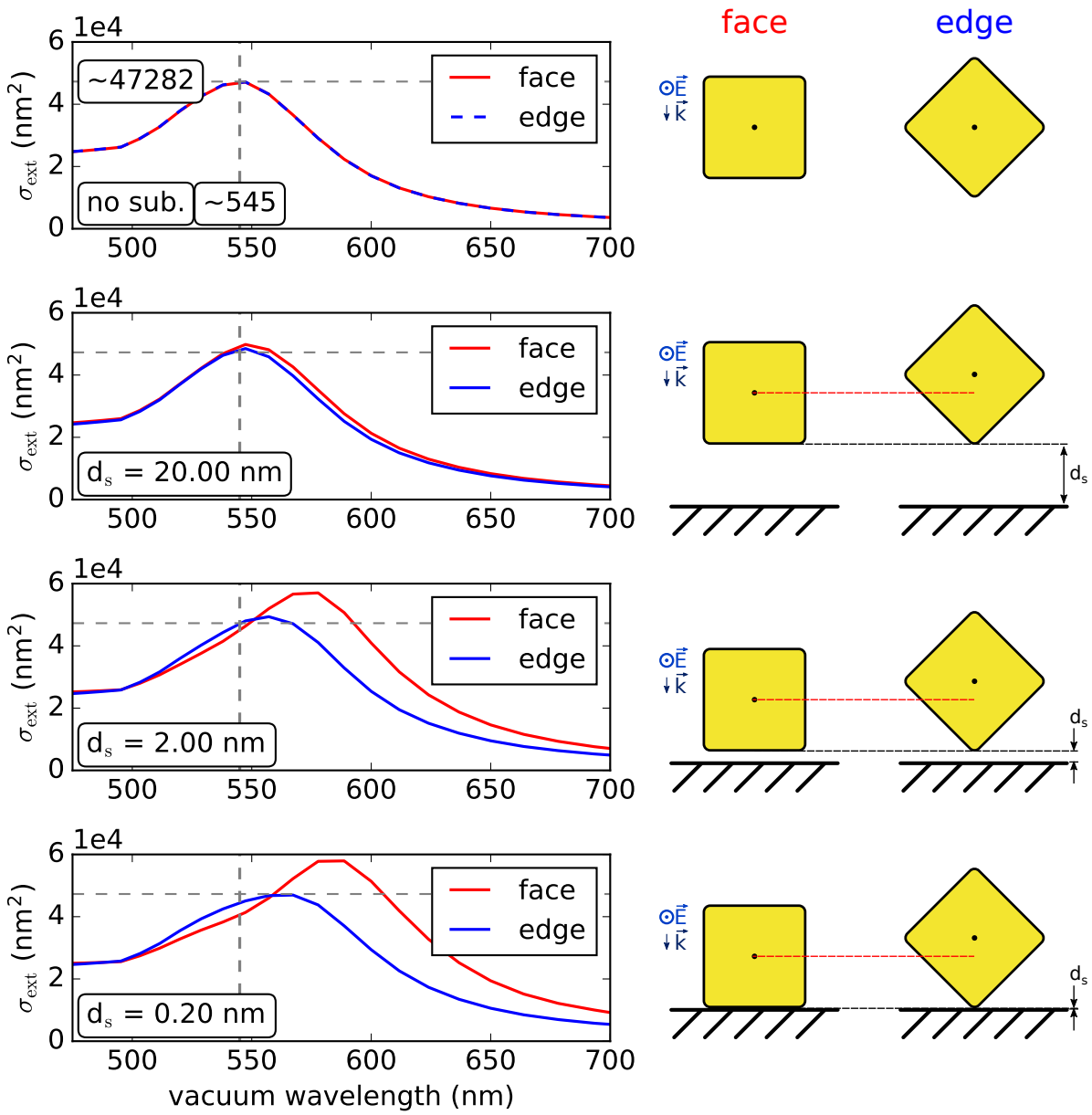

Figure 1.38: Effects of orientation of a rounded cube ($l = 80.76\,\text{nm}$, $r = 5\,\text{nm}$) in air ($n = 1$) at a given surface-to-surface distance above a glass substrate ($n = 1.5$). Left: Dashed lines show position of LSPR peak at $d_s = \infty$. Right: Black dashed line shows that surface-to-surface distances (d_s) are equal. Red dashed line shows that barycenter distances are not equal. See also figures 1.35a and 1.35b [FEM calculations]

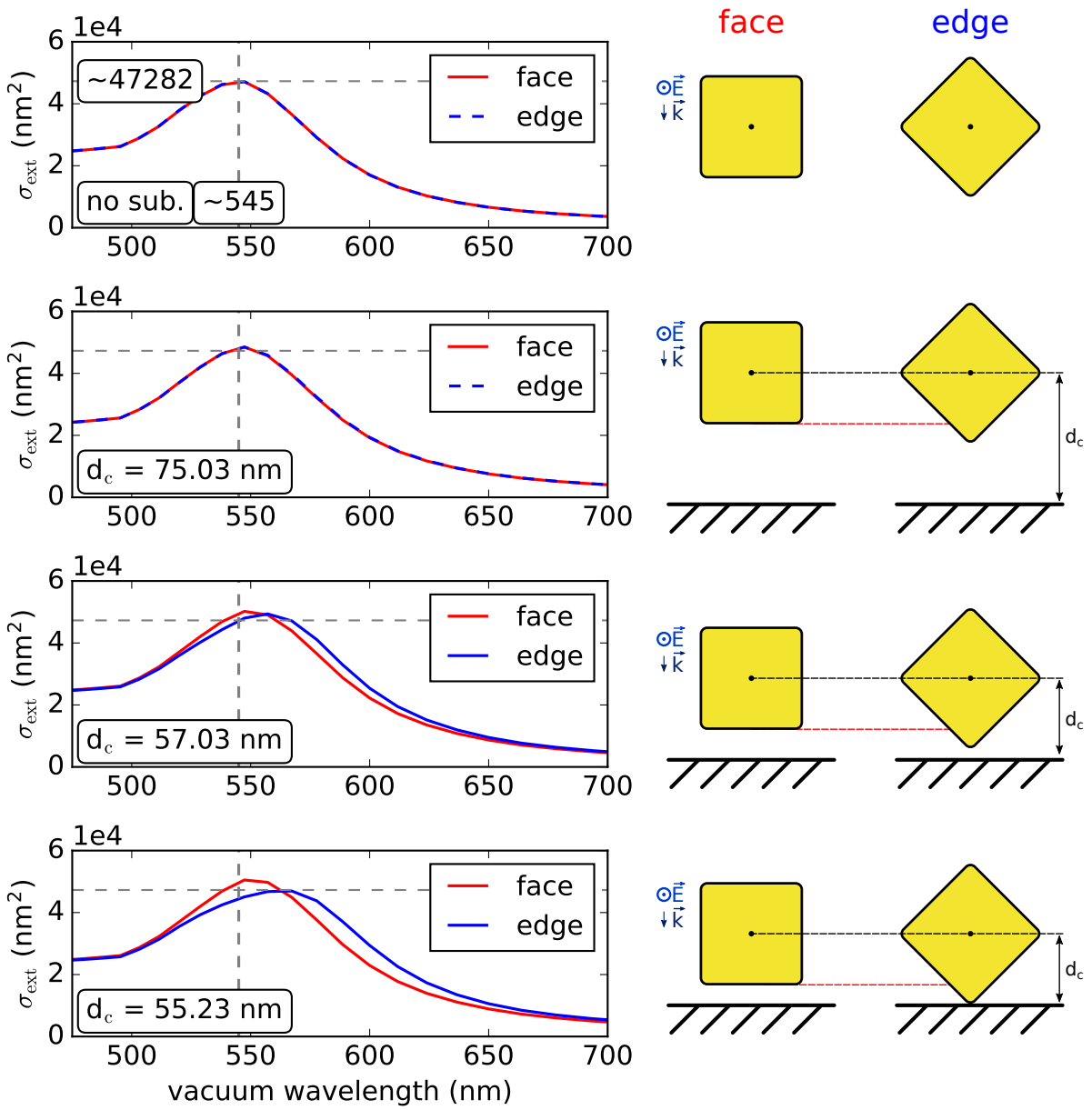

Figure 1.39: Effects of orientation of a rounded cube ($l = 80.76\,\text{nm}$, $r = 5\,\text{nm}$) in air ($n = 1$) at a given cube-barycenter-to-surface distance above a glass substrate ($n = 1.5$). Left: Dashed lines show position of LSPR peak at $d_c = \infty$. Right: Black dashed line shows that barycenter distances (d_c) are equal. Red dashed line shows that surface-to-surface distances are not equal. See also figure 1.35b [FEM calculations]

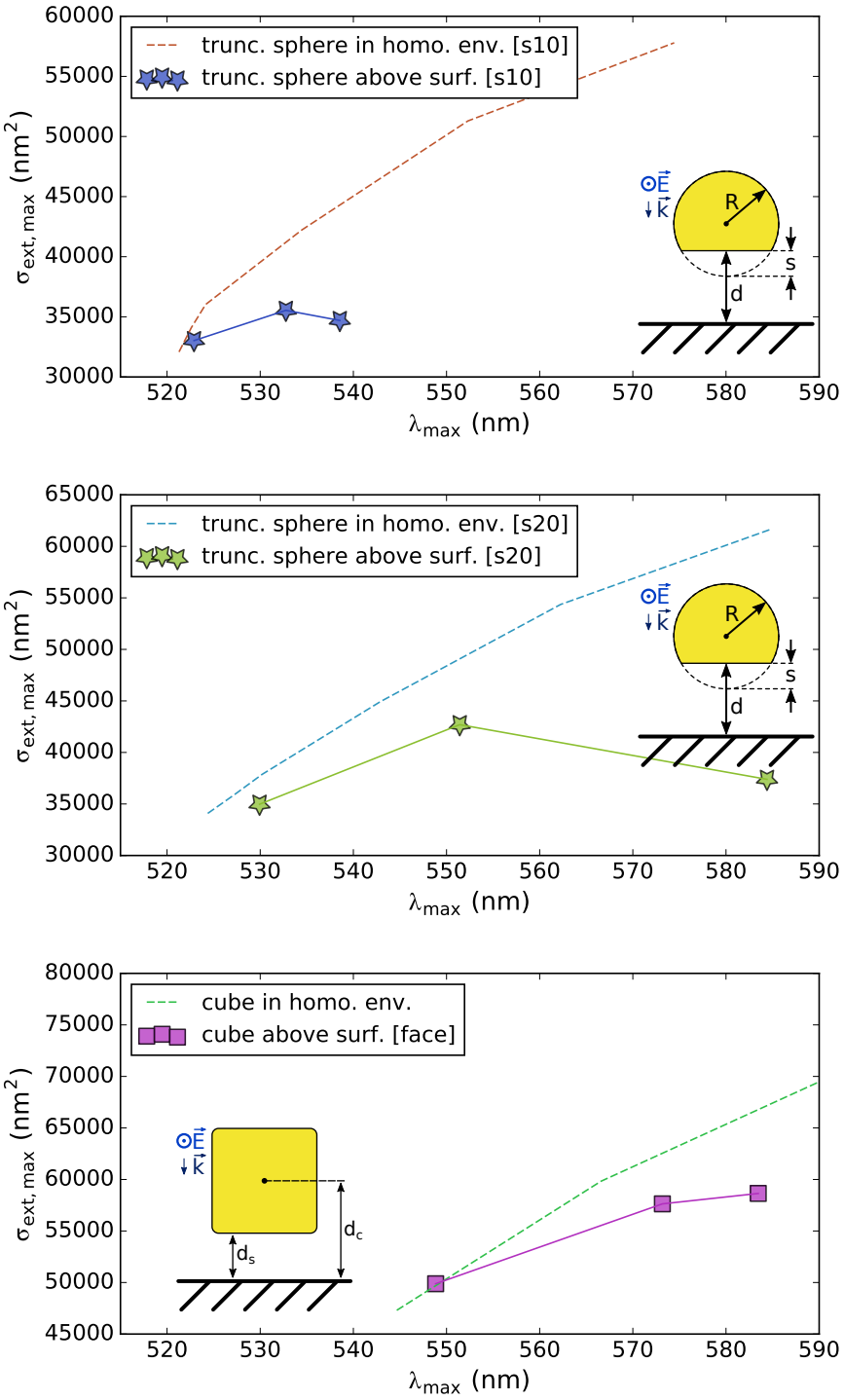

Figure 1.40: Comparison of the LSPR peak maxima of the truncated spheres in figure 1.28 and the face-oriented cube in figure 1.35a at 20, 2 and 0.2 nm from the surface. The curves for the equivalent objects in a homogeneous environment are shown as dotted lines in each figure.

significantly from the response of the equivalent object in a homogeneous environment of increasing index n.

The descriptions given in this section are general and qualitative. It is difficult to draw further conclusions about the response of cubes from the cursory studies presented here. Deeper insight can be gained from modeling the near fields around the object and the distribution of charges on the cube's surface to investigate the activation of higher-order modes and their relative contributions to the total absorption, scattering and extinction cross-sections[49, 53–55, 57]. The key point here is to illustrate the importance of both the shape and orientation of a plasmonic object near a dielectric interface and thereby show that the complexity of the interactions defies a simplified model through the use of an effective real RI n_{eff}.

Conclusion

In this chapter we have seen how the electron configuration of the noble metals gives rise to the phenomenon of LSPR in noble MNOs and how this phenomenon may be modeled both analytically and numerically. Using the numerical methods, we have undertaken an investigation of several factors expected to influence the optical response of an object in a real system. We have seen that these factors may significantly influence the LSPR of an object.

In the case of spheres, we have shown that the presence of a substrate, wetting effects and mild deformations modify the optical response in a way that resembles the response induced by a homogeneous environment of a specific real RI n. The response of a real system for which these factors are beyond experimental determination may therefore be modelled as the response of an object in a homogeneous environment of effective real RI n_{eff} in some cases. For small variations, the different factors may induce equally small effects that are roughly linear and cumulative. This allows one effect to be studied independently while accounting for other effects through the use of n_{eff}. This is an important result for sensing applications where these other effects are likely unknown.

The shape and orientation of the object must be taken into account when attempting to model a system with n_{eff}. In the case of a sphere, we have shown that small facets and deformations induce effects similar to those of a simpler system of homogeneous environment of increasing real RI. The evolution of these responses nevertheless diverges from the simpler system as the deformations increase and can no longer be accounted for with n_{eff}. Even small deformations may be significant when the object is near a substrate due to complex interactions that are difficult to predict. This has been shown to be true even when the response is compared to the deformed object in a homogeneous environment of increase n: the ellipsoids evolved along the same curve as the equivalent object whereas the truncated spheres deviated significantly from it. The same effects were

observed with cubes. In general, the proximity of a substrate induces a red-shift of the LSPR response as would be observed with an increasing real RI, but the LSPR is damped by other effects such as the induction of multipolar modes which cannot be accounted for through a simpler homogeneous environment of index n_{eff}. For such systems, a more complex model is needed.

The validity of the simple model of a homogeneous environment of n_{eff} depends on the agreement between the idealized response and the real response and must remain "physical". It should represent a weighted average of the different effects expected in the modeled system. In the hypothetical "real" system of a faceted gold sphere on a glass substrate in air surrounded by a liquid residue with an index slightly above that of water, we have estimated n_{eff} to be around 1.18. This is in good agreement with the spectra of real systems that we have measured in our group and shows that this simplification can be applied to real systems.

References

[1] J. Lermé. Nanoparticle above a Dielectric Interface: Plasmon Hybridization Model, Comparison with the Dimer System, and against Exact Electrodynamics Calculations. *The Journal of Physical Chemistry C*, 118(48):28118–28133, December 2014. ISSN 1932-7447. doi:10.1021/jp509238j.

[2] J. Lermé, C. Bonnet, M. Broyer, E. Cottancin, D. Manchon, and M. Pellarin. Optical Properties of a Particle above a Dielectric Interface: Cross Sections, Benchmark Calculations, and Analysis of the Intrinsic Substrate Effects. *The Journal of Physical Chemistry C*, 117(12):6383–6398, March 2013. ISSN 1932-7447. doi:10.1021/jp3121963.

[3] J. Lermé. Plasmon Hybridization Model for a Nanoparticle above a Dielectric Interface: Dielectric Effects, Comparison with the Dimer System, Range of Applicability, and Limits. *The Journal of Physical Chemistry C*, 119(36):21087–21104, September 2015. ISSN 1932-7447, 1932-7455. doi:10.1021/acs.jpcc.5b06129.

[4] COMSOL AB, Stockholm, Sweden. COMSOL Multiphysics®. URL `http://www.comsol.com`.

[5] P. B. Johnson and R. W. Christy. Optical Constants of the Noble Metals. *Physical Review B*, 6(12):4370–4379, December 1972. doi:10.1103/PhysRevB.6.4370.

[6] E. Jones, T. Oliphant, P. Peterson, et al. SciPy: Open source scientific tools for Python, 2001–. URL `http://www.scipy.org/`.

[7] T. E. Oliphant. Python for Scientific Computing. *Computing in Science & Engineering*, 9(3):10–20, 2007. ISSN 1521-9615. doi:10.1109/MCSE.2007.58.

[8] K. J. Millman and M. Aivazis. Python for Scientists and Engineers. *Computing in Science & Engineering*, 13(2):9–12, March 2011. ISSN 1521-9615. doi:10.1109/MCSE.2011.36.

[9] J. D. Hunter. Matplotlib: A 2d Graphics Environment. *Computing in Science & Engineering*, 9(3):90–95, 2007. ISSN 1521-9615. doi:10.1109/MCSE.2007.55.

[10] P. Billaud. *Propriétés optiques de nanoparticules uniques de métaux nobles.* PhD thesis, Université Claude Bernard Lyon 1, Lyon, France, 2006.

[11] C. Kittel. *Introduction to solid state physics.* Wiley, Hoboken, NJ, 8th edition, 2005. ISBN 978-0-471-41526-8.

[12] N. W. Ashcroft and N. D. Mermin. *Solid state physics.* Holt, Rinehart and Winston, New York, 1976. ISBN 978-0-03-083993-1.

[13] O. Madelung. *Introduction to solid-state theory.* Number v. 2 in Springer series in solid-state sciences. Springer-Verlag, Berlin ; New York, 1978. ISBN 978-0-387-08516-6.

[14] E. Cottancin, M. Broyer, J. Lermé, and M. Pellarin. Optical Properties of Metal Clusters and Nanoparticles. In *Handbook of Nanophysics: Nanoelectronics and Nanophotonics*, page 779. CRC Press, September 2010. ISBN 978-1-4200-7550-2.

[15] M. Guerrisi, R. Rosei, and P. Winsemius. Splitting of the interband absorption edge in Au. *Physical Review B*, 12(2):557–563, July 1975. doi:10.1103/PhysRevB.12.557.

[16] CRC Handbook of Chemistry and Physics, 89th Edition, June 2008.

[17] M. Fox. *Optical properties of solids.* Oxford master series in condensed matter physics. Oxford University Press, Oxford ; New York, 2001. ISBN 978-0-19-850613-3 978-0-19-850612-6.

[18] J. D. Jackson. *Classical electrodynamics.* Wiley, New York, 3rd edition, 1999. ISBN 978-0-471-30932-1.

[19] C. F. Bohren and D. R. Huffman. *Absorption and scattering of light by small particles.* Wiley-VCH, Weinheim, 2004. ISBN 978-0-471-29340-8 978-0-471-05772-7. OCLC: 254937169.

[20] B. E. A. Saleh and M. C. Teich. *Fundamentals of photonics.* Wiley series in pure and applied optics. Wiley Interscience, Hoboken, N.J, 2nd edition, 2007. ISBN 978-0-471-35832-9.

[21] E. Hecht. *Optics.* Pearson education. Addison-Wesley, San Francisco, 4th edition, 2010. ISBN 978-0-321-18878-6. OCLC: 846202400.

[22] D. Manchon. *Réponse optique de nano-objets uniques anisotropes : de l'or aux métaux de transition.* PhD thesis, Université Claude Bernard Lyon 1, Lyon, France, October 2012.

[23] R. Rosei. Temperature modulation of the optical transitions involving the Fermi surface in Ag: Theory. *Physical Review B*, 10(2):474–483, July 1974. doi:10.1103/PhysRevB.10.474.

[24] G. Celep, E. Cottancin, J. Lermé, M. Pellarin, L. Arnaud, J. R. Huntzinger, J. L. Vialle, M. Broyer, B. Palpant, O. Boisron, and P. Mélinon. Optical properties of copper clusters embedded in alumina: An experimental and theoretical study of size dependence. *Physical Review B*, 70(16):165409, October 2004. doi:10.1103/PhysRevB.70.165409.

[25] U. Kreibig and C. v. Fragstein. The limitation of electron mean free path in small silver particles. *Zeitschrift für Physik*, 224(4):307–323, August 1969. ISSN 0044-3328. doi:10.1007/BF01393059.

[26] U. Kreibig and M. Vollmer. *Optical properties of metal clusters*. Number 25 in Springer series in materials science. Springer, Berlin ; New York, 1995. ISBN 978-0-387-57836-1 978-3-540-57836-9.

[27] S. Marhaba. *Influence de la morphologie sur les proprétés optiques de nano-objets métalliques uniques.* PhD thesis, Université Claude Bernard Lyon 1, Lyon, France, 2008.

[28] K. A. Willets and R. P. Van Duyne. Localized Surface Plasmon Resonance Spectroscopy and Sensing. *Annual Review of Physical Chemistry*, 58(1):267–297, May 2007. ISSN 0066-426X, 1545-1593. doi:10.1146/annurev.physchem.58.032806.104607.

[29] A. C. Lind and J. M. Greenberg. Electromagnetic Scattering by Obliquely Oriented Cylinders. *Journal of Applied Physics*, 37(8):3195–3203, July 1966. ISSN 0021-8979, 1089-7550. doi:10.1063/1.1703184.

[30] R. Gans. Über die form ultramikroskopischer goldteilchen. *Annalen der Physik*, 342 (5):881–900, 1912.

[31] S. Asano and G. Yamamoto. Light Scattering by a Spheroidal Particle. *Applied Optics*, 14(1):29–49, January 1975. ISSN 1539-4522. doi:10.1364/AO.14.000029.

[32] N. V. Voshchinnikov and V. G. Farafonov. Optical properties of spheroidal particles. *Astrophysics and Space Science*, 204(1):19–86, June 1993. ISSN 0004-640X, 1572-946X. doi:10.1007/BF00658095.

[33] G. Mie. Beiträge zur Optik trüber Medien, speziell kolloidaler Metallösungen. *Annalen der Physik*, 330(3):377–445, January 1908. ISSN 1521-3889. doi:10.1002/andp.19083300302.

[34] H. C. van de Hulst. *Light scattering by small particles*. Dover Publications, New York, 1981. ISBN 978-0-486-64228-4.

[35] M. I. Mishchenko, L. D. Travis, and A. A. Lacis. *Scattering, absorption, and emission of light by small particles*. Cambridge University Press, Cambridge ; New York, 2002. ISBN 978-0-521-78252-4. OCLC: ocm48932103.

[36] J. Lermé, G. Bachelier, P. Billaud, C. Bonnet, M. Broyer, E. Cottancin, S. Marhaba, and M. Pellarin. Optical response of a single spherical particle in a tightly focused light beam: application to the spatial modulation spectroscopy technique. *Journal of the Optical Society of America A*, 25(2):493–514, February 2008. doi:10.1364/JOSAA.25.000493.

[37] K. L. Kelly, E. Coronado, L. L. Zhao, and G. C. Schatz. The Optical Properties of Metal Nanoparticles: The Influence of Size, Shape, and Dielectric Environment. *The Journal of Physical Chemistry B*, 107(3):668–677, January 2003. ISSN 1520-6106, 1520-5207. doi:10.1021/jp026731y.

[38] M. M. Miller and A. A. Lazarides. Sensitivity of Metal Nanoparticle Surface Plasmon Resonance to the Dielectric Environment. *The Journal of Physical Chemistry B*, 109 (46):21556–21565, November 2005. ISSN 1520-6106. doi:10.1021/jp054227y.

[39] C. Noguez. Surface Plasmons on Metal Nanoparticles: The Influence of Shape and Physical Environment. *The Journal of Physical Chemistry C*, 111(10):3806–3819, March 2007. ISSN 1932-7447, 1932-7455. doi:10.1021/jp066539m.

[40] O. L. Muskens, P. Billaud, M. Broyer, N. Del Fatti, and F. Vallée. Optical extinction spectrum of a single metal nanoparticle: Quantitative characterization of a particle

and of its local environment. *Physical Review B*, 78(20):205410, November 2008. doi:10.1103/PhysRevB.78.205410.

[41] M. I. Mishchenko, J. W. Hovenier, and L. D. Travis. *Light Scattering by Nonspherical Particles: Theory, Measurements, and Applications*. Academic Press, September 1999. ISBN 978-0-08-051020-0. Google-Books-ID: qT3DwjHXA9cC.

[42] E. Fucile, P. Denti, F. Borghese, R. Saija, and O. I. Sindoni. Optical properties of a sphere in the vicinity of a plane surface. *JOSA A*, 14(7):1505–1514, July 1997. ISSN 1520-8532. doi:10.1364/JOSAA.14.001505.

[43] T. Wriedt and A. Doicu. Light scattering from a particle on or near a surface. *Optics Communications*, 152(4–6):376–384, July 1998. ISSN 0030-4018. doi:10.1016/S0030-4018(98)00099-6.

[44] J. Parsons, C. P. Burrows, J. R. Sambles, and W. L. Barnes. A comparison of techniques used to simulate the scattering of electromagnetic radiation by metallic nanostructures. *Journal of Modern Optics*, 57(5):356–365, March 2010. ISSN 0950-0340. doi:10.1080/09500341003628702.

[45] C. G. Khoury, S. J. Norton, and T. Vo-Dinh. Investigating the plasmonics of a dipole-excited silver nanoshell: Mie theory versus finite element method. *Nanotechnology*, 21(31):315203, August 2010. ISSN 1361-6528. doi:10.1088/0957-4484/21/31/315203.

[46] M. Schmid, P. Andrae, and P. Manley. Plasmonic and photonic scattering and near fields of nanoparticles. *Nanoscale Research Letters*, 9(1):50, January 2014. ISSN 1931-7573. doi:10.1186/1556-276X-9-50.

[47] N. Grillet, D. Manchon, F. Bertorelle, C. Bonnet, M. Broyer, E. Cottancin, J. Lermé, M. Hillenkamp, and M. Pellarin. Plasmon Coupling in Silver Nanocube Dimers: Resonance Splitting Induced by Edge Rounding. *ACS Nano*, 5(12):9450–9462, December 2011. ISSN 1936-0851, 1936-086X. doi:10.1021/nn2041329.

[48] M. Pellarin, J. Ramade, J. M. Rye, C. Bonnet, M. Broyer, M.-A. Lebeault, J. Lermé, S. Marguet, J. R. Navarro, and E. Cottancin. Fano Transparency in Rounded Nanocube Dimers Induced by Gap Plasmon Coupling. *ACS Nano*, 10(12):11266–11279, December 2016. ISSN 1936-0851, 1936-086X. doi:10.1021/acsnano.6b06406.

[49] L. J. Sherry, S.-H. Chang, G. C. Schatz, R. P. Van Duyne, B. J. Wiley, and Y. Xia. Localized Surface Plasmon Resonance Spectroscopy of Single Silver Nanocubes. *Nano Letters*, 5(10):2034–2038, October 2005. ISSN 1530-6984. doi:10.1021/nl0515753.

[50] J. M. McMahon, Y. Wang, L. J. Sherry, R. P. Van Duyne, L. D. Marks, S. K. Gray, and G. C. Schatz. Correlating the structure, optical spectra, and electrodynamics of single silver nanocubes. *The Journal of Physical Chemistry C*, 113(7):2731–2735, 2009.

[51] W. J. Galush, S. A. Shelby, M. J. Mulvihill, A. Tao, P. Yang, and J. T. Groves. A Nanocube Plasmonic Sensor for Molecular Binding on Membrane Surfaces. *Nano Letters*, 9(5):2077–2082, May 2009. ISSN 1530-6984, 1530-6992. doi:10.1021/nl900513k.

[52] Q. Zhang, W. Li, C. Moran, J. Zeng, J. Chen, L.-P. Wen, and Y. Xia. Seed-Mediated Synthesis of Ag Nanocubes with Controllable Edge Lengths in the Range of 30-200 nm and Comparison of Their Optical Properties. *Journal of the American Chemical Society*, 132(32):11372–11378, August 2010. ISSN 0002-7863, 1520-5126. doi:10.1021/ja104931h.

[53] V. Klimov, G.-Y. Guo, and M. Pikhota. Plasmon Resonances in Metal Nanoparticles with Sharp Edges and Vertices: A Material Independent Approach. *The Journal of Physical Chemistry C*, 118(24):13052–13058, June 2014. ISSN 1932-7447, 1932-7455. doi:10.1021/jp412349f.

[54] R. Fuchs. Theory of the optical properties of ionic crystal cubes. *Physical Review B*, 11(4):1732–1740, February 1975. doi:10.1103/PhysRevB.11.1732.

[55] D. Langbein. Normal modes at small cubes and rectangular particles. *Journal of Physics A: Mathematical and General*, 9(4):627, 1976. ISSN 0305-4470. doi:10.1088/0305-4470/9/4/019.

[56] I. O. Sosa, C. Noguez, and R. G. Barrera. Optical Properties of Metal Nanoparticles with Arbitrary Shapes. *The Journal of Physical Chemistry B*, 107(26):6269–6275, July 2003. ISSN 1520-6106. doi:10.1021/jp0274076.

[57] C. Noguez. Optical properties of isolated and supported metal nanoparticles. *Optical Materials*, 27(7):1204–1211, April 2005. ISSN 0925-3467. doi:10.1016/j.optmat.2004.11.012.

Chapter 2

Spatial Modulation Spectroscopy In A Liquid Environment

Contents

Introduction

We have seen in the previous chapter that metallic nano-objects (MNOs) exhibit localized surface plasmon resonance (LSPR) and that this response depends on the composition, size, shape and environment of the object. In order to study this response and eventually exploit it for sensing applications, we require a way to measure it experimentally. One possible approach is to study ensembles of identical objects, the collective response of which will generate a strong enough signal for direct measurement via standard spectroscopy. Colloidally synthesized objects can be separated by size to reduce their dispersion[1–3] but nanometric irregularities are difficult to eliminate. As we have seen in the previous chapter, even small variations may have a large effect on the optical response which will create averaging effects in ensemble measurements. Lithographic techniques hold promise for producing highly regular objects[4, 5], but morphological variations in the objects themselves are not the only issue with ensemble measurements. Even with monodisperse MNOs, applications that seek to explore properties of the local environment via the LSPR response will still suffer from inhomogeneities therein, such as differential molecular binding in the case of sensing applications, which will again be masked by averaging effects.

In the last decade, several methods have been developed to overcome these difficulties by studying the response of individual nano-objects directly [6–17]. Here we will be primarily concerned with the linear optical techniques[1]. The first categorical division among these techniques is between those that measure the near-field and those that measure the far-field around an object. Scanning near-field optical microscopy (SNOM), which constitutes the former, uses a tip to probe the field around the object. In the two principle modes of operation, the tip is either used to induce scattering in the object via an evanescent field, which is then measured in the far-field, or it is used to measure the field around an object under far-field illumination. While SNOM permits nanoscale mapping of the near-field of the object with phase information and high spatial resolution, it is difficult to directly interpret the results and a detailed model of the object-tip interactions is needed to obtain quantitative measurements of the object's optical response[6, 8, 11, 16].

Among the far-field methods, there is again a categorical division between dark-field and bright-field measurements. In dark-field measurements, the object is illuminated and a detector outside of the illumination path measures the induced far-field scattering. Although this approach provides no information about the absorption, dark-field techniques are very sensitive and relatively direct and are therefore the most widely used[7, 9, 10, 15, 16]. The principal difficulty is that quantitative measurements require a precise model of the ob-

[1]The interested read may find a complete review of single nano-object spectroscopies in Crut et al. [17].

ject's shape, size and environment in order to calculate the angle-dependent scattering diagram and thereby deduce the scattering cross-section[12, 14]. Even when this information is available, quantitative analysis also requires a precisely characterized spot profile at the studied wavelengths, which may be difficult to determine.

Instead of measuring the scattered light, bright-field measurements of single nano-objects directly measure changes in the incident illumination. These techniques rely on modulation and lock-in detection to isolate the relatively weak signal of the object from the stronger fluctuations in the irradiance on the object. Among these are the non-linear photo-thermal techniques, in which the object is heated under periodic irradiation and a second beam is used to measure the effects of the heating on the refractive index (RI) of the object's environment. These techniques are limited to indirect absorption measurements and depend on the thermal properties and kinetics of the environment around the object[18, 19]. The other bright-field techniques measure the extinction of the object, which is the combined effect of absorption and scattering. In polarization modulation microscopy (PMM), the polarization is rapidly modulated between orthogonal directions to measure the difference in the extinction cross-sections along different axes of anisotropic objects. While high frequencies can be used to obtain good signal-to-noise ratios, the technique is limited to anisotropic objects and can only measure the difference between the response along different axes[13]. In spatial modulation spectroscopy (SMS), the focused beam is oscillated relative to the sample and the measured signal is directly proportional to the absolute extinction cross-section[20]. The technique can also be used to characterize the focused spot profile on the sample, which in turn allows for the experimental determination of the absolute extinction cross-section. Another particular advantage of this technique is that an intense light source is not required[16, 20]. After several years of working with SMS, our group has developed both experimental and theoretical expertise with this technique and it is therefore the technique that has been chosen for this work.

In this chapter we will present the principles of SMS and how it can be used to map samples and measure the extinction spectra of individual nano-objects[2]. We will also see that these measurements can be correlated to electron microscopy to determine the real morphology of the studied object. We will then discuss our work to adapt a SMS setup for biosensing applications in a liquid environment. In particular, we will show how we have overcome various challenges to create a SMS setup capable of measuring the optical response of individual MNOs in a macroscopic fluid cell and we will show that these measurements are in agreement with theoretical calculations for both colloidally synthesized and lithographed objects.

[2]For a full review of the SMS technique, see Billaud et al. [20]. For a detailed description of the optical response of a spherical particle subject to SMS under a focused spot, see Lermé et al. [21].

2.1 Principles of Spatial Modulation Spectroscopy

As we have seen in the previous chapter, an irradiated nano-object will both absorb and scatter some of the incident light. If the object is placed in the path of a focused beam as depicted in figure 2.1, the transmitted power will be the sum of the incident light that did not react with the object along with the scattered light collected by the objective. If the numerical aperture (NA) of the objective is not too large, the power of collected scattered light is negligible[3] and the transmitted power may then be expressed as

$$P_{\text{trans}} \approx P_{\text{inc}} - P_{\text{abs}} - P_{\text{sca}} = P_{\text{inc}} - P_{\text{ext}} \tag{2.1}$$

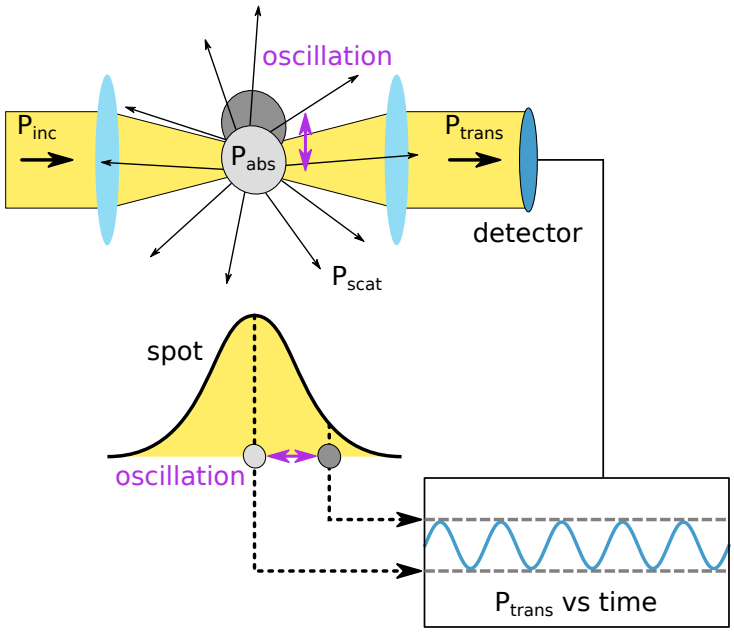

Figure 2.1: Simplified schematic overview of the principle of SMS. The relative oscillation of the object modulates the transmitted signal through extinction.

If the MNO is relatively small compared to the focused spot size, the irradiance at its center may be taken as uniform over the object in the so-called local approximation. In the linear regime, the extinguished power is then directly proportional to the irradiance at its center[20, 21]. Recalling the definition of the extinction cross-section in (1.20) ($\sigma_{\text{ext}} = P_{\text{ext}}/I_{\text{inc}}$), the difference in the transmitted power will thus be proportional to the local irradiance and the object's scattering cross-section:

[3]For example, about 10 % of the scattered light of a 100 nm-diameter gold nanosphere is collected with our Cassegrain-reflector objective, which is described later in section 2.2.2.

$$(\Delta P)(x,y) = P_{\text{inc}} - P_{\text{trans}}(x,y) \simeq P_{\text{ext}}(x,y) \simeq \sigma_{\text{ext}} I(x,y) \tag{2.2}$$

where $I(x,y)$ is the irradiance of the spot, centered at $(0,0)$, at the object's position (x,y). We may normalize $I(x,y)$ in (2.2) through division by P_{inc}:

$$\frac{(\Delta P)(x,y)}{P_{\text{inc}}} \simeq \sigma_{\text{ext}} \frac{I(x,y)}{P_{\text{inc}}} \simeq \sigma_{\text{ext}} I_{\text{N}}(x,y) \tag{2.3}$$

where $I_{\text{N}}(x,y)$ is the normalized spot profile and has the units of inverse area.

Under ideal conditions, the extinction cross-section could be measured directly but in practice, the intensity of the light source is 3-5 orders of magnitude greater than the extinguished power and the latter is lost in the fluctuations of the former[22].

To overcome this, a spatial oscillation of the object may be induced along an arbitrary axis in the focal plane of the spot. For an oscillation along the y-axis about the point (x_0, y_0) relative to the spot profile's center at $(0,0)$, the position of the object will be

$$x(t) = x_0 \tag{2.4}$$
$$y(t) = y_0 + \delta_y \sin(2\pi f t) \tag{2.5}$$

where δ_y is the oscillation amplitude and f is the frequency. For *small* amplitudes *relative to the spot size*, we may expand 2.3 about (x_0, y_0) to the second order:

$$\begin{aligned}\frac{\Delta P}{P_{\text{inc}}}(t) = \sigma_{\text{ext}} &\left[I_{\text{N}}(x_0,y_0) + \frac{1}{4} \frac{\partial^2 I_{\text{N}}(x,y)}{\partial y^2}\bigg|_{(x_0,y_0)} \delta_y^2 \right] \\ &+ \underbrace{\left[\sigma_{\text{ext}} \frac{\partial I_{\text{N}}(x,y)}{\partial y}\bigg|_{(x_0,y_0)} \delta_y \right]}_{b_1} \sin(2\pi f t) \\ &+ \underbrace{\left[-\sigma_{\text{ext}} \frac{1}{4} \frac{\partial^2 I_{\text{N}}(x,y)}{\partial y^2}\bigg|_{(x_0,y_0)} \delta_y^2 \right]}_{a_2} \cos\big(2\pi(2f)t\big)\end{aligned} \tag{2.6}$$

Within this approximation, the signal thus consists of a constant term followed by the first and second harmonics of the modulation frequency f. By examination of (2.6), the coefficient of the first harmonic is b_1 while that of the second is a_2. If the position, amplitude of oscillation and spot profile are known, σ_{ext} can be extracted from either of these coefficients.

To get an idea of their form as a function of the object's position, a typical spot profile is shown in figure 2.2 along with its first and second derivatives. We note immediately that as the wavelength increases, the spot broadens and flattens due to diffraction and thus its derivatives along with it. This dependence on wavelength shows that the spot must be characterized across the full spectrum over which one wishes to determine the absolute extinction cross-section.

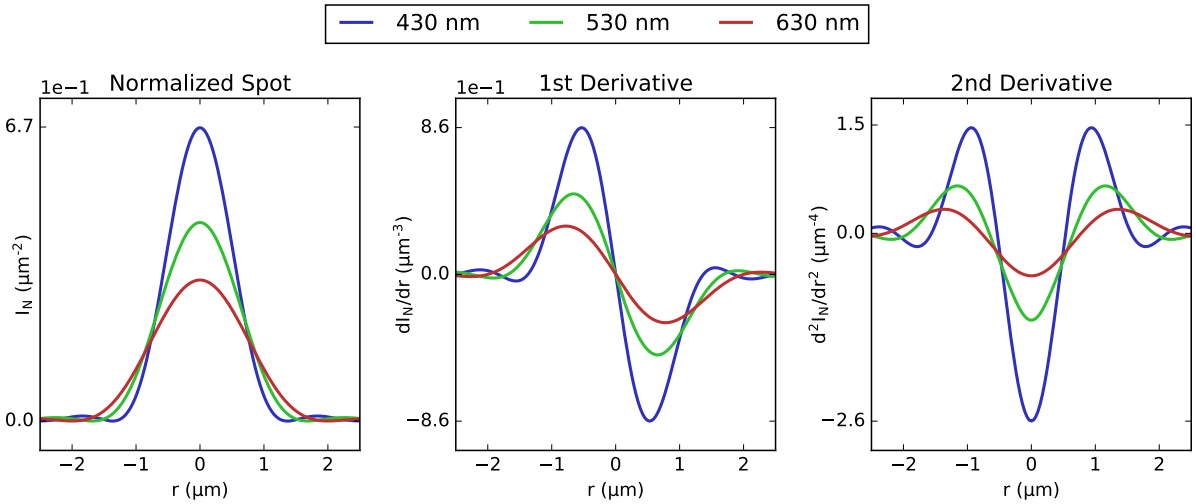

Figure 2.2: Illustrative example of a typical normalized spot profile and its first and second derivatives.

Second, we see that the first and second derivatives of the spot profile have very different shapes. In the case of the former, the signal is anti-symmetric about the object with extrema at a wavelength-dependent distance on either side of the object. In the case of the latter, the absolute maximum is found at the object's position with lesser, symmetric peaks of opposite sign on either side of the object. This will have direct consequences on the appearance of objects in SMS maps. These variations are taken into account in calibration curves to obtain spectra of absolute extinction cross-sections, which we will discuss in the following sections.

The small-amplitude approximation provides insights into the signal generation in SMS but it is only valid for relatively small oscillations compared to the spot size ($\delta_y \approx\leq$ 10 nm). Due to the dependence on δ_y, optimization of the signal leads to oscillation amplitudes that are comparable to the spot size ($\delta_y \approx 400$ nm) and thus beyond the

approximation[4]. To understand how SMS works under typical experimental conditions, we must consider the components of a generic setup and how the signals are measured.

2.1.1 Generic Setup

Figure 2.3 presents a schematic overview of a generic SMS setup. This setup is presented for the sake of illustrating the principles of SMS and will only be discussed in general terms. Details of the actual setup used in this work will be given in section 2.2.4.

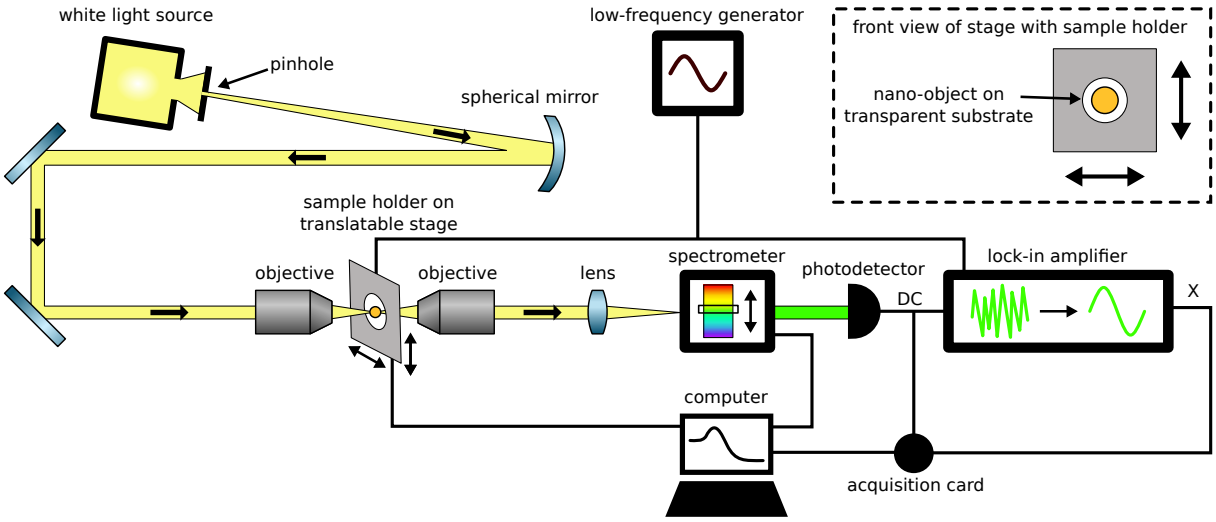

Figure 2.3: Illustrative schematic overview of a generic SMS setup.

Light from a white light source is passed through a pinhole and collimated into a beam with a spherical mirror. The beam is focused to a spot on the sample with a reflective objective. The sample is held on a translatable piezoelectric stage in the focal plane of the spot. The stage is controlled by a computer and is also connected to a low-frequency generator (LFG) that oscillates the stage. The transmitted light is collected by a second objective and passed to a photospectrometer. The selected wavelength is measured by a detector such as a photomultiplier or a photodiode, which produces a signal DC through a preamplifier. This signal is both recorded by the computer and sent to a lock-in amplifier that also receives the signal from the LFG that oscillates the stage, which it uses as a reference signal.

In the lock-in amplifier, the DC signal is amplified and multiplied by the reference signal. The in-phase and quadrature components of the resulting root mean square (RMS) signal are then provided, respectively, as X_{1f} and Y_{1f} at the first harmonic $1f$ or X_{2f} and Y_{2f} at the second harmonic $2f$ of the reference signal. The harmonic is chosen via a setting

[4]Increasing the amplitude further will again reduce the signal.

on the lock-in amplifier. Another setting can be used to adjust the phase to cancel the quadrature component and maximize the in-phase component. The in-phase component is then recorded by the computer as X. The SMS signal is obtained by dividing X_{1f} or X_{2f} by DC, which may be expressed as[20]:

$$\frac{X_{1f}}{DC} = -\frac{1}{\sqrt{2}}\sigma_{\text{ext}}\frac{2}{T}\int_{-T/2}^{T/2} I_{\text{N}}\big(x, y(t)\big)\sin(2\pi f t)dt \tag{2.7}$$

$$\frac{X_{2f}}{DC} = -\frac{1}{\sqrt{2}}\sigma_{\text{ext}}\frac{2}{T}\int_{-T/2}^{T/2} I_{\text{N}}\big(x, y(t)\big)\cos\big(2\pi(2f)t\big)dt \tag{2.8}$$

where $T = 1/f$ and the factor of $1/\sqrt{2}$ is due to the RMS signal of the lock-in amplifier. The calibration curve is the curve by which the measured X/DC signal must be multiplied to obtain σ_{ext}. From (2.7) and (2.8), we see that this is

$$F_{\text{cal}}(f) = \frac{\sqrt{2}}{\frac{2}{T}\int_{-T/2}^{T/2} I_{\text{N}}\big(x, y(t)\big)\sin(2\pi f t)dt} \tag{2.9}$$

$$F_{\text{cal}}(2f) = \frac{\sqrt{2}}{\frac{2}{T}\int_{-T/2}^{T/2} I_{\text{N}}\big(x, y(t)\big)\cos\big(2\pi(2f)t\big)dt} \tag{2.10}$$

(2.7) and (2.8) differ from (2.6) and are no longer directly proportional to the first and second derivatives of the spot profile, respectively. Nevertheless, as we shall see in the following sections, the signal profiles bear a resemblance to the profiles predicted in the small-angle approximation, with anti-symmetric extrema at a wavelength-dependent distance from the object at $1f$ and a central extremum at the object's position at $2f$. The dependence of the extremum's position on the wavelength at $1f$ is inconvenient when trying to maximize the signal, but the signal at $1f$ is about twice as strong as at $2f$[20]. Although weaker, the advantage of the extremum of the signal at $2f$ is that it remains at a the location of the object. The second advantage of measurements at $2f$ is that they are insensitive to smooth variations in the background signal on the order of the oscillation amplitude. The choice to work at $1f$ or $2f$ thus depends on the signal strength of the studied object and the homogeneity of the sample, but both are possible[20].

The two principle modes of operation of a SMS setup are sample mapping and spectra acquisition. The former involves the measurement of X/DC at different points in a regular two-dimensional array in the sample plane at a given wavelength. The latter involves the measurement of X/DC at different wavelengths at a fixed position.

2.1.2 Sample Mapping

Before the spectra of individual objects can be acquired, the objects must first be located. This is achieved by scanning the sample stage over regular steps along both axes while simultaneously oscillating along one of them and measuring the signal at a target wavelength at each point. Only those objects that generate a detectable signal at this wavelength will appear on the map. The wavelength must therefore be chosen as a function of the objects' optical response. If this cannot be estimated a priori, the sample must be scanned at multiple wavelengths until the objects are detected.

An example map is shown in figure 2.4 for a sample of 100 nm gold spheres deposited on a glass substrate. The sample has been mapped at 560 nm, which is approximately the wavelength at which the object's response was expected to be the strongest, with a horizontal oscillation of $\delta_x = 400\,\text{nm}$ at $f = 186\,\text{Hz}$ along the x axis and a step size of 200 nm along the x and y axes.

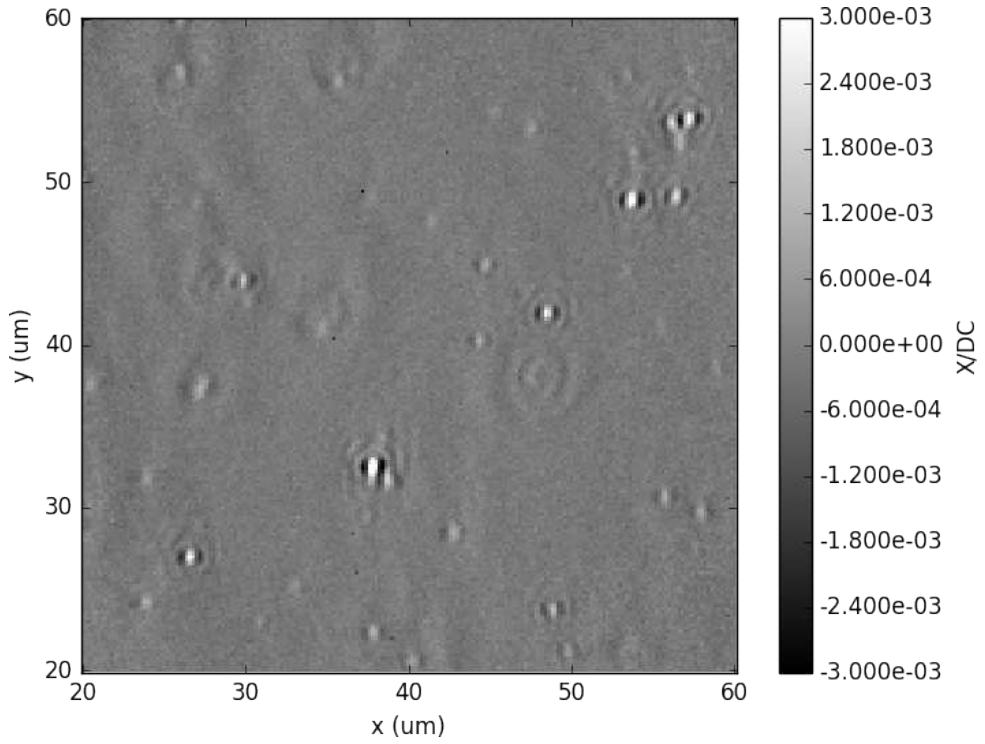

Figure 2.4: Example of a sample mapped with SMS at $2f$ in air. The sample consists of 100 nm gold spheres deposited on a glass slide. Numerous objects are visible as light spots flanked by dark ones. $f = 186\,\text{Hz}$, $\delta_x = 400\,\text{nm}$, $\lambda = 560\,\text{nm}$, step size: 200 nm.

A number of objects appear as a positive bright lobe flanked by two smaller negative dark lobes. The size of the focused spot is limited by diffraction so the objects are smaller than the spot size. Their image on a SMS map is therefore a function of the spot profile and

oscillation amplitude and provides no information about the object's morphology directly. The image of an object at $1f$ or $2f$ (figure 2.5) depends on the first or second derivative of the spot profile (figure 2.2), respectively, when the amplitude is comparable to the spot size. Each line through an object on the map along the direction of oscillation provides a profile of the signal.

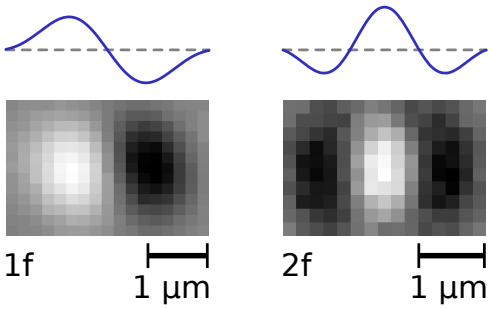

Figure 2.5: In a SMS map, each scanline through an object along the axis of oscillation is a profile that depends on the nth derivative of the spot, where n is the harmonic. Images of objects at $1f$ therefore appear as 2 lobes of opposite sign on either side of the object while images at $2f$ appear as a strong lobe centered on the object flanked by two weaker lobes of opposite sign on either side.

As mentioned in the previous section, the phase setting of the lock-in amplifier is set to maximize the in-phase component of the signal. Although the value of the second derivative of the spot profile is negative at its center (figure 2.2), maximizing the signal at $2f$ at the center of the object will result in a positive signal at the center. The phase could be adjusted by π to negate the sign but it is only the absolute value of the signal that is important and so the phase setting that yields a positive central signal is typically used.

The real morphology of an object on a SMS map can be determined with electron microscopy. Although the image of each object in a SMS map is unrelated to its shape, the constellation of objects, i.e. their arrangement and relative distances to each other, does provide spatial information that can be correlated with electron microscopy images to match the optically characterized objects with their real morphology. The sample substrate will determine which type of electron microscopy can be used to image the sample. Objects on thin substrates such as microscope grids with polyvinyl formal (formvar) resin films can be imaged with transmission electron microscopy (TEM) with high resolution[23] while thicker substrates such as glass slides limit imaging to scanning electron microscopy (SEM) and atomic force microscope (AFM) with lower resolution compared to TEM[24]. If the substrate is non-conductive then SEM will also suffer from charge build-up which will distort the images.

Figure 2.6 shows a side-by-side comparison of the SMS-mapped region of figure 2.4 and the same zone of the sample imaged with SEM. Several objects which appear in both

images have been highlighted with circles. Of note is that there are darker areas on the sample in the SEM image that do not appear in the SMS map. SMS is only able to image objects that generate a signal at the target wavelength as they are oscillated under the spot. If the extinction does not change along the axis of oscillation then no SMS signal will be generated. This will mask the response of some large objects with a uniform response over the illuminated area. The edges of such areas where the signal changes will appear in maps at $1f$. If the change is slow and smooth then it may remain invisible at $2f$ because the signal at this harmonic is related to the second derivative of the spot profile. Because of this, we often choose to measure at $2f$ in this work. Of course, objects which do not respond at the mapping wavelength will not appear in the map. We also note that there are several objects that appear in the SMS map that are not visible at the magnification of the SEM image.

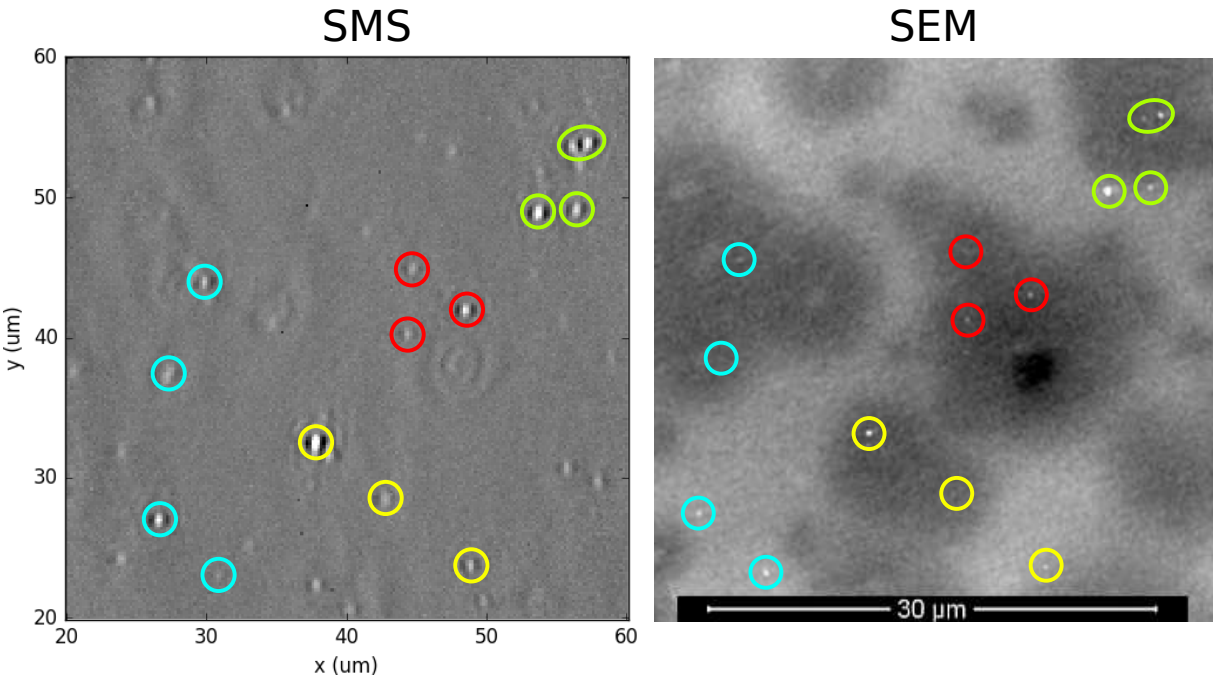

Figure 2.6: Correlation of the SMS map in figure 2.4 with a SEM image of the same region. Several objects that appear in both figures have been highlighted with circles.

The usual procedure for characterizing a new sample is to first visualize it at low resolution using electron microscopy to locate regions of interest with the object that one wishes to study. This is done at low magnification to avoid degradation of the sample with the electron beam prior to the optical study. To be suitable for SMS studies, the sample must not be too dense, i.e. objects must be far enough apart that the spot can oscillate over one without simultaneously oscillating over others, otherwise the signals will be mixed and reduced. For a typical spot size of about 1 µm and a typical oscillation amplitude of

350 nm to 500 nm, the objects should be at least a couple of microns apart[5].

Once a region of interest has been located, it can be mapped with SMS to (re)locate objects for optical study. The SEM pre-imaging of the sample is not necessary as objects may readily be found with SMS alone, but mapping a region with SMS is slower than imaging the same region with electron microscopy, in part due to the time taken to map a given area and in part due to the area that can be mapped by the stage without manual intervention to move the sample. The area of a map is typically limited to about 75 µm × 75 µm and typically takes a few hours depending on the step size and the integration time constant τ. Furthermore, as discussed above, the map itself provides no direct information about the object's morphology. Spectra, described next, are needed in this case to confirm the identity of the discovered objects. After the sample has been studied with SMS, high-resolution electron microscopy is required to determine the fine morphology of the investigated objects.

2.1.3 Spectra

Once an object has been located, the wavelength-dependent response can be measured over a broad-range spectrum by scanning the spectrometer, typically from 400 nm to 1000 nm, depending on the limits of the spectrophotometer and photodetector. The stage is positioned to place the object at the desired location under the spot, either at the center when measuring at $2f$ or at an offset along the axis of oscillation when measuring at $1f$.

The X/DC signal of a 100 nm nanoparticle (NP) is on the order of 10^{-3}. The noise of the signal depends on the lock-in amplifier's integration time constant τ. For a setting of 1 s the noise is $\geq 5 \cdot 10^{-4}$. The noise can be reduced by increasing τ at the cost of longer acquisition times. τ is typically set to 300 ms or 1 s. With a typical wavelength step size of 3 nm, a full spectrum can be measured in just a few minutes.

The setup measures X/DC, which is proportional to σ_{ext} as per (2.7) and (2.8). To determine the value of σ_{ext} across the spectrum, the calibration curve for the selected harmonic is required, which can be calculated with (2.9) at $1f$ or (2.10) at $2f$. For these calculations, the spot must be fully characterized over the full spectrum. This may be done using small latex NPs or other objects with a broad-spectrum optical response. The signal profile of an object is measured along the direction of oscillation at different wavelengths. This signal profile can be used to determine the shape of the spot profile. When possible, the spot profile should also be calculated theoretically. Ideally this should use an exact model of the optical configuration of the setup. This is not possible with some commercially available objectives that do not provide specifications of the objective's optical system. Even when the specifications are provided, there may be a difference

[5]When speaking of density, coupled systems such as dimers and other nano-antennas are considered as a single object.

between the theoretical and experimental spot profiles. In the absence of specifications, a simplified model using perfect lenses may provide a sufficient approximation.

Given the dependence of the anti-symmetric extrema of the signal at $1f$ on the wavelength (figures 2.2 and 2.5), the position that maximizes the signal also depends on the wavelength. This is taken into account in the calibration curve for $1f$ to enable an accurate spectrum to be calculated when oscillating about a fixed position. The relative position to the object must therefore be noted along with the X/DC spectrum to be able to correctly calibrate the σ_{ext} spectrum.

The signal profile at $2f$ is symmetric about the center with the maximum absolute amplitude remaining at the center for all wavelengths, which simplifies optimization of the signal and avoids the need to note the relative position of the acquisition. Because of this and the previously discussed masking of smooth irregularities, we often prefer to work at $2f$ even though the signal is weaker at this harmonic.

Figure 2.7 shows raw X/DC extinction spectra of gold NPs on Formvar resin measured at $1f$ and $2f$. Because the raw X/DC spectra depend on σ_{ext} at $1f$ and $2f$ (equations 2.7 and 2.8), they provide immediate information about the spectral dependence and relative intensity of an object's optical response. The interband transition regions are visible on the blue end of the spectrum and the LSPR peak appears around 530 nm. The raw spectrum at $2f$ is nevertheless weaker, as mentioned previously.

The figure also shows the calibration curves for $1f$ and $2f$ on the same setup. The calibration curves account for the change in intensity of the spot profile as a function of wavelength. The curve for $2f$ is stronger to compensate for the weaker signal at $1f$. Multiplication of the raw spectra with the calibration curves yields the calibrated absolute extinction spectra shown at the bottom of the figure. Despite the differences in the raw spectra, the calibrated spectra are the same and show that either harmonic can be used to accurately measure the response of a NP.

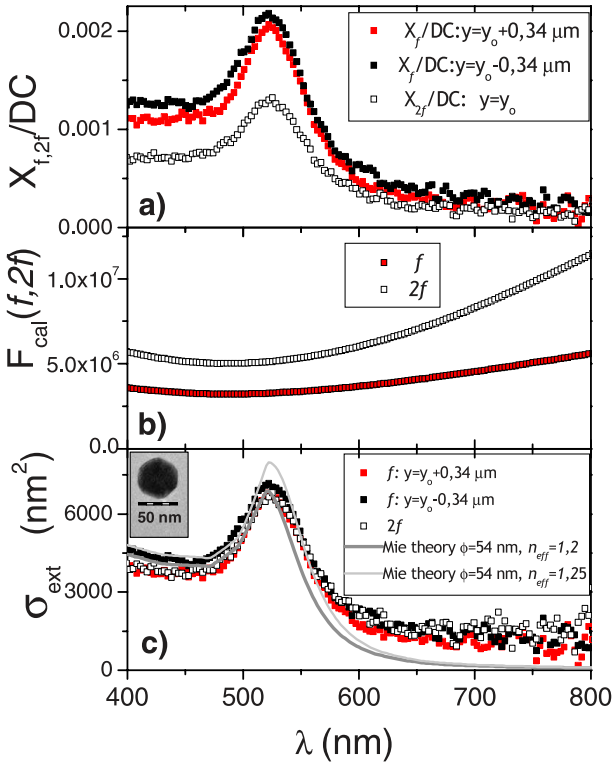

Figure 2.7: Example of raw and calibrated SMS spectra of gold NPs on Formvar resin. (a) Raw X/DC extinction spectra at $1f$ and $2f$. (b) Calibration curves for $1f$ and $2f$. (c) Calibrated extinction spectra at $1f$ and $2f$ and Mie-theory extinction spectra. Source: Billaud et al. [20]

Once the optical response of an object has been measured, it can be correlated with electron microscopy and compared to theoretical calculations. For example, figure 2.8 shows calibrated spectra that were measured on the same object. The two spectra correspond to orthogonal orientations of a polarizer used during the measurement. The position of the object and the direction of the polarization were noted. A TEM image of the same object is presented in the inlay of the figure. The noted polarization directions have been superimposed on the image. Through this correlation the dimensions of the object have been determined and the two spectra have been shown to correspond to the optical response along the long and the short axes of the object.

Using the determined dimensions of the object, theoretical spectra have been calculated for the optical response of the object along each axis in a homogeneous environment of real RI n. These correspond to the measured spectra and show that the polarizer can be used to independently measure the optical response along different axes of an anisotropic object.

The light source is the principle limitation on the sensitivity of a SMS setup[20]. The

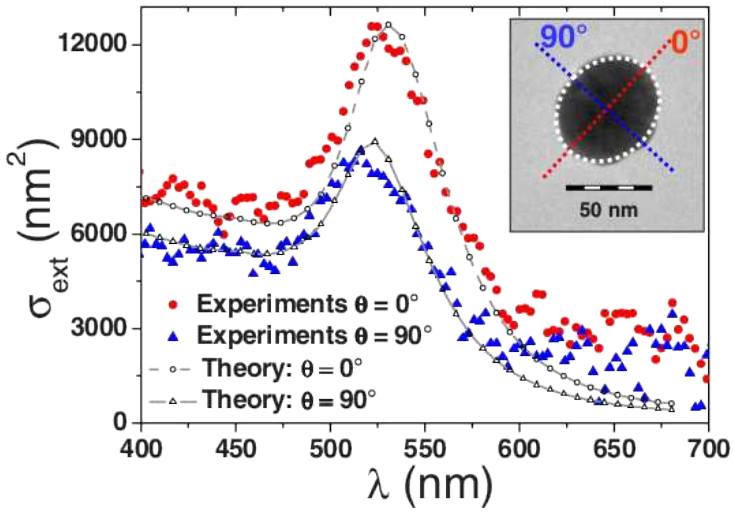

Figure 2.8: Example of spectra of an approximately 50 nm ellipsoid gold NP measured with SMS. The response along perpendicular axes has been measured with a polarizer. A TEM image of the same object is presented in the inlay where the polarization directions have been indicated. The theoretical spectra have been calculated with DDA and plotted alongside the empirical data. Source: Billaud et al. [20]

setup used in this work (described later section 2.2.4) uses a xenon lamp, which is less limited by the shot noise of the quartz-tungsten-halogen lamp used by Billaud et al. [20]. The response of single NPs down to a few 10s of nm can be measured with these white light sources. Even smaller objects down to 5 nm can be measured using a laser light source[25], but this requires much longer measurement times as the laser must be regularly adjusted to scan the spectrum.

2.2 Adaptation To A Liquid Environment

In order to use SMS for biosensing applications, a setup must be able to make measurements in the liquid environment in which biological interactions occur. A large part of this work was therefore to develop such a setup and test it. This required the development of a custom fluid cell prototype and several changes to accommodate it on the existing setup, which will now be described before presenting the final setup used in this work.

2.2.1 Sample Holder

The first challenge of the adaptation to liquid measurements was the method of sample immersion. Numerous methods were considered to meet the following constraints:

- Accommodate samples prepared on glass substrates.
- Inexpensive.
- Easy to assemble.
- Ability to pump liquid through system.
- Easy to disassemble for electron microscopy imaging.

The accommodation of samples on glass substrates ensures that both deposited and lithographed samples can be studied with the setup. Initially, microfluidic systems based on stamped poly(methyl methacrylate) (PMMA) and similar polymers were considered but were soon rejected because they would not be easy to disassemble for imaging even through the microfluidic aspects of such a system would be interesting.

The first sample-holder prototype (figure 2.9, fabricated by Alain Bourgey, a technician at Institute of Light and Matter (ILM)) consisted of a cylindrical, custom-designed teflon block in a metal casing with two glass windows. Teflon was chosen for its chemical inertness, which is important for biosensing applications. Small channels were bored into the block for liquid flow and the sample was held in place by friction with a teflon ring through external pressure from the glass windows. The inner chamber was sealed with rubber toric joints that were also held in place by friction. The entire chamber was sealed by tightening bolts along the perimeter of the outer metal casing and liquid was injected and removed via syringes inserted into the bored channels. This system proved impractical as the pressure required to hold the sample firmly in place and prevent leaking applied too much force to the glass windows which were then prone to shattering. The cell was also bulky and heavy with poor liquid flow near the sample that often trapped bubbles in the optical path and prevented sample immersion and imaging.

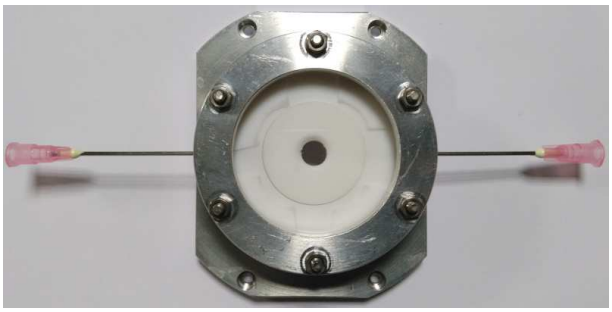

Figure 2.9: Photo of the first custom-made sample holder prototype. See text for details.

The design of the first prototype could be improved, but we have chosen a second, lighter prototype (figure 2.10 that consists of a custom-fabricated metal dipper, also fabricated by Alain Bourgey. The sample is placed on one end of the dipper and fastened with a

metal cover plate and 4 stainless steel screws. A circular hole in the dipper aligns with a hole in the cover plate to provide an optical window. The other end of the dipper is attached to a metal cap with 2 screws. The dipper is then lowered into a quartz cell[6] up to the cap which lies across the top of the cell. A second cap is placed under the cell and the two caps are held against the cell by long bolts. Both caps have lips that hold the cell in place. The second cap is attached to a mounting plate with two bolts and the mounting plate is attached to the sample stage on the SMS setup where the cell is held in the upright position. The upper cap has two small holes through which needles can be inserted to introduce and extract liquid. The dipper, cover plate and caps are made of duralumin. The screws, bolts and nuts are made of stainless steel.

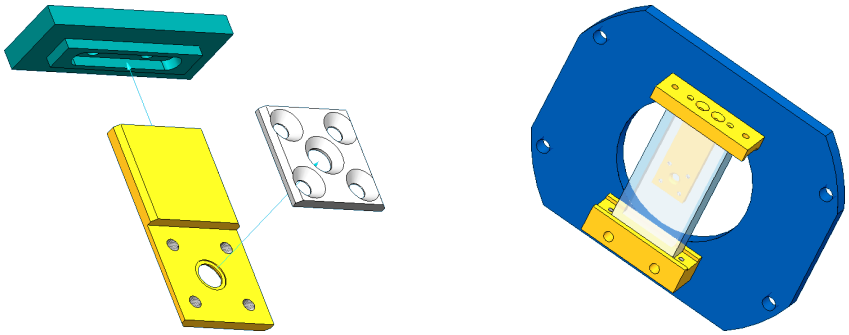

(a) Exploded view of dipper. **(b)** Assembled sample holder.

Figure 2.10: Schematic diagram of the second version of the liquid spatial modulation spectroscopy (LSMS) sample holder. The sample is mounted on the dipper (a) with a small cover-plate fastened with 4 screws. The dipper itself is attached to a metal cap which sits on top of a quartz cell (b). The cap has two holes through which needles may be inserted to inject and remove liquid.

As we shall show at the end of this chapter and in those that follow, this prototype has allowed us to successfully study samples in various fluid environments and the results have been in good agreement with theory. Nevertheless, it has presented some issues under certain conditions. For example, dark patches have been observed on the duralumin dipper (figure 2.11a) when working with samples on which a microscope grid has been attached with silver lacquer. These may be due to corrosion or due to a precipitate formed from the silver lacquer or a derivative thereof. Their appearance is not systematic. An unidentified white precipitate is also sometimes observed on the dipper (figure 2.11b) and on the quartz cell near the dipper (2.11c). This precipitate occurs in the absence of the silver lacquer and microscope grid and its origin is unclear. It has appeared when using distilled water from 3 independent sources so it is unlikely to be a contaminant in the solution. The quantity that appears over time exceeds that of any surfactant or other substance that may remain on the sample. It may be due to a redox reaction between the different metals present in the liquid (duralumin, stainless steel nickel) but no reaction has yet been determined.

[6] 6.5 mm × 20 mm × 60 mm, 1.60 ml, 2.5 mm path length, purchased from Starna: model 97.60 G 2.5

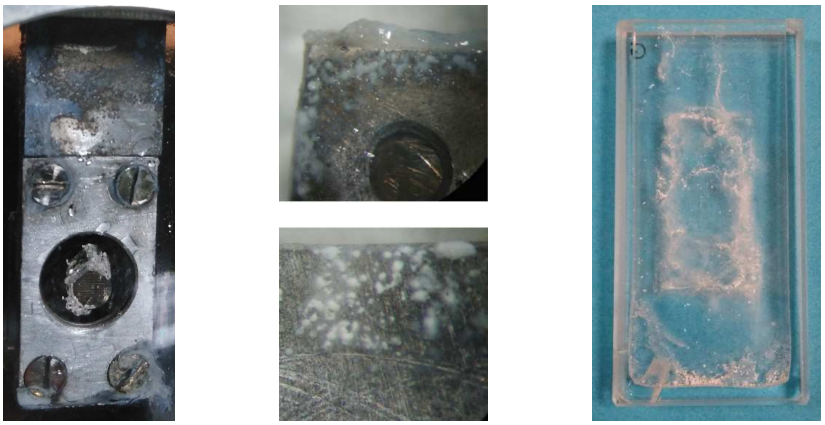

(a) dipper **(b)** dipper **(c)** quartz cell

Figure 2.11: Examples of different precipitates on the sample holder. (a) Visible corrosion and unidentified precipitate in the presence of a sample with a microscope grid and silver lacquer. (b) Salt-like precipitate on sample holder. (c) Precipitate on quartz cell concentrated around the edges of the dipper.

These precipitates highlight the importance of an inert environment and it was in anticipation of such effects that the first prototype was fabricated with teflon. While the following work has not been impeded by issues with the cell, it is clear that a new design based on inert and biocompatible materials will likely be necessary for future biosensing applications.

2.2.2 Objectives

The introduction of the fluid cell imposes an important minimum working distance on the objects that may be used with the setup and introduces two dielectric interfaces in the path between the objective and the sample. In the case of the quartz cell, the beam must be focused through 2 mm of quartz and 1 mm of water. SMS requires a tightly focused spot to ensure that a nano-object will be sufficiently illuminated to generate a detectable signal and that the spot will be small enough for practical oscillation amplitudes. A "G" Plan Apochromatic (GAPO) 50x objective from Mitutoyo[7] with a NA of 0.5, a focal distance of 4 mm and a working distance of 13.89 mm that is designed to compensate a glass thickness of 3.5 mm was therefore purchased to focus the beam on the sample. An "M" Plan Apochromatic (MAPO) 50X objective with a NA of 0.55, a focal distance of 4 mm and a working distance of 13 mm was also purchased from Mitutoyo[8] to collect the light from the sample. The MAPO objective is not corrected for the layers of quartz and water but this is not necessary for SMS because the beam is not imaged after the sample.

[7] model 378-848-3
[8] model 378-805-3

Only the total power is measured.

In addition to the GAPO and MAPO objectives, Cassegrain-reflector objectives (hereafter referred to simply as "reflective objectives") with a focal distance of 3.55 mm and a NA of 0.5 were also available. These have an outer cone angle of 40.5° and an inner cone angle of 15° and can be used for measurements in air in the absence of the fluid cell. Because of their broadband reflective properties, these objectives are largely achromatic[22].

2.2.3 Oscillating Mirror

The weight of the filled fluid cell and connected syringes and tubing adds strain to the translatable stage which is normally used to oscillate the sample. While testing the first fluid cell prototype, which was relatively large and heavy, it was therefore necessary to add an oscillating mirror to the setup. An oscillating mirror was purchased from THORLABS[9] along with a "Scanning Galvo System" power supply unit.

SMS requires a relative oscillation between the spot and the studied object. The oscillating mirror is used to introduce a periodic variation of the angle of the beam before it is focused on the sample. The spatial amplitude of oscillation δ on the sample will therefore be

$$\delta = F \tan(\theta_{\max}) \tag{2.11}$$

where F is the focal length and $\theta_{\max}$ is the angular oscillation amplitude. For a focal length of 4 mm and a target spatial oscillation amplitude of 400 nm, the small-angle approximation of $\tan(\theta) \approx \theta$ may be used. From this we see that the spatial oscillation is directly proportional to the angular oscillation and that the necessary angular oscillation amplitude is only 100 µrad. Nevertheless, this angular oscillation occurs along the entire optical path after the mirror and can sometimes unintentionally modulate the DC signal at the oscillation frequency f. In particular, the beam enters the spectrometer through a vertical slit and is focused on a vertically aligned diffraction grating. To minimize the effects of the oscillation, the mirror was mounted in such a way as to oscillate the beam vertically and thus along the direction of the slit and the diffraction grating. We also note that the angular oscillation is on the order of 100 µrad and is therefore not expected to deform the spot profile. We shall return to the effects of beam oscillation on SMS measurements later.

A full study was undertaken to characterize the mirror and develop a robust LabView Virtual Instrument (VI) to control it before mounting it on the setup (some of this work is described in appendix B). Briefly, this controller includes a feedback loop with the

[9] model GVS011 TSH 38077-X

mirror controller's reported position to ensure that the target oscillation is achieved at the desired frequency and amplitude without an angular offset. This ensures the desired spatial modulation on the sample and the alignment of the beam along the optical path.

2.2.4 Final Setup Overview

Now that we have seen the required modifications to develop a SMS setup for measurements in a liquid environment, we will present the setup used in this work in detail. A schematic overview of the final LSMS setup is presented in figure 2.12. The adaptions have been marked with dashed red lines.

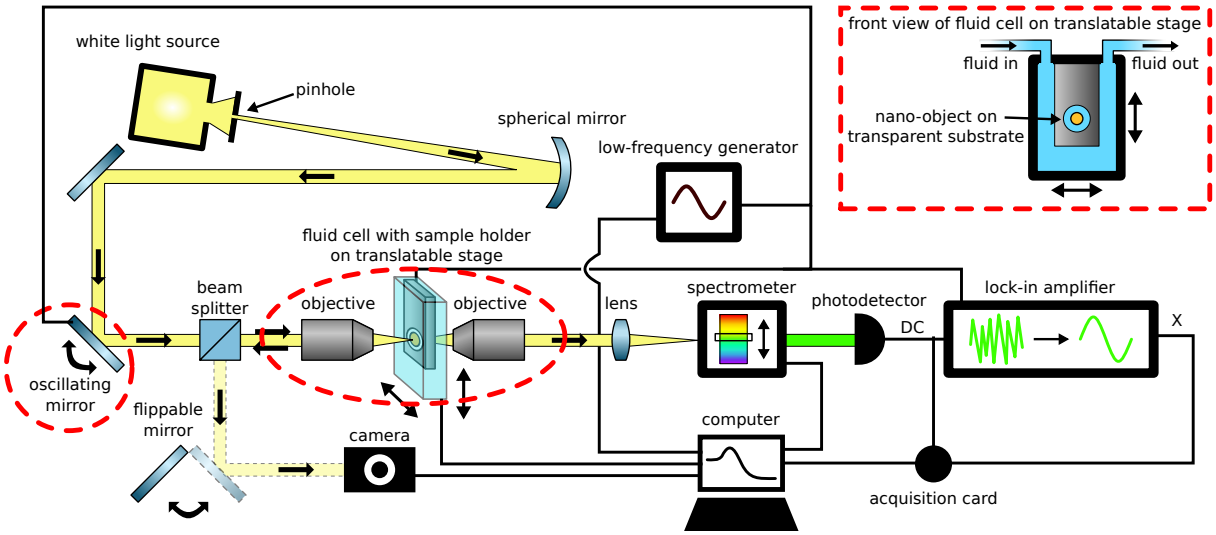

Figure 2.12: Schematic overview of the SMS setup adapted to a liquid environment. The beam of collimated white light is reflected by an optionally oscillating mirror through a beam splitter. The light is then focused on the sample in the fluid cell by the GAPO objective and collected with the MAPO objective. A schematic overview of the fluid cell with a sample is shown in the inlay in the upper right corner. The components are described in the text.

The oscillating mirror and fluid cell are as described in the preceding sections. The collimated white light source consists of a 75 W HAMAMATSU xenon lamp. The light emitted from the lamp passes through a pinhole and is then collimated with a spherical mirror. The angle of incidence of the beam on the spherical mirror is minimized to render spherical aberrations negligible.

The computer-controlled piezo-electric translatable sample stage[10] and its controller[11]

[10] model 501929
[11] Nano-Drive 85

were produced by Mad City Labs (MCL) Inc. The stage can be translated over a range of 75 µm along each axis with a spatial resolution of 1 nm. The maximum oscillation frequency supported by the stage is 200 Hz. The piezo-electric stage is itself mounted on a mechanical Newport XY translation stage which is used to position the zone of interest prior to sample mapping.

A beam splitter is inserted in the optical path before the focusing objective. Light reflected from the sample is imaged with a charge-coupled device (CCD) camera connected to the computer. The camera image is used to focus the spot on the sample and adjust the position of the sample using the mechanical and piezo-electric stages.

A HORIBA JOBIN YVON microHR spectrometer is used to select the target wavelength which is then measured by a photodiode with a response range of 400 nm to 1100 nm. A model SR830 DSP Lock-In amplifier from Stanford Research Systems (SRS) is used to demodulate the signal. The entire setup is arranged on a Newport RS 2000^{TM} "Sealed Hole Table Top with Tuned Damping" to isolate the table from ambient vibrations.

The computer interfaces with instruments and measures signals via a National Instruments BNC-2120 acquisition card and National Instruments GPIB-USB-HS controller. To control the setup and its various components, I have developed a full object-oriented application named Multi-Instrument Controller and Automator (MICA) in LabVIEW with extensive automation and visualization capabilities. This software is able, for example, to automatically map a sample at multiple wavelengths, detect objects on the map, locally remap them and then acquire their spectra. It includes functionality for real-time visualization of interactive measurements and produces output in a standardized format for further post-processing. MICA is described further in appendix C on page 223.

2.3 Tests and Calibration

The introduction of new components and software required multiple tests to confirm the accuracy of the results obtained with the setup. Some of these results will be presented in this section. Several others have been omitted, such as those with the first sample holder prototype that was later abandoned as well as several samples which were shown to be too dense or which displayed unsuitable optical properties after preparation. The results presented here were obtained with two samples that were expected to exhibit well-known optical properties.

2.3.1 Samples

The first sample was prepared with gold spheres of radius 50 nm (synthesized by Hélène Gehan of the SOPRANO group at ILM). The TEM image shown in figure 2.13 was taken after synthesis and shows that the spheres are relatively round and monodisperse albeit not perfectly. The solution was immersed in an ultrasound bath just before deposition to ensure object separation. A small drop of solution was then used to cover a glass slide and the drop was allowed to stand for several minutes before being removed with absorbing paper placed against the edge of the slide. Once the sample had completely dried, an electronic microscope grid was attached to the surface with silver lacquer to identify different areas of the sample for repeated studies.

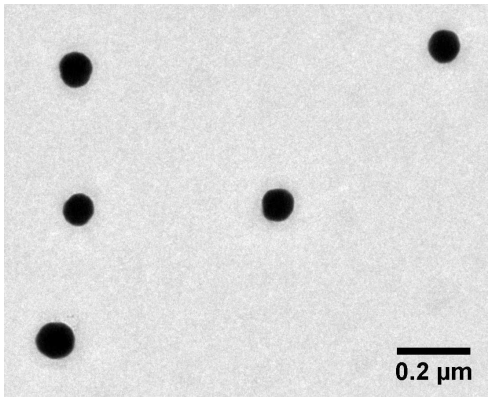

Figure 2.13: TEM images of 100 nm Au spheres synthesized by Hélène Gehan.

This sample proved useful for mapping tests but the spectra of the deposited objects did not correspond to the expected spectra of unique gold nanospheres of the given radius. It was concluded that the sample consisted of unstable aggregates of gold spheres. While the positions of these aggregates remained stable, the spectra did not and no interpretations were possible based on the latter.

Given these difficulties, a regular lithographed sample of gold disks that had previously been used in other work was obtained. The sample was fabricated by Cécile Jamois of Institut des Nanotechnologies de Lyon (INL) and consists of zones of disks. Each disk consists of a gold layer of height 50 nm on top of a chromium adhesion layer of height 5 nm that attaches the gold to the glass substrate. The disks in each zone are arranged in a regular rectangular array with a spatial interval of 5 µm (figure 2.14a) and each zone contains disks of the same radius.

At the time of the study, the sample exhibited various imperfections. SEM images revealed that some objects may have been partially lost from the sample, such as seen in the lower right of figure 2.14b where a weaker spot is visible at the expected position of a disk. The right inlay shows a zoomed image of the partially lost object. The left inlay shows

a zoomed image of a normal object.. Other disks display imperfections such as dents (zoomed inlay in figure 2.14c) or apparent deviations from radial symmetry (left inlay in figure 2.14b), but the exact morphology remains elusive due to charging effects.

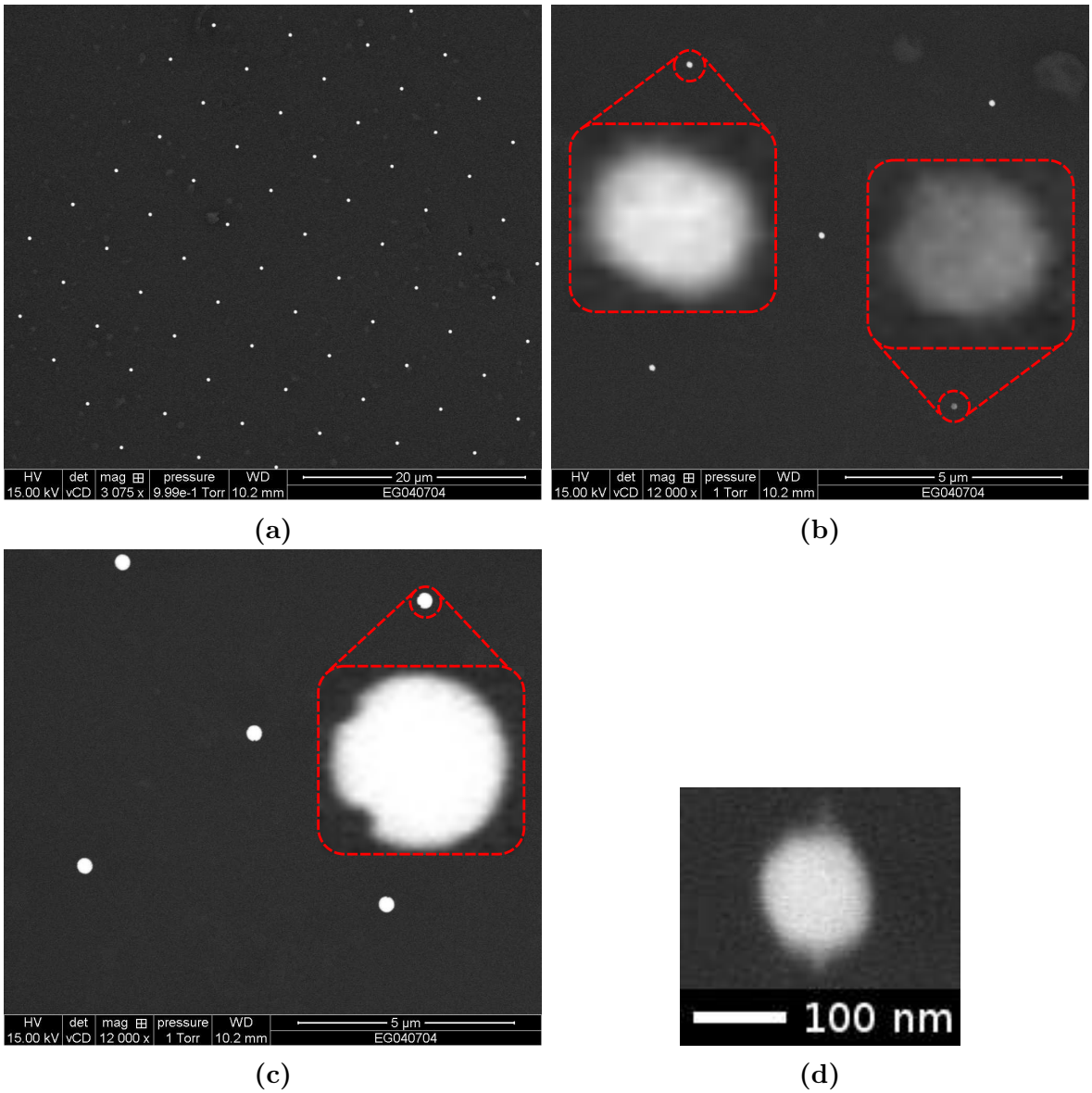

Figure 2.14: Low-vacuum SEM images of the lithographed sample. The sample consists of multiple zones of regularly arranged disks. Each disk consists of a gold layer of height 50 nm on top of a chromium adhesion layer of height 5 nm that attaches the gold to the glass substrate. Different zones have different radii. (a) 2D pattern of disks. (b) Example of partially lost disk. (c) Example of imperfections. (d) Object from the studied zone.

A zone of objects that were designed to be 100 nm in diameter were chosen for study due to their relative homogeneity and cleanliness of the zone. One of these disks is shown in

figure 2.14d. The objects are designed to have a diameter of 100 nm but they appear to be larger in SEM images. The interpretation of the size in the SEM image is difficult due to charging effects and the size is estimated to lie between 100 nm and 125 nm.

2.3.2 Tests

A series of tests that have been performed on these samples will be presented in the remaining sections of this chapter.

2.3.2.1 Comparison Of Mirror And Stage Oscillations

After introducing the oscillating mirror, multiple tests were performed in air to compare the results of maps and spectra obtained with either an oscillating stage or an oscillating mirror under different conditions. Both oscillation methods produced similar results when mapping samples and may therefore be considered equivalent.

Spectra obtained with the oscillating mirror occasionally exhibit spurious background signals due to alignment issues with the oscillating beam. Figure 2.15 shows spectra measured at empty positions on the lithographed sample using either mirror or stage oscillations. The mirror oscillations produce a wavelength-dependent signal. This is a common problem when oscillating the beam instead of the sample[17, 26].

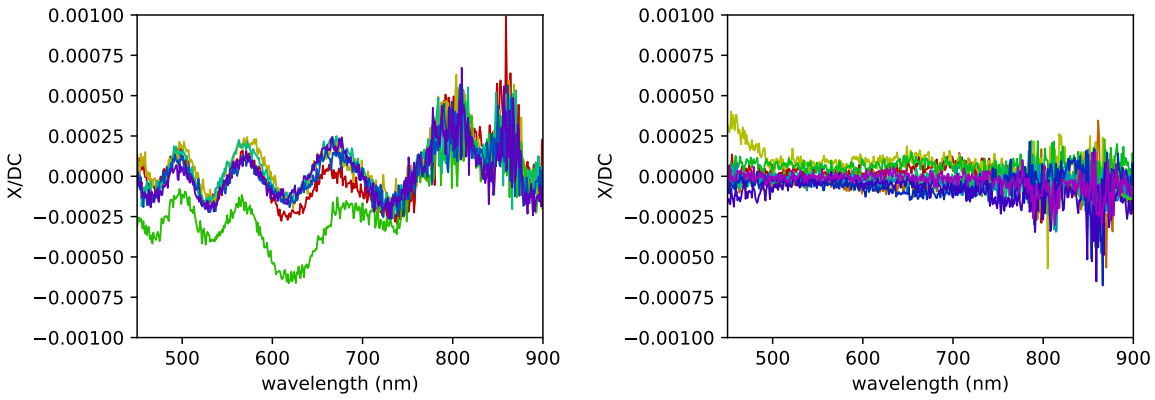

(a) mirror oscillations **(b)** stage oscillations

Figure 2.15: Spectra showing wavelength-dependent background signal when using the oscillating mirror. Lithographed sample.

This background signal can be cancelled by subtracting its average over several empty points near the studied objects from the spectra of those objects. Functionality was

therefore added to the control software MICA (described in appendix C on page 223) to automatically determine empty areas of the sample and collect background spectra that can be averaged and subtracted via scripts in post-processing. The adjusted spectra were comparable to spectra obtained with the oscillating stage (figure 2.16).

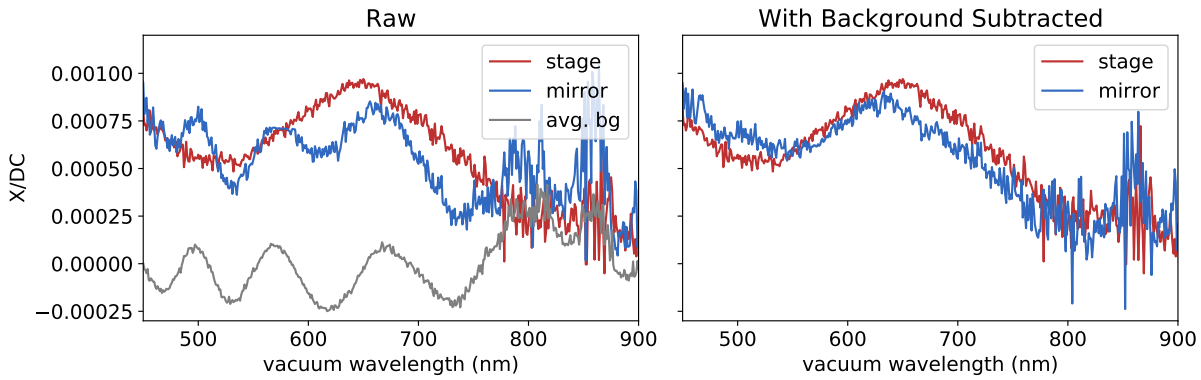

Figure 2.16: (Left) Raw spectra measured on the same object with stage and mirror oscillations. The average background signal from the mirror (figure 2.15) is shown (the average stage background is zero). (Right) The average mirror background signal has been subtracted from the spectrum measured with the mirror.

Other tests were performed to determine if the setup is able to support stage oscillations when the filled fluid cell is mounted on the stage. Due to the weight of the filled cell, it was necessary to limit the oscillation frequency f to 186 Hz to obtain linear sinusoidal oscillations with amplitudes around 400 nm. Nevertheless, tests with these settings yielded comparable results to stage oscillations without the fluid cell. Stage oscillations were therefore preferred throughout most of this work to avoid concerns with the spurious background signal, even if this can be accounted for in post-processing.

2.3.2.2 Comparison Of The Reflective And GAPO Objectives

Tests were also performed to compare measurements with the new GAPO objective to those of the well-characterized reflective objective. The GAPO is designed to compensate a glass thickness of 3.5 mm (section 2.2.2). Several initial tests were undertaken to determine if it could nevertheless be used with the empty fluid cell, in which case the beam is focused through 2 mm of glass and ∼1 mm of air. Maps of the same zone of the gold sphere sample acquired with each objective are shown in figure 2.17. The same constellations of objects have been highlighted in each figure for comparison. The upper right corner shows the beveled corner of the attached microscope grid.The apparent saturation of the left figure is due to the use of the same scale for both figures.

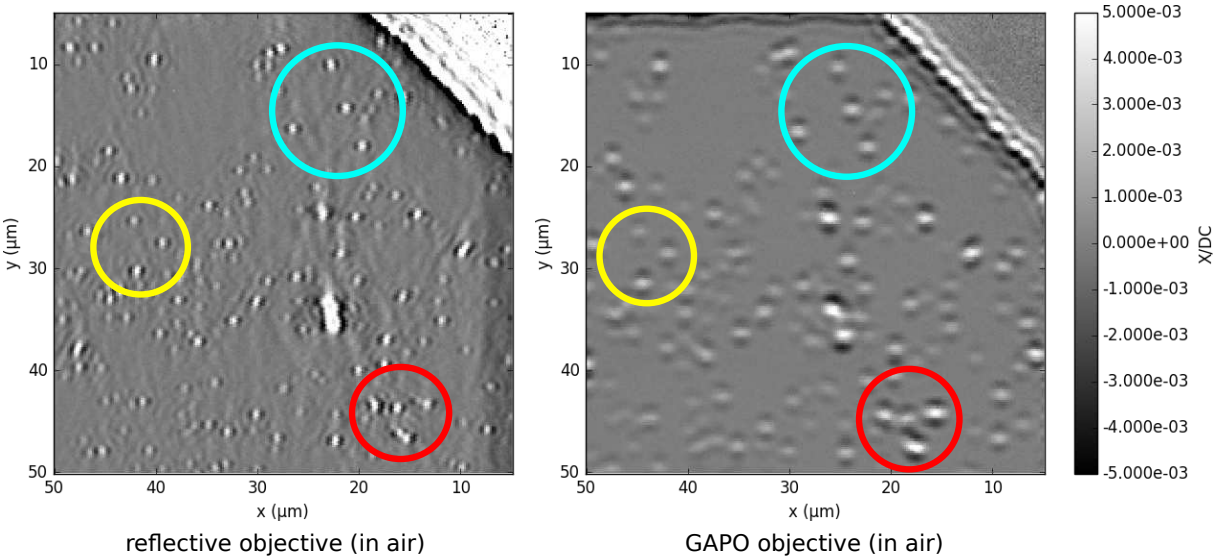

Figure 2.17: Maps in air of the same zone of the 100 nm Au nanosphere sample with either the reflective objective (left) or the GAPO objective (right). The beveled corner of the microscope grid is visible in the upper right corner. The sample was mapped at 560 nm. The same scale is used in both images for comparison. Some constellations of objects which appear in both images have been highlighted with circles. The orientation of lobes in each image is due to the direction of oscillation: horizontal on the left, vertical on the right.

The map with the GAPO objective is poorly focused with a large spot size that results in lower mapping resolution and a loss of signal and contrast. This is confirmed by a graph of the X/DC profile for a single object along the direction of oscillation in figure 2.18. The profile is wider and weaker with the GAPO objective. The GAPO objective is indeed not designed for these conditions. Despite the unfavorable conditions, the objects nevertheless remain identifiable in the image.

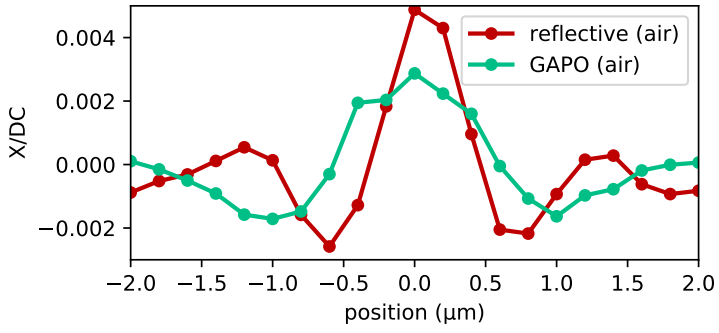

Figure 2.18: Profiles of the same object along the axis of oscillation extracted from the maps in figure 2.17. The object is labeled "27" in the reflective-objective map and "12" in the GAPO-objective map (figure 2.19).

One of the design goals of the MICA software was the automatic tracking of objects on a sample following a map. This was also tested using various samples and configurations. In figure 2.19, the objects detected by MICA in each map in figure 2.17, respectively, have been highlighted with numbered circles. Each of these objects was locally remapped to set the optimal position before automatically measuring the object's spectrum. The software is able to accurately track objects under different conditions, including when the spot is incorrectly focused on the sample.

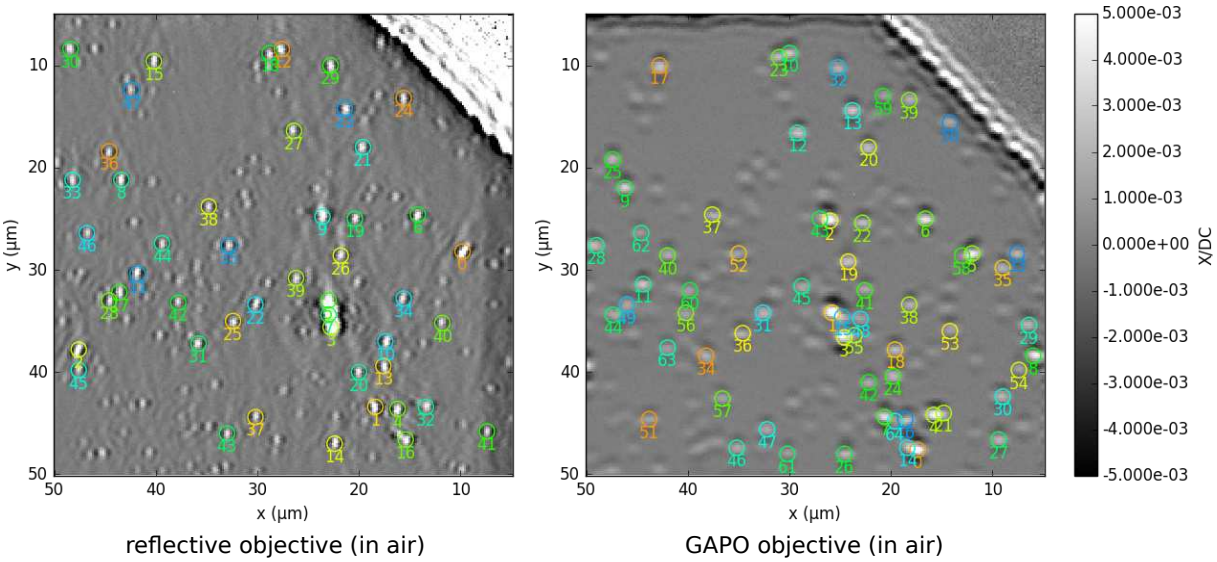

Figure 2.19: Maps from figure 2.17. The objects automatically tracked by the interface software MICA are shown with numbered circles.

2.3.2.3 Comparison Of Maps In Air And Water

A different area of the sample of gold spheres was mapped in air and in water with the GAPO objective to determine if the setup is able to correctly map samples in water. The results are shown in figure 2.20. A subset of the same objects that were autotracked in both cases have been numbered identically in each map. The comparable lack of contrast and poor resolution indicates that the spot was improperly focused under both conditions and that this is likely due to human error and not an intrinsic limitation of the objective. The results were nevertheless promising as the setup was able to detect the same objects in both air and water with recognizable constellations and comparable signals. However, not all objects in the first map appear in the second map, such as those to the lower left of object 4 near the center of the map. This indicates that the sample is not stable under immersion and that these objects were likely washed away. The disappearance is not due to a shift of the LSPR as the spectra of these objects are very broad and larger than any expected shift due to immersion in water (figure 2.21). We also note that the spectrum

does not decrease towards the red as expected for a single gold nanosphere of diameter 100 nm.

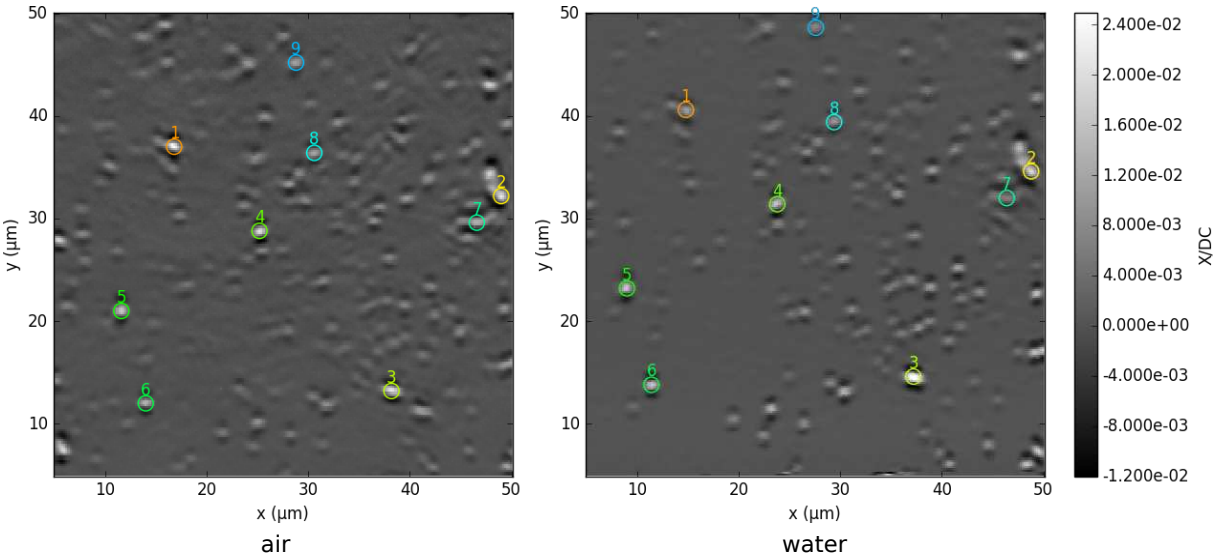

Figure 2.20: Maps of a region of a glass slide with deposited Au nanospheres of radius 50 nm in air and water. Among the objects that appear in both maps, 9 have been highlighted and numbered. Both maps were measured at 560 nm. The same scale is used in both maps for comparison.

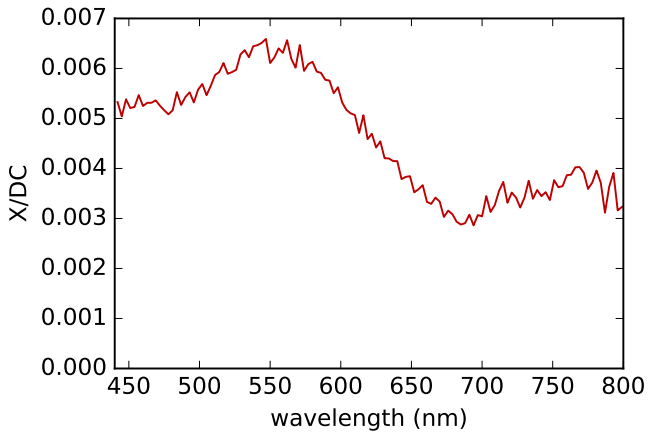

Figure 2.21: X/DC spectrum of a typical object from the gold spheres sample.

2.3.2.4 Signal Optimization Procedure

When configuring the setup, the spot is focused on the sample using the CCD camera as described in section 2.2.4. In order to focus the reflective object correctly, the objective's

distance is adjusted to minimize the spot in the image of the CCD camera. Initially, the same approach was used to focus the GAPO objective but the previous results show that this leads to suboptimal focalization. In order to improve the signal and contrast with the GAPO objective, a brief study was undertaken to improve the focalization with the GAPO objective . A table of the different CCD camera spot images along with the local map of one of the disks from the lithographed sample is shown in figure 2.22. The table shows that the signal and resolution are improved when the spot is focused as shown in the CCD image of column d. This focalization was used for the rest of this work.

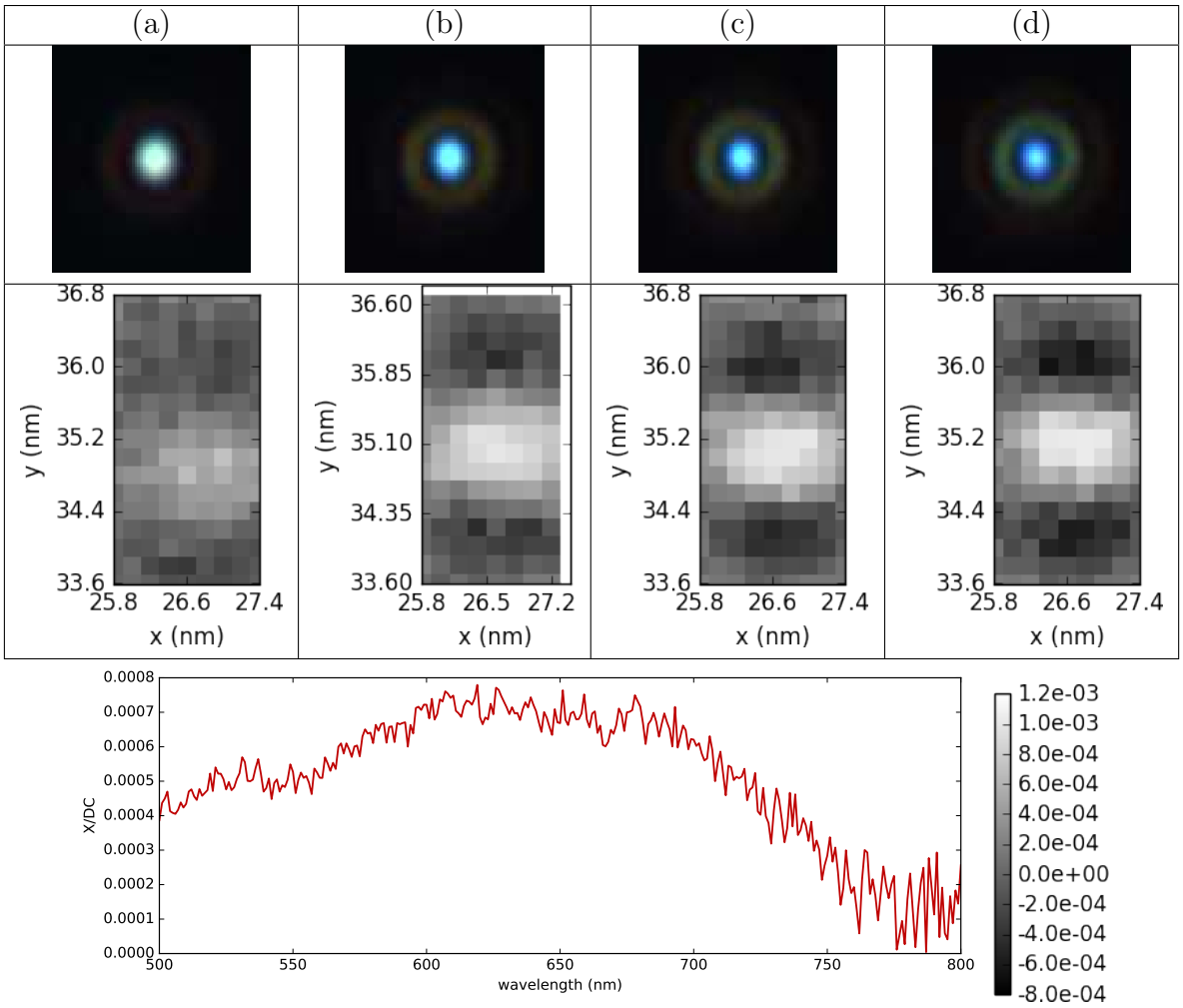

Figure 2.22: Comparison of the different focalizations of the spot in air with the GAPO objective as seen in the CCD camera vs the SMS map of an object with that focalization at 610 nm. The SMS maps are shown with the same Z-scales for comparison. The spectrum of the object is shown below along with the z-scale legend for the SMS maps and is one of the disks of the lithographed sample. The focalization was varied over a few microns.

2.3.2.5 Optical Response Of Single Nano-objects In Air And In Water

A stable sample of model objects is required to compare the optical response of single NPs in air and water. Given the loss of objects from the gold sphere sample after immersion in water and spectra that deviate from the expected response of single gold nanospheres, the lithographed sample was used for a second study of objects in air and in water. The sample was mapped with the GAPO objective using the optimized focalization first in air and then in water. The results are shown in figure 2.23. The map in air on the left shows a weaker signal with a lower signal-to-noise ratio (SNR), resolution and contrast, confirming again that the objective is not ideal for working in air. The displayed region shows a recognizable bright constellation of 7 objects. A careful examination of the image reveals very weak signals where other objects are expected to be in the patterned 2D array. The weaker signal at these positions indicates that these objects have been partially lost prior to the SMS study as shown in figure 2.14b.

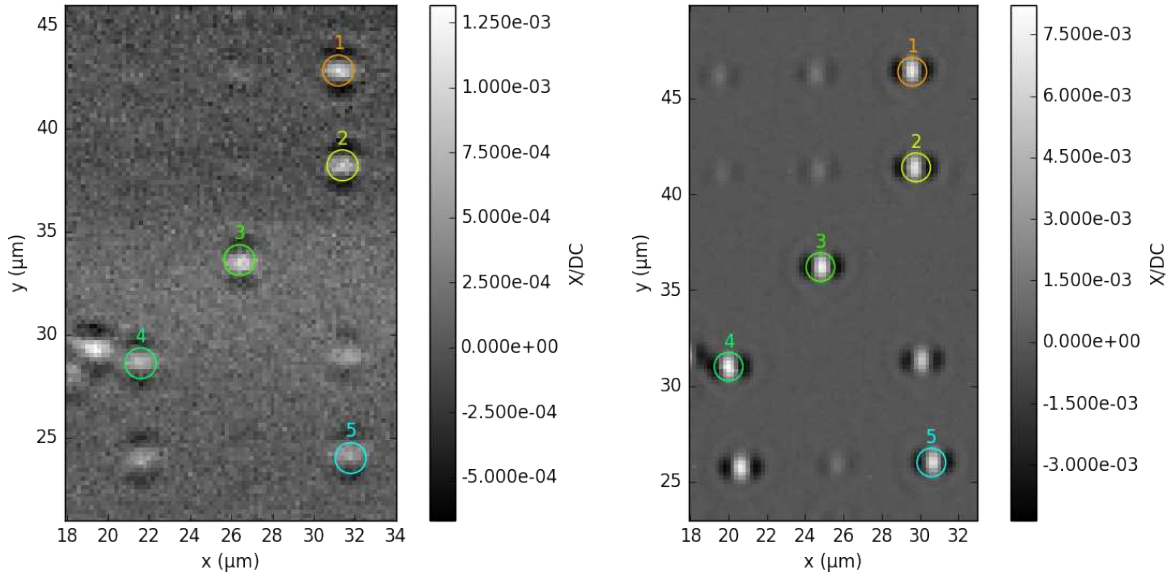

(a) air **(b)** water

Figure 2.23: Maps of the lithographed sample with the GAPO objective in air and water. (a) In air at 630 nm (oscillating mirror). (b) In water at 635 nm (oscillating stage).

The same region is shown in water on the right. With the optimized focalization, the image is very clear with nearly no relative background noise. The signal is about three times stronger than the signal in air and the partially lost objects are more visible at their expected positions in the array. The same five objects have been highlighted and equivalently numbered in each map. These objects were selected for further study and comparison of their spectra because they exhibited a similar optical response.

Spectra of the highlighted objects in air are shown in figure 2.24a. The averaged back-

ground signal (figure 2.15a) has been subtracted from the spectra. The spectra are relatively uniform and present what appears to be a LSPR peak around 625 nm. The second apparent peak near 750 nm is due to an artifact of the noise in the background signal and the dips in the lamp's intensity around these wavelengths (figure F.4 on page 243 of the appendix).

The spectra of the same objects in water are shown in figure 2.24b. The spectra are again relatively uniform with an apparent LSPR peak around 662 nm which is red-shifted about 37 nm from the spectra in air. The signals of the spectra in water are about 6 times stronger than the equivalent spectra in air.

These empirical spectra are compared to theoretical calculations of a gold disk of radius 50 nm and height 50 nm on a glass substrate in air and water (figure 2.24c). This model predicts spectra of a shape very similar to those observed experimentally with a shift of approximately 43 nm when moving from air to water and slight increase in peak signal strength. The fact that the experimental peaks lie further to the red than those predicted by the model likely indicate that the radius of the disks are indeed larger than 100 nm as suggested by figure 2.14d. The lower shift may also indicate the presence of contaminants around the objects that increase the effective index n_{eff} and thus reduce the sensitivity to water as discussed in section 1.3.2.5. The wider LSPR peaks of the empirical spectra may be partially due to the 5 nm adhesion layer of chromium between the gold disks and the substrate of the lithographed sample[27, 28]. This layer was omitted from the model. Imperfections in the disks' shape such as those seen in figure 2.14 may also play a role. It is also possible that the sidewalls of the disks are not perfectly vertical due to limitations of the lithography technique. We have observed such deformities before with lithographed platinum parallelepipeds[24]. This would not be visible with SEM.

Despite these discrepancies, the results are in good agreement with the model with regard to the positions of the LSPR peaks. Most importantly, this study shows that the LSMS setup is able to produce correct maps and spectra with strong signals and low noise when properly configured with the GAPO objective in water.

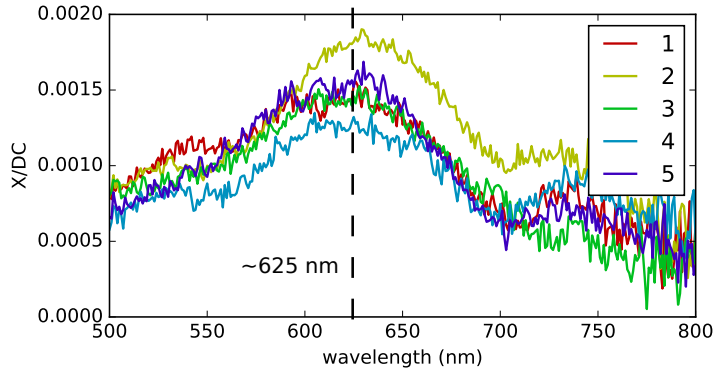

(a) air, mirror

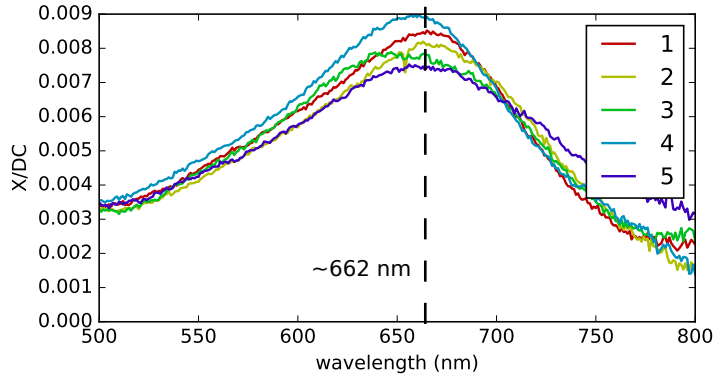

(b) water, stage

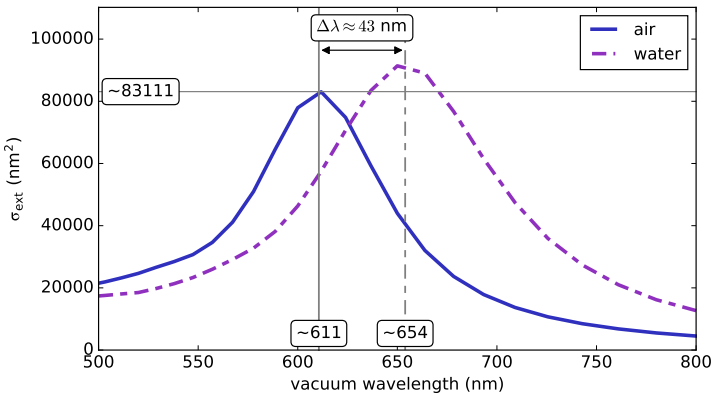

(c) FEM calculations

Figure 2.24: (a) and (b) Spectra of the selected disks shown in figure 2.23 in air and in water, respectively. (c) Calculated spectra of a gold disk of radius 50 nm and height 50 nm on a glass substrate in air and water.

2.3.2.6 Spectra Calibration

To estimate the size of the spot of the GAPO objective in air and water, an object was selected and used to measure X/DC profiles at various wavelengths along the axis of oscillation. These profiles were then used to determine parameters that yield the best fit of a simplified spot profile calculated with a perfect lens and convolved with the pinhole image. This simplified model[12] was used because the internal optical configuration of the GAPO objective is not known. The X/DC profiles of the object in air and in water are shown at various wavelengths in figures 2.25 and 2.26, respectively. For each profile, the fitted curve is also shown. The measurements were made at $2f$ so that the maximum signal would remain centered on the object irrespective of the wavelength, as discussed in section 2.1.2.

[12]This approach assumes that the object is relatively small compared to the spot size. Larger objects will artificially broaden the profile due to convolution with the object's shape, similar to the way an AFM will broaden all features due to convolution with the tip. However, smaller objects produce less signal, so a compromise must be made between signal strength and profile resolution. In practice, objects up to about 100 nm yield good results for a spot size of 1 µm.

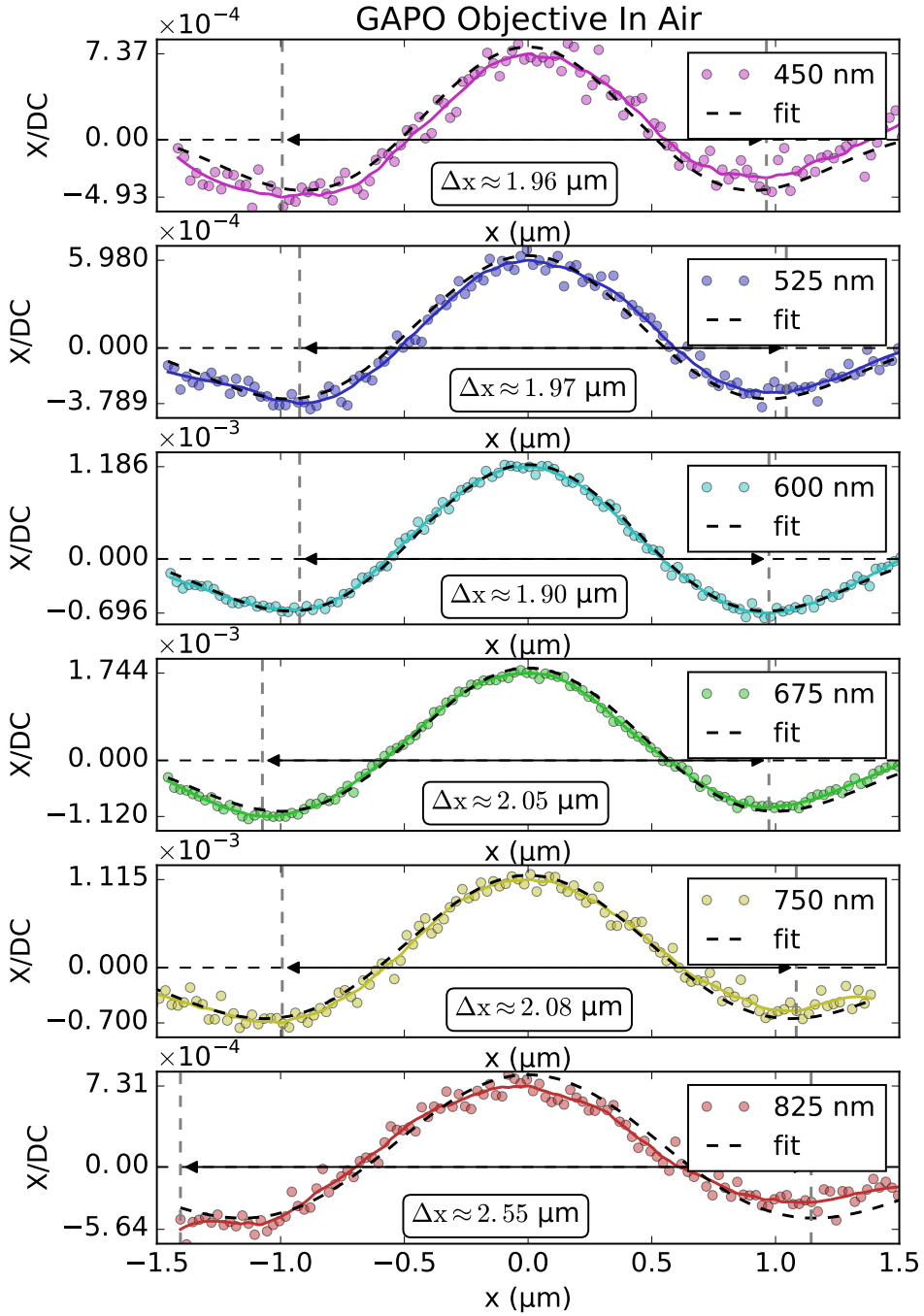

Figure 2.25: X/DC profiles along the axis of oscillation of a lithographed gold disk ($R \approx 125\,\text{nm}$, $h = 50\,\text{nm}$) with an oscillation of 400 nm at 186 Hz. Profiles were measured using the GAPO objective in air.

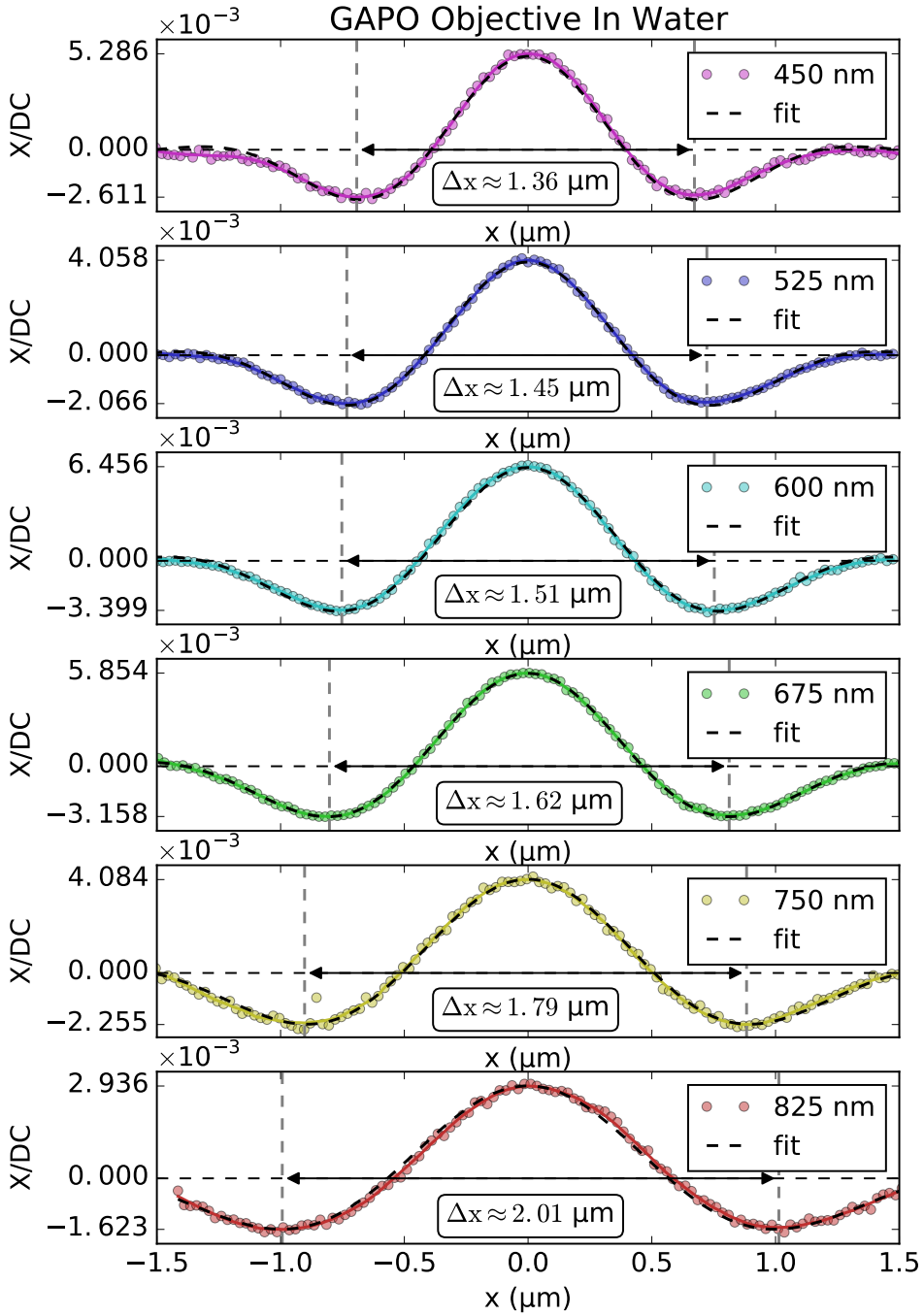

Figure 2.26: X/DC profiles along the axis of oscillation of a lithographed gold disk ($R \approx 125\,\text{nm}$, $h = 50\,\text{nm}$) with an oscillation of 400 nm at 186 Hz. Profiles were measured using the GAPO objective in water.

Using these parameters, the approximate size of the spot has been calculated at different wavelengths in figure 2.27. At each wavelength, the calculated spot in water is narrower and more intense at the center than the spot in air. This shows that the focal properties of the GAPO objective are indeed better when focusing through the filled fluid cell, which more closely resembles conditions for which it was designed. We also note that the calculated profile is much simpler than what was observed in the spot images in figure 2.22, further confirming that the perfect lens is a relatively gross oversimplification of the unknown internal optics of the GAPO objective.

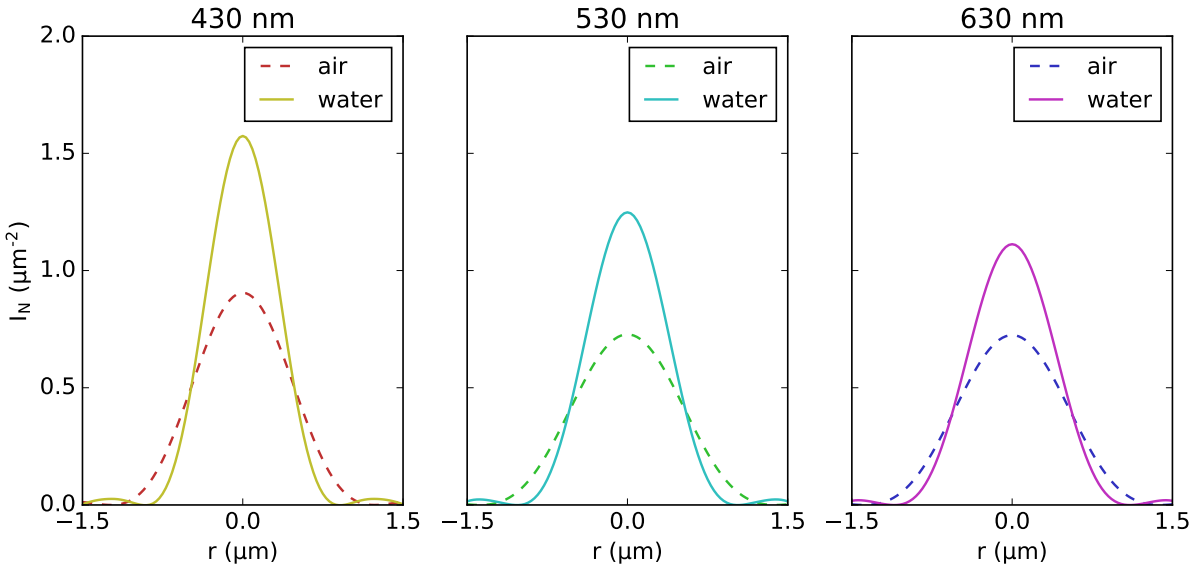

Figure 2.27: Estimated spot profile sizes for the GAPO object in air vs water. The profiles were determined by fitting the signal profiles shown in figures 2.25 and 2.26.

From the calculated spot profile it is possible to calculate calibration curves at $2f$ using the formula (2.10). The calculate curves are shown in figure 2.28. The general shape and magnitude of the calibration curve in water is similar to other calibration curves used in our group (e.g. figure 2.7). The inflections of the curve in air is a consequence of the profile evolution in figure 2.25. There is a slight increase when moving from 450 nm to 525 nm but then a decrease at 600 nm before continuously increasing again as it moves to the red. The discrepancies between these calibration curves further highlight the different behavior of the GAPO objective under different conditions.

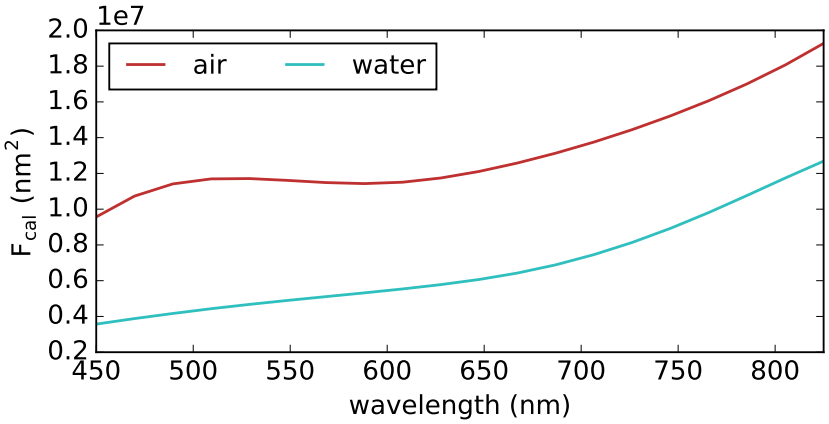

Figure 2.28: Calibration curves in air and water determined from the spot profiles in figure 2.27.

Using these curves, the experimental spectra in figure 2.24 have been calibrated and replotted alongside the theoretical spectra in figure 2.29. The calibration cannot correct for the weak signal and low SNR in air and so the calibrated curve exhibits a signal that is about 1/8 of what is expected. The peak is also wider than the theoretical curve and does not display the same symmetry about the LSPR peak. The calibrated spectrum is red-shifted by $\approx 10\,\text{nm}$ compared to the uncalibrated spectra.

The calibrated spectra in water more closely resemble the theoretical spectra in both strength and overall shape. The LSPR peak is nevertheless about 3/5 of the theoretical curve. The average LSPR peak of the calibrated curves is also shifted to the red by about 12 nm. The relative shift between air and water is thus about the same for the raw (37 nm) and calibrated (39 nm) spectra and in good agreement with the theoretical shift (43 nm).

Overall, the general shape of the spectra along with the LSPR peaks and their relative shifts are accurate and show that the LSMS measurement is quantitative even if it is not entirely absolute. Discrepancies with the theoretical model are likely due in part to the quality of the lithographed disks and the lack of the chromium adhesion layer in the model. The model could also be improved if the exact morphology (i.e. the height, radius and eventual imperfections) of the studied disk were known via electron microscopy or AFM. Without this information it is difficult to conclude if the discrepancies stem from errors in the setup, the calibration, or from a model that differs significantly from the real object studied.

Nevertheless, the measured spectra display the correct order of magnitude and optical characteristics, especially in liquid.

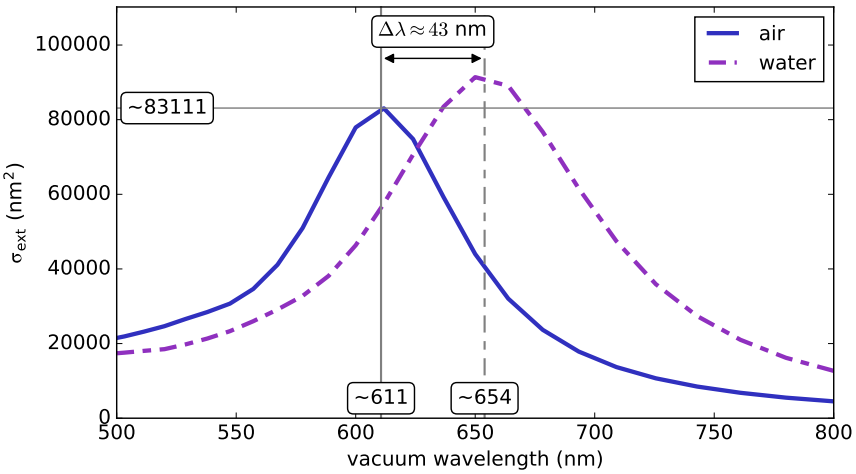

(a) FEM calculations

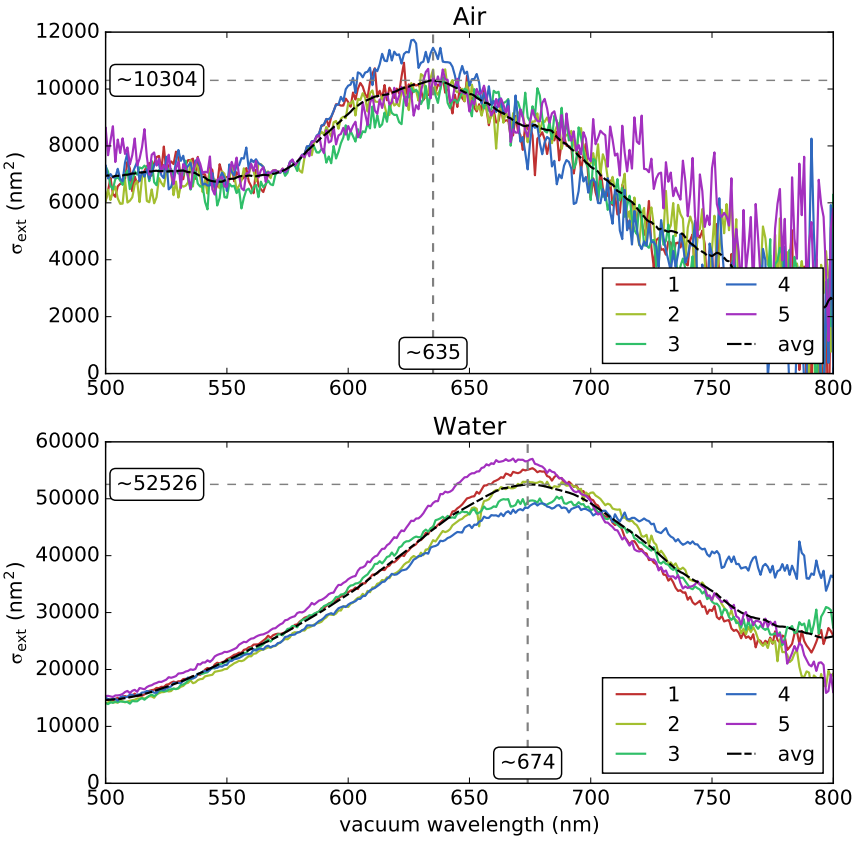

(b) calibrated spectra

Figure 2.29: (a) Calculated spectra of a gold disk of radius 50 nm and height 50 nm on a glass substrate in air and water from figure 2.29a. (b) Calibrated spectra of the lithographed sample in air and in water from figure 2.24 using the calibration curves in figure 2.28.

Conclusion

A SMS setup has been successfully adapted to measure the optical response of individual nano-objects in a liquid environment. The introduction of the fluid cell, oscillating mirror and new refractive objectives increases the optical complexity of the setup and requires a more careful configuration that the previous setup with achromatic reflective objectives in air.

The oscillating mirror sometimes generates a spurious background signal that distorts raw X/DC spectra. This can be corrected by subtracting an averaged background signal from the spectra via scripts in post-processing using background spectra automatically measured by the interface software MICA that I have developed. The corrected spectra are comparable to spectra measured with stage oscillations.

The oscillating mirror is not necessary for measurements with the second prototype fluid cell. The stage is able to oscillate with an amplitude of 400 nmunder the weight of the filled fluid cell if the frequency is reduced to about 186 Hz. The stage can therefore be used to avoid additional post-processing of the background signal generated by the mirror.

The MICA interface software that has been developed for the setup works reliably and is able to automate several tedious tasks. It is able to automatically and accurately track and measure objects. For example, tracked objects may be selected for local remapping and spectra acquisition or profiling and tracking works even when the imaging properties of the setup are suboptimal.

When working in air with the GAPO objective, the spot is poorly focalized compared to the reflective objective and the GAPO objective in water. This results in larger object profiles, weaker signals and less contrast on maps. The GAPO objective is designed to work through 3 mm of glass: working in air significantly deviates from these conditions. Nevertheless, the GAPO objective can be used in air to map samples, locate objects and measure spectra, even if it is suboptimal.

The optimal focalization of the objective has been determined by correlating CCD-camera images of the spot with SMS signal strength and contrast, which led to improved measurements in both air and water. The setup is able to accurately map samples in liquid, track objects and measure their spectra. The resulting maps and spectra are comparable to those measured in air with the reflective objective and so the setup can be used to study objects in air and different liquids.

Calibration curves have been calculated for the setup and these yield accurate spectra to within an order of magnitude of theoretical spectra but discrepancies in the total signal strength remain. We have not determined if these discrepancies are due to errors with the setup or inaccuracies in the simplified theoretical model used to calculate the control

spectra. Despite these discrepancies, the setup is able to correctly measure relative shifts of the LSPR when moving from air to liquid. These shifts will be explored further in the next chapter.

The immersion of samples in liquid presents new challenges. Samples prepared with standard methods such as spin-coating or simple deposition are unstable and objects may be lost upon immersion. This has prompted the development of a new sample preparation technique that will also be presented in the next chapter.

References

[1] Y. Mori. Size-Selective Separation Techniques for Nanoparticles in Liquid. *KONA Powder and Particle Journal*, 32(0):102–114, 2015. ISSN 0288-4534, 2187-5537. doi:10.14356/kona.2015023.

[2] B. Kowalczyk, I. Lagzi, and B. A. Grzybowski. Nanoseparations: Strategies for size and/or shape-selective purification of nanoparticles. *Current Opinion in Colloid & Interface Science*, 16(2):135–148, April 2011. ISSN 13590294. doi:10.1016/j.cocis.2011.01.004.

[3] N. Surugau and P. L. Urban. Electrophoretic methods for separation of nanoparticles. *Journal of Separation Science*, 32(11):1889–1906, June 2009. ISSN 16159306, 16159314. doi:10.1002/jssc.200900071.

[4] A. Pimpin and W. Srituravanich. Review on Micro- and Nanolithography Techniques and their Applications. *Engineering Journal*, 16(1):37–56, January 2012. ISSN 01258281. doi:10.4186/ej.2012.16.1.37.

[5] Z. Xie, W. Yu, T. Wang, H. Zhang, Y. Fu, H. Liu, F. Li, Z. Lu, and Q. Sun. Plasmonic Nanolithography: A Review. *Plasmonics*, 6(3):565, September 2011. ISSN 1557-1955, 1557-1963. doi:10.1007/s11468-011-9237-0.

[6] T. Klar, M. Perner, S. Grosse, G. von Plessen, W. Spirkl, and J. Feldmann. Surface-Plasmon Resonances in Single Metallic Nanoparticles. *Physical Review Letters*, 80 (19):4249–4252, May 1998. doi:10.1103/PhysRevLett.80.4249.

[7] S. Schultz, D. R. Smith, J. J. Mock, and D. A. Schultz. Single-target molecule detection with nonbleaching multicolor optical immunolabels. *Proceedings of the National Academy of Sciences of the United States of America*, 97(3):996–1001, February 2000. ISSN 0027-8424.

[8] J. Prikulis, H. Xu, L. Gunnarsson, M. Käll, and H. Olin. Phase-sensitive near-field imaging of metal nanoparticles. *Journal of Applied Physics*, 92(10):6211–6214, November 2002. ISSN 0021-8979, 1089-7550. doi:10.1063/1.1516249.

[9] C. Sönnichsen, T. Franzl, T. Wilk, G. von Plessen, J. Feldmann, O. Wilson, and P. Mulvaney. Drastic Reduction of Plasmon Damping in Gold Nanorods. *Physical Review Letters*, 88(7):077402, January 2002. doi:10.1103/PhysRevLett.88.077402.

[10] G. Raschke, S. Kowarik, T. Franzl, C. Sönnichsen, T. A. Klar, J. Feldmann, A. Nichtl, and K. Kürzinger. Biomolecular Recognition Based on Single Gold Nanoparti-

cle Light Scattering. *Nano Letters*, 3(7):935–938, July 2003. ISSN 1530-6984. doi:10.1021/nl034223+.

[11] L. Novotny and S. J. Stranick. Near-Field Optical Microscopy and Spectroscopy with Pointed Probes. *Annual Review of Physical Chemistry*, 57(1):303–331, 2006. doi:10.1146/annurev.physchem.56.092503.141236.

[12] L. J. E. Anderson, K. M. Mayer, R. D. Fraleigh, Y. Yang, S. Lee, and J. H. Hafner. Quantitative Measurements of Individual Gold Nanoparticle Scattering Cross Sections. *The Journal of Physical Chemistry C*, 114(25):11127–11132, July 2010. ISSN 1932-7447. doi:10.1021/jp1040663.

[13] C. R. Carey, T. LeBel, D. Crisostomo, J. Giblin, M. Kuno, and G. V. Hartland. Imaging and Absolute Extinction Cross-Section Measurements of Nanorods and Nanowires through Polarization Modulation Microscopy †. *The Journal of Physical Chemistry C*, 114(38):16029–16036, September 2010. ISSN 1932-7447, 1932-7455. doi:10.1021/jp101891a.

[14] M. W. Knight, J. Fan, F. Capasso, and N. J. Halas. Influence of excitation and collection geometry on the dark field spectra of individual plasmonic nanostructures. *Optics Express*, 18(3):2579, February 2010. ISSN 1094-4087. doi:10.1364/OE.18.002579.

[15] G. Hartland, H. Okamoto, M. Orrit, and P. Zijlstra. Optical studies of single metal nanoparticles. *Physical Chemistry Chemical Physics*, 15(12):4090, 2013. ISSN 1463-9076, 1463-9084. doi:10.1039/c3cp90022c.

[16] E. Ringe, B. Sharma, A.-I. Henry, L. D. Marks, and R. P. Van Duyne. Single nanoparticle plasmonics. *Physical Chemistry Chemical Physics*, 15(12):4110, 2013. ISSN 1463-9076, 1463-9084. doi:10.1039/c3cp44574g.

[17] A. Crut, P. Maioli, N. D. Fatti, and F. Vallée. Optical absorption and scattering spectroscopies of single nano-objects. *Chemical Society Reviews*, 43(11):3921–3956, May 2014. ISSN 1460-4744. doi:10.1039/C3CS60367A.

[18] D. Boyer, P. Tamarat, A. Maali, B. Lounis, and M. Orrit. Photothermal Imaging of Nanometer-Sized Metal Particles Among Scatterers. *Science*, 297(5584):1160–1163, August 2002. ISSN 0036-8075, 1095-9203. doi:10.1126/science.1073765.

[19] S. Berciaud, D. Lasne, G. A. Blab, L. Cognet, and B. Lounis. Photothermal heterodyne imaging of individual metallic nanoparticles: Theory versus experiment. *Physical Review B*, 73(4):045424, January 2006. doi:10.1103/PhysRevB.73.045424.

[20] P. Billaud, S. Marhaba, N. Grillet, E. Cottancin, C. Bonnet, J. Lermé, J.-L. Vialle, M. Broyer, and M. Pellarin. Absolute optical extinction measurements of single nano-objects by spatial modulation spectroscopy using a white lamp. *Review of Scientific Instruments*, 81(4):043101, 2010. ISSN 00346748. doi:10.1063/1.3340875.

[21] J. Lermé, G. Bachelier, P. Billaud, C. Bonnet, M. Broyer, E. Cottancin, S. Marhaba, and M. Pellarin. Optical response of a single spherical particle in a tightly focused light beam: application to the spatial modulation spectroscopy technique. *Journal of the Optical Society of America A*, 25(2):493–514, February 2008. doi:10.1364/JOSAA.25.000493.

[22] D. Manchon. *Réponse optique de nano-objets uniques anisotropes : de l'or aux métaux de transition*. PhD thesis, Université Claude Bernard Lyon 1, Lyon, France, October 2012.

[23] P. Billaud, S. Marhaba, E. Cottancin, L. Arnaud, G. Bachelier, C. Bonnet, N. Del Fatti, J. Lermé, F. Vallée, J.-L. Vialle, M. Broyer, and M. Pellarin. Correlation between the Extinction Spectrum of a Single Metal Nanoparticle and Its Electron Microscopy Image. *The Journal of Physical Chemistry C*, 112(4):978–982, January 2008. ISSN 1932-7447, 1932-7455. doi:10.1021/jp076955m.

[24] D. Manchon, J. Lermé, T. Zhang, A. Mosset, C. Jamois, C. Bonnet, J.-M. Rye, A. Belarouci, M. Broyer, M. Pellarin, and E. Cottancin. Plasmonic coupling with most of the transition metals: a new family of broad band and near infrared nanoantennas. *Nanoscale*, 7(3):1181–1192, November 2014. ISSN 2040-3364, 2040-3372. doi:10.1039/C4NR05383D.

[25] A. Arbouet, D. Christofilos, N. Del Fatti, F. Vallée, J. R. Huntzinger, L. Arnaud, P. Billaud, and M. Broyer. Direct Measurement of the Single-Metal-Cluster Optical Absorption. *Physical Review Letters*, 93(12):127401, September 2004. doi:10.1103/PhysRevLett.93.127401.

[26] M. Husnik, S. Linden, R. Diehl, J. Niegemann, K. Busch, and M. Wegener. Quantitative Experimental Determination of Scattering and Absorption Cross-Section Spectra of Individual Optical Metallic Nanoantennas. *Physical Review Letters*, 109(23): 233902, December 2012. doi:10.1103/PhysRevLett.109.233902.

[27] T. G. Habteyes, S. Dhuey, E. Wood, D. Gargas, S. Cabrini, P. J. Schuck, A. P. Alivisatos, and S. R. Leone. Metallic Adhesion Layer Induced Plasmon Damping and Molecular Linker as a Nondamping Alternative. *ACS Nano*, 6(6):5702–5709, June 2012. ISSN 1936-0851. doi:10.1021/nn301885u.

[28] T. Siegfried, Y. Ekinci, O. J. Martin, and H. Sigg. Engineering metal adhesion layers that do not deteriorate plasmon resonances. *ACS nano*, 7(3):2751–2757, 2013.

Chapter 3

Gold Bipyramids As Biosensors: Theoretical Properties, Sample Fabrication And Experimental Investigations Of Sensitivity And Robustness

Contents

Introduction

In the previous chapter the development of the liquid spatial modulation spectroscopy (LSMS) setup has been presented and initial tests have demonstrated that it is indeed possible to study single nanoparticles (NPs) in liquid. The ultimate aim of this work is to use the setup for biosensing applications with plasmonic probes. In this chapter we shall therefore focus on the choice of a suitable probe for such applications and we shall see that multiple factors must be considered to make the best choice. We shall therefore begin with a brief overview of the general criteria by which plasmonic probes are evaluated for sensing applications. We will then discuss the choice of composition of a probe and show that gold is currently one of the most promising choices for biosensing applications. We will also discuss some of the most commonly used shapes in current research. We will see that nanorods and bipyramids (BPs) receive the most attention due to several desirable properties for sensing applications.

In this work we have chosen to work with gold BPs. Several of their properties such as refractive index (RI) sensitivity and local field enhancement will be further examined through numerical simulations in this chapter. We will also describe their synthesis and the parameters that can be controlled to alter their optical properties. We will then describe a novel sample preparation protocol that can be used to graft gold nano-objects to a glass substrate via silane linker molecules for studies in liquid with the LSMS setup. This will be followed by a presentation of tests to determine the effects of silanization on the LSMS measurements and the silanized object's optical response.

This will be followed by studies of the sensitivity and robustness of BP samples prepared with the new protocol. Sensitivity will be studied via measurements of the localized surface plasmon resonance (LSPR) in response to media of different real refractive RI and the results will be compared to our theoretical investigations and values reported in the literature. We will also show that it is possible to observe dynamic processes with these

samples and the LSMS setup. To test the stability and robustness of the samples, the optical response of individual objects will be consecutively studied in different media to determine if it undergoes an irreversible evolution over the course of the study.

3.1 Rational Selection Of Probes For Biosensing

3.1.1 General Metrics For Probe Evaluation

The probe is a critical component of any sensing application and there is a growing number of different types for biosensing applications. It is therefore useful to consider the characteristics by which their suitability may be evaluated and compared in order to select an appropriate probe.

In this work we are concerned with plasmonic nanoprobes for biosensing applications. The operating principle of a plasmonic nanoprobe is that the presence of a target analyte will modify the local RI around the probe and thereby induce a change in the LSPR frequency (and wavelength). The success of the application is determined by the ability to measure that change.

Because LSPR probes are nanoscale resonators, they are readily characterized by the same formalism as other resonant systems. K. S. Johnson originally invented the term "Q factor" to characterize coils and condensers in the early 1920s. By the 1950s, the term had become ubiquitous in the description of various types of resonant systems as disparate as mechanical oscillators and spectral lines[1–3] and continues to be used today. In general terms, the Q factor of a resonant system is defined as[4]

$$Q = 2\pi \frac{\text{energy stored}}{\text{average energy dissipated per cycle}} \tag{3.1}$$

and it is an indicator of the damping of the system and thus the lifetime of the oscillation[5]. From (3.1), the Q factor may be expressed in terms of the resonant angular frequency ω_{lspr} and the full width at half maximum (FWHM) Γ (expressed in the same units as ω)[4]:

$$Q = \frac{\omega_{\text{lspr}}}{\Gamma} \tag{3.2}$$

A plasmonic probe with a high Q factor thus presents a narrow LSPR peak in its optical spectrum. This is important for biosensing applications that seek to detect minor shifts

in the resonance frequency in the presence of a target analyte: frequency shifts in the presence of noise are easier to detect when the peak is narrow[6]. The quest for high-Q optical probes for sensing applications is an area of active research and has led to extensive development of plasmonic probes[7–38], whispering gallery mode (WGM) probes[39–41] and novel metamaterials[42–45] for sensing applications, among others.

For comparison of plasmonic probes for biosensing applications, Sherry et al. [46][1] have defined a figure of merit (FOM), now commonly used in the literature[7, 14, 19, 20, 36, 38, 48–51]:

$$\mathrm{FOM} = \frac{m}{\Gamma} = \frac{mQ}{\omega_{\mathrm{lspr}}} \tag{3.3}$$

where m is the RI sensitivity[2], which is usually expressed in wavelength or energy units as[25][3]

$$m = \begin{cases} m_\lambda = \dfrac{\mathrm{d}\lambda_{\mathrm{lspr}}}{\mathrm{d}n} & (\mathrm{nm \cdot RIU^{-1}}) \\ m_{\mathrm{E}} = \dfrac{\mathrm{d}E_{\mathrm{lspr}}}{\mathrm{d}n} = m_\lambda \dfrac{\mathrm{d}E}{\mathrm{d}\lambda} \approx \dfrac{-m_\lambda}{\lambda^2} \cdot (1240\,\mathrm{eV \cdot nm}) & (\mathrm{eV \cdot RIU^{-1}}) \end{cases} \tag{3.4}$$

where λ_{lspr} is the LSPR wavelength (nm), ω_{lspr} is the LSPR resonance angular frequency, $E_{\mathrm{lspr}} = \hbar\omega_{\mathrm{lspr}}$ is the LSPR energy (eV), and n is the RI around the object (refractive index units (RIU)). The convention of units used with m varies in the literature[4] and both often co-exist for ease of comparison of different works[8]. Occasionally, $m_\omega = \frac{\mathrm{d}\omega_{\mathrm{lspr}}}{\mathrm{d}n} = \frac{m_{\mathrm{E}}}{\hbar}$ is also used, in which case it is expressed in $\mathrm{rad \cdot s^{-1} \cdot RIU^{-1}}$. The general preference in the literature seems to be for $\mathrm{nm \cdot RIU^{-1}}$. Given that the terms may be readily interconverted, we will simply use m to refer to the sensitivity when there is no risk of ambiguity.

In the literature, m and FOM refer to the bulk sensitivity, i.e. the sensitivity of the probe to changes in the RI of a homogeneous environment around it. Because biosensing applications rely on sensitivity to RI changes in the probe's immediate environment

[1] We note that Lee and El-Sayed [47] also highlighted the need to consider line broadening when considering the increased sensitivities of larger gold nanorods at about the same time, although without explicitly evoking the term FOM.

[2] S is also used in the literature for the sensitivity (e.g. Mayer and Hafner [8]). m is used by some authors to avoid confusion with the signal, usually given as S, and seems to be the most common in the literature.

[3] There is an error in the units of $\frac{\mathrm{d}E}{\mathrm{d}\lambda}$ in that paper that has been corrected here.

[4] Although m is not strictly linear in n in either system of units, it may be approximated as linear for very small changes of n in both[8, 21]. In such cases, it may be determined by linear regression[46].

(i.e. the binding of molecules to its surface), some authors dismiss the utility of such metrics[52–54] while others have proposed modified FOMs and alternative metrics that may be more relevant[21, 25, 55]. These are discussed further in appendix E on page 231 along with other developments to evaluate probes for biosensing applications. Nevertheless, the common definitions of sensitivity and FOM found in the literature remain widely used and provide useful guidelines for the rational selection of probes for biosensing applications even if the real performance of a probe must be evaluated experimentally with each application.

3.1.2 Composition Effects

Most plasmonic probes studied in the literature are made of silver or gold. Compared to gold, silver possesses attractive optical properties for plasmonic sensors: the imaginary part of its dielectric function is low in the range 400 nm to 500 nm, which leads to more scattering and less damping in this region[8, 56].

The LSPR peak positions and bulk RI sensitivities of comparable NPs of silver and gold are presented in table 3.1[8]. For each shape, silver is blue-shifted compared to gold and displays a greater sensitivity[5]. Due to the reduced damping and absence of visible-range interband transitions, the FWHM of silver's LSPR peak are also relatively narrow compared to gold (not shown in table), which gives it a greater FOM.

particle type	size (nm)	LSPR peak (nm)	sensitivity (nm/RIU)
gold nanospheres	50	530	60
silver nanospheres	60	435	160
gold nanocube	44	538	83
silver nanocube	30	510	146

Table 3.1: Comparison of peak positions and RI sensitivities for gold and silver in spheres and cubes of comparable sizes. Source: Mayer and Hafner [8]

Gold is nevertheless preferred in biosensing assays due to its greater chemical stability[8, 10, 56]. Biosensing assays necessarily expose the sensing probe to a chemical environment where stability is crucial. Silver has been shown to undergo cycle shifts, i.e. after adsorption and desorption of a target, the response does not return to the baseline[57]. Silver also requires ultraviolet (UV) filters in the optical setup to avoid oxidation and heating

[5] Lee et al. [29] have also shown greater RI sensitivity for silver compared to gold in cubes of similar size. Their analysis also offers an interesting comparison of the sensitivity and FOM of higher-order modes in a silver nanocube.

effects[57] whereas gold is resistant to oxidation and stable under the same conditions. In this work we therefore choose to work with gold NPs.

Despite the prevalence of gold and silver, copper[58–60],aluminium[61–63], palladium[37], platinum[64], rhodium[65] and other transition metals are also actively investigated for potential plasmonic applications. Most of these are unsuitable for biosensing applications because they present LSPR in the UV to near-ultraviolet (NUV) range. Although biomolecules such as proteins, DNA and lipids absorb in this range, the radiation induces chemical modifications and denaturation that perturbs biomolecular processes such as recognition and binding[66–71]. However, recent work by McMahon et al. [72], Manchon et al. [73] and Golmohammadi and Ahmadivand [74] has shown that plasmonic coupling can be used to induce LSPR in the NUV to visible spectrum with these metals. In their work, Golmohammadi and Ahmadivand propose aluminium clusters with RI-sensitive Fano-resonant[6] dips for biosensing applications even though the Fano dips lie in the NUV range. Another interesting finding comes from Sekhon and Verma [77] who have used theoretical models to determine the optimum size and aspect ratio of rods of gold, silver, copper and aluminium. They have shown that although silver has the best FOM under the modeled conditions, aluminium presents the highest sensitivity. The authors conclude that silver, copper and aluminium may become viable alternatives to gold in sensing applications. Theoretical calculations by Sugawa et al. [37] based on Mie theory predict higher sensitivities of pure palladium NPs compared to silver and gold NPs of the same size and shape. In the same work, the authors reported RI sensing with palladium-coated gold core-shell plasmonic NPs that displayed sensitivity intermediate between that of comparable silver or gold NPs and the calculated sensitivity of the pure palladium NPs.

The search for probes with improved physical properties is not the only motivation for current research into alternatives to gold and silver. Because these metals are expensive, cheaper alternatives may be favorable in some cases where reduced performance is not critical. For example, due to the similarity between the optical properties of copper and gold[7], and copper's lower relative price, it may offer a cost-effective alternative to gold in some applications. For example, Kim et al. [60] have developed an inexpensive disposable biosensing chip based on copper-coated silicon spheres. Nevertheless, copper suffers from the same chemical instability issues as silver and has not received the same attention for biosensing applications as gold.

Work in probe development has also considered probes composed of multiple materials such as the palladium-coated gold spheres mentioned above, elongated objects with a Fe_2O_3 core covered in gold (so-called "nanorice")[13] and silver-coated BPs[35] (BPs are discussed in the next section). This is an active area of research and probes based on

[6]Fano resonance is a phenomenon that occurs when the energy of a resonant system interferes with a continuum of states of another system. This leads to characteristic asymmetric line shapes that may involve abrupt spectra changes[75, 76].

[7]For example, similar interband transition energy thresholds around 1.9 eV, as mentioned in section 1.1.1, and dipolar plasmon modes in the visible spectrum.

uncommon materials and novel compositions may be expected to appear in the future.

3.1.3 Shape Effects

Composition is only one aspect of a probe. The shape of the material will ultimately determine how the intrinsic optical properties manifest themselves as we have seen in chapter 1. Because of this critical influence on LSPR characteristics, a wide range of shapes beyond simple spheres have been developed for plasmonic probes. Colloidally synthesized examples include cubes[46, 78–85], nanorods[11, 17, 19, 20, 25, 27, 35, 38, 55, 57, 86–102], bipyramids[17, 19, 20, 27, 32, 34, 35, 38, 89, 95, 98, 100, 103–106], nanostars[12, 24, 26, 32, 33], nanojavellins[34], nanotubes[28], nanoprisms[23], nanorings[16], nanoframes[27], nanorattles[107] and nanoshells[108]. A wide range of lithographed shapes also exist such as bowties[109, 110], bowties apertures[111], crosses[112], mushrooms[50] and crescents[14, 15, 18, 21, 22].

Several of these shapes and their variations are illustrated in figure 3.1a[19]. The figure shows spheres, cubes, branches, rods and BPs. Branches are star-like objects with multiple spikes oriented in different directions. Rods are long cylindrical objects of varying length and aspect ratio (3 different sizes are shown in the figure). Bipyramids are elongated shapes consisting of two pyramids attached to each other at their base. As with rods, their length and aspect ratio can vary considerably (as the aspect ratio increases, they become "javellins"[34]).

These shapes are compared by λ_{lspr} ("plasmon wavelength"), m ("index sensitivity") and FOM in the table in figure 3.1b[8]. A number of tendencies appear in the table. First, there seems to be a rough correlation between sensitivity and plasmon wavelength. Second, for lower λ_{lspr}, rods are more sensitive than BPs of comparable λ_{lspr} but become comparatively less sensitive as λ_{lspr} increases. Third, the FOM of rods decreases with increasing λ_{lspr} whereas the FOM of BPs increases. The comparison may not be that useful though, because the sizes are necessarily different in order to obtain rods of comparable plasmon wavelengths to BPs.

In general, anisotropic structures show greater RI sensitivity, and shapes with higher aspect ratios are preferred[10]. Increasing the aspect ratios leads to a red-shift of the LSPR. For example, Lombardi et al. [98] have shown that both rods and BPs exhibit a nearly quadratic dependence of λ_{lspr} on the aspect ratio. Various studies have shown that the sensitivity m is proportional to λ_{lspr} and so such shapes are more suited for biosensing[8, 87, 113].

Increasing the size of the object also leads to red-shifted LSPR peaks. However, as the size

[8]The interested reader may refer to table 2 of Mayer and Hafner [8] for a similar comparison of even more shapes.

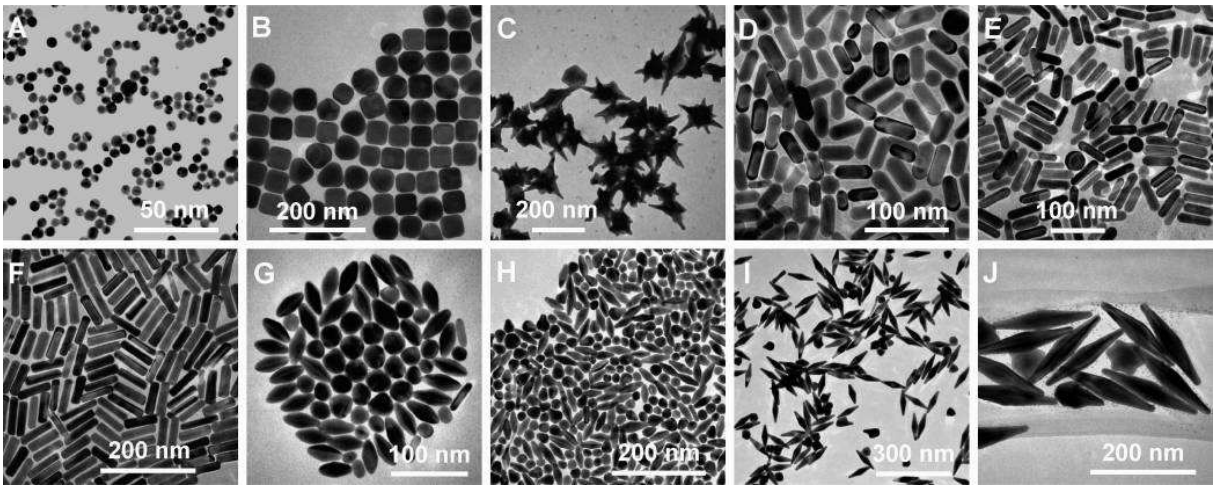

(a) images of different shapes

Au nanoparticles	length[a] (nm)	diameter[b] (nm)	aspect ratio[c]	plasmon wavelength[d] (nm)	index sensitivity[e] (nm/RIU)	figure of merit
nanospheres		15 (1)		527	44 (3)	0.6
nanocubes	44 (2)			538	83 (2)	1.5
nanobranches	80 (14)			1141	703 (19)	0.8
nanorods	40 (6)	17 (2)	2.4 (0.3)	653	195 (7)	2.6
nanorods	55 (7)	16 (2)	3.4 (0.5)	728	224 (4)	2.1
nanorods	74 (6)	17 (2)	4.6 (0.8)	846	288 (8)	1.7
nanobipyramids	27 (4)	19 (7)	1.5 (0.3)	645	150 (5)	1.7
nanobipyramids	50 (6)	18 (1)	2.7 (0.2)	735	212 (6)	2.8
nanobipyramids	103 (7)	26 (2)	3.9 (0.2)	886	392 (7)	4.2
nanobipyramids	189 (9)	40 (2)	4.7 (0.2)	1096	540 (6)	4.5

[a] For nanocubes, the edge length was measured. For nanobranches, the length from the center to the branch tip was measured. The numbers in the parentheses are standard deviations. [b] For nanobipyramids, the diameter at the middle was measured. [c] The ratio between the length and the diameter. [d] Measured when Au nanoparticles are dispersed in aqueous solutions. For nanobranches, it is the longer plasmon wavelength. For nanorods and nanobipyramids, it is the longitudinal plasmon wavelength. [e] For nanobranches, it is the refractive index sensitivity of the longer-wavelength plasmon peak. For nanorods and nanobipyramids, it is the index sensitivity of the longitudinal plasmon resonance peak.

(b) comparison of corresponding characteristics

Figure 3.1: Examples of different colloidally synthesized Au nanoparticle shapes: (A) spheres (B) cubes (C) "branches" (D-F) rods (G-J) bipyramids. The shapes are compared by their LSPR characteristics in the table. Source: Chen et al. [19]

of an object increases, the LSPR peak is broadened by multipolar excitations and radiative damping and so FWHM increases, which may lead to a reduced FOM[8, 10, 47, 114]. It is therefore preferable to increase the aspect ratio instead of the size.

As the aspect ratio increases, the object will exhibit greater curvature and/or edges at its surface. These areas may concentrate the localized electric field enhancement into so-called "hot-spots" as mentioned in section 1.2.3. The sensitivity of the object will be a function of both the enhancement and the confinement of the field in these regions[115, 116].

Given the importance of aspect ratio, local field effects, and expected sensitivity for longer LSPR wavelengths, rods and BPs have received considerable attention in the literature for biosensing applications and are often compared[17, 19, 20, 35, 38, 98]. Although rods and

BPs have been found to have comparable volume-normalized extinction cross-sections[98], rods generally display greater sensitivities to RI changes[20, 38]. This is, however, offset by BPs' narrower LSPR peaks which lead to higher values for the FOM[19, 20, 38]. Theoretical calculations also predict field enhancements with a factor of over 300 for BPs but only 60-80 for rods of comparable aspect ratio when the incident electromagnetic (EM) field is polarized along the longitudinal axis[17, 98].

The dispersion of colloidally synthesized rods and BPs has also been compared. Peters et al. [38] have shown that although both display similar dispersions in their widths (7 % for rods vs 8 % for BPs) and lengths (12 % for rods vs 6 % for BPs), the polycrystallinity of BPs leads to strong correlation (0.78) between the length and the height and thus less dispersion in the critical aspect ratio compared to rods. Because rods are monocrystalline[86], different sides of the rods display different crystal facets. The authors surmise that these will exhibit more variation in growth rates for different growth conditions. BPs, however, are polycrystalline[32] and display equivalent crystal facets with equivalent growth rates. It may therefore be easier to consistently obtain monodisperse BPs with a desired aspect ratio and optical properties.

3.2 Gold Bipyramids As Biosensing Probes

There have been reports of single-molecule detection with both BPs[105] and rods[99, 117, 118]. Both present favorable sensing properties and there is no current consensus on whether one is superior to the other[17, 19, 20, 35, 38, 98]. Given existing expertise in our group[32, 34, 103], we have thus chosen to focus on gold BPs in this work.

3.2.1 General Properties

A transmission electron microscopy (TEM) image and a spectrum of a unique BP previously synthesized and studied in our group is presented in figure 3.2. The spectra have been measured with spatial modulation spectroscopy (SMS) along the longitudinal and transverse axes of the BP using a polarizer. The longitudinal LSPR presents a strong and narrow extinction cross-section in the near-infrared (NIR) region of the spectrum.

The wavelength at which this resonance occurs is a function of the size and aspect ratio of the object as discussed above. By carefully controlling the synthesis parameters, which will be discussed in section 3.2.2, the BP's LSPR may be tailored to a desired wavelength, as seen for different preparations[9] in figure 3.3. This spectral range is of particular interest

[9]It should be noted that these spectra are ensemble measurements of BPs in solution, as opposed to the spectrum of the single BP presented in figure 3.2b.

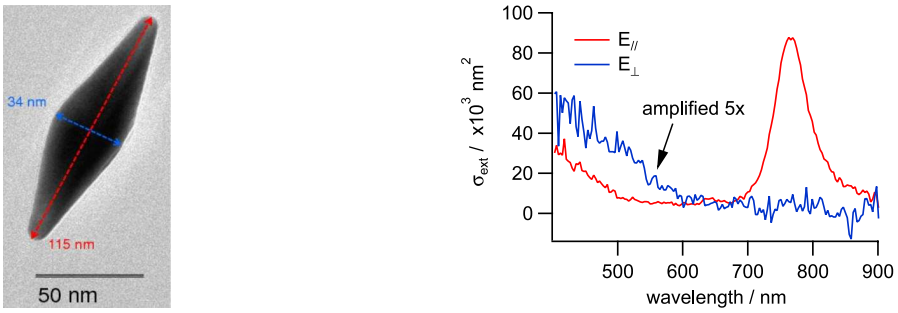

(a) TEM image **(b)** longitudinal and transverse spectra

Figure 3.2: TEM image and spectra of a unique BP. The characteristic strong and narrow LSPR peak arises from an oscillation along the longitudinal axis of the object. Source: Navarro et al. [32]

for biosensing applications as it overlaps with the so-called therapeutic window of biological tissues (approximately 700 nm to 900 nm in which there is decreased absorption and scattering of important biological molecules such as water and haemoglobin.[119, 120].

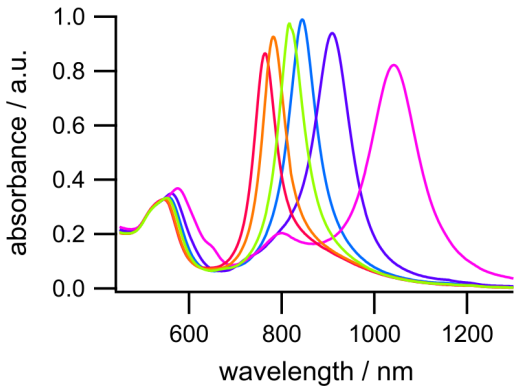

Figure 3.3: Spectra of different suspensions of gold bipyramids. The spectral position of the LSPR peak can be controlled by varying the concentration of the gold seeds during synthesis. Note that these are ensemble measurements, not of individual objects. Source: Navarro et al. [32]

We may explore the suitability of these BPs for sensing applications through numerical models based on finite element method (FEM) calculations as were used in section 1.3. In order to obtain the most realistic results, the simulated BP's morphology is based on previous 3D-electron-tomography studies in our group (figure 3.4). These studies have shown that our BPs are twisted at the middle with 5 facets on each pyramidal half and have rounded tips and edges.

As a model we therefore use a gold BP of length 100 nm and width 30 nm with rounding radius 5 nm. The dimensions have been chosen to approximately match those of the

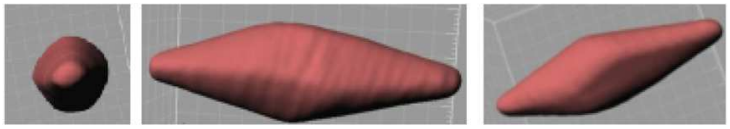

Figure 3.4: 3D shape of a gold BP reconstructed from tomographic TEM. The reconstruction shows that each pyramidal half of the BP has five facets and that there is a short, twisted elongation in the middle. Source: Navarro et al. [32]

BPs used in this work. Although not all samples are of the same size, the results of the numerical simulations should be generally applicable to the limited range of sizes used in this work.

3.2.1.1 Sensitivity

The spectra of a BP in a homogeneous environment of varying real RI n are plotted in figure 3.5. Characteristic values of the LSPR peak are shown in table 3.2. The interesting points to note in the figure and table are that the evolution of $\sigma_{\text{ext,max}}$ flattens out around $n = 1.11$ while Γ begins to increase at this point. The shift in λ_{max} is also approximately linear in n after $n = 1.11$, which is in agreement with the previous remarks on sensing linearity. This is interesting for sensing applications as the linearity may enable quantification of the local RI changes for a given $\Delta\lambda_{\text{max}}$.

n (RIU)	$\sigma_{\text{ext,max}}$ (nm^2)	λ_{max} (nm)	Γ (nm)
1.00	46363	650	38
1.04	51836	665	38
1.11	57245	695	39
1.22	60323	743	44
1.33	60289	792	50
1.44	60265	843	55

Table 3.2: LSPR peak characteristics of the BP spectra shown in figure 3.5. Γ: FWHM

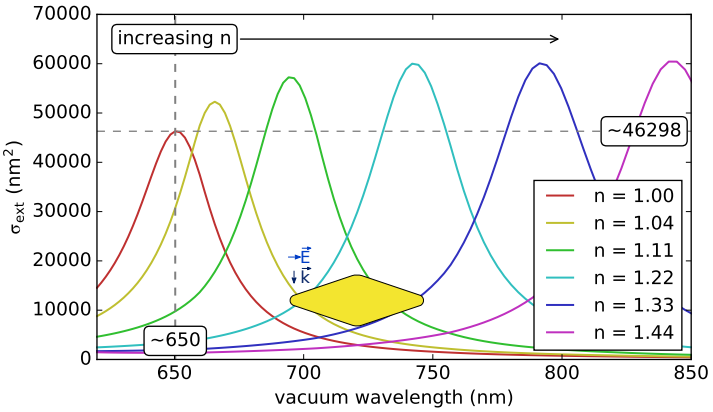

Figure 3.5: Extinction cross-sections of a gold BP of length 100 nm and width 30 nm with rounding radius 5 nm in a homogeneous environment of varying real RI n. [FEM calculations]

We compare the BP's optical response to that of the previously studied sphere in a homogeneous environment (section 1.3) to highlight how important the shape effects are and how they confer properties favorable for sensing applications. In figure 3.6, we compare the maxima of the BP's LSPR peaks in figure 3.5 to those of the sphere (see figure 1.16 on page 54 and figure 1.23 on page 59 for the full spectra). The results show several interesting features. First, curves with similar tendencies are encountered for both shapes although the BP is shifted further to the red. Second, for the same index, the BP lies further to the red along this curve. Third, for the same change in index, the shift in the BP's peak is greater. Fourth, the curve for the BP system flattens out at a lower value of n. Fifth, the extinction cross-sections are comparable despite the sphere's volume exceeding the BP's by a factor of approximately 20.

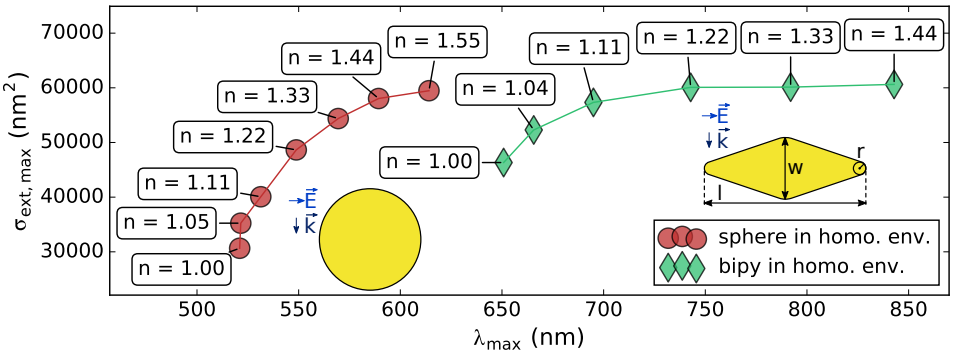

Figure 3.6: Comparison of the LSPR peak maxima of a gold BP of length 100 nm and width 30 nm with rounding radius 5 nm and a sphere of radius 50 nm in homogeneous environments of different real RI n. The spectra may be found in figures 1.16 (sphere in a homogeneous environment) and 3.5 (BP in a homogeneous environment).

λ_{max} is plotted against n to compare the sensitivity m of both systems in figure 3.7. The figure confirms the approximate linearity of the sensitivity in both systems and the greater sensitivity of the BPs. m has been calculated in $\mathrm{nm} \cdot \mathrm{RIU}^{-1}$ at $n = 1.33$ (water) for both shapes and is shown on the graph. These calculations show that a BP is about 2.5 times more sensitive to bulk RI changes in water than a sphere. The length, width, λ_{max} (plasmon wavelength) and m (sensitivity) of this BP are comparable to those of one of the BPs presented in the table in figure 3.1b. The plasmon wavelength calculated here is nevertheless blue-shifted compared to that BP. We also note that the calculated sensitivity here is higher, but it lies within the range of values of the sensitivities of the BPs in the table. Taking the value of $\Gamma = 50\,\mathrm{nm}$ from table 3.2 at $n = 1.33$, we arrive at a value of 9.1 for the FOM. This value is high compared to the value of 4.2 for the most similar BP in the table in figure 3.1b. It is also higher than any of the values tabulated by Mayer and Hafner [8] (table 3 in the article). We note that the values of Γ used to calculate FOM in those tables were determined by ensemble measurements in solution. The values of Γ are therefore larger due to NP dispersion and lead to lower values of FOM. This highlights the interest of single-NP measurements.

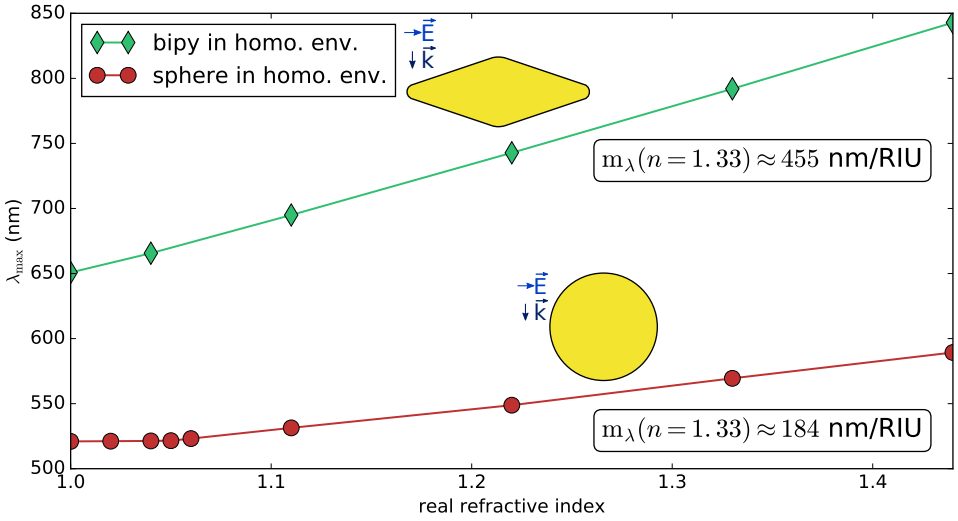

Figure 3.7: Plot of $\lambda_{\max}$ vs n from figure 3.6. The shift of the plasmonic peak is approximately linear. The sensitivity m_λ has been calculated for both shapes at $n = 1.33$.

3.2.1.2 Surface Effects

To check if this apparent greater sensitivity is expected in a "real" system, a second comparison has been made between a sphere and a BP on a glass substrate in air and in water (figure 3.8). Again, a greater change is observed when moving from air to water for the BP. We may compare the sensitivities of the objects on the substrate to those in a homogeneous medium to see if the substrate has a significant impact on the sensitivity. We find $m \approx 51/0.33 \approx 155$ nm $\cdot$ RIU^{-1} for the sphere and $m \approx 137/0.33 \approx 415$ nm $\cdot$ RIU^{-1} for the BP. The effect of the substrate is to decrease the bulk sensitivity of the sphere by 16 % and of the BP by 9 %. The effect is thus relatively weak.

The presence of the substrate has little influence on Γ for either shape. For the BP, Γ on the surface in air ($n = 1$) is 40 nm, which is only 2 nm wider than Γ of the BP in a homogeneous environment of air (table 3.2). In the presence of water ($n = 1.33$), Γ is approximately 50 nm with or without the substrate. The FOM thus lies between 8.3 and 10.4 and is only slightly affected by the presence of the substrate, which should therefore not impede sensing applications.

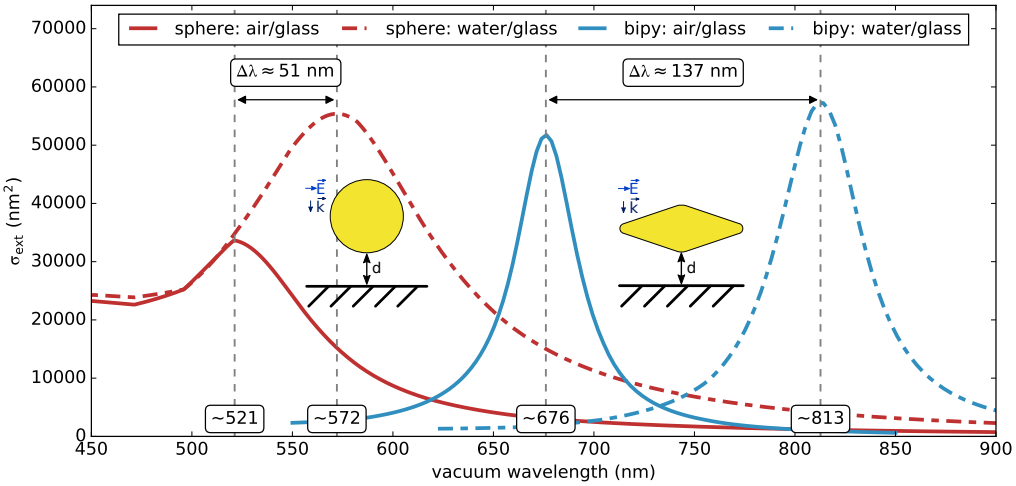

Figure 3.8: Extinction cross-sections of a gold sphere of radius 50 nm and a gold BP of length 100 nm and width 30 nm with rounding radius 5 nm at $d = 2$ nm from a glass surface in air and in water. Compared to the sphere, the BP's LSPR peak shifts significantly further to the red for the same change in medium yet broadens much less. [GMT and FEM calculations]

3.2.1.3 From Bulk To Local Sensitivity

A target analyte near a functionalized BP is expected to bind to the BP's surface and thus change the effective index around it. To investigate the influence of analytes near a BP, we consider an ideal spherical molecule with a radius of 3 nm and a RI of 1.42 [10] [11]. In a first approximation, such a system may be modeled as a film around the BP on a glass surface in water to get a rough estimate of the effect and the feasibility of detecting it with SMS. We use a film of thickness of 3 nm and a real RI of $n = 1.42$, where the thickness is equal to one radius of the ideal molecule to give a conservative estimate of imperfect surface coverage[12]. This results in a shift of nearly 10 nm (figure 3.9), which should be easily measurable with the LSMS setup.

Due to their elongated morphology, the field enhancement around the BP should also display high anisotropy. The influence of an analyte near the object is therefore expected to depend significantly on its relative position, as it does for nanorods (see supporting

[10] This is comparable to avidin and streptavidin with a conservative estimate of the RI[121–123].

[11] To determine the induced shift of the LSPR in the following simulations, the response must be calculated in the presence and absence of the sensing targets. However, adding sensing targets to the base model changes its meshing. To avoid possible effects of differential meshing, each shift was determined by first adding the targets to the base model and then simulating their absence and presence by changing the target's RI. This allows the comparison to be made between equivalent meshes.

[12] For simplicity, the system has been modeled with a uniform film around the object, which would not occur with an object on a substrate.

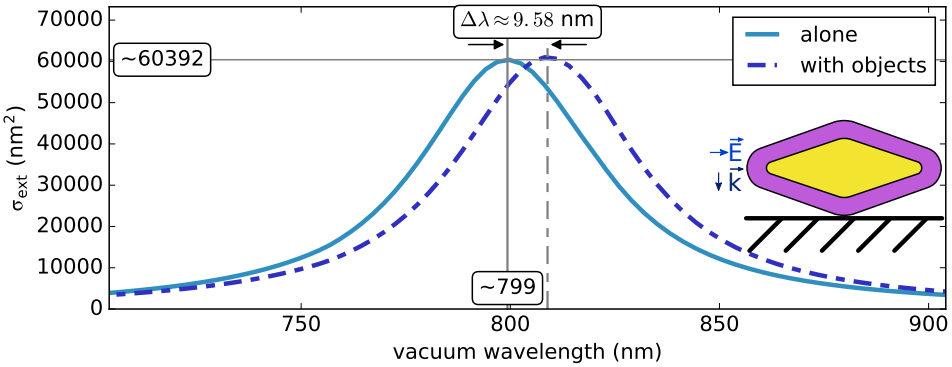

Figure 3.9: Extinction cross-sections of a gold BP of length 100 nm and width 30 nm with rounding radius 5 nm in water ($n = 1.33$) at a distance of 3.02 nm from a glass substrate ($n = 1.5$) in the absence and presence of a 3 nm thick "film" of objects with a real RI of 1.42.[FEM calculations]

information for Ament et al. [117]). In the case of a BP on a glass substrate, there may also be orientation effects depending on how the BP lies on the surface. The field enhancements have therefore been studied in two orientations as shown in figure 3.10. In the first orientation (figure 3.10a), the BP lies flat on along the surface with its longitudinal axis parallel to the substrate. In the second (figure 3.10b), it has been tilted by 15° to lie with one tip against the surface and the other raised in the air. In both cases, the effects of the morphology on the field enhancement are apparent: the field is enhanced by over 2 orders of magnitude near the tips along the longitudinal axis. These regions are called "hot-spots". This enhancement is about 25 times greater than that seen for a sphere (the field enhancement around a sphere, shown in figure 1.11 on page 45, is about a factor of 5) and so the BP is expected to be more sensitive to targets near the tips.

Interestingly, these calculations show that the enhancement near the tips are nearly unaffected by the orientation except in the region where it is confined between the substrate and the lower tip of the tilted BP. Tilting the BP induces a LSPR shift of only approximately 7 nm. This is less than the shift of 21 nm induced by the substrate itself in water (compare the LSPR in water at 792 nm in a homogeneous environment in figure 3.5 and table 3.2 and at 813 nm in the presence of the substrate in figure 3.8) and comparable to the shift induced by the film in figure 3.9. Regardless, sensing applications only rely on the shift induced by the refractive index change in the presence of an analyte, which the previous calculations show to be nearly linear and thus unexpected to be affected by the initial offset due to the orientation.

Different orientations have been reported in the literature: atomic force microscope (AFM) studies by Burgin et al. [104] found that the BPs lie tilted on a glass substrate whereas 3D-electron-tomography studies by Pertreux et al. [35] found that the BPs lie flat on a carbon substrate. Pertreux et al. [35] surmise that this discrepancy may be due

to differences in synthesis and surfactant coating or object-substrate interactions. They also note that the orientation only plays a minor role on non-absorbing substrates. We therefore use the flat orientation in the following simulations for convenience.

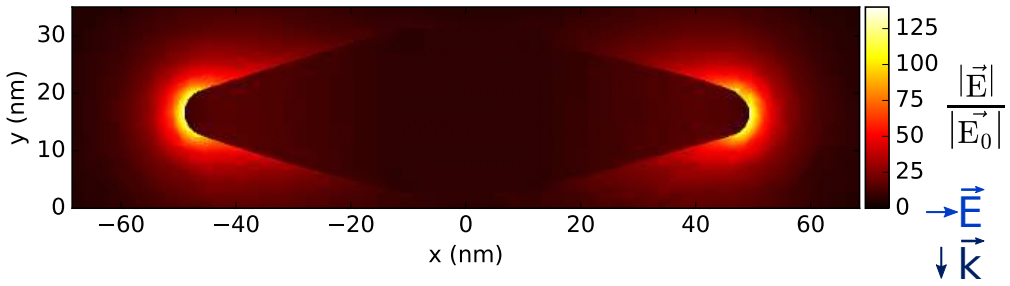

(a) flat, $\lambda_{\text{lspr}} \approx 813\,\text{nm}$

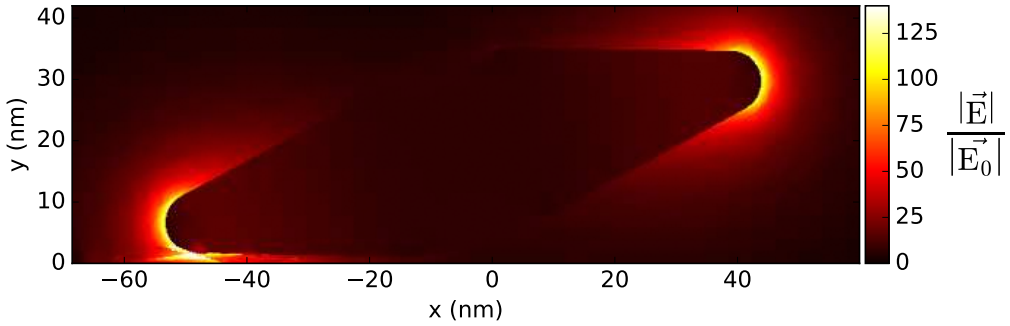

(b) tilted, $\lambda_{\text{lspr}} \approx 820\,\text{nm}$

Figure 3.10: The relative enhancement of the electric field around a gold BP of length 100 nm and width 30 nm with rounding radius 5 nm at the LSPR wavelength in water 2 nm above a glass substrate as a function of the orientation. Tilting the BP by 15° greatly enhances the field (∼400x) in the space between the lower tip and the substrate while elsewhere it remains comparable to that of the flat bipyramid. The relative enhancement is shown with the same scale in both images for comparison. The LSPR peak of the flat BP is ∼813 nm while that of the tilted one is ∼820 nm. [FEM calculations]

Simulations may also be used to determine if the "hot-spots" are indeed more sensitive to the local environment than other regions around the BP. Figure 3.11 shows the results of placing 14 objects of radius 3 nm and real RI 1.42 in different regions around the object. In the first arrangement, 7 objects have been placed at a distance of 1 nm from each tip, with 6 in a circle and one along the longitudinal axis. In the second, 7 objects have been placed in a semi-circle at 1 nm from the surface and 35 nm from each tip. The orientation of the semi-circle leaves a gap between the BP and the substrate to account for steric hindrances.

Comparing the two, the arrangement with the objects around the tip induces a shift that is an order of magnitude greater than the other, which shows that the BP's LSPR is indeed

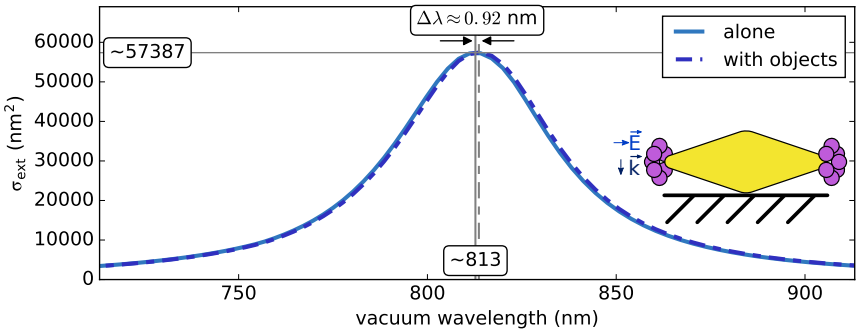

(a) near tip

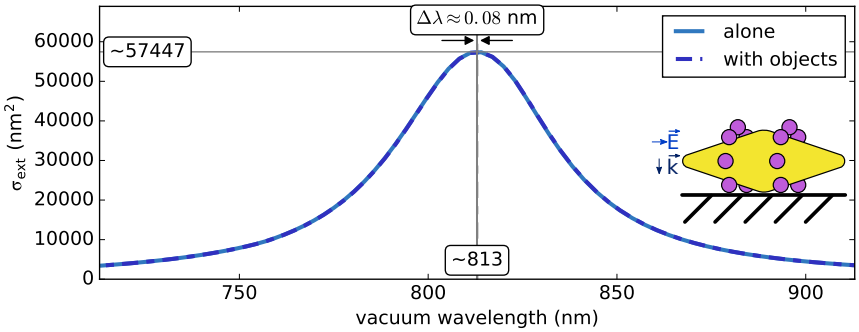

(b) near waist

Figure 3.11: Extinction cross-sections of a gold BP of length 100 nm and width 30 nm with rounding radius 5 nm in water ($n = 1.33$) at a distance of 2 nm from a glass substrate ($n = 1.5$) in the absence and presence of 14 discrete objects. The objects are of radius 3 nm with a real RI of 1.42. The surface-to-surface distance between the objects and the gold bipyramid is 1 nm. (a) 7 objects are aligned around each tip: 6 in a full circle and 1 along the longitudinal axis of the bipyramid. (b) 7 objects are regularly distributed along a circle at 35 nm from each tip with a gap left between the bipyramid and the glass substrate where an object would not fit. [FEM calculations]

more sensitive to changes near the "hot-spots", as predicted. This shift is nevertheless itself an order of magnitude less than that calculated with the uniform film, but the volume of the 14 objects is also an order of magnitude less and also further away from the object. The relative shift remains important and promising for biosensing applications and BPs. We will discuss approaches for detecting such minute shifts in the conclusion at the end of the dissertation.

Given the dependency of the sensitivity on the location of the objects near the BP's surface, we nevertheless note that it would not be possible to quantify the amount of analyte for a given shift. It may be possible to overcome this limitation with site-directed functionalization, which would restrict analyte binding to a given area of the surface[124, 125]. The magnitude of the shifts would then provide quantitative information about the

quantity of bound analyte.

3.2.2 Synthesis

The method of BP seed-mediated synthesis used in this work has been described previously.[32, 34] Briefly, spherical polycrystalline gold seeds are synthesized by the reduction of $HAuCl_4$ (250 µM) in a 10 ml aqueous solution of cetyltrimethylammonium chloride (CTAC) (200 mM). The solution is stirred under ambient temperature and 600 µL of a freshly prepared 100 µM solution of $NaBH_4$ at 4 °C is added drop by drop. As the seeds are formed, the solution will change from orange to brownish yellow. Stirring is then stopped and the solution is left to age in the dark at 40 °C for several days.

To grow the seeds into BPs, a growth solution is prepared by adding 40 µL of aqueous $HAuCl_4$ (25 mM) to 4 ml of a 45 mM aqueous solution of cetyltrimethylammonium bromide (CTAB). The solution is then vigorously stirred while sequentially adding 35 µL of $AgNO_3$ (5 mM), 60 µL of hydroxyquinoline (HQL) (400 µM in ethanol) and finally a volume of the previously synthesized seed solution. The solution is then stirred for 25 s and stored in the dark at 40 °C for 45 min, after which the BPs are washed 3 times by centrifugation to remove excess CTAB and then resuspended in water.

The critical parameter is the volume of the seed solution added to the growth solution. The variations in the spectra seen in figure 3.3 were obtained by varying the seed solution volume from 25 µL to 200 µL. Smaller volumes produce longer BPs with higher aspect ratios due to the greater availability of gold salt for growth, which leads to red-shifted LSPR peaks. As the number of seeds in the grown solution is increased, the number of BPs will increase but they will be shorter with lower aspect ratio and thus blue-shifted.

For further variability, it is possible to use a mixture of CTAC and CTAB instead of just CTAB. Both are surfactants which stabilize the seeds and BPs in solution but with CTAC's lower affinity for the gold surface, it is possible to obtain longer and thinner BPs with LSPR peaks over a broader range (e.g. figure 3.12). Using this approach, Chateau et al. [34] have recently reported on the synthesis of highly elongated BPs, or "javellins".

Seed synthesis is the most sensitive step in the production of BPs. The purity of the reactants, the rate of reduction with $NaBH_4$, the temperature and the pH of the solutions must all be carefully controlled to obtain polycrystalline seeds. The quality and purity of the seeds determines the quality and purity of the BPs that can be produced. With our current synthesis protocol we obtain BP yields of 95 % on average.

Several BP-based samples were initially prepared for the new LSMS setup using the same techniques as for "classic" SMS: spin-coating, precipitation and evaporation. In addition to the problems discussed in section 2.3.2 (e.g. the loss of objects when immersing the

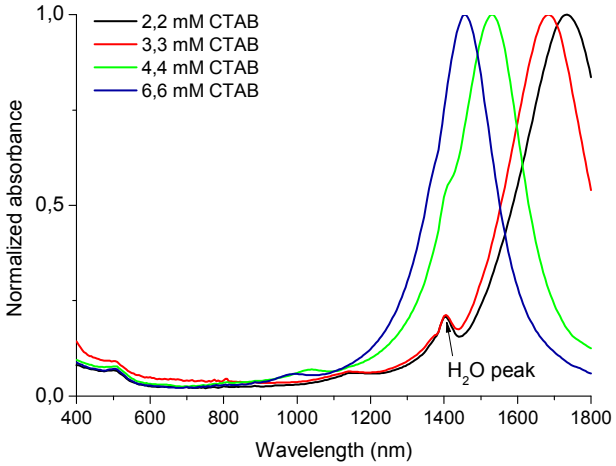

Figure 3.12: Effects of CTAB concentration on the LSPR of synthesized BPs for a CTAC concentration of 140 mM. Source: Chateau et al. [34]

sample in water), a further impediment was discovered with BPs: after several days, the extinction spectrum of studied objects would diminish and disappear as if the BP had lost its shape. This was confirmed with TEM microscopy, in which it was observed that the studied BPs had become irregular clumps (figure 3.13). It was therefore determined that a robust method of sample preparation would be necessary to stabilize both the location of objects on the sample and the anisotropic morphology of the objects in the absence of surfactant.

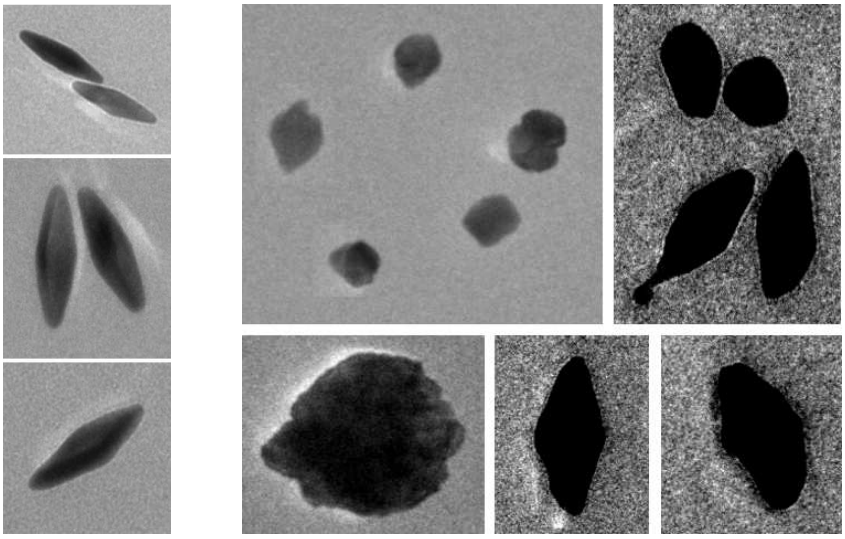

(a) before **(b)** after

Figure 3.13: TEM images of BPs deposited on a glass substrate by precipitation, before and after optical studies. The BPs were about 100 nm by 30 nm.

3.2.3 Silanized Sample Preparation

Silanization is a technique for immobilizing NPs on a substrate and has been reported previously[56, 126]. A protocol was developed to produce stable samples using silanized glass substrates to overcome the problems encountered with classically prepared samples. The goal has been to produce samples of gold nano-objects and BPs in particular that remain firmly fixed to the sample when immersed and removed from a liquid environment. In addition to attaching the objects to the surface, the silanes also stabilize the morphology of anisotropic gold nanoparticles and thus acts as a surrogate for the surfactants on the NPs in suspension.

3.2.3.1 Silanization Protocol

An overview of the process is presented in figure 3.14. The surface treatment is performed in several 15 min steps in an ultrasound bath at 40 °C. First, the 10 mm × 10 mm × 0.5 mm glass slides are washed in a DFT4 detergent (5 % Gigapur) in order to "activate" their surface with the formation of OH groups. The excess DFT4 is then rinsed twice with distilled water, once with acetone to remove the remaining water, and finally once with methanol to prepare the surface for the next step.

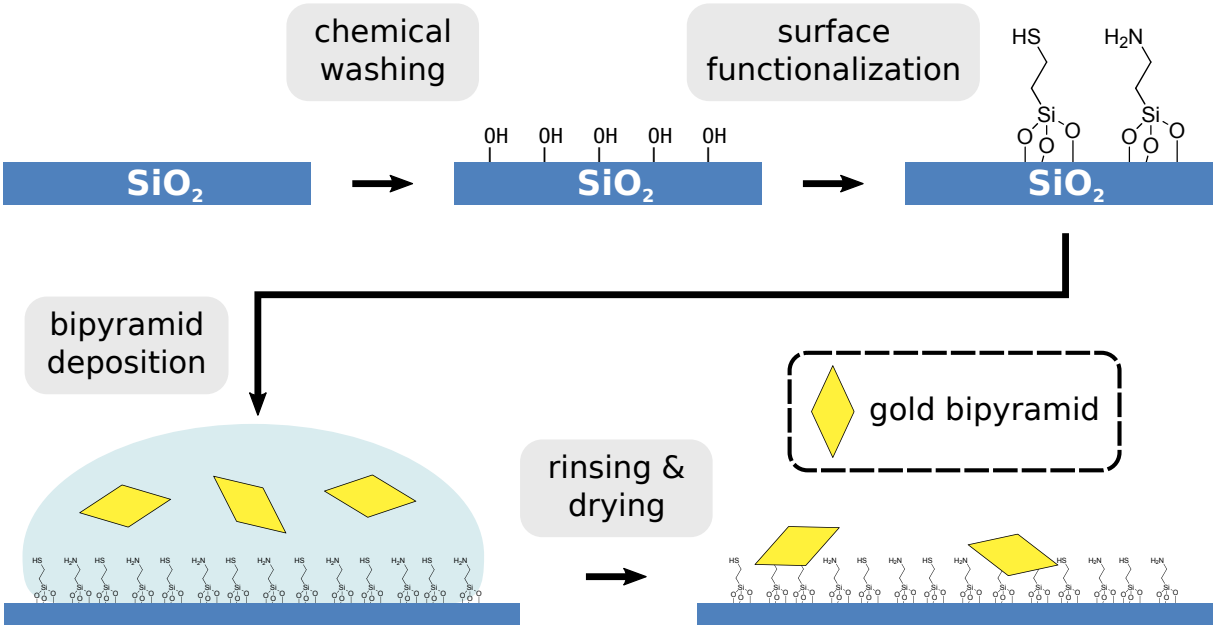

Figure 3.14: Schematic overview of the production of samples with gold BPs grafted to a glass substrate via silanes.

The clean substrates are then transferred to glass pill jars which prevent them from resting

flat on a surface. The slides are immersed in a methanol-based silane solution (5 % N-(2-aminoethyl)-3-aminopropylmethyldimethoxysilane (95 %), 5 % 3-mercaptopropylmethyldimethoxysilane (95 %)) and incubated at 45 °C for 60 min. The solution is then removed and the slides are rinsed 3 times with methanol to remove excess silanes before being dried at 120 °C for 30 min.

The BPs are then grafted to the silanized surface as follows: 50 µL of a diluted BP solution prepared as described above is spread evenly over the glass substrate and left to stand for 5 min before rinsing vigorously 3 times with distilled water. The slide is then placed in a fresh pill jar, either with or without water, until it is mounted on the LSMS setup.

3.2.3.2 Initial Tests And Difficulties

Several iterations of the protocol were necessary to reliably produce suitable samples for LSMS. After each iteration, the samples were studied using LSMS and low-vacuum (1 Torr H_2O vapor) scanning electron microscopy (SEM) to determine their properties and identify which parameters of the protocol should be changed to improve the produced samples.

Figure 3.15 shows several SEM images of early samples produced with the protocol that were unsuitable for further study. One of the main challenges was obtaining suitable BP densities for SMS measurements. As figures 3.15a and 3.15b show, initial samples were very dense with large clusters of BPs deposited together. The density was adjusted by varying the concentration of BPs in the solution before grafting as well as the time of reaction.

Another issue was that of surfactant crystallization and deposition which greatly affected the optical properties of the sample. This was extensive in initial studies, as shown in figures 3.15c and 3.15d. Better results were obtained by using Tween as the surfactant instead of CTAB in the BP solution during grafting, which permitted greater dilutions to be used due to the higher reactivity of Tween-stabilized BPs. Other impurities have sometimes appeared on the sample which we were unable to identify, such as the strange crystals in figures 3.15e and 3.15f. These were only observed once and their origin remains unclear.

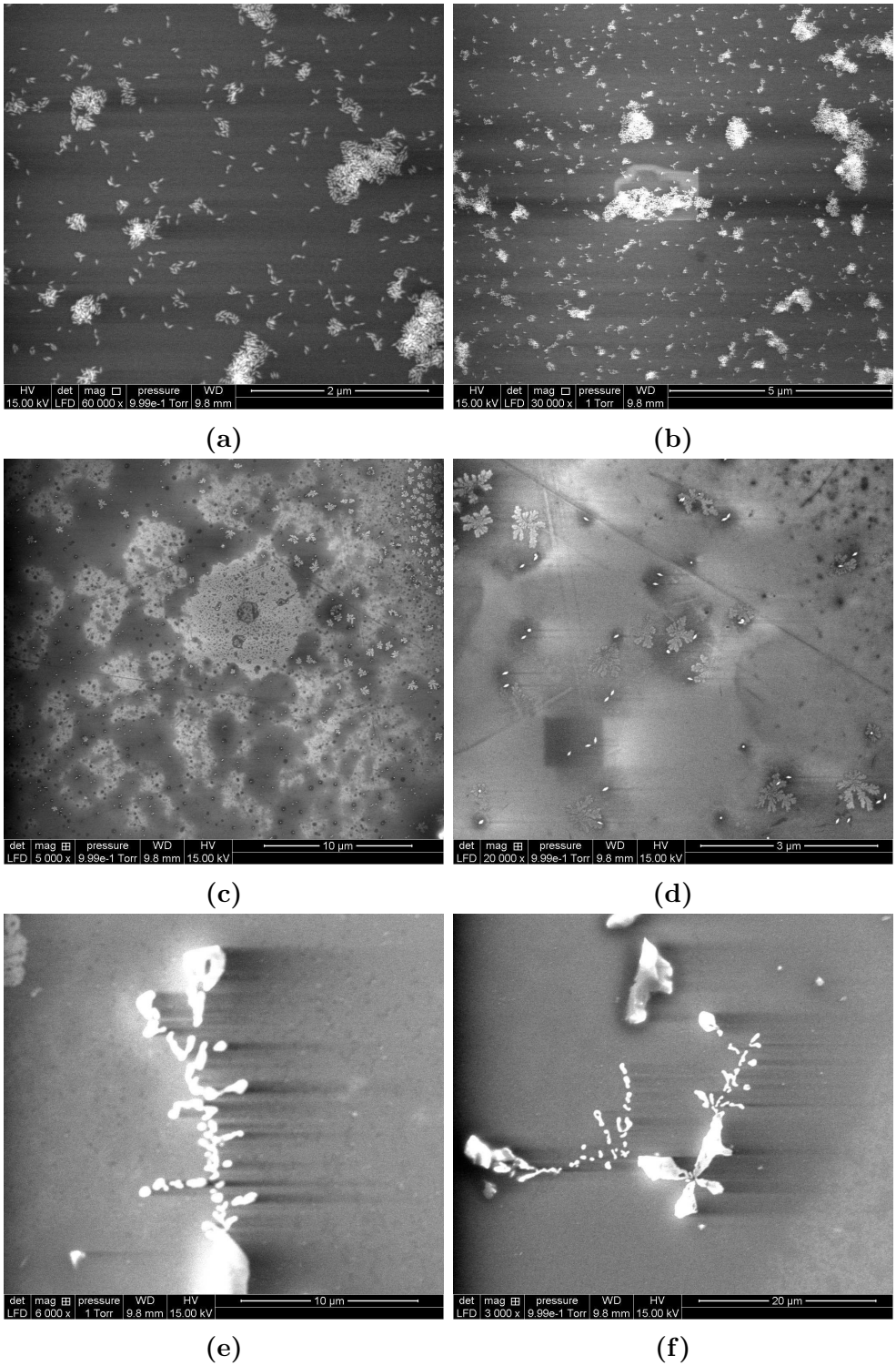

Figure 3.15: SEM images of silanized samples showing a number of issues encountered with early samples. (a) & (b) Density is too high. (c) & (d) Large deposits of what is believed to be crystallized surfactant. (e) & (f) Unidentified deposits.

In addition to these deposits, excess silanes sometimes remained on samples prepared with earlier versions of the silanization protocol. Figure 3.16 shows the SEM image of an early silanized sample of gold spheres with a radius of approximately 100 nm (the same spheres as in section 2.3.1). The excess silanes appear as slightly darker patches in the image that extend over 10s of microns.

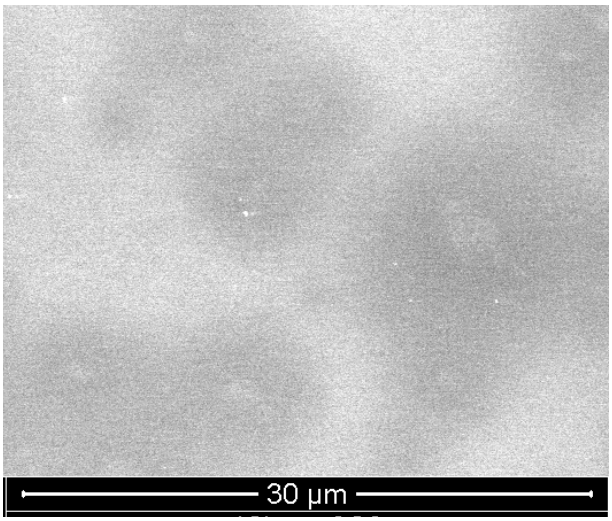

Figure 3.16: SEM image of a silanized sample of gold nanospheres of 100 nm. Excess silanes appear as dark patches.

After imaging with SEM, a microscope grid was attached to the sample with silver lacquer and the sample was mounted on the LSMS setup to be studied in air. Because the grid was attached after SMS imaging, it was not possible to locate the zone shown in figure 3.16. The zone in that image was nevertheless representative of the entire sample. The camera and focusing objective were used to obtain an optical image of the sample[13], which is shown in figure 3.17 along with the SMS DC and X/DC maps of the same zone. A constellation of 4 contaminants is marked with red circles to aid orientation. Green circles mark the location of gold sphere monomers and yellow circles mark the location of gold sphere dimers. Marked objects that are not visible in a given image have been indicated with a dashed circle.

The dark spots in the camera image and the DC map are unidentified contaminants. These are likely viscous residues that exhibit lensing effects due to surface tension. The silanes are weakly visible in the camera image as darker patches. Their presence is also responsible for the rugosity that we see in the image. The silanes are also visible in the DC map as dark patches with the same extension as we observed in the previous SEM image. The silanes are nevertheless not visible in the X/DC map of the same zone.

[13]By placing a lamp between the collecting objective and the focal lens of the spectrometer (figure 2.12), the sample can be illuminated from behind and imaged with the objective that normally focuses light on the sample. This image can be viewed with the CCD camera and captured by the computer.

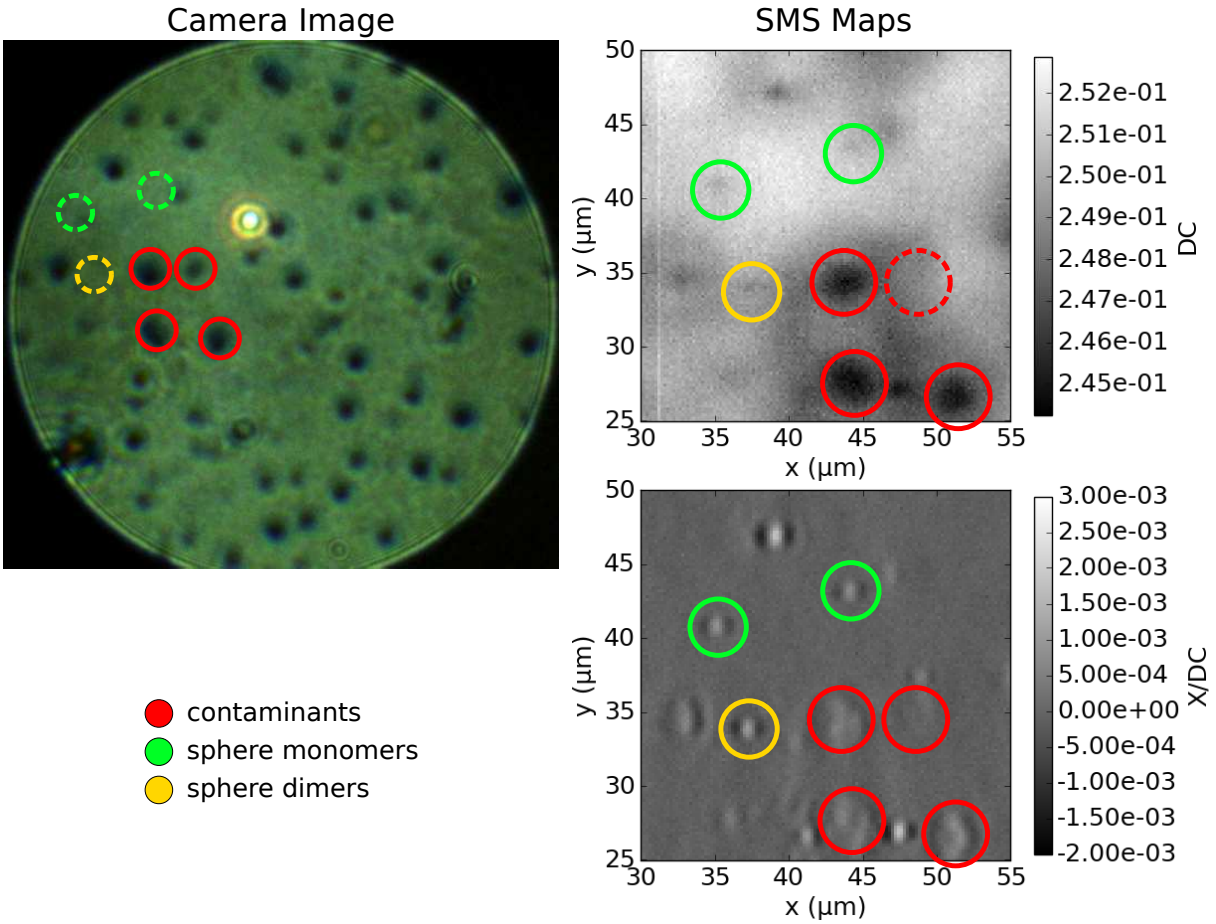

Figure 3.17: Correlated camera images and SMS DC and X/DC $(2f)$ maps of the same zone. This is not the same region of the sample shown in figure 3.16.

The spatial variation of the silane patches is low enough that they do not generate a signal when working at $2f$ (see section 2.1.2 for details) and therefore do not disturb SMS measurements.

Two monomers and a dimer have been marked in the SMS map. These objects are just barely visible in the DC map as light spots. We note that they cannot be seen in the optical image. To confirm that the SMS measurements at $2f$ are indeed unperturbed by the excess silanes, the spectra of several objects were studied. A representative spectrum of a single nanosphere is presented in figure 3.18. The spectrum is in very good agreement with the theoretical Mie spectrum and the effective RI is around the value that we normally find for a sphere of this size on a glass substrate in air, which shows that excess silanes do not impede the measurements.

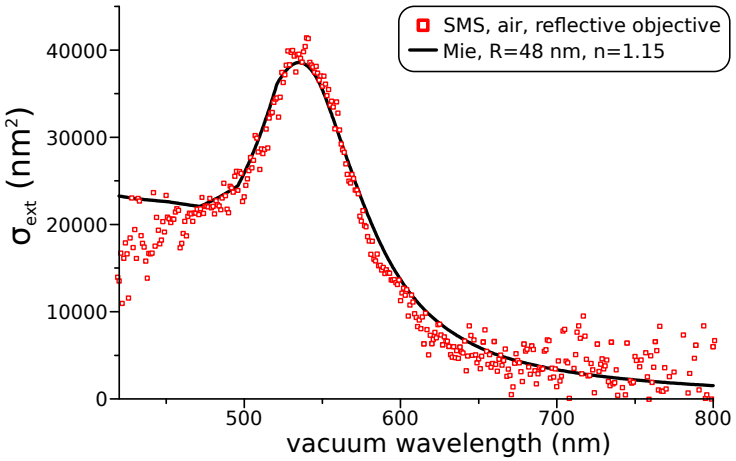

Figure 3.18: Calibrated SMS spectrum of a gold nanosphere with a radius of approximately 50 nm on a silanized substrate. A theoretical spectrum has been calculated with Mie theory to match the spectrum.

Despite the ability to work around the rugosity of the silane layer, the protocol was further modified to rinse the excess and unreacted silanes from the substrate with methanol 3 times after grafting. With this additional step, the resulting surfaces no longer displayed any visible rugosity due to the silane layer. Using this most recent version of the protocol, it is possible to reliably obtain optically clean samples of suitable density for LSMS samples as shown figure 3.19.

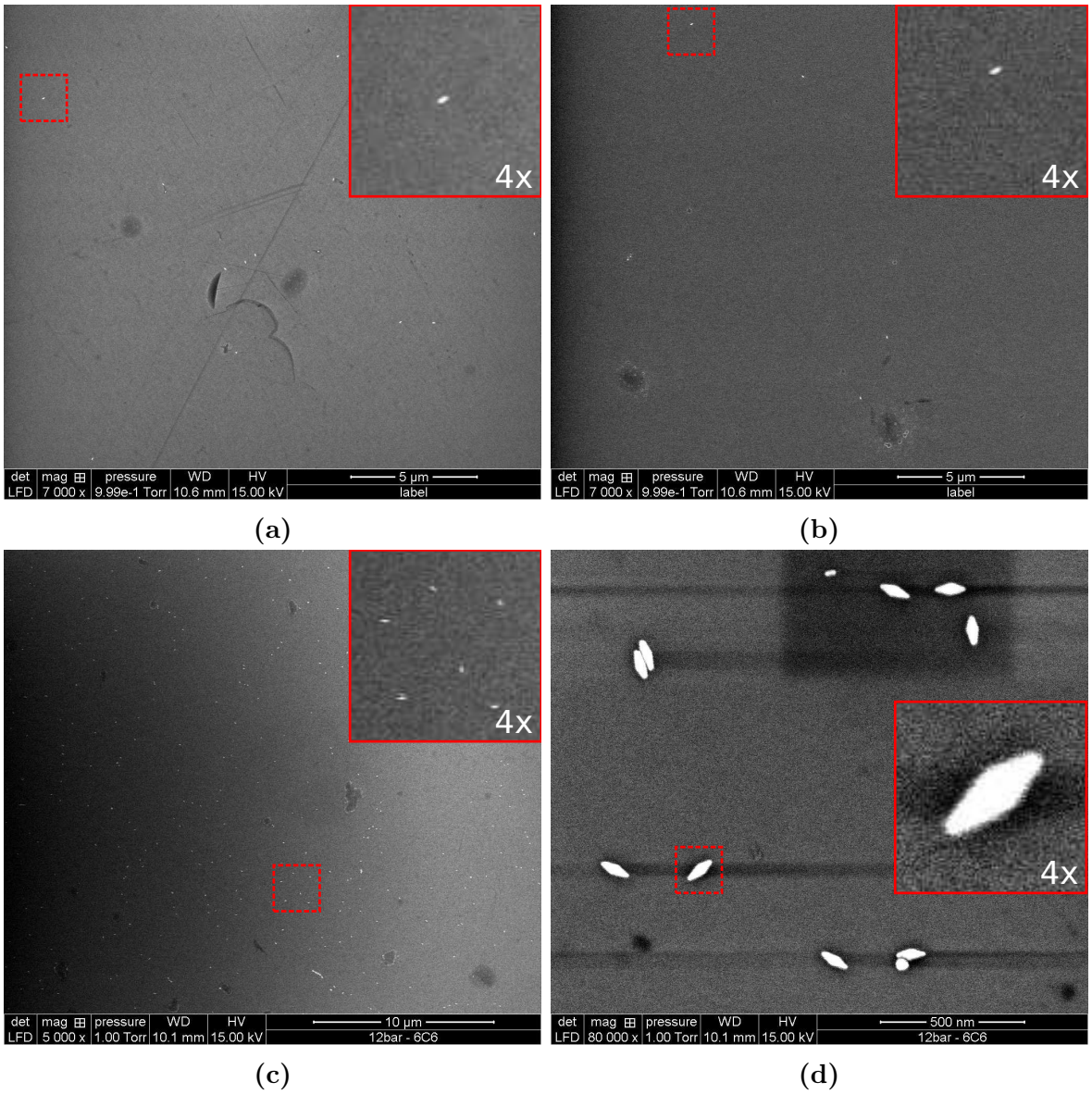

Figure 3.19: SEM images of silanized samples after refinement of the sample preparation protocol. The samples are optically clean with suitable densities of BPs for SMS measurements. (a) & (b) Lower density. (c) Higher density. (d) The samples contain mostly monodisperse, isolated bipyramids.

3.2.3.3 Effects Of Silanization On The Optical Response

Grafting a NP to a surface via silanization modifies the local environment of the NP. A test was therefore performed to determine if silanization modifies the LSPR response of the grafted object or its sensitivity to the local environment. Spheres were chosen for this test because they are a model system that can easily be compared with Mie theory.

A sample was prepared using the silanization protocol and the same gold nanospheres described in section 2.3.The sample was studied with SEM prior to the optical study to locate zones of interest with unique nanospheres at a suitable density. Numerous unique spheres where located (figure 3.20) along with groups of objects ranging from dimers to tetramers.

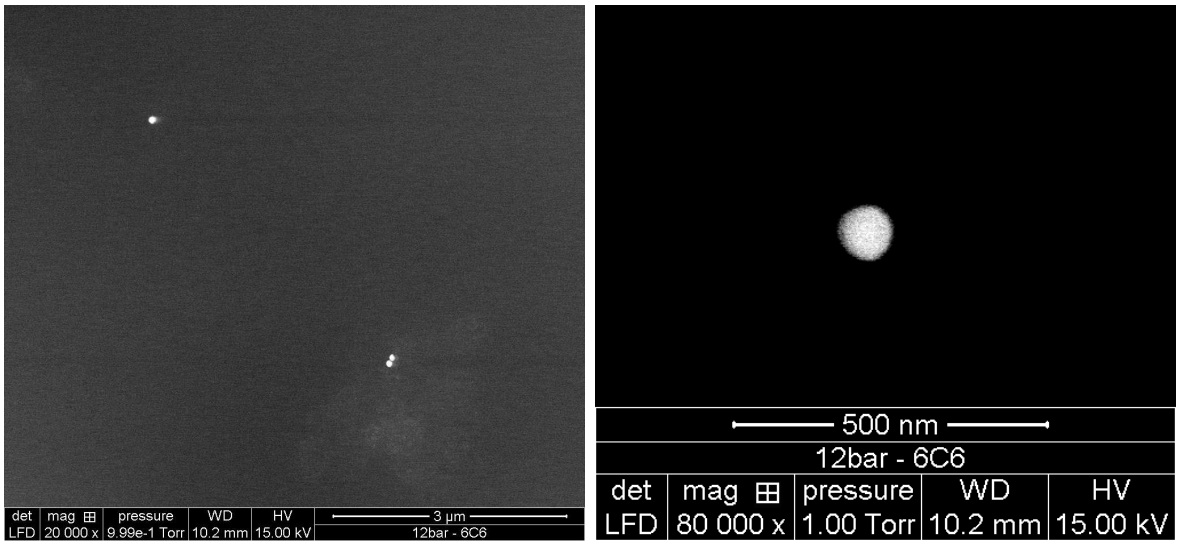

Figure 3.20: SEM images of the second sample of deposited gold nanospheres. The deposition was made using the silanization technique described in section 3.2.3.

The sample was then mapped in air at 540 nm and water at 570 nm (figure 3.21). In both cases the spatial oscillation was affected by the stage with an amplitude of 400 nm at 136 Hz and the GAPO objective (see section 2.2.2) was used to focus on the sample. Despite the sub-optimal conditions for the objective, the air map shows relatively high resolution with low background noise and shows that this objective can be used under these conditions with careful configuration. As expected, the map in water is clearer with a stronger signal due to the conditions more closely resembling the design conditions of the objective.

The maps present recognizable constellations of objects that allow the identification of unique objects under both conditions. Green circles have been drawn around a subset of common constellations in figure 3.21 to aid orientation. Red triangles mark objects that appear on the map in air but are absent in water. Two of these objects were automatically tracked and measured in air. The spectra confirm that they were both gold spheres. A blue rectangle also marks 4 objects that appear to have slightly moved between mappings. Despite these discrepancies, most of the objects remain stably grafted to the sample, which shows that the silanization is effective.

A number of objects were selected for study in air and then restudied in water to compare their response in both environments. Unlike the previous sample of nanospheres, several

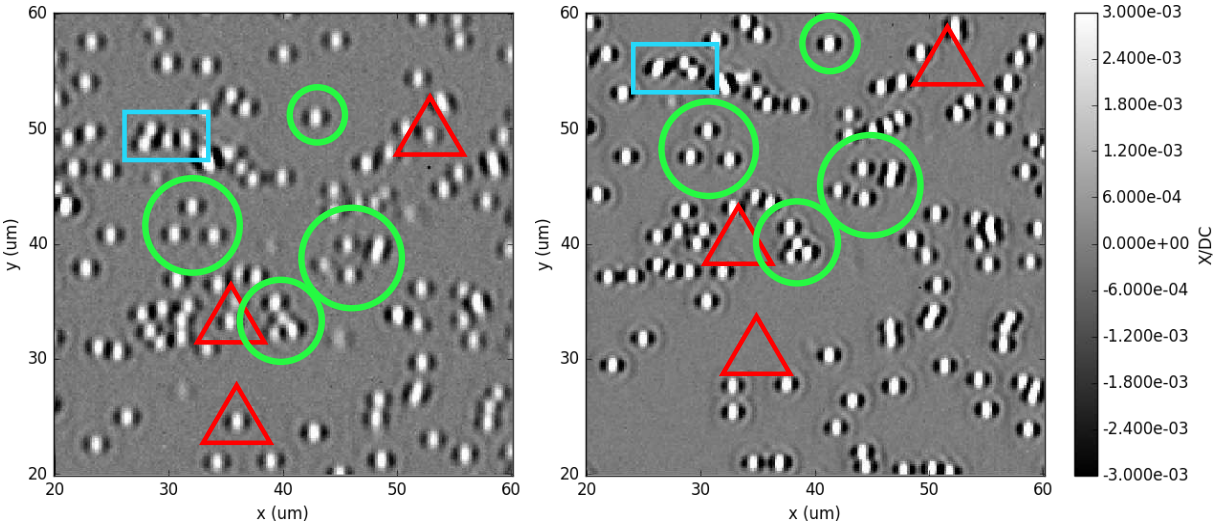

Figure 3.21: Maps of silanized gold sphere sample in air and water. The spheres are 100 nm and are the same as those previously discussed in section 2.3.2. The sample was mapped at 540 nm in air and at 570 nm in water.

objects were identified as unique gold nanospheres of about the expected size via their characteristic optical spectra with a clear interband region and a plasmonic peak between 530 nm and 550 nm.

The calibrated spectra of a representative object under both conditions are shown in figure 3.22. The spectra have been calibrated using the calibration curves described in section 2.3.2.6. Manually fitted Mie spectra of a sphere in a homogeneous environment have been plotted alongside the empirical spectra. The agreement between the curves is good in both cases and appears to indicate a change in n_{eff} of approximately 0.25. Given the discussion of cumulative effects in section 1.3.2.5, a change in n_{eff} of less than 0.33 is expected. The values of n_{eff} are higher than the theoretical model of a sphere on a substrate (see section 1.3.2.1), which likely indicates the influence of additional factors such as the presence of silanes, surfactants and spherical imperfections, although the relative contribution of each is indeterminable in this case. Nevertheless, these factors do not seem to significantly impact the relative shift when moving from air to water.

The shift of 45 nm is very close to the shift of 51 nm between air and water predicted by the theoretical model of a sphere on a substrate in figure 3.8. Taking $\Delta n = 0.33\,\text{RIU}$, the measured sensitivity is $135\,\text{nm} \cdot \text{RIU}^{-1}$, which is close to the theoretical sensitivity of $153\,\text{nm} \cdot \text{RIU}^{-1}$.

Looking at it another way, we may consider the sensitivity in terms of the change in n_{eff}: $m = \Delta\lambda/\Delta n_{\text{eff}} = 45\,\text{nm}/0.25\,\text{RIU} = 190\,\text{nm} \cdot \text{RIU}^{-1}$. This value is also close to the value of $184\,\text{nm} \cdot \text{RIU}^{-1}$ predicted by the model of a sphere in a homogeneous environment in figure 3.7.

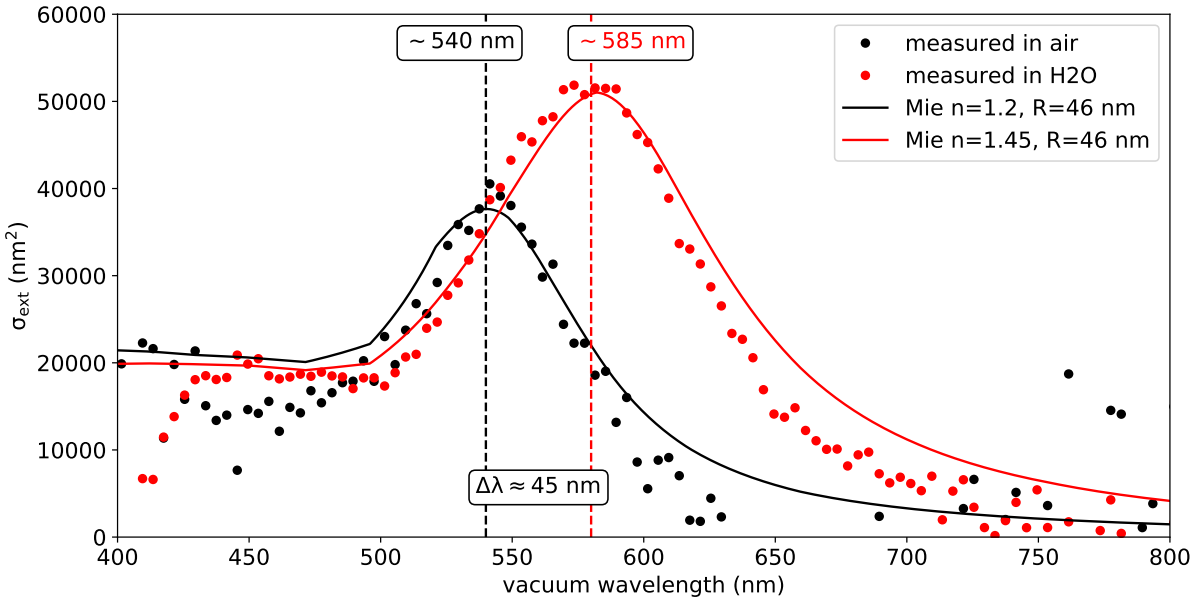

Figure 3.22: Extinction cross-section of a single gold sphere on a glass substrate in solution measured by LSMS. Calculated spectra for a gold sphere of radius 46 nm in a homogeneous environment of $n = 1.2$ and $n = 1.45$ are also shown. The radius and values of n were chosen via a manual fit. [GMT calculations]

Measurements of other spheres on the sample yielded equivalent results. We conclude that silanization does not impede SMS measurements and that the measured objects are able to correctly report changes in the RI of the local environment. These samples should therefore be suitable for sensing applications.

3.3 Experimental Investigations

The tests with the silanized sample of gold spheres shows that the sample is stable in water and that the silanization does not noticeably affect the grafted probe's sensitivity. Following these tests, silanized samples of gold BPs were prepared to probe RI changes in different media to determine the sensitivity of the BP samples and their robustness. The following tests were performed in parallel with work to improve the silanization protocol. Sample B was prepared with the current version of the protocol that includes the extra rinsing step to remove the excess silanes. The other samples were prepared with a previous version that lacked this step.

The samples were placed in different media (air, water, glycerol, water+glycerol mixes) to observe the influence of the RI on the BP's LSPR and thus determine the bulk sensitivity of the sample. To test the stability and robustness of the silanized BPs, further tests

were performed to determine if the optical response would remain constant under fixed conditions irrespective of the sample's history (e.g. the response in air before and after immersion in water).

In the following sections, the raw X/DC spectra are presented instead of calibrated spectra because we are primarily concerned with detecting spectral shifts. The ability to detect a shift with the SMS setup depends entirely on the ability to detected shifts in the raw data. While the calculated magnitude of any detected shift is expected to be slightly larger than the raw shift due to the general form of the calibration curves (figure 2.28 on page 121), calibration only introduces a constant factor for each data point. To determine the spectral position of the LSPR peaks, the raw spectra were fit to Cauchy-Lorentzian curves in the frequency domain using a least-squares algorithm, which is valid for such objects in the region away from the interband transitions[25, 35, 38, 127, 128].

3.3.1 Bulk Sensing

Detecting refractive index changes in the surrounding medium (bulk sensing) is the first step towards validating probes for more precise sensing applications. Several tests were therefore performed with media of different RI to determine the sensitivity of the fabricated samples. The results of these studies are presented in the following sections.

3.3.1.1 Sample A: Air, Water and Glycerol

A silanized sample was prepared with BPs on a glass substrate and a microscope grid was attached with silver lacquer to facilitate object localization. Despite being prepared before the additional washing step was added to the preparation protocol, SEM images of the sample showed no crystalline deposits (figure 3.23). Overall the sample was relatively clean but large contaminants are nevertheless visible in the SEM images (red rectangles). Most BPs on the sample occur as monomers but as the image shows, their density is limiting for SMS studies. Given the size of the spot, objects must be 1 µm to 2 µm apart to be able to measure the isolated signal of a single object.

Despite the average density, several objects occur without immediate neighbors and so the sample was mounted for study on the LSMS setup in an attempt to locate them. SMS maps of the sample such as the one in figure 3.24 confirm the SEM observations. The objects with the strongest response in the map are not BPs but rather uninteresting contaminants with broad spectra (not shown). The other objects are BPs but nearly all of them are indeed too closely spaced for SMS studies.

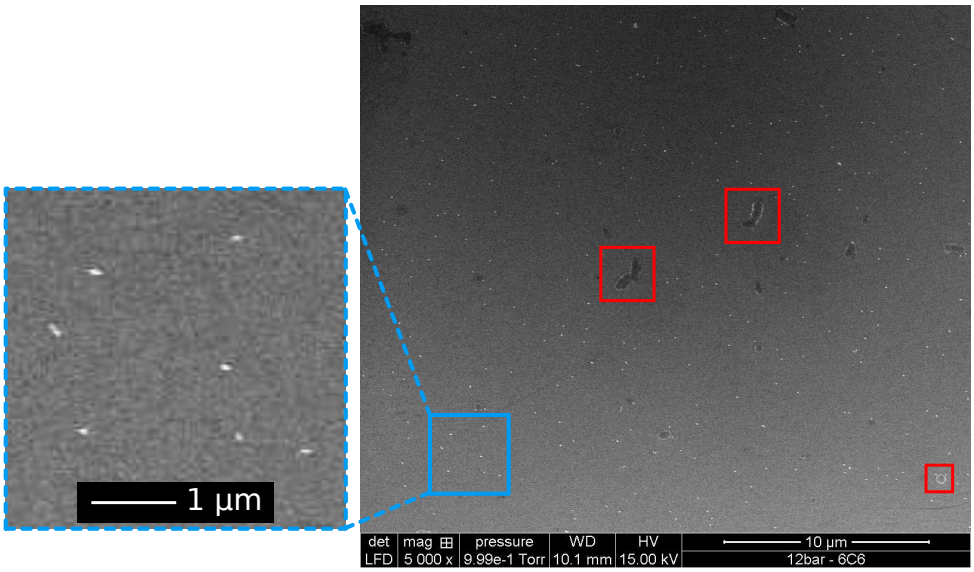

Figure 3.23: SEM image of a silanized BP/glass sample. There are no crystalline deposits but several large contaminants are visible. Some have been highlighted with red squares. Most objects on the sample are individual BPs but their density, highlighted in the zoomed window, was limiting for SMS studies.

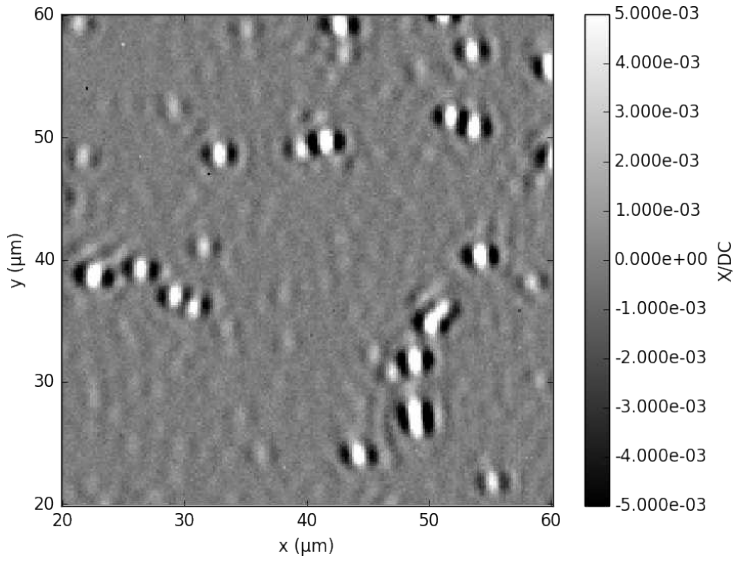

Figure 3.24: SMS map of the sample using the GAPO objective in air. The objects with the strongest response are contaminants. The objects with the weaker response are BPs. The z-scale has been adjusted to increase the contrast of the latter. The map confirms the density of the sample observed with SEM.

We therefore decided to explore other areas of this sample in an attempt to locate isolated

BPs. Several objects that yielded recognizable BP spectra were finally discovered and these were studied in air, in water and finally in glycerol ($n = 1.473$[129]).

The results of the measurements in these different media are shown in figure 3.25 where the wavelength of the LSPR peak has been plotted against the RI of the medium. The matching spectra are shown in figure 3.26. We note that the bumps that appear near 850 nm are due to dips in the Xenon lamp's intensity (see figure F.4 on page 243 of the appendix). Figure 3.25 confirms that the shift is roughly linear in n_{eff} over this range as discussed previously and that the transition from a local environment of water to glycerol was effective.

The determined sensitivity is approximately $168\,\text{nm} \cdot \text{RIU}^{-1}$ which is significantly lower than the theoretical value of $415\,\text{nm} \cdot \text{RIU}^{-1}$ calculated for the BP on a glass substrate (see figure 3.8 and related discussion). While this discrepancy may be due to a combination of factors such as differences in the real and modeled morphology of the object and various cumulative effects of the sample, it is nevertheless disappointing that the LSPR shift here (46 nm) remains comparable to both the empirical (45 nm) and theoretical (51 nm) shifts of the sphere seen in the previous sections. One possible explanation is that a larger portion of the BP's surface may be covered in silanes. For a BP with a width of 30 nm, half of the object's surface is within 15 nm of the substrate whereas for a gold sphere of diameter 100 nm, only 15 % of its surface area is within 15 nm of the substrate. Occupation of the probe's surface will reduce its sensitivity, especially around the hotspots. Given that this sample was prepared with a previous version of the silanization protocol that lacked the additional washing step, the presence of excess silanes is likely. The dispersion of the LSPR peaks in figure 3.26 may also indicate presence of a variable quantity of excess silanes in the local environment around each BP. Such results clearly show the need for samples of high quality.

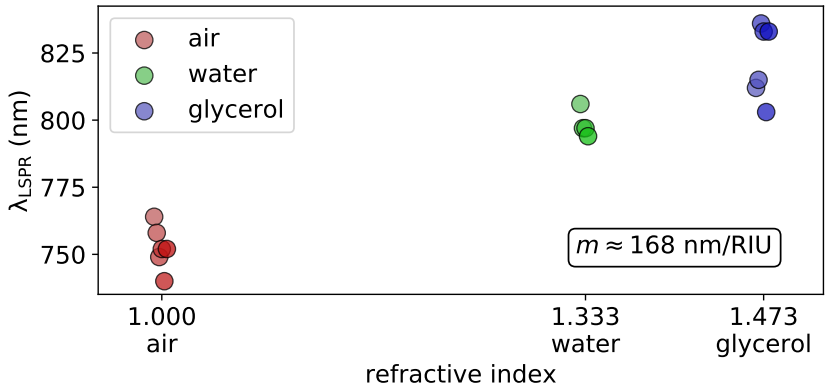

Figure 3.25: The position of the LSPR peak of several different BPs in air, water and glycerol. The matching spectra are shown in figure 3.26.

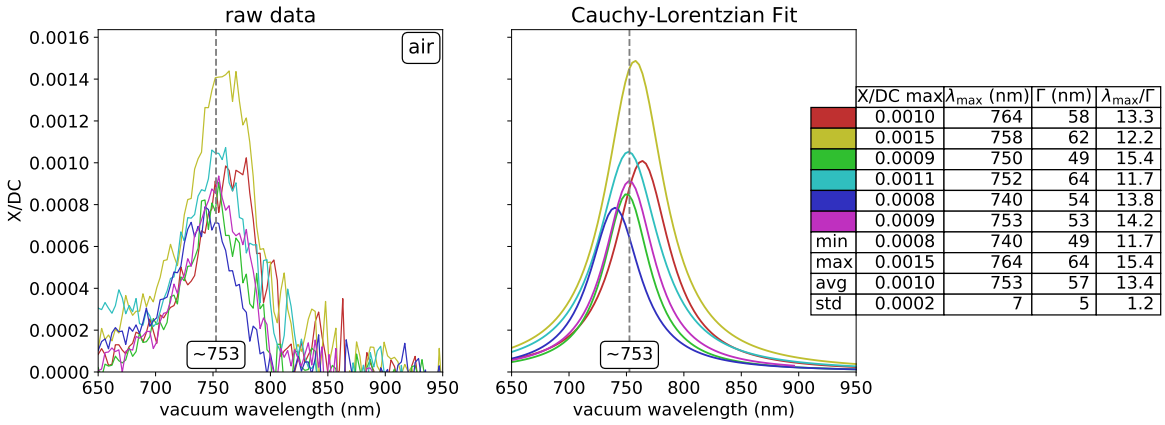

	X/DC max	λ_{max} (nm)	Γ (nm)	λ_{max}/Γ
	0.0010	764	58	13.3
	0.0015	758	62	12.2
	0.0009	750	49	15.4
	0.0011	752	64	11.7
	0.0008	740	54	13.8
	0.0009	753	53	14.2
min	0.0008	740	49	11.7
max	0.0015	764	64	15.4
avg	0.0010	753	57	13.4
std	0.0002	7	5	1.2

(a) air

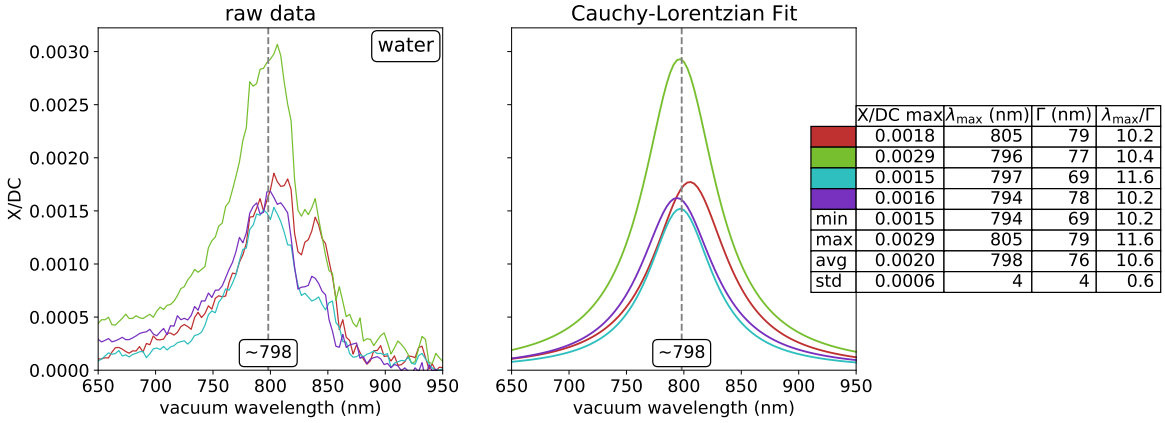

	X/DC max	λ_{max} (nm)	Γ (nm)	λ_{max}/Γ
	0.0018	805	79	10.2
	0.0029	796	77	10.4
	0.0015	797	69	11.6
	0.0016	794	78	10.2
min	0.0015	794	69	10.2
max	0.0029	805	79	11.6
avg	0.0020	798	76	10.6
std	0.0006	4	4	0.6

(b) water

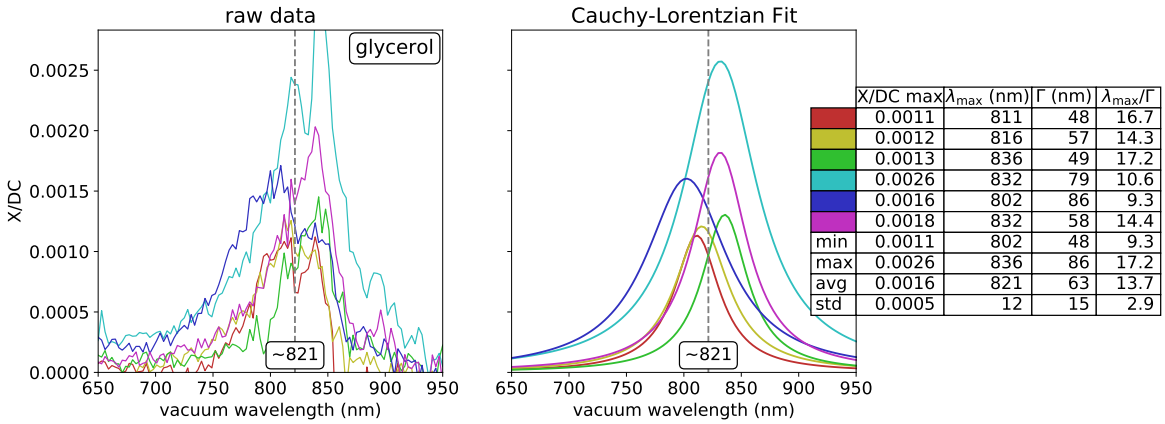

	X/DC max	λ_{max} (nm)	Γ (nm)	λ_{max}/Γ
	0.0011	811	48	16.7
	0.0012	816	57	14.3
	0.0013	836	49	17.2
	0.0026	832	79	10.6
	0.0016	802	86	9.3
	0.0018	832	58	14.4
min	0.0011	802	48	9.3
max	0.0026	836	86	17.2
avg	0.0016	821	63	13.7
std	0.0005	12	15	2.9

(c) glycerol

Figure 3.26: Spectra in (a) air, (b) water and (c) glycerol corresponding to figure 3.25. Left: raw spectra. Right: Cauchy-Lorentzian fits and tabulated parameters. The average LSPR wavelength is marked on the graph.

3.3.1.2 Sample B: Air, Water and Water+Glycerol Mixes

After modifying the silanization protocol to include the additional washing step to remove excess silanes, new samples were prepared with BPs. SEM images of the sample (figure 3.27a) show that these samples were very clean with no visible rugosity or deposits of silanes or surfactants. SEM images and SMS maps (figure 3.27b) show that the object densities were also suitable for SMS.

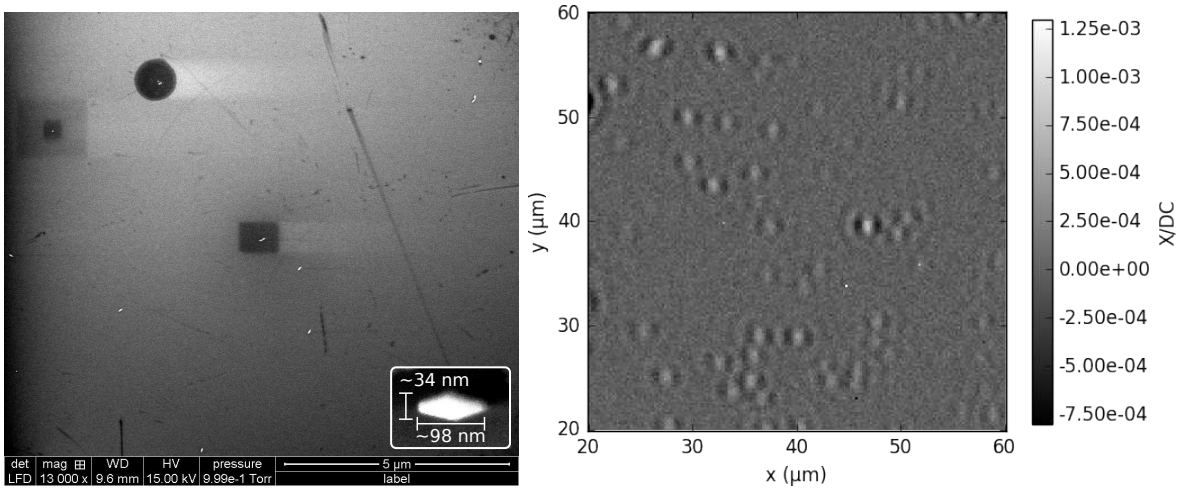

(a) SEM **(b)** SMS

Figure 3.27: SEM images and SMS map in air at 750 nm of the silanized bipyramid sample prepared after modification of the protocol to remove excess silanes. The sample is very clean with no visible depositions from the preparation. Dark rectangular areas are deposits from high-magnification scanning with the SEM. Dark lines and spots are blemishes on the glass surface.

Due to the improved density and stable optical properties of the sample, it was possible to locate and study the same objects in air, water and mixes of glycerol and water. Figure 3.28 shows maps of the 6 studied objects in air, glycerol and a 2:1 volumetric mix of water and glycerol ($n = 1.368$[129]). The maps clearly display the same distinctive constellation of objects with comparable signal. There is very little background noise in each map and the objects are suitably spaced for individual measurements. All studies were performed with the GAPO objective.

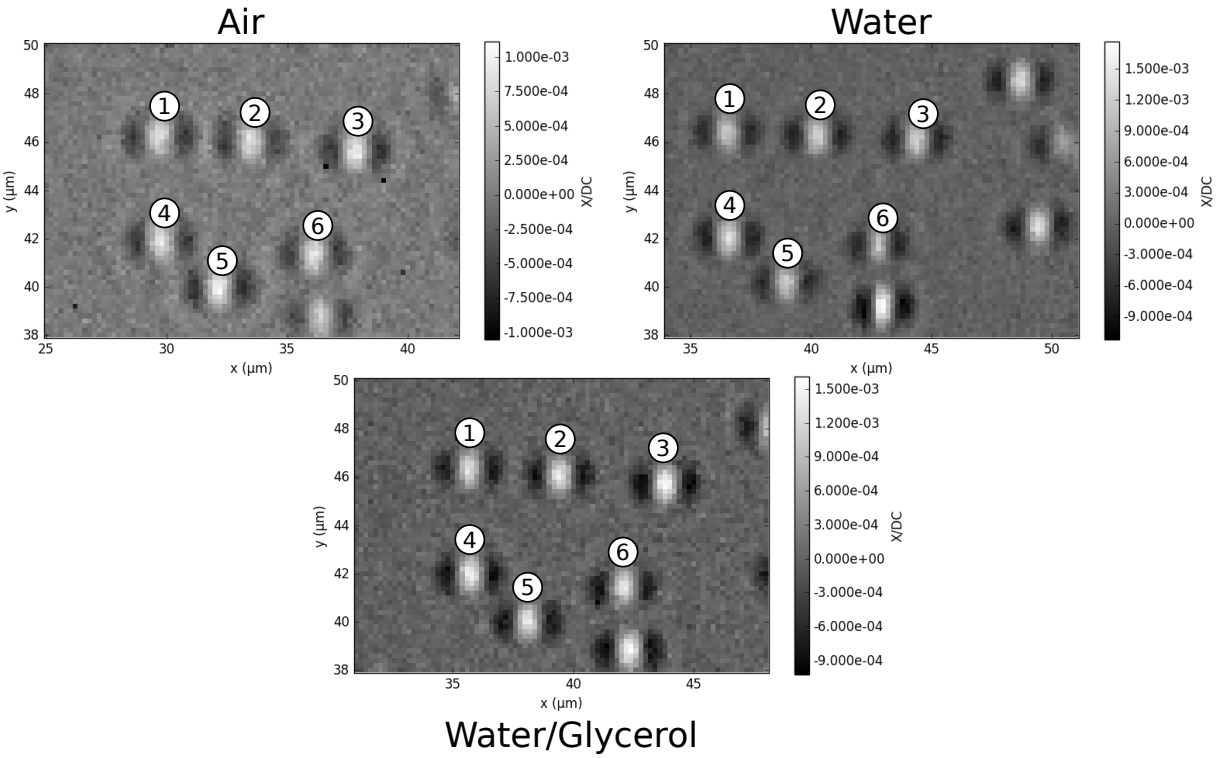

Figure 3.28: Maps of the sample showing the same 6 objects in air (725 nm), water (790 nm), and a 2:1 volumetric mix of water and glycerol (810 nm).

The LSPR peak wavelengths of each object are plotted against the refractive indices of each medium in figure 3.29 (the spectra are presented in figure 3.30). Moving from air to water induces an average red-shift of about 60 nm, which is slightly better than what was observed with sample A ($\sim$ 45 nm) presented in the previous study. Immersing the sample in the 2:1 volumetric mix of water and glycerol induces a further average change of about 8 nm. From these measurements, the sensitivity m is approximately $224\,\text{nm} \cdot \text{RIU}^{-1}$, which is an increase of 33 % over the sensitivity of the previous studiy with sample A. Sample B was optically cleaner than sample A due to the extra washing step, which also removed excess silanes. The improved sensitivity may thus be a confirmation that the reduced sensitivity of sample B was in part due to the silanes' occupation of the probe surface.

The FWHMs of the spectra in air and in water is given for both samples in table 3.3. The average values differ by only $\sim$ 3 % in water but by about $\sim$ 10 % in air. Using the average value in air, we calculate FOM $\approx 168/57 \approx 2.9$ RIU^{-1} for the previous sample (A) and FOM $\approx 224/63 \approx 3.6$ RIU^{-1} for the current sample (B). Compared to the BPs in table 3.1b, we note that although the measured sensitivity of this sample is relatively low, the FOM is relatively high due to the narrower LSPR peaks of individual BPs.

Several other factors show that the quality of this sample is better than the previous

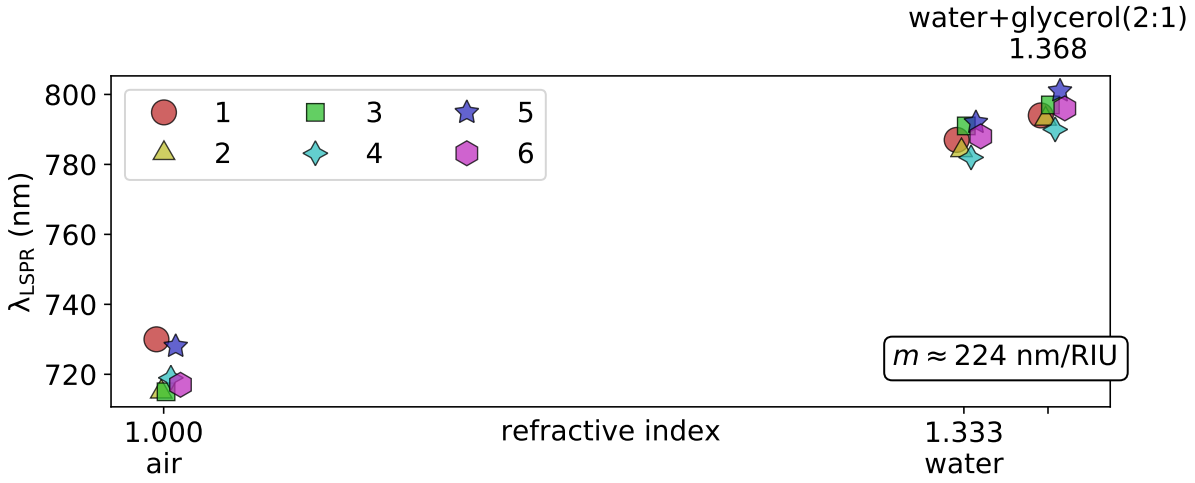

Figure 3.29: The spectral position of the LSPR peak of the labeled objects in figure 3.28 as a function of n under the same conditions. The RI of the 2:1 water+glycerol mix was calculated using values in Glycerine Producers' Association [129]. Corresponding spectra are shown in figure 3.30

sample: the relative average variation in FWHM of this sample is $(74-63)/74 = 15\,\%$ compared to $(76-57)/76 = 25\,\%$ of the previous one; the standard deviation of Γ is lower for this sample by a factor of 2; the variation in $\lambda_{\max}/\Gamma$ is lower by a factor of 3-4. The reduced dispersion of sample B is attributed to the removal of the excess silanes and shows that the quality of the sample is crucial for sensing applications. We note that the spectral dispersion in air in figure 3.29 is likely due in part to residual wetting which would explain why the dispersion is reduced when the sample is immersed in liquid. We also note that relative spectral positions of the 6 objects to each other show much less variation when moving from water to the water+glycerol mix.

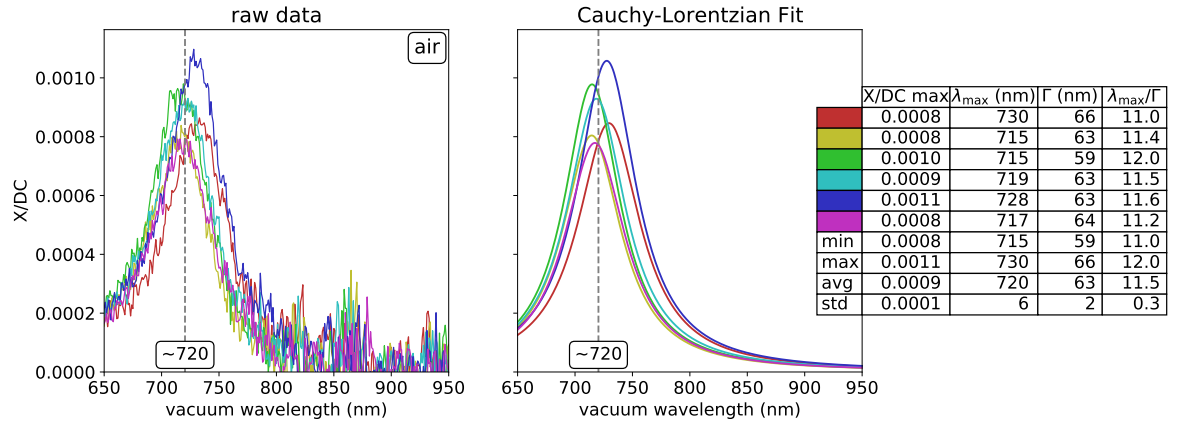

	X/DC max	λ_{max} (nm)	Γ (nm)	λ_{max}/Γ
	0.0008	730	66	11.0
	0.0008	715	63	11.4
	0.0010	715	59	12.0
	0.0009	719	63	11.5
	0.0011	728	63	11.6
	0.0008	717	64	11.2
min	0.0008	715	59	11.0
max	0.0011	730	66	12.0
avg	0.0009	720	63	11.5
std	0.0001	6	2	0.3

(a) air

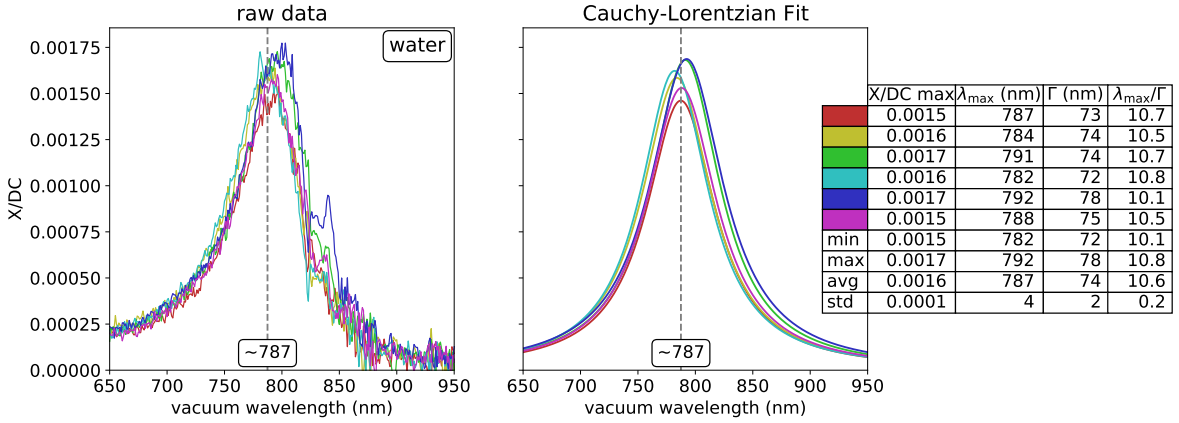

	X/DC max	λ_{max} (nm)	Γ (nm)	λ_{max}/Γ
	0.0015	787	73	10.7
	0.0016	784	74	10.5
	0.0017	791	74	10.7
	0.0016	782	72	10.8
	0.0017	792	78	10.1
	0.0015	788	75	10.5
min	0.0015	782	72	10.1
max	0.0017	792	78	10.8
avg	0.0016	787	74	10.6
std	0.0001	4	2	0.2

(b) water

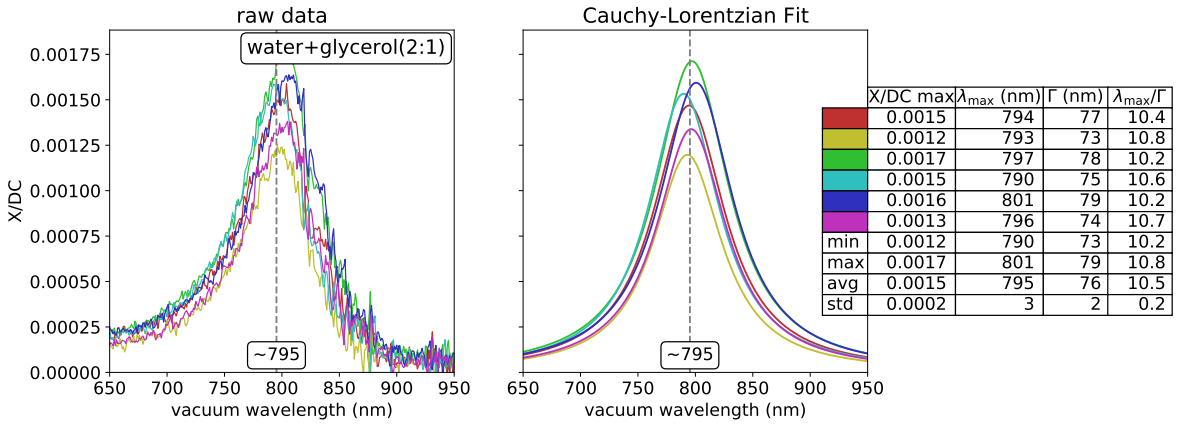

	X/DC max	λ_{max} (nm)	Γ (nm)	λ_{max}/Γ
	0.0015	794	77	10.4
	0.0012	793	73	10.8
	0.0017	797	78	10.2
	0.0015	790	75	10.6
	0.0016	801	79	10.2
	0.0013	796	74	10.7
min	0.0012	790	73	10.2
max	0.0017	801	79	10.8
avg	0.0015	795	76	10.5
std	0.0002	3	2	0.2

(c) 2:1 volumetric mix of water and glycerol

Figure 3.30: Corresponding spectra for the objects in figure 3.29. Left: raw spectra. Right: Cauchy-Lorentzian fits and tabulated parameters. The average LSPR wavelength is marked on the graph.

	air		water	
sample	A	B	A	B
figure	3.26a	3.26b	3.30a	3.30b
Γ	49 53 54 58 62 64	59 63 63 63 64 66	69 77 78 79	72 73 74 74 75 78
average Γ	57	63	76	74
standard deviation of Γ	5	2	4	2
standard deviation of λ_{max}/Γ	1.2	0.3	0.6	0.2

Table 3.3: Comparison of the FWHMs (Γ) of the LSPR spectra from the previous (A) and current (B) sample in air and in water.

3.3.1.3 Sample B: Diffusion Of Glycerol

To investigate if the setup could be used to measure changes over time, an unmeasured volume of glycerol was injected into the bottom of the fluid cell with a syringe, as indicated in figure 3.31. Glycerol is very viscous and diffuses slowly in water. As it diffuses, it gradually increases the RI of the solution. To measure this gradual change, the Multi-Instrument Controller and Automator (MICA) interface software was used to automatically track and measure objects repeatedly over a period of 24 hours. The spectral shifts are plotted in figure 3.31. To enable easier comparison of the objects, the relative shift of each is plotted instead of the peak wavelength. After about 4 hours the spectra noticeably red-shift but also become noisy due to gradual defocalization throughout the study. The defocalization is in part due to the diffusion of the glycerol which changes the RI of the medium and thus the focal distance of the objective. It may also be due in part to a gradual shift of the focal alignment of the setup (e.g. due to thermal drift). The signal strength is plotted below the spectral shifts in figure 3.31. At first sight, the shift in the wavelength appears to be correlated with the loss of signal strength, but manually re-optimizing the focalization and measuring object 4 shows that the shift is real and not due to focalization effects (figure 3.32). The other objects were not remeasured.

Given a total shift of ∼17 nm for object 4 and $m \approx 224$ nm, we may estimate n of the medium as $1.368 + \Delta n = 1.444$. According to the values in Glycerine Producers' Association [129][14], this would indicate that the medium around the object is 84 % glycerol. This is of course a very rough estimate given that the initial volume was not measured, the

[14]The values for different mixes of water and glycerol have been measured experimentally and tabulated in Glycerine Producers' Association [129]. These values can also be calculated from the refractive indices of pure water and glycerol using the Lorentz-Lorenz equation with good approximation[19, 130, 131].

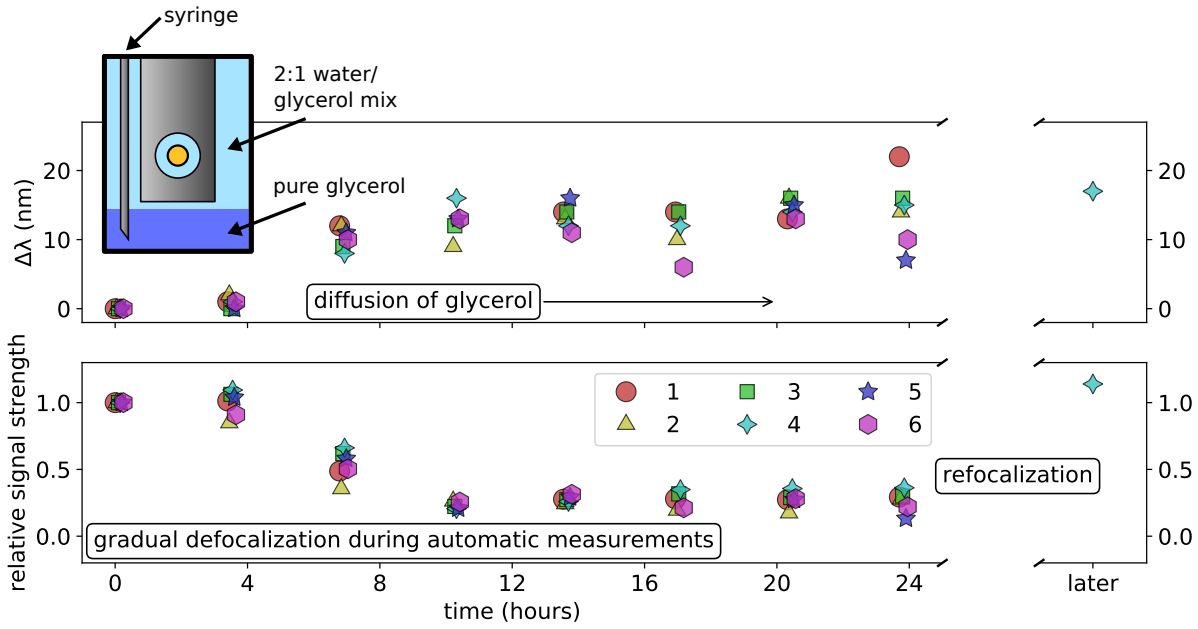

Figure 3.31: Evolution of the LSPR peaks of 6 gold BPs under the diffusion of glycerol. The initial solution contained a 2:1 volumetric mix of water and glycerol. Spectra of object 4 are presented in figure 3.32.

dissolution of the glycerol was imperfect under visual inspection, and the peak positions are not absolutely certain, but it is nevertheless realistic[15].

It is thus possible to study kinetics in a liquid environment with the LSMS setup and silanized BP samples. The MICA interface software is able to track objects on the sample over an indefinite period and regularly measure their spectra. Although we have tested this with bulk RI changes here, the same procedure would work for gradual changes in the concentration of an analyte over a shorter time period. The tracking interval used in this experiment was chosen as a function of the diffusion rate of glycerol: the spectra could just as well have been measured every few minutes[16].

These measurements are nevertheless not yet optimized. The gradual defocalization must be corrected to enable dynamic studies. One solution would be to add a computer-controlled objective mount to the setup to enable automatic refocalization of the object during tracking.

[15]Unfortunately we did not have the time to repeat this experiment with more rigorous controls.
[16]We will discuss ways to reduce this interval even further at the end of the dissertation.

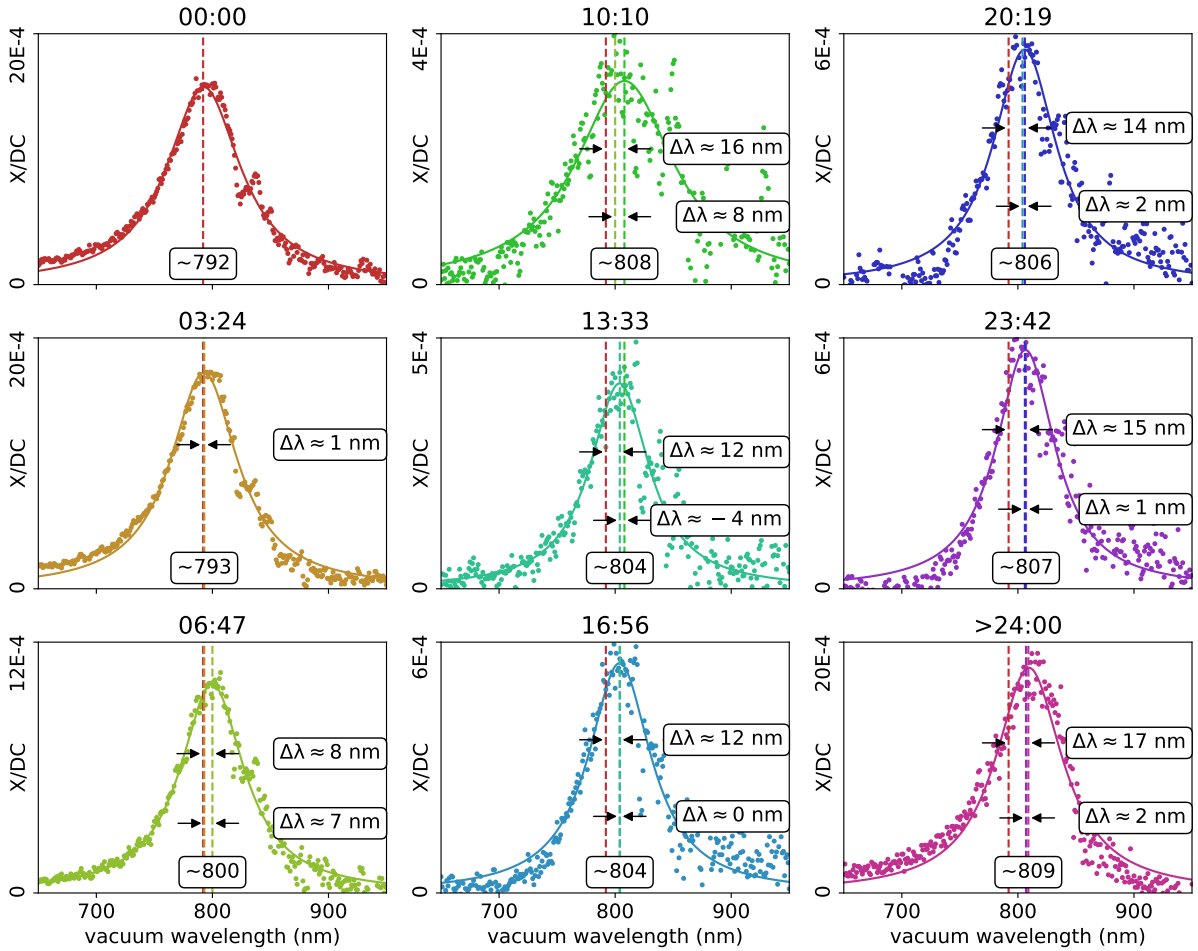

Figure 3.32: Corresponding spectra of object 4 in figure 3.31. $\Delta\lambda$ indicates the relative shift of the LSPR maximum from the first and the previous time point.

3.3.2 Sample Stability And Reusability

Aside from its sensitivity, the robustness and stability of a probe are important factors for biosensing applications. A probe should be reusable under conditions which are not expected to modify the probe and it should yield the same results under the same conditions for reliable measurements. It should also remain stable over time to permit storage. These properties are investigated in the following sections.

3.3.2.1 Sample C: Successive Measurements In Air And Water

A silanized sample of gold BPs was prepared before the protocol was modified to remove excess silanes. A microscope grid was fixed to the sample using silver lacquer and the

sample was imaged with SEM before mounting it on the LSMS setup for optical studies. As figure 3.33 shows, the sample appears clean without any visible crystalline deposits or rugosity despite using this earlier version of the protocol. The zoomed region to the left shows that the sample predominantly consists of isolated BPs with suitable spacing for SMS studies. Images of greater magnification of several BPs, one of which is presented in the inlay, showed that the BPs were around 80 nm × 30 nm and relatively monodisperse.

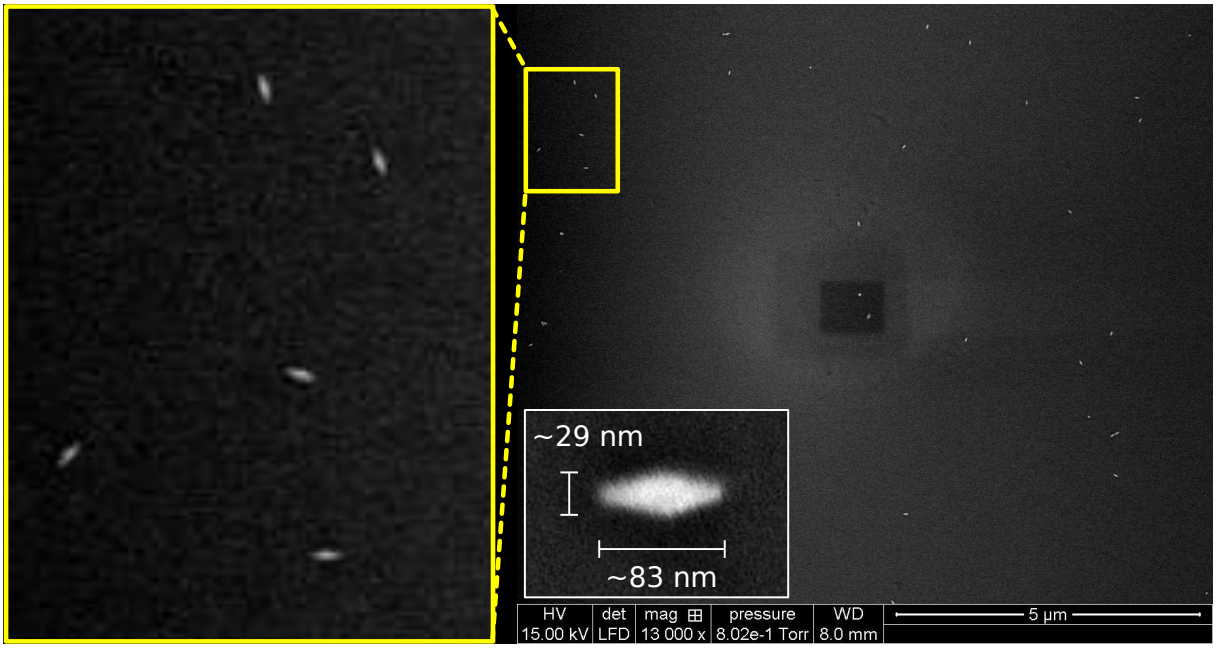

Figure 3.33: SEM image of silanized sample of gold BPs on a glass substrate before the optical study. The optical properties and density of unique BPs are suitable for SMS studies. The darker rectangular area at the center shows deposits from SEM scanning. A zoom of the image region outlined in yellow shows that the objects are unique BPs. Inlay: SEM image of an individual gold bipyramid with greater magnification.

The aim of this study was to determine if the sample would evolve under successive measurements in air and water. If the sample is stable and robust, we expect the red-shift induced when changing from air to water to be followed by an equal and opposite blue shift when returning to air. The spectra of the first air-water-air cycle are shown in figure 3.34 along with their Cauchy-Lorentzian fits. Moving from air to water induced an average red-shift of the LSPR peak of about 76 nm, which is comparable to the previous theoretical and experimental shifts. Moving back to air, a blue-shift of equal magnitude was expected but the observed shift was much weaker, leaving an average shift of 51 nm to the red relative to the initial study in air.

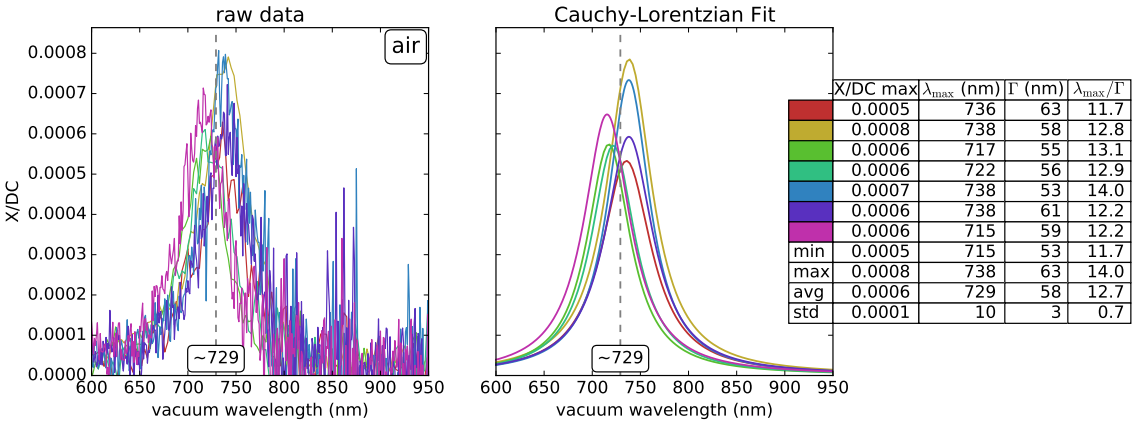

	X/DC max	λ_{max} (nm)	Γ (nm)	λ_{max}/Γ
	0.0005	736	63	11.7
	0.0008	738	58	12.8
	0.0006	717	55	13.1
	0.0006	722	56	12.9
	0.0007	738	53	14.0
	0.0006	738	61	12.2
	0.0006	715	59	12.2
min	0.0005	715	53	11.7
max	0.0008	738	63	14.0
avg	0.0006	729	58	12.7
std	0.0001	10	3	0.7

(a) first study in air

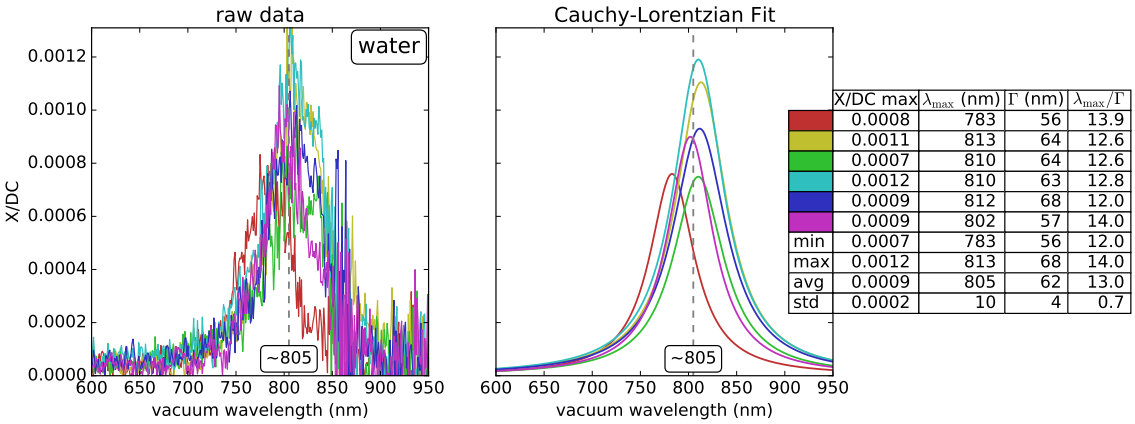

	X/DC max	λ_{max} (nm)	Γ (nm)	λ_{max}/Γ
	0.0008	783	56	13.9
	0.0011	813	64	12.6
	0.0007	810	64	12.6
	0.0012	810	63	12.8
	0.0009	812	68	12.0
	0.0009	802	57	14.0
min	0.0007	783	56	12.0
max	0.0012	813	68	14.0
avg	0.0009	805	62	13.0
std	0.0002	10	4	0.7

(b) first study in water

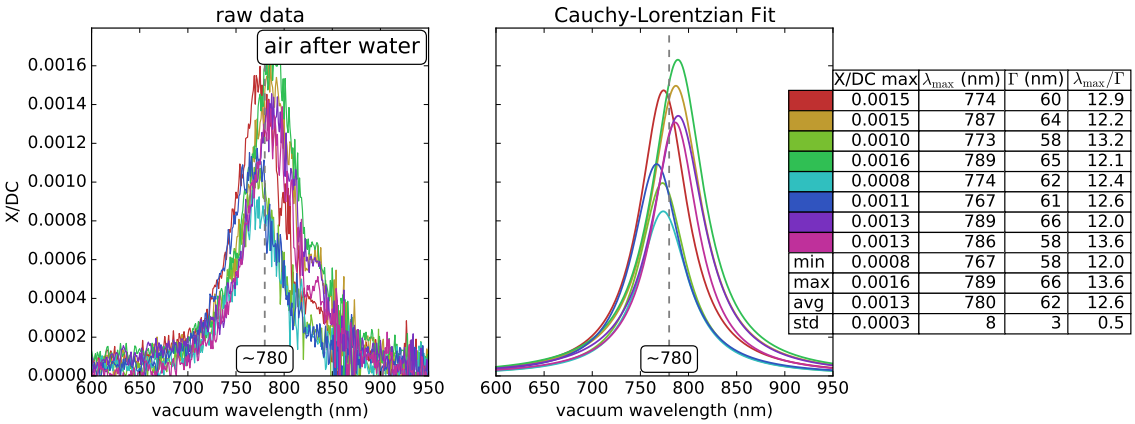

	X/DC max	λ_{max} (nm)	Γ (nm)	λ_{max}/Γ
	0.0015	774	60	12.9
	0.0015	787	64	12.2
	0.0010	773	58	13.2
	0.0016	789	65	12.1
	0.0008	774	62	12.4
	0.0011	767	61	12.6
	0.0013	789	66	12.0
	0.0013	786	58	13.6
min	0.0008	767	58	12.0
max	0.0016	789	66	13.6
avg	0.0013	780	62	12.6
std	0.0003	8	3	0.5

(c) second study in air

Figure 3.34: Spectra of BPs from the sample in figure 3.33 studied (a) in air, (b) in water, (c) again in air. Measurements in air were made with the reflective objects without the fluid cell. Measurements in water were made with the GAPO objective. Left: raw spectra. Right: Cauchy-Lorentzian fits and tabulated parameters. The average LSPR wavelength is marked on the graph.

This was taken as an indication of residual wetting and so the sample was placed in an oven at 80 °C overnight. This had no visible effect on the average intensity, spectral position or FWHM of the LSPR (figure 3.35).

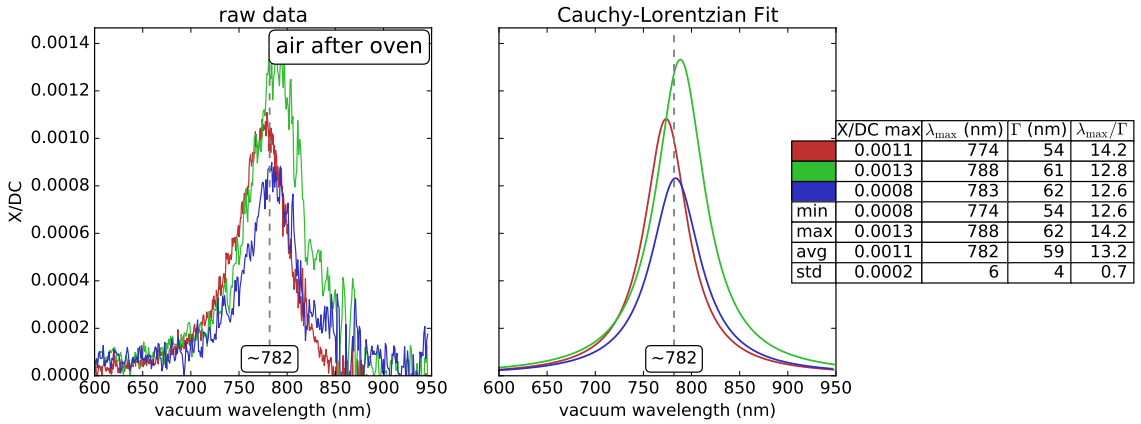

	X/DC max	λ_{max} (nm)	Γ (nm)	λ_{max}/Γ
	0.0011	774	54	14.2
	0.0013	788	61	12.8
	0.0008	783	62	12.6
min	0.0008	774	54	12.6
max	0.0013	788	62	14.2
avg	0.0011	782	59	13.2
std	0.0002	6	4	0.7

Figure 3.35: Study in air after heating overnight in an oven at 80 °C. Left: raw spectra. Right: Cauchy-Lorentzian fits and tabulated parameters. The average LSPR wavelength is marked on the graph.

The sample was then re-imaged with SEM to investigate possible changes (e.g. changes in the aspect ratios or deposits around the BPs) and correlate the optical results with electron microscopy. No changes were observed that could explain the persistent red-shift in to air and the sample appeared to be clean. The sample was remounted on the LSMS setup and studied again in air and water (figure 3.36). Following the SEM study, the average LSPR peak in air was found to be blue-shifted from the measurement in air before the SEM, which indicates that the vacuum may have had an effect on eliminating residual wetting or depositions from around the objects. Despite this effect, the average LSPR peak did not return to the initial spectral position at the beginning of the study. Upon re-immersion in water after the SEM, an average red-shift of approximately 60 nm was observed. While less than the first average red-shift of 76 nm when moving from air to water, the final average LSPR position was ∼10 nm to the red of the previous average in water.

It also seems that the SEM has increased the dispersion of the FWHMs. Before the SEM, the average value was around 60 nm with a standard deviation of 3 to 4. After the SEM, the average value jumped to 87 nm with a standard deviation of 9 and then back down to 65 nm with a standard deviation of 25. The number of objects studied is insufficient to draw broad conclusions about the effects of the SEM but we surmise that the SEM may have degraded the sample.

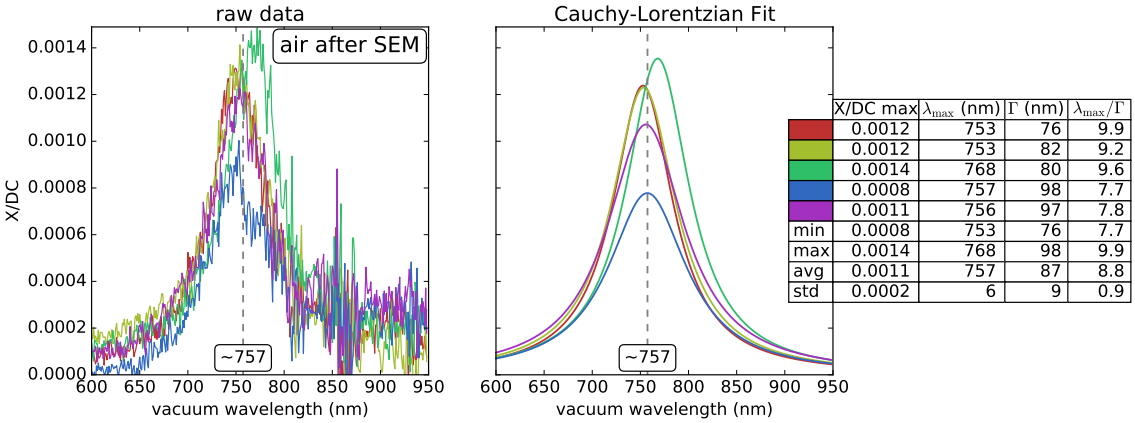

	X/DC max	λ_{max} (nm)	Γ (nm)	λ_{max}/Γ
	0.0012	753	76	9.9
	0.0012	753	82	9.2
	0.0014	768	80	9.6
	0.0008	757	98	7.7
	0.0011	756	97	7.8
min	0.0008	753	76	7.7
max	0.0014	768	98	9.9
avg	0.0011	757	87	8.8
std	0.0002	6	9	0.9

(a) post-SEM study in air

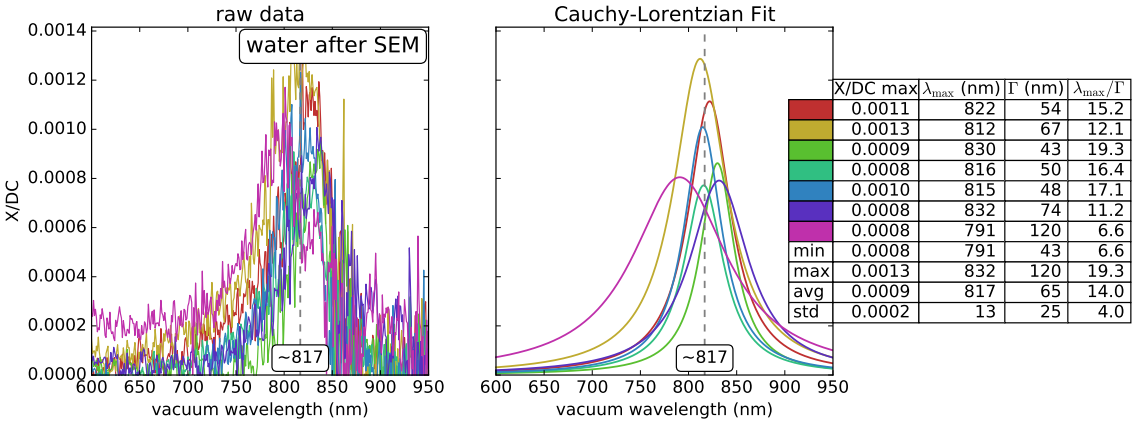

	X/DC max	λ_{max} (nm)	Γ (nm)	λ_{max}/Γ
	0.0011	822	54	15.2
	0.0013	812	67	12.1
	0.0009	830	43	19.3
	0.0008	816	50	16.4
	0.0010	815	48	17.1
	0.0008	832	74	11.2
	0.0008	791	120	6.6
min	0.0008	791	43	6.6
max	0.0013	832	120	19.3
avg	0.0009	817	65	14.0
std	0.0002	13	25	4.0

(b) post-SEM study in water

Figure 3.36: Study after SEM in (a) in air and (b) in water. Left: raw spectra. Right: Cauchy-Lorentzian fits and tabulated parameters. The average LSPR wavelength is marked on the graph.

The results of the spectral shifts are summarized in figure 3.37. Despite the apparent effect of the SEM on the dispersion of FWHM, the spectral position of the LSPR does not seem to have been similarly affected. Because of the limited spectral dispersion, clear tendencies emerge even though the measurements were not made on the same objects in each case.

After the second study in water ("post-SEM"), the sample was again examined with SEM to correlate the studied objects with their spectra (figure 3.38). The objects were all BPs with no discernible abnormalities or local changes.

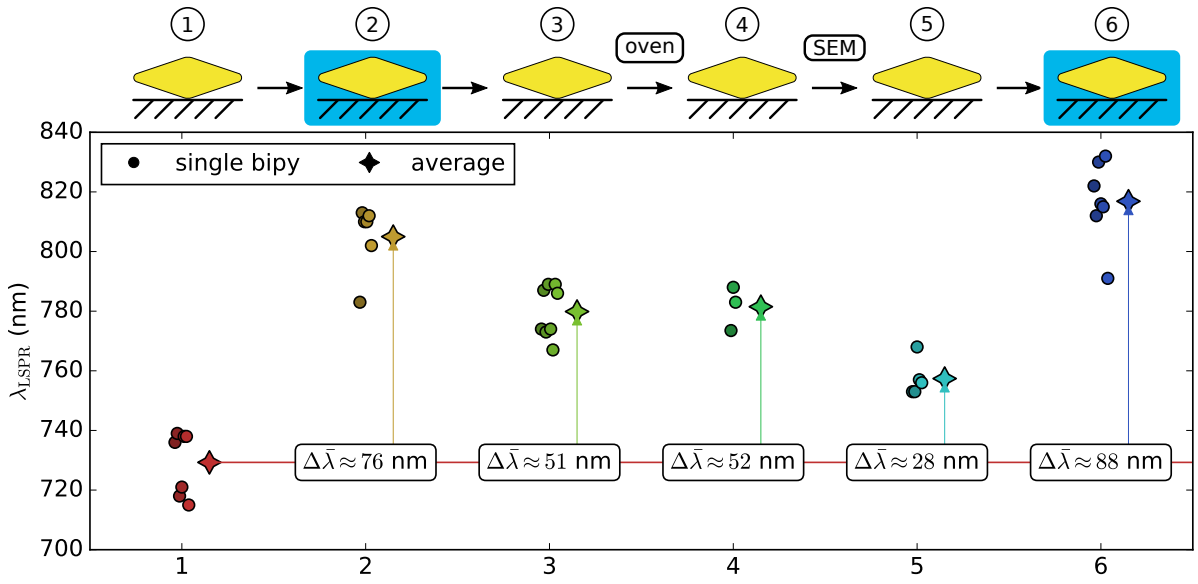

Figure 3.37: LSPR peak positions of multiple BPs under different sequential conditions. (1) air (2) water (3) air (4) air after oven (5) air after SEM (6) water. The matching spectra are shown in figures 3.34 (1-3) and 3.36 (4-6).

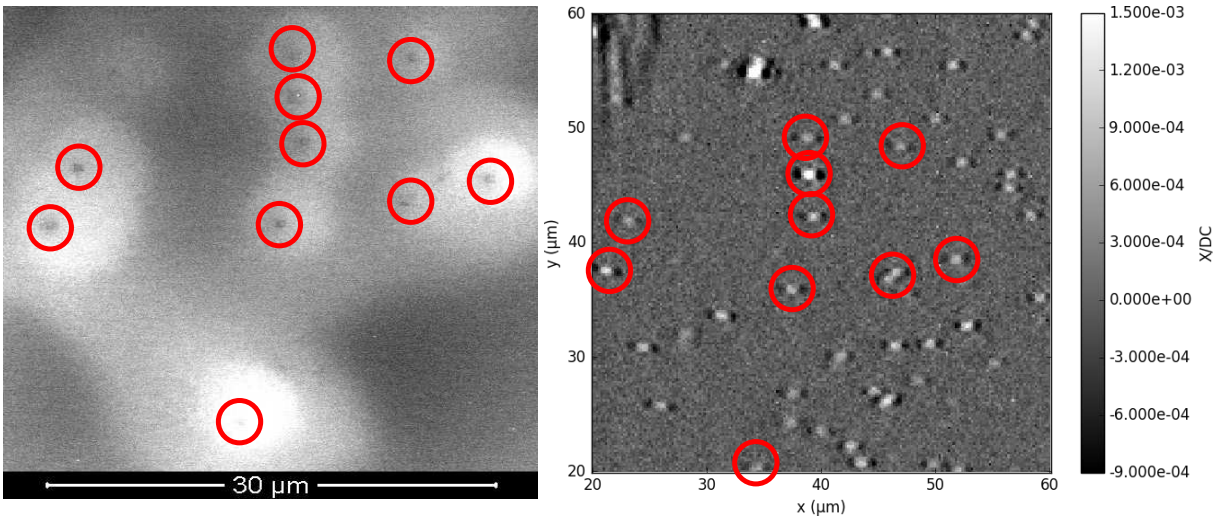

Figure 3.38: Post-SMS correlation with SEM. The SEM image is shown on the left and the SMS map in air at 760 nm is shown on the right. The location of several corresponding objects have been encircled in red. The bright areas of the SEM image indicate charging effects.

The spectra of one BP that was studied under all 6 conditions are shown in figure 3.39 along with its SEM image. The peak shifts are summarized in figure 3.40. Overall, the

tendencies are the same as those discussed for the averages, in which these results were included. Of note here is the blue-shift of ∼13 nm following heating in the oven, which indicates that this step may have had an influence that was masked by the averaging over different objects. The shift after the second immersion in water is also weaker than the average, with a final position that was blue-shifted 17 nm from the previous position in water. We note, however, that the final spectrum in water is both wider and noisier than the others and that the fit is not as good (figure 3.39).

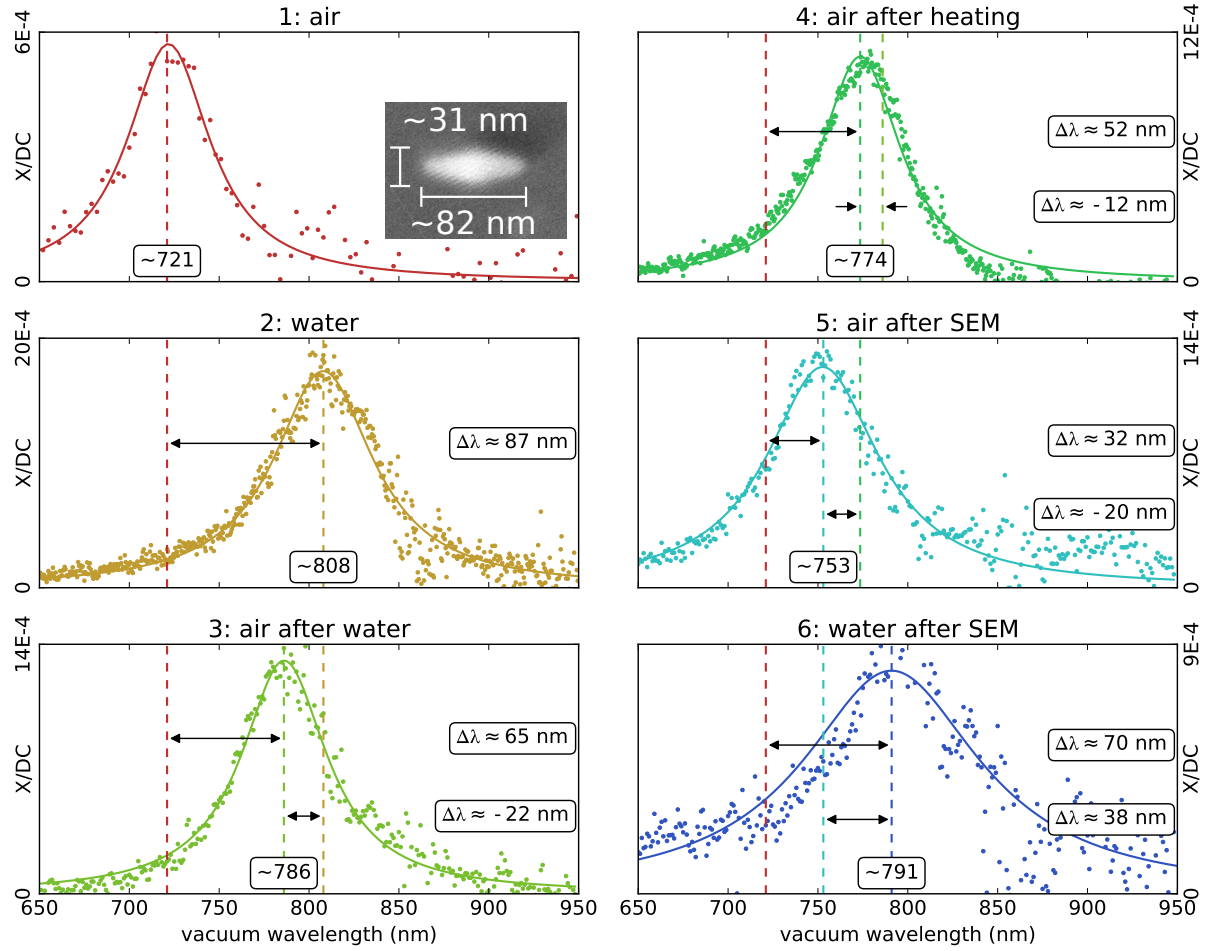

Figure 3.39: Spectra of a single bipyramid used to create figure 3.40. Each subplot after the first displays the offset from the original peak in air (red dotted line). Each subplot after the second also shows the relative shift to the previous peak. Inlay: SEM image of the BP.

It is difficult to conclude from these results. The oven heating and SEM vacuum appear to have an effect on deshifting the LSPR peak towards their original position, which may indicate residual wetting. This would be surprising though because during the preparation of the sample, the BPs are deposited in solution (see figure 3.14). The initial state of the

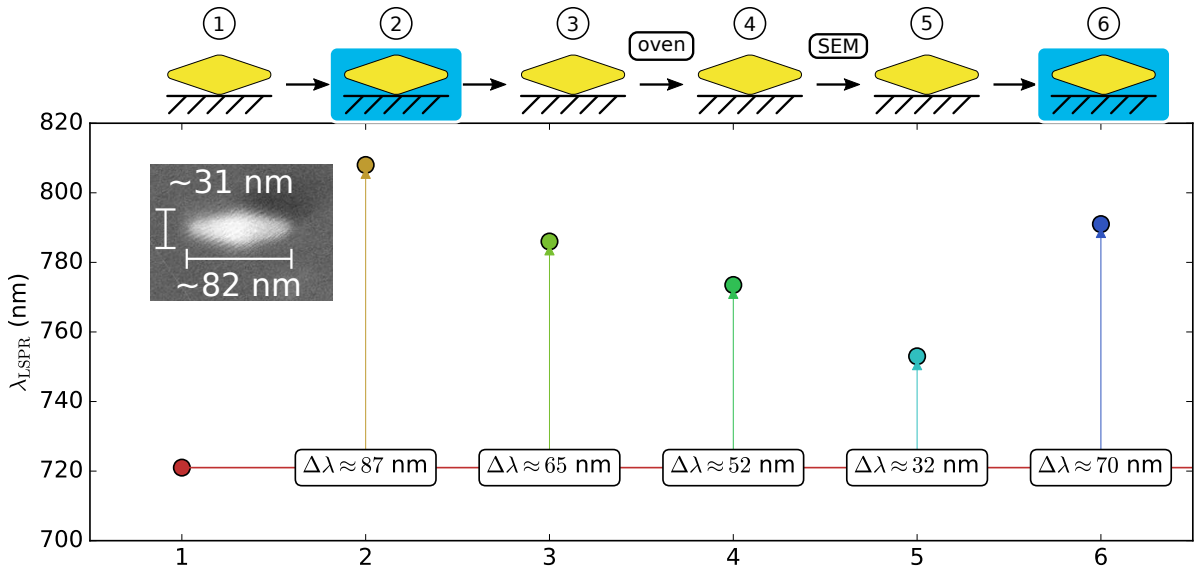

Figure 3.40: LSPR peak positions of the single BP studied under all of the conditions summarized in figure 3.37. Inlay: SEM image of the BP.

sample is therefore wet. If residual water were removed by the vacuum of the SEM prior to the SMS study then exposure to the vacuum a second time would be expected to restore the sample to the original state, which was not observed. It would have been interesting to subject the sample to a high vacuum to see if it would have had an effect on the average spectral position of the LSPR peaks.

We are also left to wonder if the effects may be due to the evolution of surfactants or silanes on the sample. Given that this sample was prepared prior to the additional rinsing step, there may be excess silanes that were simply not visible in the SEM images. The tests should be repeated with a new sample prepared with the current protocol.

A final study of this sample was performed several months later in air and in water to investigate if there was any evolution of the spectra. The studied objects are not the same as before but are from a nearby zone of the sample. The spectra and fits are shown in figure 3.41. The results are summarized alongside the previous results in figure 3.42.

The first striking result of this subsequent study in air is that the average LSPR peak position lies slightly further to the red than either of the previous studies in water, although the dispersion of the previous measurements likely skew their average. The second striking result is that re-immersion in water does not induce a further red-shift. In fact, the average spectral position was even slightly blue-shifted by about 4 nm, but this is likely insignificant. Given the regularity of the objects observed under SEM and their spectra, which retain the expected line shape of a BP, these results strongly indicate a

local change on the sample that renders the BPs insensitive to the environment.

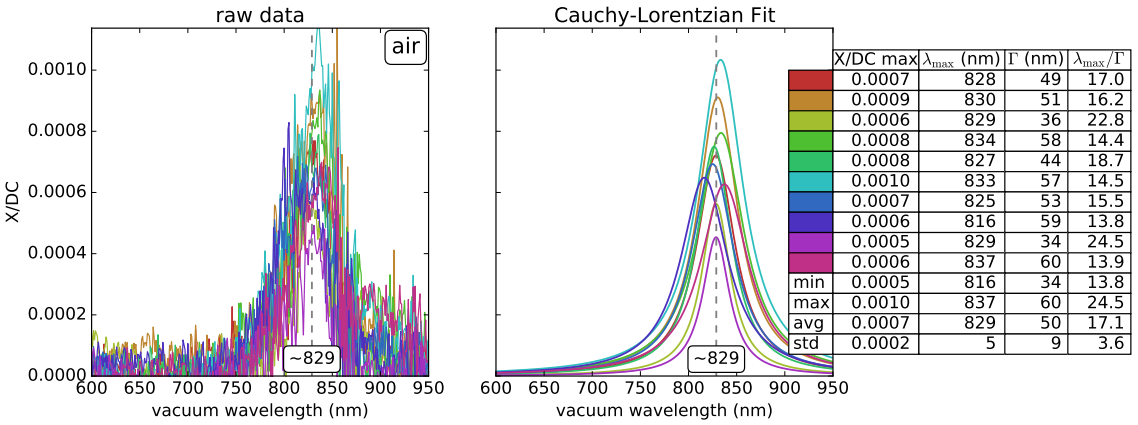

	X/DC max	λ_{max} (nm)	Γ (nm)	λ_{max}/Γ
	0.0007	828	49	17.0
	0.0009	830	51	16.2
	0.0006	829	36	22.8
	0.0008	834	58	14.4
	0.0008	827	44	18.7
	0.0010	833	57	14.5
	0.0007	825	53	15.5
	0.0006	816	59	13.8
	0.0005	829	34	24.5
	0.0006	837	60	13.9
min	0.0005	816	34	13.8
max	0.0010	837	60	24.5
avg	0.0007	829	50	17.1
std	0.0002	5	9	3.6

(a) air

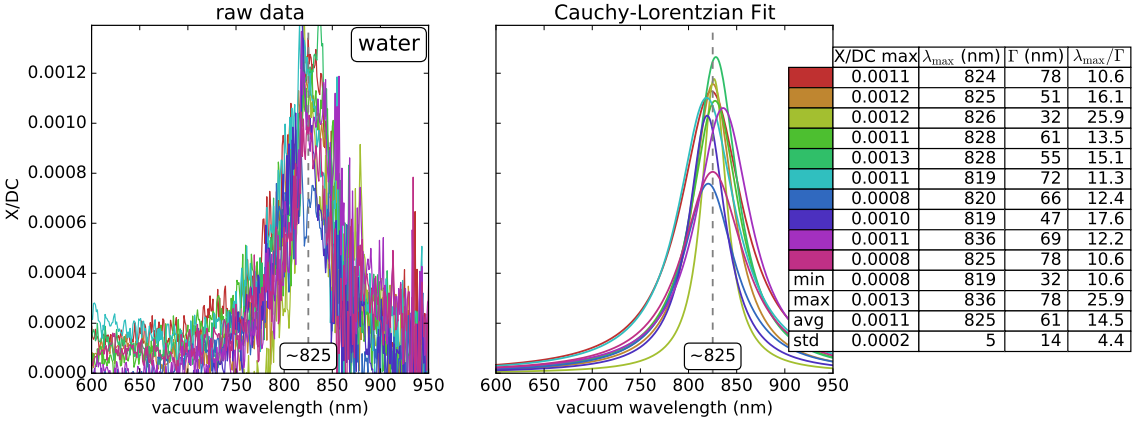

	X/DC max	λ_{max} (nm)	Γ (nm)	λ_{max}/Γ
	0.0011	824	78	10.6
	0.0012	825	51	16.1
	0.0012	826	32	25.9
	0.0011	828	61	13.5
	0.0013	828	55	15.1
	0.0011	819	72	11.3
	0.0008	820	66	12.4
	0.0010	819	47	17.6
	0.0011	836	69	12.2
	0.0008	825	78	10.6
min	0.0008	819	32	10.6
max	0.0013	836	78	25.9
avg	0.0011	825	61	14.5
std	0.0002	5	14	4.4

(b) water

Figure 3.41: Returning to the sample after several months, the spectra in (a) air and (b) water exhibit an average peak around 829 nm and 823 nm, respectively. Left: raw spectra. Right: Cauchy-Lorentzian fits and tabulated parameters. The average LSPR wavelength is marked on the graph.

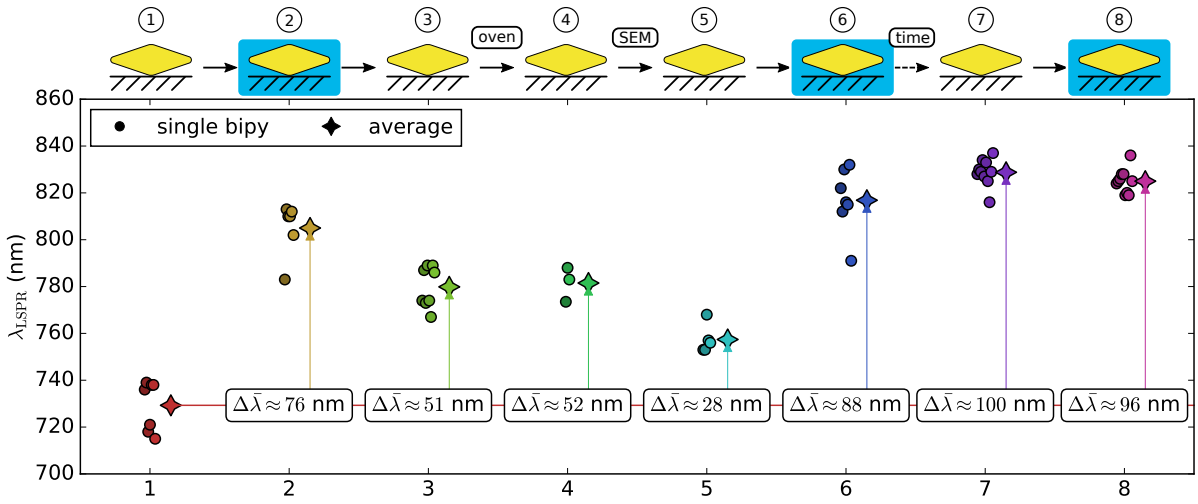

Figure 3.42: Extension of figure 3.37 to include a final study in air (7) and water (8) several months (6). The objects in (7) and (8) are from a different zone of the sample.

The sample was again imaged with SEM to check for local changes that could explain these results. The sample was shown to be coated with an irregular, unidentified substance (figure 3.43). It may be a precipitation of the same substance seen previously in figure 2.11 (page 2.11), or it may be due to degradation of the (excess) silanes after months of storage in air. While the origin of this substance is uncertain, its presence likely explains the red-shift of the observed spectra along with their insensitivity to the environment. Regardless of its origin, these results show the need for high-quality samples and careful storage.

During the optical studies, there was no indication of any irregularities in the X/DC maps (figure 3.44a). After observing the substance under SEM, the DC map was examined but it did not present any irregularities (figure 3.44b). The background is smooth with a variation of only $\sim 5/192 \approx 3\,\%$. This highlights the importance of correlation with electron microscopy to fully characterize the sample.

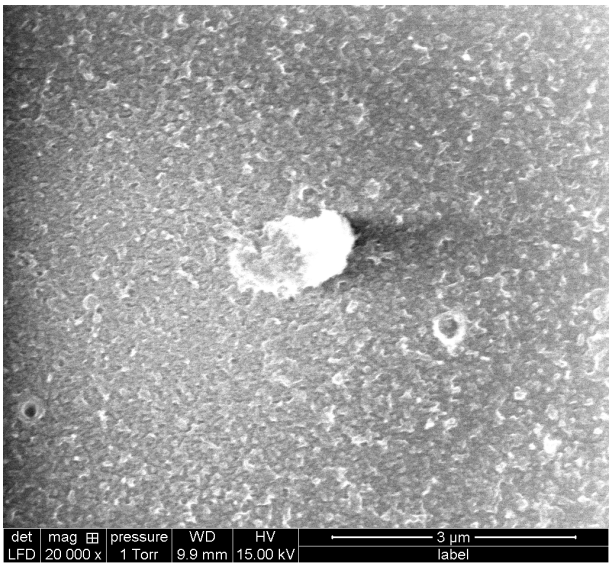

Figure 3.43: SEM images of unidentified deposits on sample C.

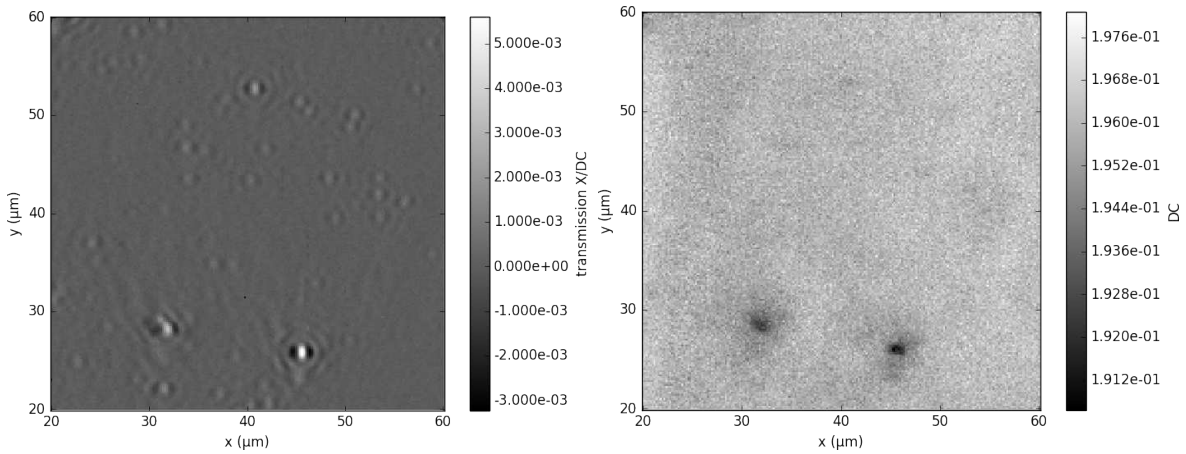

(a) X/DC **(b)** DC

Figure 3.44: SMS DC and X/DC maps of sample C in air at 830 nm after months of storage.

3.3.2.2 Sample B: Return To Air

Following the bulk sensing tests, the high quality sample B studied in air, water and water+glycerol mixes in sections 3.3.1.2 and 3.3.1.3 was rinsed with water and allowed to dry before remapping it in air. The same 6 objects were relocated (figure 3.45a) and their spectra in air were measured again. The LSPR spectral positions are compared to the previous spectra in figure 3.45b. The corresponding spectra are shown in figure 3.46. The

spectra nearly return to their original positions on average with a residual average offset of approximately 19 nm, which is closer than what was observed in the previous studies (figure 3.37). This may be ascribed at least in part to the improved sample quality due to the removal of excess silanes with the new protocol. Given its viscosity, this remaining offset may be due to residual glycerol on the sample.

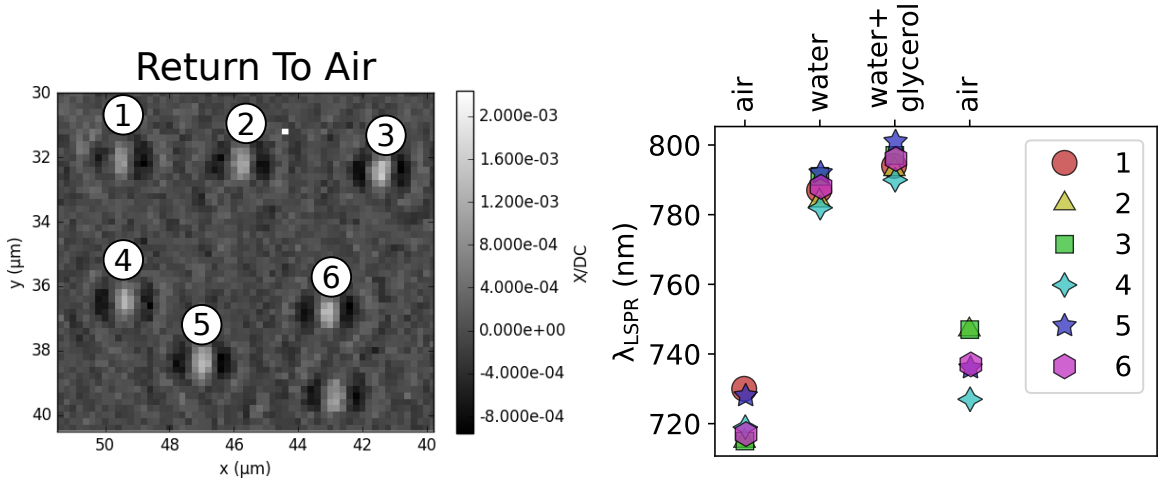

(a) SMS map in air. **(b)** Comparison to previous LSPR peaks.

Figure 3.45: Return to air after water and glycerol studies. (a): SMS map in air at (740 nm) (b): Extension of figure 3.29 to show the LSPR peaks upon returning to air. Corresponding spectra are presented in figure 3.46

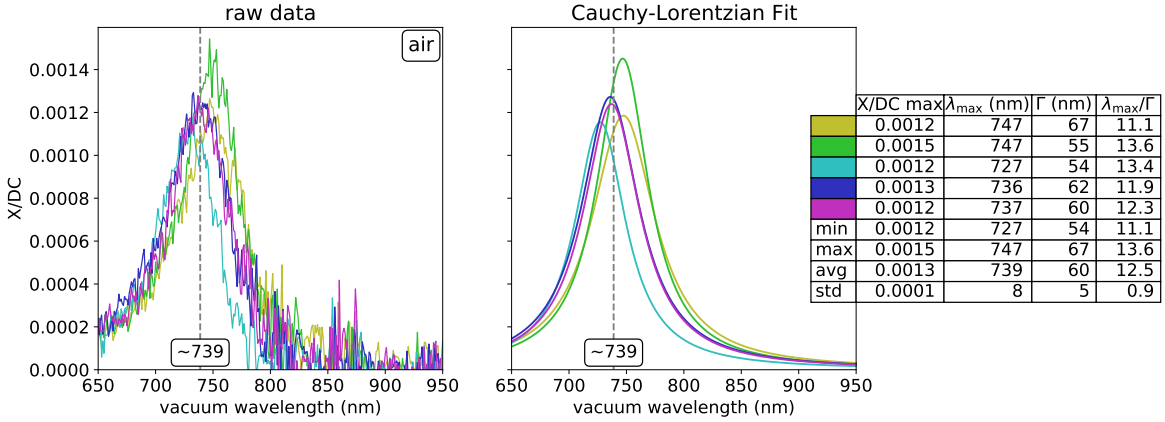

	X/DC max	λ_{max} (nm)	Γ (nm)	λ_{max}/Γ
	0.0012	747	67	11.1
	0.0015	747	55	13.6
	0.0012	727	54	13.4
	0.0013	736	62	11.9
	0.0012	737	60	12.3
min	0.0012	727	54	11.1
max	0.0015	747	67	13.6
avg	0.0013	739	60	12.5
std	0.0001	8	5	0.9

Figure 3.46: Corresponding spectra for the return to air in figure 3.45b. Left: raw spectra. Right: Cauchy-Lorentzian fits and tabulated parameters. The average LSPR wavelength is marked on the graph.

The sample was mapped again in air after several months of dry storage to study any eventual evolution of the optical response. Again, the same 6 objects were relocated

(figure 3.47a) and their spectra in air were measured. The positions of their LSPR peaks is plotted alongside the previous results in figure 3.47b. The corresponding spectra are plotted in figure 3.48. Comparing these spectra to the last spectra in air (figure 3.46), we note that the average spectral position has blue-shifted even further by about 8 nm and is in better agreement with the first measurements in air on these objects. There is also a slightly reduced dispersion in the spectral position and the width of the LSPR peaks, which may indicate that residual water and glycerol has evaporated from the sample during storage. Some may nevertheless remain as the sample was stored in a sealed pill jar. The average FWHM is within the same range as the first and the previous measurements in air.

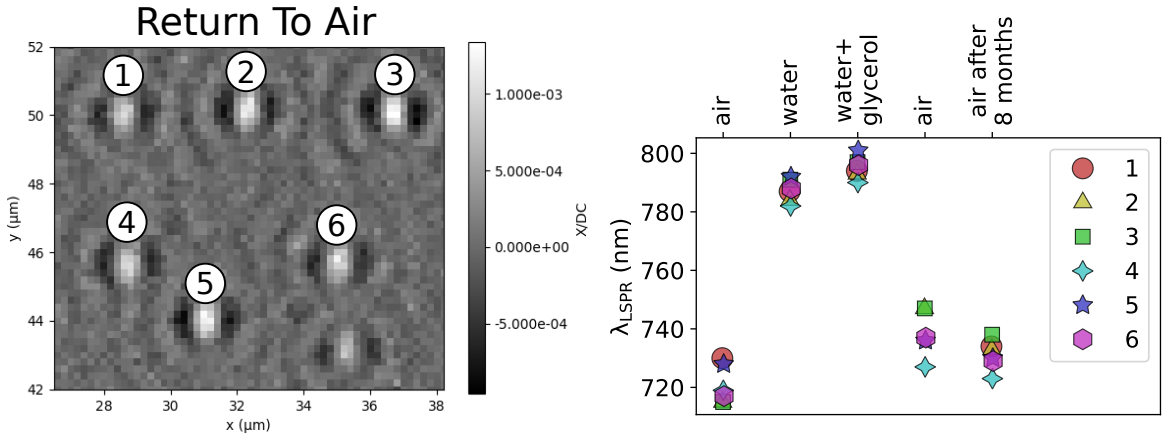

(a) SMS map in air after several months. **(b)** Comparison to previous LSPR peaks.

Figure 3.47: Return to air after several months of dry storage in air. (a): SMS map in air at (740 nm) (b): Extension of figure 3.45b to show the evolution of the LSPR peaks after several months of dry storage in air. Corresponding spectra are presented in figure 3.48

The line shapes of the spectra (figure 3.48) strongly indicate that the 6 objects have retained their bipyramidal shape despite the prolonged dry storage. This was confirmed with SEM images of the objects (figure 3.49). Comparison of these images to the previous images of the unsilanized BPs after a much shorter interval (figure 3.13, page 146) highlights the importance of the silanization for the stabilization of such anisotropic shapes. Furthermore, the SEM study was also able to verify that there is no contamination as observed on sample C (figure 3.43, page 177).

As an additional test of the sample stability, a different zone of sample B was also mapped in air (prior to obtaining the preceding SEM images) and the detected BPs were measured. Their spectra are shown in figure 3.50. These objects, which have also been immersed in the same water and water+glycerol mixes during the previous study, exhibit a similar response to the 6 objects studied above, with very similar spectral positions and widths of their LSPR peaks. The stability of these spectra after months of dry storage further confirms that the silanization protocol is able to stabilize the anisotropic morphology

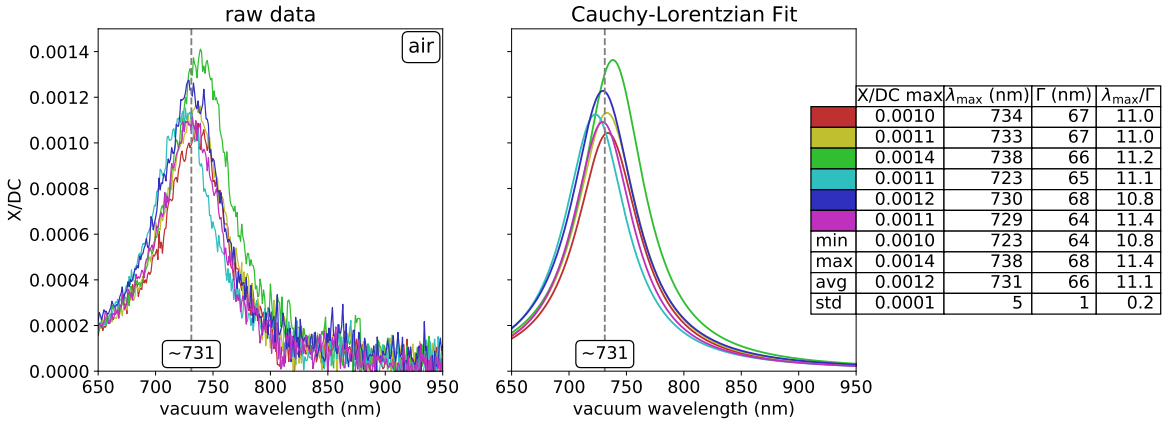

	X/DC max	λ_{max} (nm)	Γ (nm)	λ_{max}/Γ
	0.0010	734	67	11.0
	0.0011	733	67	11.0
	0.0014	738	66	11.2
	0.0011	723	65	11.1
	0.0012	730	68	10.8
	0.0011	729	64	11.4
min	0.0010	723	64	10.8
max	0.0014	738	68	11.4
avg	0.0012	731	66	11.1
std	0.0001	5	1	0.2

Figure 3.48: Corresponding spectra figure 3.47b for the final measurements in air after several months of dry storage in air. Left: raw spectra. Right: Cauchy-Lorentzian fits and tabulated parameters. The average LSPR wavelength is marked on the graph.

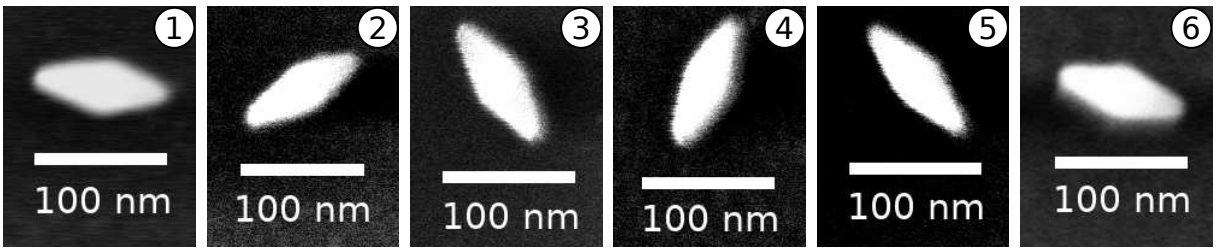

Figure 3.49: SEM images of the 6 studied objects after months of dry storage.

of the BPs. The lack of dispersion of these spectra also supports the hypothesis that the previous sample C suffered from excess silanes that are now removed with the extra rinsing step during sample preparation. To conclude on sample B, a second study in water and water+glycerol mixes is needed to determine if it has retained its sensitivity. Unfortunately, there was not enough time to perform these studies.

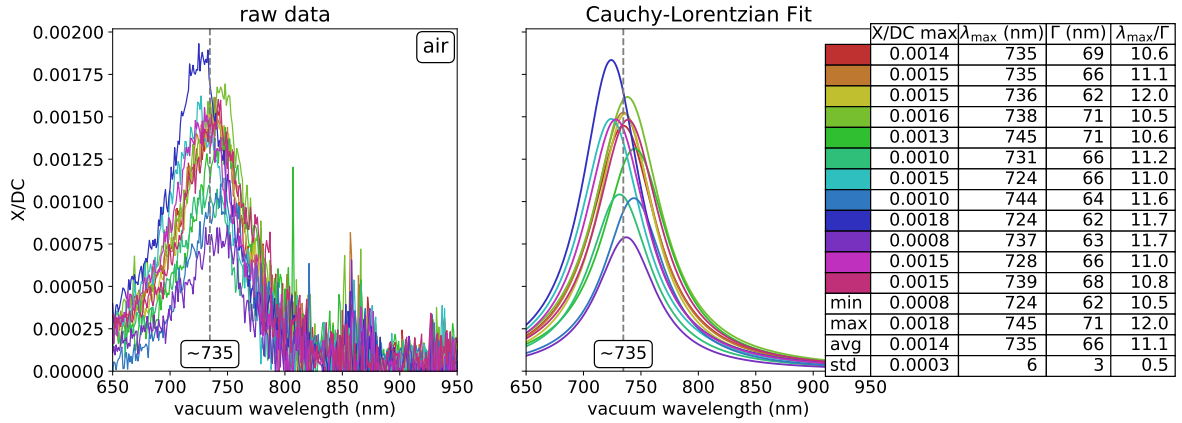

	X/DC max	λ_{max} (nm)	Γ (nm)	λ_{max}/Γ
	0.0014	735	69	10.6
	0.0015	735	66	11.1
	0.0015	736	62	12.0
	0.0016	738	71	10.5
	0.0013	745	71	10.6
	0.0010	731	66	11.2
	0.0015	724	66	11.0
	0.0010	744	64	11.6
	0.0018	724	62	11.7
	0.0008	737	63	11.7
	0.0015	728	66	11.0
	0.0015	739	68	10.8
min	0.0008	724	62	10.5
max	0.0018	745	71	12.0
avg	0.0014	735	66	11.1
std	0.0003	6	3	0.5

Figure 3.50: Spectra of multiple BPs after several months of storage in air. Left: raw spectra. Right: Cauchy-Lorentzian fits and tabulated parameters. The average LSPR wavelength is marked on the graph.

Conclusion

In this chapter we have seen that the suitability of potential plasmonic probes for biosensing applications depends on a number of important factors such as size, shape and composition, and we have discussed some of the basic metrics for comparing different probes and their performance. While many different types of probes are under active investigation in the literature, gold BPs currently receive considerable attention due to a number of properties that are promising for biosensing applications.

Using numerical investigations, several of these properties of gold BPs reported in the literature have been confirmed. We have shown that BPs are far more sensitive to bulk RI changes than spheres. Due to their anisotropy, BPs exhibit strong localized field enhancements around their tips under longitudinal excitation. Simulations have confirmed that the LSPR is more sensitive to local RI changes near these hot-spots as opposed to near the waist of the object and that the LSPR resonance position is a roughly linear function of the bulk RI of the BP's environment.

The synthesis of BPs has been presented and the relevant parameters that control size and aspect ratio have been discussed. We have seen that these parameters can be used to tailor the LSPR over a wide range in the visible to NIR spectrum.

A new protocol has been developed to prepare robust samples of colloidally synthesized gold NPs for liquid measurements with the LSMS setup described in chapter 2. The protocol uses silanization to graft gold NPs to the sample. These samples overcome the stability issues encountered with previous samples prepared using traditional techniques for SMS. After initial difficulties with sample density, surfactant precipitates and excess

silanes, the protocol now reliably produces optically clean and stable samples with suitable density for SMS measurements.

Using this protocol, silanized samples of gold nanospheres have been produced and studied with the LSMS setup to confirm that SMS measurements are not impeded by the silanization and that the object's spectra are not significantly altered. Unique nanospheres have been located and measured and their calibrated spectra have been shown to correlate well with theoretical spectra based on Mie theory.

Silanized samples with BPs have been prepared and used to study their bulk sensitivity and robustness. The sensitivity was tested using media of different real RI: air, water, glycerol and water+glycerol mixes. Linear shifts of the LSPR's spectral position have been detected for changes in RI but their magnitude and thus the BPs' sensitivity have been less than that predicted by the numerical simulations. The reduced sensitivity may be due to residual surfactants or the presence of silanes around the object. We also note that the reported sensitivities were calculated from the raw SMS X/DC spectra. Due to the shape of the calibration curve, the relative shifts and thus the sensitivity will increase slightly when the spectra are calibrated. Despite these concerns, the results are in qualitative agreement with theory and the literature. Even if the sensitivity is lower, the narrow FWHM of the individually measured BPs, compared to ensemble measurements in the literature, yields relatively high FOMs for the studied objects.

Using the MICA controller interface, individual BPs have been automatically tracked and measured over time in the presence of diffusing glycerol in water. Through these measurement we were able to observe the gradual change in the LSPR's peak position over a period of 24 hours. These results are promising for real-time measurements of dynamic processes and will be discussed further in the conclusion at the end of the dissertation.

The stability and reusability of the silanized BP samples were tested using consecutive measurements in air and water. Initials tests using an earlier version of the sample preparation protocol showed that the sample evolves as it is studied under different liquids and that returning it to air does not result recover the original spectra measured in air. This was likely due to excess silanes as sample prepared with the current protocol that removes excess silanes showed greater stability and robustness, although a smaller persistent red-shift was observed when returning to air after measurements in glycerol. After several months of dry storage, the sample was studied again in air and the spectra were shown to remain stable.

References

[1] K. S. Johnson. *Transmission circuits for telephonic communication: methods of analysis and design.* D. Van Nostrand Co., 1924.

[2] E. I. Green. The story of Q. *American Scientist*, 43:584–594, October 1955.

[3] K. L. Smith. On the Origins of the Quality Factor Q. *Quarterly Journal of the Royal Astronomical Society*, 27(4):695–696, 1986.

[4] R. G. Jackson. *Novel sensors and sensing*. Series in sensors. Institute of Physics Pub, Bristol ; Philadelphia, 2004. ISBN 978-0-7503-0989-9. OCLC: ocm56652674.

[5] B. Crowell. *Light and Matter, Volume 1*. November 2016.

[6] N. Bobroff. Position measurement with a resolution and noise-limited instrument. *Review of Scientific Instruments*, 57(6):1152–1157, June 1986. ISSN 0034-6748, 1089-7623. doi:10.1063/1.1138619.

[7] J. N. Anker, W. P. Hall, O. Lyandres, N. C. Shah, J. Zhao, and R. P. Van Duyne. Biosensing with plasmonic nanosensors. *Nature Materials*, 7(6):442–453, June 2008. ISSN 1476-1122. doi:10.1038/nmat2162.

[8] K. M. Mayer and J. H. Hafner. Localized Surface Plasmon Resonance Sensors. *Chemical Reviews*, 111(6):3828–3857, June 2011. ISSN 0009-2665. doi:10.1021/cr100313v.

[9] P. Zijlstra and M. Orrit. Single metal nanoparticles: optical detection, spectroscopy and applications. *Reports on Progress in Physics*, 74(10):106401, 2011. ISSN 0034-4885. doi:10.1088/0034-4885/74/10/106401.

[10] L. Guo, J. A. Jackman, H.-H. Yang, P. Chen, N.-J. Cho, and D.-H. Kim. Strategies for enhancing the sensitivity of plasmonic nanosensors. *Nano Today*, 10(2):213–239, April 2015. ISSN 1748-0132. doi:10.1016/j.nantod.2015.02.007.

[11] C. Sönnichsen, T. Franzl, T. Wilk, G. von Plessen, J. Feldmann, O. Wilson, and P. Mulvaney. Drastic Reduction of Plasmon Damping in Gold Nanorods. *Physical Review Letters*, 88(7):077402, January 2002. doi:10.1103/PhysRevLett.88.077402.

[12] C. L. Nehl, H. Liao, and J. H. Hafner. Optical properties of star-shaped gold nanoparticles. *Nano letters*, 6(4):683–688, 2006.

[13] H. Wang, D. W. Brandl, F. Le, P. Nordlander, and N. J. Halas. Nanorice: a hybrid plasmonic nanostructure. *Nano letters*, 6(4):827–832, 2006.

[14] R. Bukasov and J. S. Shumaker-Parry. Highly tunable infrared extinction properties of gold nanocrescents. *Nano letters*, 7(5):1113–1118, 2007.

[15] F. Hao, C. L. Nehl, J. H. Hafner, and P. Nordlander. Plasmon resonances of a gold nanostar. *Nano letters*, 7(3):729–732, 2007.

[16] E. M. Larsson, J. Alegret, M. Käll, and D. S. Sutherland. Sensing Characteristics of NIR Localized Surface Plasmon Resonances in Gold Nanorings for Application as Ultrasensitive Biosensors. *Nano Letters*, 7(5):1256–1263, May 2007. ISSN 1530-6984. doi:10.1021/nl0701612.

[17] M. Liu, P. Guyot-Sionnest, T.-W. Lee, and S. K. Gray. Optical properties of rodlike and bipyramidal gold nanoparticles from three-dimensional computations. *Physical Review B*, 76(23):235428, December 2007. doi:10.1103/PhysRevB.76.235428.

[18] N. L. Bocchio, A. Unger, M. Álvarez, and M. Kreiter. Thin Layer Sensing with Multipolar Plasmonic Resonances. *The Journal of Physical Chemistry C*, 112(37): 14355–14359, September 2008. ISSN 1932-7447. doi:10.1021/jp804099u.

[19] H. Chen, X. Kou, Z. Yang, W. Ni, and J. Wang. Shape- and Size-Dependent

Refractive Index Sensitivity of Gold Nanoparticles. *Langmuir*, 24(10):5233–5237, May 2008. ISSN 0743-7463, 1520-5827. doi:10.1021/la800305j.

[20] H. Chen, L. Shao, K. C. Woo, T. Ming, H.-Q. Lin, and J. Wang. Shape-Dependent Refractive Index Sensitivities of Gold Nanocrystals with the Same Plasmon Resonance Wavelength. *The Journal of Physical Chemistry C*, 113(41):17691–17697, October 2009. ISSN 1932-7447, 1932-7455. doi:10.1021/jp907413n.

[21] A. Unger and M. Kreiter. Analyzing the Performance of Plasmonic Resonators for Dielectric Sensing. *The Journal of Physical Chemistry C*, 113(28):12243–12251, July 2009. ISSN 1932-7447. doi:10.1021/jp9027047.

[22] A. Unger, U. Rietzler, R. Berger, and M. Kreiter. Sensitivity of Crescent-Shaped Metal Nanoparticles to Attachment of Dielectric Colloids. *Nano Letters*, 9(6):2311–2315, June 2009. ISSN 1530-6984. doi:10.1021/nl900505a.

[23] M. J. Banholzer, N. Harris, J. E. Millstone, G. C. Schatz, and C. A. Mirkin. Abnormally Large Plasmonic Shifts in Silica-Protected Gold Triangular Nanoprisms. *The Journal of Physical Chemistry C*, 114(16):7521–7526, April 2010. ISSN 1932-7447. doi:10.1021/jp911889a.

[24] S. Barbosa, A. Agrawal, L. Rodríguez-Lorenzo, I. Pastoriza-Santos, R. A. Alvarez-Puebla, A. Kornowski, H. Weller, and L. M. Liz-Marzán. Tuning Size and Sensing Properties in Colloidal Gold Nanostars. *Langmuir*, 26(18):14943–14950, September 2010. ISSN 0743-7463. doi:10.1021/la102559e.

[25] J. Becker, A. Trügler, A. Jakab, U. Hohenester, and C. Sönnichsen. The Optimal Aspect Ratio of Gold Nanorods for Plasmonic Bio-sensing. *Plasmonics*, 5(2):161–167, March 2010. ISSN 1557-1955, 1557-1963. doi:10.1007/s11468-010-9130-2.

[26] S. K. Dondapati, T. K. Sau, C. Hrelescu, T. A. Klar, F. D. Stefani, and J. Feldmann. Label-free Biosensing Based on Single Gold Nanostars as Plasmonic Transducers. *ACS Nano*, 4(11):6318–6322, November 2010. ISSN 1936-0851, 1936-086X. doi:10.1021/nn100760f.

[27] M. A. Mahmoud and M. A. El-Sayed. Gold Nanoframes: Very High Surface Plasmon Fields and Excellent Near-Infrared Sensors. *Journal of the American Chemical Society*, 132(36):12704–12710, September 2010. ISSN 0002-7863. doi:10.1021/ja104532z.

[28] J. McPhillips, A. Murphy, M. P. Jonsson, W. R. Hendren, R. Atkinson, F. Höök, A. V. Zayats, and R. J. Pollard. High-Performance Biosensing Using Arrays of Plasmonic Nanotubes. *ACS Nano*, 4(4):2210–2216, April 2010. ISSN 1936-0851. doi:10.1021/nn9015828.

[29] Y. H. Lee, H. Chen, Q.-H. Xu, and J. Wang. Refractive Index Sensitivities of Noble Metal Nanocrystals: The Effects of Multipolar Plasmon Resonances and the Metal Type. *The Journal of Physical Chemistry C*, 115(16):7997–8004, April 2011. ISSN 1932-7447. doi:10.1021/jp202574r.

[30] M. Rycenga, C. M. Cobley, J. Zeng, W. Li, C. H. Moran, Q. Zhang, D. Qin, and Y. Xia. Controlling the Synthesis and Assembly of Silver Nanostructures for Plasmonic Applications. *Chemical Reviews*, 111(6):3669–3712, June 2011. ISSN 0009-2665, 1520-6890. doi:10.1021/cr100275d.

[31] S. Hong, T. Kang, D. Choi, Y. Choi, and L. P. Lee. Self-Assembled Three-

Dimensional Nanocrown Array. *ACS Nano*, 6(7):5803–5808, July 2012. ISSN 1936-0851. doi:10.1021/nn204967k.

[32] J. R. G. Navarro, D. Manchon, F. Lerouge, E. Cottancin, J. Lermé, C. Bonnet, F. Chaput, A. Mosset, M. Pellarin, and S. Parola. Synthesis, electron tomography and single-particle optical response of twisted gold nano-bipyramids. *Nanotechnology*, 23(14):145707, April 2012. ISSN 0957-4484. doi:10.1088/0957-4484/23/14/145707.

[33] L. Shao, A. S. Susha, L. S. Cheung, T. K. Sau, A. L. Rogach, and J. Wang. Plasmonic Properties of Single Multispiked Gold Nanostars: Correlating Modeling with Experiments. *Langmuir*, 28(24):8979–8984, June 2012. ISSN 0743-7463. doi:10.1021/la2048097.

[34] D. Chateau, A. Liotta, F. Vadcard, J. R. G. Navarro, F. Chaput, J. Lermé, F. Lerouge, and S. Parola. From gold nanobipyramids to nanojavelins for a precise tuning of the plasmon resonance to the infrared wavelengths: experimental and theoretical aspects. *Nanoscale*, 7(5):1934–1943, January 2015. ISSN 2040-3372. doi:10.1039/C4NR06323F.

[35] E. Pertreux, A. Lombardi, I. Florea, M. Spuch-Calvar, S. Gómez-Graña, D. Ihiawakrim, C. Hirlimann, O. Ersen, J. Majimel, M. Tréguer-Delapierre, M. Hettich, P. Maioli, A. Crut, F. Vallée, and N. D. Fatti. Surface Plasmon Resonance of an Individual Nano-object on an Absorbing Substrate: Quantitative Effects of Distance and 3d Orientation. *Advanced Optical Materials*, pages n/a–n/a, December 2015. ISSN 2195-1071. doi:10.1002/adom.201500548.

[36] J. Prasad, I. Zins, R. Branscheid, J. Becker, A. H. R. Koch, G. Fytas, U. Kolb, and C. Sönnichsen. Plasmonic Core–Satellite Assemblies as Highly Sensitive Refractive Index Sensors. *The Journal of Physical Chemistry C*, 119(10):5577–5582, March 2015. ISSN 1932-7447, 1932-7455. doi:10.1021/jp510985n.

[37] K. Sugawa, H. Tahara, A. Yamashita, J. Otsuki, T. Sagara, T. Harumoto, and S. Yanagida. Refractive Index Susceptibility of the Plasmonic Palladium Nanoparticle: Potential as the Third Plasmonic Sensing Material. *ACS Nano*, 9(2):1895–1904, February 2015. ISSN 1936-0851, 1936-086X. doi:10.1021/nn506800a.

[38] S. M. E. Peters, M. A. Verheijen, M. W. J. Prins, and P. Zijlstra. Strong reduction of spectral heterogeneity in gold bipyramids for single-particle and single-molecule plasmon sensing. *Nanotechnology*, 27(2):024001, January 2016. ISSN 0957-4484, 1361-6528. doi:10.1088/0957-4484/27/2/024001.

[39] F. Vollmer and S. Arnold. Whispering-gallery-mode biosensing: label-free detection down to single molecules. *Nature Methods*, 5(7):591–596, July 2008. ISSN 1548-7091, 1548-7105. doi:10.1038/nmeth.1221.

[40] M. S. Luchansky and R. C. Bailey. High-Q Optical Sensors for Chemical and Biological Analysis. *Analytical Chemistry*, 84(2):793–821, January 2012. ISSN 0003-2700, 1520-6882. doi:10.1021/ac2029024.

[41] F. Vollmer and L. Yang. Review Label-free detection with high-Q microcavities: a review of biosensing mechanisms for integrated devices. *Nanophotonics*, 1(3-4), January 2012. ISSN 2192-8614, 2192-8606. doi:10.1515/nanoph-2012-0021.

[42] A. V. Kabashin, P. Evans, S. Pastkovsky, W. Hendren, G. A. Wurtz, R. Atkinson,

R. Pollard, V. A. Podolskiy, and A. V. Zayats. Plasmonic nanorod metamaterials for biosensing. *Nature Materials*, 8(11):867–871, November 2009. ISSN 1476-1122. doi:10.1038/nmat2546.

[43] T. Chen, S. Li, and H. Sun. Metamaterials application in sensing. *Sensors*, 12(3): 2742–2765, 2012.

[44] J. J. Yang, M. Huang, H. Tang, J. Zeng, and L. Dong. Metamaterial sensors. *International Journal of Antennas and Propagation*, 2013, 2013.

[45] R. Singh, W. Cao, I. Al-Naib, L. Cong, W. Withayachumnankul, and W. Zhang. Ultrasensitive terahertz sensing with high-Q Fano resonances in metasurfaces. *Applied Physics Letters*, 105(17):171101, October 2014. ISSN 0003-6951, 1077-3118. doi:10.1063/1.4895595.

[46] L. J. Sherry, S.-H. Chang, G. C. Schatz, R. P. Van Duyne, B. J. Wiley, and Y. Xia. Localized Surface Plasmon Resonance Spectroscopy of Single Silver Nanocubes. *Nano Letters*, 5(10):2034–2038, October 2005. ISSN 1530-6984. doi:10.1021/nl0515753.

[47] K.-S. Lee and M. A. El-Sayed. Gold and Silver Nanoparticles in Sensing and Imaging: Sensitivity of Plasmon Response to Size, Shape, and Metal Composition. *The Journal of Physical Chemistry B*, 110(39):19220–19225, October 2006. ISSN 1520-6106, 1520-5207. doi:10.1021/jp062536y.

[48] H. Liao, C. L. Nehl, and J. H. Hafner. Biomedical applications of plasmon resonant metal nanoparticles. *Nanomedicine*, 1(2):201–208, August 2006. ISSN 1743-5889, 1748-6963. doi:10.2217/17435889.1.2.201.

[49] Y. Tang and M. Ouyang. Tailoring properties and functionalities of metal nanoparticles through crystallinity engineering. *Nature Materials*, 6(10):754–759, October 2007. ISSN 1476-1122. doi:10.1038/nmat1982.

[50] Y. Shen, J. Zhou, T. Liu, Y. Tao, R. Jiang, M. Liu, G. Xiao, J. Zhu, Z.-K. Zhou, X. Wang, and others. Plasmonic gold mushroom arrays with refractive index sensing figures of merit approaching the theoretical limit. *Nature communications*, 4, 2013.

[51] H.-H. Jeong, A. G. Mark, M. Alarcón-Correa, I. Kim, P. Oswald, T.-C. Lee, and P. Fischer. Dispersion and shape engineered plasmonic nanosensors. *Nature Communications*, 7:11331, April 2016. ISSN 2041-1723. doi:10.1038/ncomms11331.

[52] M. Svedendahl, S. Chen, A. Dmitriev, and M. Käll. Refractometric Sensing Using Propagating versus Localized Surface Plasmons: A Direct Comparison. *Nano Letters*, 9(12):4428–4433, December 2009. ISSN 1530-6984. doi:10.1021/nl902721z.

[53] O. Kedem, A. Vaskevich, and I. Rubinstein. Critical Issues in Localized Plasnnon Sensing. *Journal of Physical Chemistry C*, 118(16):8227–8244, April 2014. ISSN 1932-7447. doi:10.1021/jp409954s. WOS:000335114200001.

[54] M. Svedendahl, R. Verre, and M. Käll. Refractometric biosensing based on optical phase flips in sparse and short-range-ordered nanoplasmonic layers. *Light: Science & Applications*, 3(11):e220, November 2014. doi:10.1038/lsa.2014.101.

[55] G. J. Nusz, A. C. Curry, S. M. Marinakos, A. Wax, and A. Chilkoti. Rational Selection of Gold Nanorod Geometry for Label-Free Plasmonic Biosensors. *ACS Nano*, 3(4):795–806, April 2009. ISSN 1936-0851, 1936-086X. doi:10.1021/nn8006465.

[56] K. L. Göeken, V. Subramaniam, and R. Gill. Enhancing spectral shifts of plasmon-coupled noble metal nanoparticles for sensing applications. *Phys. Chem. Chem. Phys.*, 17(1):422–427, 2015. ISSN 1463-9076, 1463-9084. doi:10.1039/C4CP03739A.

[57] A. Jakab, C. Rosman, Y. Khalavka, J. Becker, A. Trügler, U. Hohenester, and C. Sönnichsen. Highly Sensitive Plasmonic Silver Nanorods. *ACS Nano*, 5(9):6880–6885, September 2011. ISSN 1936-0851. doi:10.1021/nn200877b.

[58] D. B. Pedersen and S. Wang. Surface Plasmon Resonance Spectra of 2.8 *pm* 0.5 nm Diameter Copper Nanoparticles in Both Near and Far Fields. *The Journal of Physical Chemistry C*, 111(47):17493–17499, November 2007. ISSN 1932-7447, 1932-7455. doi:10.1021/jp075076x.

[59] I. Pastoriza-Santos, A. Sánchez-Iglesias, B. Rodríguez-González, and L. M. Liz-Marzán. Aerobic Synthesis of Cu Nanoplates with Intense Plasmon Resonances. *Small*, 5(4):440–443, February 2009. ISSN 16136810, 16136829. doi:10.1002/smll.200801088.

[60] D.-K. Kim, S. M. Yoo, T. J. Park, H. Yoshikawa, E. Tamiya, J. Y. Park, and S. Y. Lee. Plasmonic Properties of the Multispot Copper-Capped Nanoparticle Array Chip and Its Application to Optical Biosensors for Pathogen Detection of Multiplex DNAs. *Analytical Chemistry*, 83(16):6215–6222, August 2011. ISSN 0003-2700, 1520-6882. doi:10.1021/ac2007762.

[61] G. H. Chan, J. Zhao, G. C. Schatz, and R. P. V. Duyne. Localized Surface Plasmon Resonance Spectroscopy of Triangular Aluminum Nanoparticles. *The Journal of Physical Chemistry C*, 112(36):13958–13963, September 2008. ISSN 1932-7447, 1932-7455. doi:10.1021/jp804088z.

[62] C. Langhammer, M. Schwind, B. Kasemo, and I. Zorić. Localized Surface Plasmon Resonances in Aluminum Nanodisks. *Nano Letters*, 8(5):1461–1471, May 2008. ISSN 1530-6984, 1530-6992. doi:10.1021/nl080453i.

[63] M. W. Knight, N. S. King, L. Liu, H. O. Everitt, P. Nordlander, and N. J. Halas. Aluminum for Plasmonics. *ACS Nano*, 8(1):834–840, January 2014. ISSN 1936-0851, 1936-086X. doi:10.1021/nn405495q.

[64] I. Zorić, M. Zäch, B. Kasemo, and C. Langhammer. Gold, Platinum, and Aluminum Nanodisk Plasmons: Material Independence, Subradiance, and Damping Mechanisms. *ACS Nano*, 5(4):2535–2546, April 2011. ISSN 1936-0851, 1936-086X. doi:10.1021/nn102166t.

[65] A. M. Watson, X. Zhang, R. Alcaraz de la Osa, J. M. Sanz, F. González, F. Moreno, G. Finkelstein, J. Liu, and H. O. Everitt. Rhodium Nanoparticles for Ultraviolet Plasmonics. *Nano Letters*, 15(2):1095–1100, February 2015. ISSN 1530-6984, 1530-6992. doi:10.1021/nl5040623.

[66] H. Mach, D. B. Volkin, C. J. Burke, and C. R. Middaugh. Ultraviolet Absorption Spectroscopy. In *Protein Stability and Folding*, volume 40, pages 91–114. Humana Press, New Jersey, March 1995. ISBN 978-0-89603-301-6.

[67] H. Durchschlag, C. Fochler, B. Feser, S. Hausmann, T. Seroneit, M. Swientek, E. Swoboda, A. Winklmair, C. Wlček, and P. Zipper. Effects of X- and UV-irradiation on proteins. *Radiation Physics and Chemistry*, 47(3):501–505, March 1996. ISSN 0969806X. doi:10.1016/0969-806X(95)00138-N.

[68] R. P. Sinha and D.-P. Häder. UV-induced DNA damage and repair: a review. *Photochemical & Photobiological Sciences*, 1(4):225–236, April 2002. ISSN 1474905X, 14749092. doi:10.1039/b201230h.

[69] J. Kiefer. Effects of Ultraviolet Radiation on DNA. In G. Obe and Vijayalaxmi, editors, *Chromosomal Alterations*, pages 39–53. Springer Berlin Heidelberg, Berlin, Heidelberg, 2007. ISBN 978-3-540-71413-2.

[70] R. P. Rastogi, Richa, A. Kumar, M. B. Tyagi, and R. P. Sinha. Molecular Mechanisms of Ultraviolet Radiation-Induced DNA Damage and Repair. *Journal of Nucleic Acids*, 2010:1–32, 2010. ISSN 2090-021X. doi:10.4061/2010/592980.

[71] A. L. Santos, C. Moreirinha, D. Lopes, A. C. Esteves, I. Henriques, A. Almeida, M. R. M. Domingues, I. Delgadillo, A. Correia, and A. Cunha. Effects of UV Radiation on the Lipids and Proteins of Bacteria Studied by Mid-Infrared Spectroscopy. *Environmental Science & Technology*, page 130605071029004, June 2013. ISSN 0013-936X, 1520-5851. doi:10.1021/es400660g.

[72] J. M. McMahon, G. C. Schatz, and S. K. Gray. Plasmonics in the ultraviolet with the poor metals Al, Ga, In, Sn, Tl, Pb, and Bi. *Phys. Chem. Chem. Phys.*, 15(15): 5415–5423, 2013. ISSN 1463-9076, 1463-9084. doi:10.1039/C3CP43856B.

[73] D. Manchon, J. Lermé, T. Zhang, A. Mosset, C. Jamois, C. Bonnet, J.-M. Rye, A. Belarouci, M. Broyer, M. Pellarin, and E. Cottancin. Plasmonic coupling with most of the transition metals: a new family of broad band and near infrared nanoantennas. *Nanoscale*, 7(3):1181–1192, November 2014. ISSN 2040-3364, 2040-3372. doi:10.1039/C4NR05383D.

[74] S. Golmohammadi and A. Ahmadivand. Fano Resonances in Compositional Clusters of Aluminum Nanodisks at the UV Spectrum: a Route to Design Efficient and Precise Biochemical Sensors. *Plasmonics*, 9(6):1447–1456, December 2014. ISSN 1557-1955, 1557-1963. doi:10.1007/s11468-014-9762-8.

[75] U. Fano. Effects of Configuration Interaction on Intensities and Phase Shifts. *Physical Review*, 124(6):1866–1878, December 1961. doi:10.1103/PhysRev.124.1866.

[76] A. Bianconi. Ugo Fano and Shape Resonances. arXiv e-print cond-mat/0211452, November 2002.

[77] J. S. Sekhon and S. S. Verma. Rational Selection of Nanorod Plasmons: Material, Size, and Shape Dependence Mechanism for Optical Sensors. *Plasmonics*, 7(3):453–459, September 2012. ISSN 1557-1955, 1557-1963. doi:10.1007/s11468-012-9328-6.

[78] C. Noguez. Surface Plasmons on Metal Nanoparticles: The Influence of Shape and Physical Environment. *The Journal of Physical Chemistry C*, 111(10):3806–3819, March 2007. ISSN 1932-7447, 1932-7455. doi:10.1021/jp066539m.

[79] W. J. Galush, S. A. Shelby, M. J. Mulvihill, A. Tao, P. Yang, and J. T. Groves. A Nanocube Plasmonic Sensor for Molecular Binding on Membrane Surfaces. *Nano Letters*, 9(5):2077–2082, May 2009. ISSN 1530-6984, 1530-6992. doi:10.1021/nl900513k.

[80] J. M. McMahon, Y. Wang, L. J. Sherry, R. P. Van Duyne, L. D. Marks, S. K. Gray, and G. C. Schatz. Correlating the structure, optical spectra, and electrodynamics of single silver nanocubes. *The Journal of Physical Chemistry C*, 113(7):2731–2735, 2009.

[81] Q. Zhang, W. Li, C. Moran, J. Zeng, J. Chen, L.-P. Wen, and Y. Xia. Seed-Mediated Synthesis of Ag Nanocubes with Controllable Edge Lengths in the Range of 30-200 nm and Comparison of Their Optical Properties. *Journal of the American Chemical Society*, 132(32):11372–11378, August 2010. ISSN 0002-7863, 1520-5126. doi:10.1021/ja104931h.

[82] N. Grillet, D. Manchon, F. Bertorelle, C. Bonnet, M. Broyer, E. Cottancin, J. Lermé, M. Hillenkamp, and M. Pellarin. Plasmon Coupling in Silver Nanocube Dimers: Resonance Splitting Induced by Edge Rounding. *ACS Nano*, 5(12):9450–9462, December 2011. ISSN 1936-0851, 1936-086X. doi:10.1021/nn2041329.

[83] H.-J. Wu, J. Henzie, W.-C. Lin, C. Rhodes, Z. Li, E. Sartorel, J. Thorner, P. Yang, and J. T. Groves. Membrane-protein binding measured with solution-phase plasmonic nanocube sensors. *nature methods*, 9(12):1189–1191, 2012.

[84] V. Klimov, G.-Y. Guo, and M. Pikhota. Plasmon Resonances in Metal Nanoparticles with Sharp Edges and Vertices: A Material Independent Approach. *The Journal of Physical Chemistry C*, 118(24):13052–13058, June 2014. ISSN 1932-7447, 1932-7455. doi:10.1021/jp412349f.

[85] M. Pellarin, J. Ramade, J. M. Rye, C. Bonnet, M. Broyer, M.-A. Lebeault, J. Lermé, S. Marguet, J. R. Navarro, and E. Cottancin. Fano Transparency in Rounded Nanocube Dimers Induced by Gap Plasmon Coupling. *ACS Nano*, 10(12):11266–11279, December 2016. ISSN 1936-0851, 1936-086X. doi:10.1021/acsnano.6b06406.

[86] B. Nikoobakht and M. A. El-Sayed. Preparation and Growth Mechanism of Gold Nanorods (NRs) Using Seed-Mediated Growth Method. *Chemistry of Materials*, 15 (10):1957–1962, May 2003. ISSN 0897-4756. doi:10.1021/cm020732l.

[87] M. M. Miller and A. A. Lazarides. Sensitivity of Metal Nanoparticle Surface Plasmon Resonance to the Dielectric Environment. *The Journal of Physical Chemistry B*, 109(46):21556–21565, November 2005. ISSN 1520-6106. doi:10.1021/jp054227y.

[88] C. Sönnichsen and A. P. Alivisatos. Gold Nanorods as Novel Nonbleaching Plasmon-Based Orientation Sensors for Polarized Single-Particle Microscopy. *Nano Letters*, 5(2):301–304, February 2005. ISSN 1530-6984. doi:10.1021/nl048089k.

[89] M. Hu, J. Chen, Z.-Y. Li, L. Au, G. V. Hartland, X. Li, M. Marquez, and Y. Xia. Gold nanostructures: engineering their plasmonic properties for biomedical applications. *Chemical Society Reviews*, 35(11):1084–1094, October 2006. ISSN 1460-4744. doi:10.1039/B517615H.

[90] C.-D. Chen, S.-F. Cheng, L.-K. Chau, and C. C. Wang. Sensing capability of the localized surface plasmon resonance of gold nanorods. *Biosensors and Bioelectronics*, 22(6):926–932, 2007.

[91] S. M. Marinakos, S. Chen, and A. Chilkoti. Plasmonic detection of a model analyte in serum by a gold nanorod sensor. *Analytical chemistry*, 79(14):5278–5283, 2007.

[92] C. Yu, H. Nakshatri, and J. Irudayaraj. Identity Profiling of Cell Surface Markers by Multiplex Gold Nanorod Probes. *Nano Letters*, 7(8):2300–2306, August 2007. ISSN 1530-6984. doi:10.1021/nl070894m.

[93] P. K. Jain, X. Huang, I. H. El-Sayed, and M. A. El-Sayed. Noble Metals on the Nanoscale: Optical and Photothermal Properties and Some Applications in Imag-

ing, Sensing, Biology, and Medicine. *Accounts of Chemical Research*, 41(12):1578–1586, December 2008. ISSN 0001-4842. doi:10.1021/ar7002804.

[94] C. Wang and J. Irudayaraj. Gold Nanorod Probes for the Detection of Multiple Pathogens. *Small*, 4(12):2204–2208, December 2008. ISSN 16136810, 16136829. doi:10.1002/smll.200800309.

[95] L. J. E. Anderson, K. M. Mayer, R. D. Fraleigh, Y. Yang, S. Lee, and J. H. Hafner. Quantitative Measurements of Individual Gold Nanoparticle Scattering Cross Sections. *The Journal of Physical Chemistry C*, 114(25):11127–11132, July 2010. ISSN 1932-7447. doi:10.1021/jp1040663.

[96] C. R. Carey, T. LeBel, D. Crisostomo, J. Giblin, M. Kuno, and G. V. Hartland. Imaging and Absolute Extinction Cross-Section Measurements of Nanorods and Nanowires through Polarization Modulation Microscopy †. *The Journal of Physical Chemistry C*, 114(38):16029–16036, September 2010. ISSN 1932-7447, 1932-7455. doi:10.1021/jp101891a.

[97] M. A. Otte, B. Sepúlveda, W. Ni, J. P. Juste, L. M. Liz-Marzán, and L. M. Lechuga. Identification of the optimal spectral region for plasmonic and nanoplasmonic sensing. *ACS nano*, 4(1):349–357, January 2010. ISSN 1936-086X. doi:10.1021/nn901024e.

[98] A. Lombardi, M. Loumaigne, A. Crut, P. Maioli, N. Del Fatti, F. Vallée, M. Spuch-Calvar, J. Burgin, J. Majimel, and M. Tréguer-Delapierre. Surface Plasmon Resonance Properties of Single Elongated Nano-objects: Gold Nanobipyramids and Nanorods. *Langmuir*, 28(24):9027–9033, June 2012. ISSN 0743-7463. doi:10.1021/la300210h.

[99] P. Zijlstra, P. M. R. Paulo, and M. Orrit. Optical detection of single non-absorbing molecules using the surface plasmon resonance of a gold nanorod. *Nature nanotechnology*, 7(6):379–382, June 2012. ISSN 1748-3395. doi:10.1038/nnano.2012.51.

[100] S. Balamurugan, K. M. Mayer, S. Lee, S. A. Soper, J. H. Hafner, and D. A. Spivak. Nanostructure shape effects on response of plasmonic aptamer sensors. *Journal of Molecular Recognition*, 26(9):402–407, September 2013. ISSN 1099-1352. doi:10.1002/jmr.2278.

[101] W. Ma, H. Kuang, L. Xu, L. Ding, C. Xu, L. Wang, and N. A. Kotov. Attomolar DNA detection with chiral nanorod assemblies. *Nature communications*, 4, 2013.

[102] C. Rosman, J. Prasad, A. Neiser, A. Henkel, J. Edgar, and C. Sönnichsen. Multiplexed Plasmon Sensor for Rapid Label-Free Analyte Detection. *Nano Letters*, 13 (7):3243–3247, July 2013. ISSN 1530-6984. doi:10.1021/nl401354f.

[103] J. R. G. Navarro, D. Manchon, F. Lerouge, N. P. Blanchard, S. Marotte, Y. Leverrier, J. Marvel, F. Chaput, G. Micouin, A.-M. Gabudean, A. Mosset, E. Cottancin, P. L. Baldeck, K. Kamada, and S. Parola. Synthesis of PEGylated gold nanostars and bipyramids for intracellular uptake. *Nanotechnology*, 23(46):465602, November 2012. ISSN 0957-4484. doi:10.1088/0957-4484/23/46/465602.

[104] J. Burgin, M. Liu, and P. Guyot-Sionnest. Dielectric Sensing with Deposited Gold Bipyramids. *The Journal of Physical Chemistry C*, 112(49):19279–19282, December 2008. ISSN 1932-7447. doi:10.1021/jp807465p.

[105] K. M. Mayer, F. Hao, S. Lee, P. Nordlander, and J. H. Hafner. A single molecule immunoassay by localized surface plasmon resonance. *Nanotechnology*, 21(25):255503, June 2010. ISSN 0957-4484. doi:10.1088/0957-4484/21/25/255503.

[106] M. J. Guffey, R. L. Miller, S. K. Gray, and N. F. Scherer. Plasmon-Driven Selective Deposition of Au Bipyramidal Nanoparticles. *Nano Letters*, 11(10):4058–4066, October 2011. ISSN 1530-6984. doi:10.1021/nl201020g.

[107] Y. Khalavka, J. Becker, and C. Sönnichsen. Synthesis of Rod-Shaped Gold Nanorattles with Improved Plasmon Sensitivity and Catalytic Activity. *Journal of the American Chemical Society*, 131(5):1871–1875, February 2009. ISSN 0002-7863, 1520-5126. doi:10.1021/ja806766w.

[108] Y. Sun and Y. Xia. Increased Sensitivity of Surface Plasmon Resonance of Gold Nanoshells Compared to That of Gold Solid Colloids in Response to Environmental Changes. *Analytical Chemistry*, 74(20):5297–5305, October 2002. ISSN 0003-2700, 1520-6882. doi:10.1021/ac0258352.

[109] A. Sundaramurthy, K. B. Crozier, G. S. Kino, D. P. Fromm, P. J. Schuck, and W. E. Moerner. Field enhancement and gap-dependent resonance in a system of two opposing tip-to-tip Au nanotriangles. *Physical Review B*, 72(16), October 2005. ISSN 1098-0121, 1550-235X. doi:10.1103/PhysRevB.72.165409.

[110] L. Novotny and N. van Hulst. Antennas for light. *Nature Photonics*, 5(2):83–90, February 2011. ISSN 1749-4885. doi:10.1038/nphoton.2010.237.

[111] Y.-M. Wu, L.-W. Li, and B. Liu. Gold Bow-Tie Shaped Aperture Nanoantenna: Wide Band Near-field Resonance and Far-Field Radiation. *IEEE Transactions on Magnetics*, 46(6):1918–1921, June 2010. ISSN 0018-9464. doi:10.1109/TMAG.2010.2043063.

[112] N. Verellen, P. Van Dorpe, C. Huang, K. Lodewijks, G. A. E. Vandenbosch, L. Lagae, and V. V. Moshchalkov. Plasmon Line Shaping Using Nanocrosses for High Sensitivity Localized Surface Plasmon Resonance Sensing. *Nano Letters*, 11(2): 391–397, February 2011. ISSN 1530-6984. doi:10.1021/nl102991v.

[113] S. J. Zalyubovskiy, M. Bogdanova, A. Deinega, Y. Lozovik, A. D. Pris, K. H. An, W. P. Hall, and R. A. Potyrailo. Theoretical limit of localized surface plasmon resonance sensitivity to local refractive index change and its comparison to conventional surface plasmon resonance sensor. *JOSA A*, 29(6):994–1002, 2012.

[114] S. Link and M. A. El-Sayed. Size and Temperature Dependence of the Plasmon Absorption of Colloidal Gold Nanoparticles. *The Journal of Physical Chemistry B*, 103(21):4212–4217, May 1999. ISSN 1520-6106, 1520-5207. doi:10.1021/jp984796o.

[115] A. J. Haes, S. Zou, G. C. Schatz, and R. P. Van Duyne. Nanoscale Optical Biosensor: Short Range Distance Dependence of the Localized Surface Plasmon Resonance of Noble Metal Nanoparticles. *The Journal of Physical Chemistry B*, 108(22):6961–6968, June 2004. ISSN 1520-6106. doi:10.1021/jp036261n.

[116] T. J. Antosiewicz, S. P. Apell, V. Claudio, and M. Käll. A simple model for the resonance shift of localized plasmons due to dielectric particle adhesion. *Optics Express*, 20(1):524–533, January 2012. ISSN 1094-4087. doi:10.1364/OE.20.000524.

[117] I. Ament, J. Prasad, A. Henkel, S. Schmachtel, and C. Sönnichsen. Single Unlabeled

Protein Detection on Individual Plasmonic Nanoparticles. *Nano Letters*, 12(2): 1092–1095, February 2012. ISSN 1530-6984, 1530-6992. doi:10.1021/nl204496g.

[118] M. A. Beuwer, M. W. J. Prins, and P. Zijlstra. Stochastic Protein Interactions Monitored by Hundreds of Single-Molecule Plasmonic Biosensors. *Nano Letters*, 15(5):3507–3511, May 2015. ISSN 1530-6984, 1530-6992. doi:10.1021/acs.nanolett.5b00872.

[119] R. Weissleder. A clearer vision for in vivo imaging. *Nature biotechnology*, 19(4): 316–317, 2001.

[120] A. M. Smith, M. C. Mancini, and S. Nie. Bioimaging: Second window for in vivo imaging. *Nature Nanotechnology*, 4(11):710–711, November 2009. ISSN 1748-3387. doi:10.1038/nnano.2009.326.

[121] R. Förch and A. T. A. Jenkins. *Surface Design: Applications in Bioscience and Nanotechnology*. John Wiley & Sons, July 2009. ISBN 978-3-527-40789-7.

[122] L. Pugliese, A. Coda, M. Malcovati, and M. Bolognesi. Three-dimensional Structure of the Tetragonal Crystal Form of Egg-white Avidin in its functional Complex with Biotin at 2·7 Å Resolution. *Journal of Molecular Biology*, 231(3):698–710, June 1993. ISSN 0022-2836. doi:10.1006/jmbi.1993.1321.

[123] A. Kuzuya, K. Numajiri, M. Kimura, and M. Komiyama. Single-Molecule Accommodation of Streptavidin in Nanometer-Scale Wells Formed in DNA Nanostructures. *Nucleic Acids Symposium Series*, 52(1):681–682, September 2008. ISSN 0261-3166, 1746-8272. doi:10.1093/nass/nrn344.

[124] P. Pramod, S. T. S. Joseph, and K. G. Thomas. Preferential End Functionalization of Au Nanorods through Electrostatic Interactions. *Journal of the American Chemical Society*, 129(21):6712–6713, May 2007. ISSN 0002-7863. doi:10.1021/ja071536o.

[125] P. Zijlstra, P. M. R. Paulo, K. Yu, Q.-H. Xu, and M. Orrit. Chemical Interface Damping in Single Gold Nanorods and Its Near Elimination by Tip-Specific Functionalization. *Angewandte Chemie International Edition*, 51(33):8352–8355, August 2012. ISSN 14337851. doi:10.1002/anie.201202318.

[126] N. Nath and A. Chilkoti. A colorimetric gold nanoparticle sensor to interrogate biomolecular interactions in real time on a surface. *Analytical chemistry*, 74(3): 504–509, 2002.

[127] R. J. Meier. On art and science in curve-fitting vibrational spectra. *Vibrational Spectroscopy*, 39(2):266–269, 2005.

[128] A. Crut, P. Maioli, N. D. Fatti, and F. Vallée. Optical absorption and scattering spectroscopies of single nano-objects. *Chemical Society Reviews*, 43(11):3921–3956, May 2014. ISSN 1460-4744. doi:10.1039/C3CS60367A.

[129] Glycerine Producers' Association. *Physical properties of glycerine and its solutions*. Glycerine Producers' Association, New York, 1963. OCLC: 5178554.

[130] R. Mehra. Application of refractive index mixing rules in binary systems of hexadecane and heptadecane withn-alkanols at different temperatures. *Journal of Chemical Sciences*, 115(2):147–154, 2003.

[131] M. Born, E. Wolf, A. B. Bhatia, P. C. Clemmow, D. Gabor, A. R. Stokes, A. M. Taylor, P. A. Wayman, and W. L. Wilcock. *Principles of Optics: Electromagnetic Theory of Propagation, Interference and Diffraction of Light*. Cambridge University

Press, Cambridge ; New York, 7th edition edition, October 1999. ISBN 978-0-521-64222-4.

Backscattering Measurements

The previous chapters have focused on the measurement of localized surface plasmon resonance (LSPR) peak shifts as a method of detecting changes in the refractive index (RI) around a plasmonic probe. We have seen that the measured shifts are not as large as expected from theoretical calculations and that the sensitivity may be insufficient to detect the presence of a small number of molecules in the vicinity of the plasmonic probe. Recently, approaches that seek instead to exploit phase-shifts have begun to appear in the literature as a possibly more sensitive method for plasmonic biosensing[1–16]. As an analogy, consider the case of a classic oscillator such as a mass on a spring (figure 3.51). There is an abrupt change in the phase relationship between the oscillator and the driving force near the resonance position. Although not identical, Mie theory predicts a similar phenomenon for the phase relationship between the incident and scattered field of a spherical plasmonic nanoparticle (NP) near the LSPR (figure 3.51).

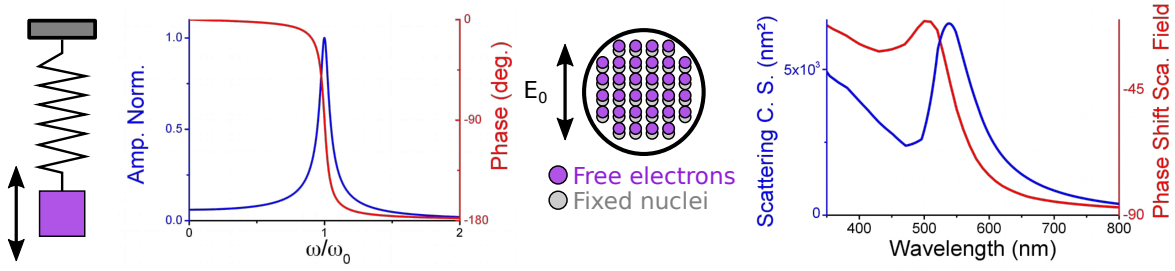

(a) classic oscillator **(b)** plasmonic oscillator

Figure 3.51: Comparison of the phase of classic and plasmonic oscillators relative to the driving frequency. (a) Normalized amplitude and relative phase of a mass on a spring. (b) Scattering cross-section and relative phase of a gold sphere of radius 40 nm (Mie theory calculations).

The idea is to exploit the abrupt change in phase through interferometry. This can be done by using a reflected field as a reference that interferes with a backscattered field. To explore such measurements, we have adapted the liquid spatial modulation spectroscopy (LSMS) setup as shown schematically in figure 3.52. Light reflected from the substrate and backscattered from the NP is directed to a second spectrometer and photodiode.

This "reflection" pathway is independent of the "transmission" pathway and generates separate DC and X signals via a second lock-in amplifier. Both of these are recorded in parallel with the transmission signals.

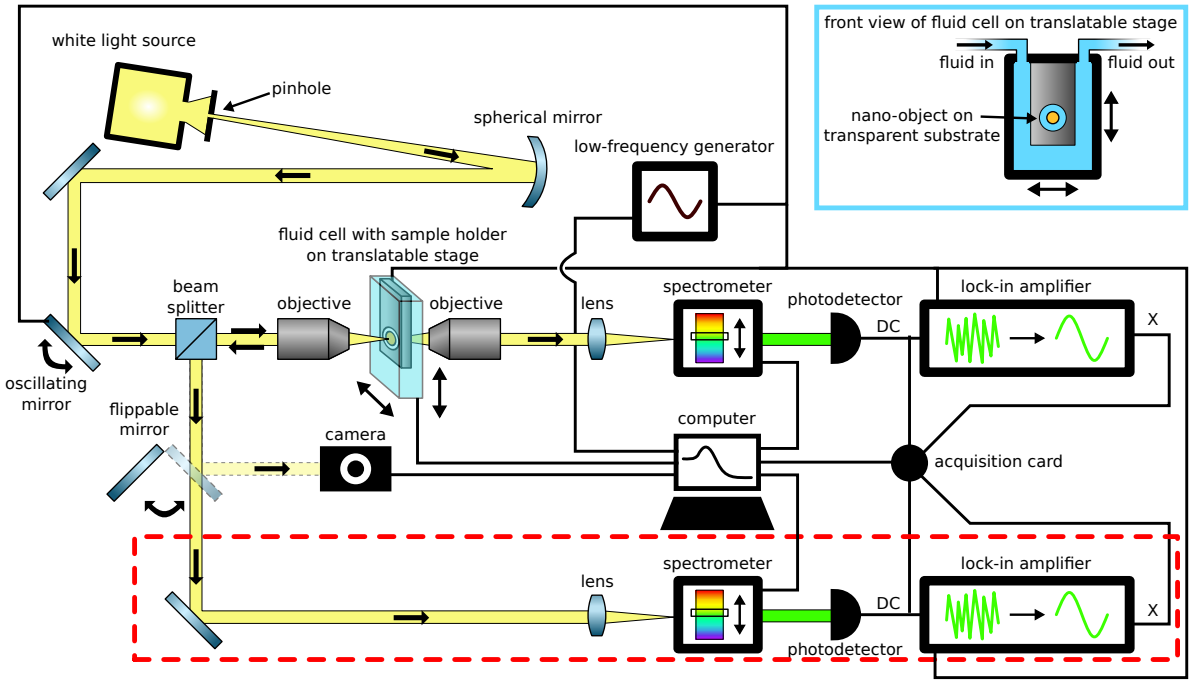

Figure 3.52: A further modification of the LSMS setup (figure on page 104): Light reflected and backscattered from the sample passes back through the first objective and through the beam splitter, which directs it to a second spectrometer, detector and lock-in amplifier. The modifications are marked with a dashed red rectangle.

Figure 3.53 presents a simplified schematic overview of the light collected along each path. Most of the incident light passes through the sample and is collected along the transmission pathway along with a fraction of the scattered light from the NP that is negligible compared to the transmitted light. The reflection pathway collects light that is reflected from the glass substrate and backscattered from the NP. The measured signal will depend on the irradiance of these two interfering fields, which may be expressed as

$$I \propto E_r^2 + E_s^2 + 2E_r E_s \cos(\phi) \tag{i}$$

where E_r and E_s are the amplitudes of the fields reflected from the substrate and backscattered from the object, respectively, and ϕ is the phase difference between them, which depends on the LSPR, among other things. Under spatial modulation spectroscopy (SMS) with a homogeneous substrate, the term in E_r^2 is constant and will generate an unmodulated DC signal. For object sizes on the order of tens of nanometers, the term in E_s^2 will

be negligible compared to $2E_rE_s\cos(\phi)$. The measurable signal X will therefore depend mostly on the phase relationship between these fields. Because the signal depends on E_s rather than E_s^2, it scales with the volume V of the object instead of with V^2 and is therefore comparable in strength to the transmission measurements and thus potentially exploitable for sensitive measurements.

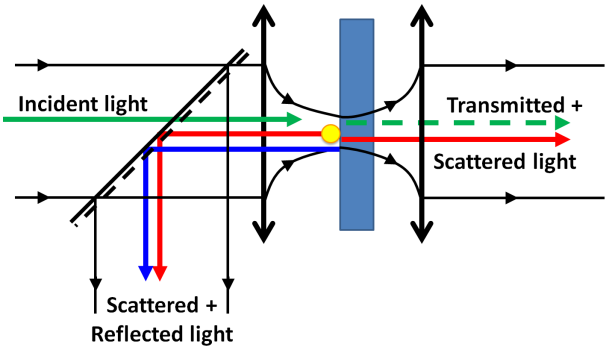

Figure 3.53: Schematic diagram of the electric fields along the transmission and reflection paths of the LSMS setup shown in figure 3.52.

The transmission and reflection spectra of a single gold bipyramid (BP) in air is shown in figure 3.54. The transmission spectrum presents a large longitudinal LSPR peak at approximately 775 nm. The reflection spectrum shows a very different line shape. The intensity of this spectrum is over 5 times greater than the transmission spectrum and abruptly switches signs near the resonance wavelength due to a phase-shift in the scattered field of the LSPR relative to the reflected field. The position of the sign inversion of this abrupt shift in the reflection spectrum is expected to be easier to detect than a shift in the peak position of the transmission spectrum and thus lead to greater sensitivity.

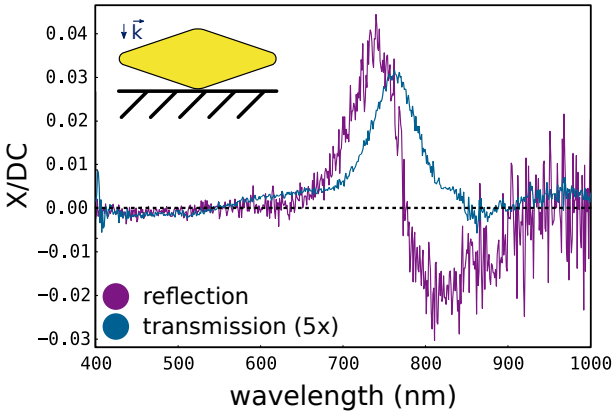

Figure 3.54: Transmission and reflection spectra of a single gold BP in air on a glass substrate. The transmission spectrum has been multiplied by 5 for comparison.

The strength of the reflected field depends on the RI of the substrate and the medium

via the Fresnel equations (section 1.3.2.2). The coefficient of reflection at an air-glass interface is 0.2. If the air is replaced with water, this falls to 0.06. From (i), we see that the measured signal strength should be directly proportional to this coefficient. To test if reflection measurements were possible on a glass substrate in water, the lithographed sample described in section 2.3.1 was immersed in water and mapped at 560 nm in transmission and reflection. The disks in the mapped region have a diameter of $\sim$ 300 nm. The results are shown in figure 3.55. The regular 2D array of objects is readily visible in both maps. Despite the lower coefficient of reflection, the signal is an order of magnitude greater than the transmission signal, similar to the result in figure 3.54. This map shows that measurements in water on glass are feasible. Even if weak reflection coefficients were to become an issue, a different substrate such as TiO_2 ($n \approx 2.5$) could be used to increase the relative RI difference between it and the medium. Of course, effects of the substrate on the studied objects such as spectral shifts and LSPR damping would need to be studied to determine if the substrate is suitable for sensing applications. Surface chemistry will also need to be considered for sample preparation and functionalization.

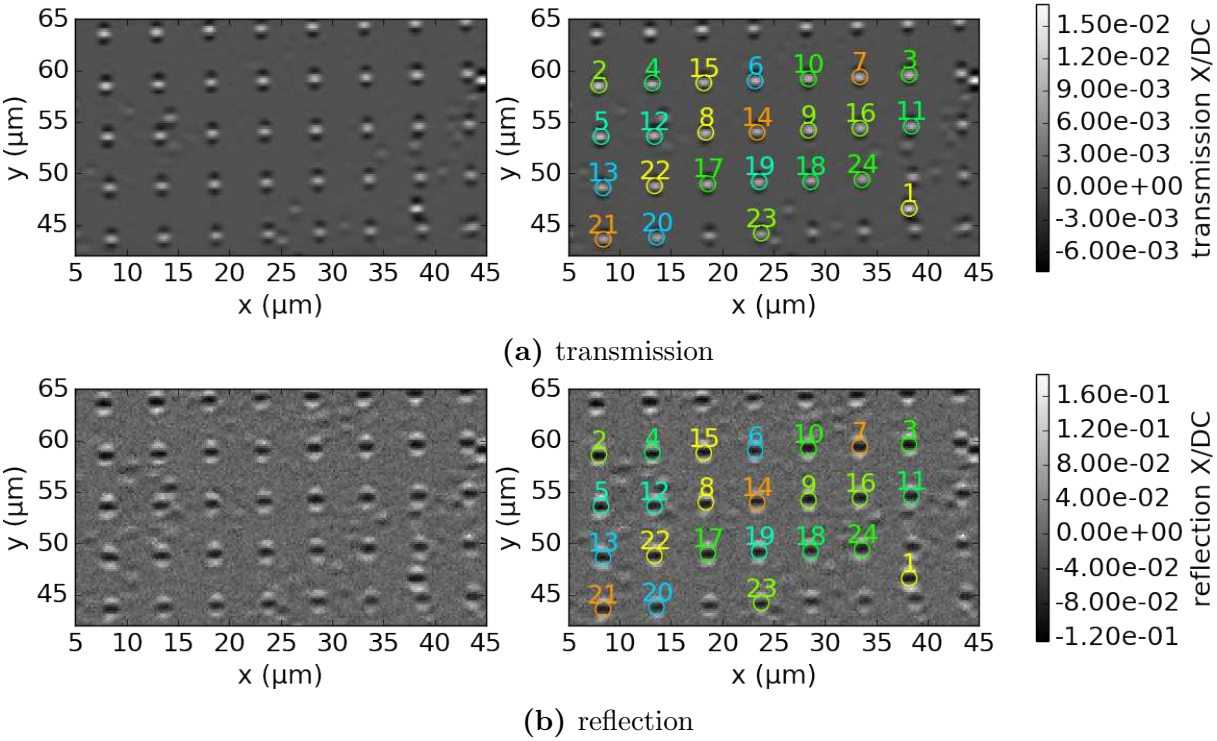

(a) transmission

(b) reflection

Figure 3.55: Transmission and reflection maps of the lithographed sample from section 2.3.1 in water at 560 nm. Automatically tracked objects are shown on the right.

The transmission and reflection spectra of the tracked disks in figure 3.55 are shown in figure 3.56. Overall, both sets of spectra show relatively little dispersion. The transmission spectra are very broad with a resonance around 600 nm. The bump around 850 nm is due to the dip in the lamp's intensity profile (figure F.4 on page 243 of the appendix). The reflection signal is relatively flat with an abrupt change in sign around 750 nm. Unlike

the previous example with the BP in air, the sign inversion does not coincide spectrally with the apparent LSPR resonance.

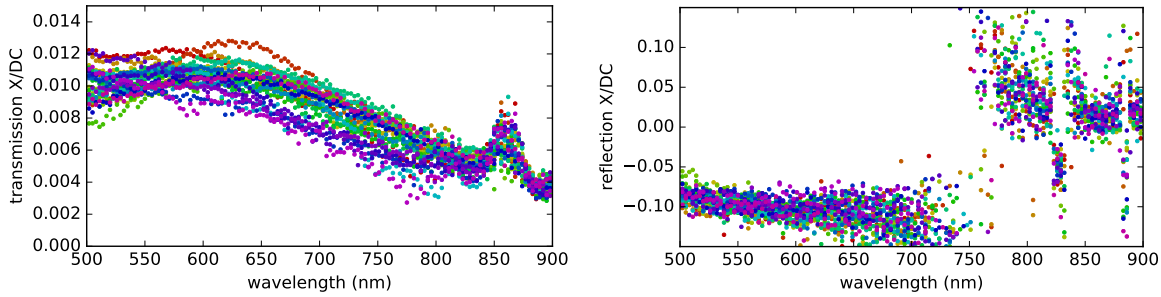

(a) transmission **(b)** reflection

Figure 3.56: Transmission and reflection spectra of objects 2-24 in figure 3.55.

This highlights the main difficulty of this approach, which is that the interference between the fields collected along the reflection pathway strongly depends on multiple factors, such as the object's distance from the surface, orientation and LSPR response. To fully exploit phase-based interferometric measurements, precise sample fabrications techniques are required to control the exact geometry of the sample. Lithographic techniques may be the best way to do this. For example, dielectric pillars could be used as spacers between the object and surface[17], whereupon precise positioning of the BPs on the micropillars may be possible using a technique such as angular trapping[18].

Despite these challenges, the abrupt shift in the reflection signal of the BP in figure 3.54 indicates that this approach has considerable potential for increasing the sensitivity of biosensing applications. We expect that advances in nano-manipulation techniques will facilitate the precise fabrication of such samples in the future and lead to a rapid development of highly sensitive phase-based sensing techniques. We would have liked to explore this avenue further during this work but there was unfortunately not enough time.

References

[1] O. Kedem, A. Vaskevich, and I. Rubinstein. Improved Sensitivity of Localized Surface Plasmon Resonance Transducers Using Reflection Measurements. *Journal of Physical Chemistry Letters*, 2(10):1223–1226, May 2011. ISSN 1948-7185. doi:10.1021/jz200482f. WOS:000290843700021.

[2] V. G. Kravets, F. Schedin, A. V. Kabashin, and A. N. Grigorenko. Sensitivity of collective plasmon modes of gold nanoresonators to local environment. *Optics Letters*, 35(7):956–958, April 2010. ISSN 1539-4794. doi:10.1364/OL.35.000956.

[3] T. Sannomiya, T. E. Balmer, C. Hafner, M. Heuberger, and J. Vörös. Optical sensing and determination of complex reflection coefficients of plasmonic structures using transmission interferometric plasmonic sensor. *Review of Scientific Instruments*, 81 (5):053102, May 2010. ISSN 0034-6748, 1089-7623. doi:10.1063/1.3405912.

[4] R. S. Moirangthem, Y.-C. Chang, and P.-K. Wei. Investigation of surface plasmon biosensing using gold nanoparticles enhanced ellipsometry. *Optics Letters*, 36(5): 775–777, March 2011. ISSN 1539-4794. doi:10.1364/OL.36.000775.

[5] Y. Huang, H. Ho, S. Kong, and A. Kabashin. Phase-sensitive surface plasmon resonance biosensors: methodology, instrumentation and applications. *Annalen der Physik*, 524(11):637–662, 2012. ISSN 1521-3889. doi:10.1002/andp.201200203.

[6] K. Lodewijks, W. Van Roy, G. Borghs, L. Lagae, and P. Van Dorpe. Boosting the Figure-Of-Merit of LSPR-Based Refractive Index Sensing by Phase-Sensitive Measurements. *Nano Letters*, 12(3):1655–1659, March 2012. ISSN 1530-6984. doi:10.1021/nl300044a.

[7] M. Svedendahl, R. Verre, and M. Käll. Refractometric biosensing based on optical phase flips in sparse and short-range-ordered nanoplasmonic layers. *Light: Science & Applications*, 3(11):e220, November 2014. doi:10.1038/lsa.2014.101.

[8] L. Piatkowski, E. Gellings, and N. F. van Hulst. Broadband single-molecule excitation spectroscopy. *Nature Communications*, 7:10411, January 2016. ISSN 2041-1723. doi:10.1038/ncomms10411. WOS:000369022500002.

[9] F. V. Ignatovich and L. Novotny. Real-Time and Background-Free Detection of Nanoscale Particles. *Physical Review Letters*, 96(1):013901, January 2006. doi:10.1103/PhysRevLett.96.013901.

[10] O. Avci, N. L. Unlu, A. Y. Ozkumur, and M. S. Unlu. Interferometric Reflectance Imaging Sensor (IRIS)-A Platform Technology for Multiplexed Diagnostics and Digital Detection. *Sensors*, 15(7):17649–17665, July 2015. ISSN 1424-8220. doi:10.3390/s150717649. WOS:000361788200144.

[11] M. Svedendahl and M. Käll. Fano Interference between Localized Plasmons and Interface Reflections. *ACS Nano*, 6(8):7533–7539, August 2012. ISSN 1936-0851. doi:10.1021/nn302879j.

[12] K. Lindfors, T. Kalkbrenner, P. Stoller, and V. Sandoghdar. Detection and Spectroscopy of Gold Nanoparticles Using Supercontinuum White Light Confocal Microscopy. *Physical Review Letters*, 93(3):037401, July 2004. doi:10.1103/PhysRevLett.93.037401.

[13] M. Piliarik and V. Sandoghdar. Direct optical sensing of single unlabelled proteins and super-resolution imaging of their binding sites. *Nature Communications*, 5, July 2014. ISSN 2041-1723. doi:10.1038/ncomms5495.

[14] S. Spindler, J. Ehrig, K. Koenig, T. Nowak, M. Piliarik, H. E. Stein, R. W. Taylor, E. Garanger, S. Lecommandoux, I. D. Alves, and V. Sandoghdar. Visualization of lipids and proteins at high spatial and temporal resolution via interferometric scattering (iSCAT) microscopy. *Journal of Physics D-Applied Physics*, 49(27):274002, July 2016. ISSN 0022-3727. doi:10.1088/0022-3727/49/27/274002. WOS:000380763700004.

[15] J. Andrecka, J. O. Arroyo, K. Lewis, R. A. Cross, and P. Kukura. Label-free

Imaging of Microtubules with Sub-nm Precision Using Interferometric Scattering Microscopy. *Biophysical Journal*, 110(1):214–217, January 2016. ISSN 0006-3495. doi:10.1016/j.bpj.2015.10.055. WOS:000367783900014.

[16] A. M. Goldfain, R. F. Garmann, Y. Jin, Y. Lahini, and V. N. Manoharan. Dynamic Measurements of the Position, Orientation, and DNA Content of Individual Unlabeled Bacteriophages. *Journal of Physical Chemistry B*, 120(26):6130–6138, July 2016. ISSN 1520-6106. doi:10.1021/acs.jpcb.6b02153. WOS:000379457200039.

[17] A. Dmitriev, C. Hägglund, S. Chen, H. Fredriksson, T. Pakizeh, M. Käll, and D. S. Sutherland. Enhanced nanoplasmonic optical sensors with reduced substrate effect. *Nano letters*, 8(11):3893–3898, 2008.

[18] M. Celebrano, C. Rosman, C. Sönnichsen, and M. Krishnan. Angular Trapping of Anisometric Nano-Objects in a Fluid. *Nano Letters*, 12(11):5791–5796, November 2012. ISSN 1530-6984, 1530-6992. doi:10.1021/nl303099c.

Conclusion And Perspectives

Conclusion

The aim of this project has been to develop a spatial modulation spectroscopy (SMS) setup to measure the optical response of individual nanoparticles (NPs) in a liquid environment for biosensing applications. This task is inherently multidisciplinary and so the project has been undertaken as a collaboration between the Clusters and Nanostructures group at the Institute of Light and Matter (ILM) of Université Claude Bernard Lyon 1 (UCBL) and the Functional Materials and Photonics group at the Laboratoire de Chimie (LC) of École Normale Supérieure de Lyon (ENS de Lyon). Working closely with the physicists at ILM, multiple challenges have been overcome to create a liquid spatial modulation spectroscopy (LSMS) setup. In parallel, sensitive plasmonic probes have been developed with the chemists at LC for use with this setup. This has involved a strong feedback loop between both groups in which I have been able to act as an intermediary. Each set of samples produced with the chemists has been studied with the physicists and the results have been used to guide further sample development to overcome the identified challenges. Alongside the experimental work, theoretical studies have also been undertaken to understand our observations and guide our efforts.

In the first chapter, we have explored the basic theory of localized surface plasmon resonance (LSPR) in metallic nano-objects (MNOs) and we have seen how this phenomenon depends on the size, shape, composition and local environment around the MNO. We have explored the influence of several factors such as the presence of a substrate, wetting and shape effects through numerical simulations and we have shown that in some cases, the cumulative effect of these factors may be taken into account through a simplified model using an effective real refractive index (RI), n_{eff}. The validity of this approach is not universal and it does not work well with faceted objects near a surface.

In the second chapter, the specific adaptations that were necessary to develop the LSMS setup have been presented. Following these adaptations, multiple tests were performed to characterize the new setup and determine the reliability of its measurements. Tests with different samples have demonstrated that the setup is able to accurately map and measure the optical response of individual NPs in both air and liquid environments. In particular,

the setup has been calibrated and can be used to measure the absolute extinction cross-section of individual NPs in a liquid environment. This in itself makes the new setup a powerful tool for fundamental research.

The main aim of this work has nevertheless been to explore biosensing applications based on plasmonic probes. The choice of the probe is a crucial aspect of such applications and so in the third chapter we have explored the various properties that should be considered when making this choice. We have shown that gold bipyramids (BPs) possess several attributes that are promising for biosensing applications: an elongated shape that leads to a strong and narrow LSPR peak and highly localized field enhancements at the tips (hot spots); a configurable synthesis that can be adjusted to control the optical response of the object; and surface chemistry that is inert to biological and oxidative reactions yet susceptible to procedures such as silanization. Furthermore, our group has worked extensively with gold BP and we are able to consistently obtain high yields with tailored sizes and LSPR responses[1–3].

In order to prepare samples of BPs for measurements with the LSMS setup, a sample preparation protocol has also been developed. The protocol uses silanization to graft gold NPs to a glass substrate and it can be used for gold NPs of any shape. Initial tests with gold spheres have shown that silanization does not impede optical measurements with the setup or significantly affect the optical response of the objects on the sample. In particular, we have measured the absolute extinction cross-section of individual gold nano spheres on a silanized sample in both air and water and shown that these measurements are in very good agreement with generalized Mie theory (GMT) calculations, both qualitatively and quantitatively.

As a first step towards sensing applications, silanized samples of BPs have been used to detect RI index changes of different media (air, water, glycerol and different water-glycerol mixes) via shifts of the LSPR peak of individual BPs. Although the detected shifts have been weaker than predicted by theory, we surmise that the model used fails to account for local changes and the exact geometry of the objects. Nevertheless, an approximately linear relationship has been found between the spectral peak position and the RI of the medium, in agreement with the literature. Furthermore, the figure of merit (FOM) of these samples compare favorably with values found in the literature. In addition to static measurements, we have also been able to follow gradual changes in the RI due to the diffusion of glycerol in water over a 24 hour period, in part due to the automation capacity of the MICA interface software that was developed during the course of this work. This shows that the LSMS setup can be used for dynamic measurements.

The stability and robustness of the silanized samples have also been studied through consecutive measurements in air and in water. These studies have shown that the quality of the sample is critical for long-term stability and reusability. With the current version of our sample preparation protocol, samples of BPs remain stable even after months of dry storage with no detectable change in the optical response of the grafted objects.

An extension of the LSMS setup has also been developed to explore interferometric backscattering measurements as a method of increasing the sensitivity of sensing applications. Although we have not had time to fully develop this approach, initial results have shown that BPs may exhibit abrupt sign inversions in their backscattered signals due to phase shifts around their LSPR. Minor changes in these inversions induced by the local environment around the object are expected to be easier to detect than the matching LSPR peak shifts, which is very promising for future applications.

Perspectives

For label-free[17] biosensing applications, the BPs must be functionalized. A protocol has been developed by our group but there was not enough time to test the protocol within this work. Initial sensing tests will be based on the biotin-streptavidin molecular recognition system. This system is widely used in molecular biology due to the high binding affinity between biotin, a small B-vitamin, and the protein streptavidin and it has become a very common proof-of-principle assay for optical biosensing applications in the literature[4–23]. If the initial tests with the biotin-streptavidin system are successful, subsequent tests will focus on the detection of biomedically relevant analytes in solution. For example, Alzheimer's disease is currently thought to be caused by assemblies of β-amyloid proteins known as amyloid-derived diffusable ligands (ADDLs) in the cerebrospinal fluid (CSF)[24–30]. The detection of ADDLs is a common clinically relevant assay for biosensing systems[31–34] and this would be the first "real" test with the LSMS setup. If these tests are successful, samples could be prepared for the label-free detection of a wide range of targets using standard biorecognition elements such as aptamers or antibody fragments[35].

In order to perform truly dynamic measurements, a pump system will be added to the setup and integrated into MICA. This will be used to automatically measure the effects of gradually changing concentrations of different analytes. The current method of measuring spectra by scanning wavelengths on the spectrometer will not be fast enough for dynamic measurements. We therefore plan to replace the spectrometer with a grating and a charge-coupled device (CCD) strip in order to measure the response at multiple wavelengths simultaneously. This will reduce the time of spectra acquisition by 2 orders of magnitude and enable observations of much faster processes. Because the CCD strip will generate a *DC* signal for each pixel, the function of the lock-in amplifier will need to be performed in software.

In addition to the aforementioned backscattering measurements, other avenues will be explored to increase the sensitivity of the setup. For example, it is possible to improve

[17] We remind the reader that, in this context, "label-free" indicates that the target analyte is not modified prior to detection via markers (labels) such as fluorescent molecules or radioactive isotopes.

the sensitivity through rigorous post-processing techniques[36, 37] such as use curve-fitting[38–45], noise filters[46] and stochastic analysis[47]. In general, a careful analysis of the setup and measured signals can be expected to identify statistically significant data.

Alternative light sources will also be considered. For example, Beuwer et al. [48] have reported shot-noise limited signals with a superluminescent diode (SLD). SLDs provide greater luminance due to high spatial coherence while avoiding interference artefacts due to low temporal coherence. Of course, the required spectral range of the application will need to be considered when considering such light sources.

The LSMS setup and sample preparation protocol are not limited to BPs. As we have seen in chapter 3, the development of plasmonic probes for biosensing is a very active area of research and other probes may prove to be much more sensitive. In particular, the interactions between coupled objects are complex and lead to interesting phenomena that may be exploitable for sensing applications. Recent work has shown the potential for systems of coupled objects of different sizes such as core-satellite systems[49–51] while recent work in our group has shown that the coupling of cubes leads to Fano-induced transparency windows in their spectra due to gap plasmon modes[52] (figure 3.57). The dip in the spectrum is therefore expected to be very sensitive to the dielectric properties of the gap, which would make the dimer a strong candidate for a sensing probe. Object-coupling may also open the doors for sensitive probes based on noble metals beyond gold and silver[53].

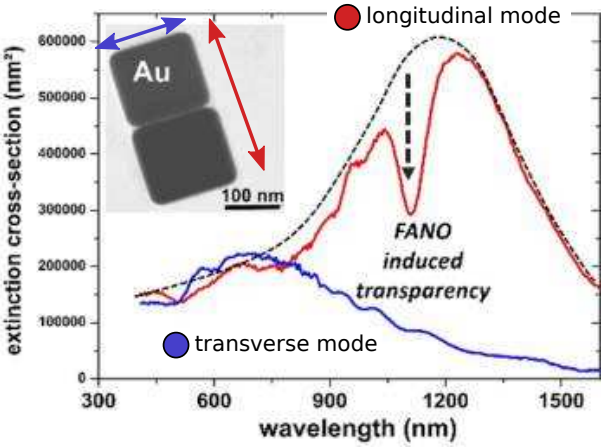

Figure 3.57: Fano-induced transparency in dimers of gold cubes. Source: Pellarin et al. [52]

In addition to sensitivity, biosensing applications will also benefit from high-throughput parallel detection. Many different approaches are under investigation to produce multiplexed probes, i.e. samples that are able to simultaneously detect different analytes[21, 34, 48, 54–68]. Multiplexed probes will lead to the rapid detection of multiple targets, minimized sample-to-sample variation, lower costs, reduced analyte volume, and reduced

times[34, 56]. For the SMS setup, several approaches to multiplexing are possible. Lithographic techniques that rely on optical[66] or capillary[69] forces can be used to place differentially functionalized NPs on the sample in regular arrays that would allow for the detection of hundreds of targets using an area of only 50 µm × 50 µm.

References

[1] J. R. G. Navarro, D. Manchon, F. Lerouge, E. Cottancin, J. Lermé, C. Bonnet, F. Chaput, A. Mosset, M. Pellarin, and S. Parola. Synthesis, electron tomography and single-particle optical response of twisted gold nano-bipyramids. *Nanotechnology*, 23(14):145707, April 2012. ISSN 0957-4484. doi:10.1088/0957-4484/23/14/145707.

[2] J. R. G. Navarro, D. Manchon, F. Lerouge, N. P. Blanchard, S. Marotte, Y. Leverrier, J. Marvel, F. Chaput, G. Micouin, A.-M. Gabudean, A. Mosset, E. Cottancin, P. L. Baldeck, K. Kamada, and S. Parola. Synthesis of PEGylated gold nanostars and bipyramids for intracellular uptake. *Nanotechnology*, 23(46):465602, November 2012. ISSN 0957-4484. doi:10.1088/0957-4484/23/46/465602.

[3] D. Chateau, A. Liotta, F. Vadcard, J. R. G. Navarro, F. Chaput, J. Lermé, F. Lerouge, and S. Parola. From gold nanobipyramids to nanojavelins for a precise tuning of the plasmon resonance to the infrared wavelengths: experimental and theoretical aspects. *Nanoscale*, 7(5):1934–1943, January 2015. ISSN 2040-3372. doi:10.1039/C4NR06323F.

[4] A. J. Haes and R. P. Van Duyne. A Nanoscale Optical Biosensor: Sensitivity and Selectivity of an Approach Based on the Localized Surface Plasmon Resonance Spectroscopy of Triangular Silver Nanoparticles. *Journal of the American Chemical Society*, 124(35):10596–10604, September 2002. ISSN 0002-7863, 1520-5126. doi:10.1021/ja020393x.

[5] N. Nath and A. Chilkoti. A colorimetric gold nanoparticle sensor to interrogate biomolecular interactions in real time on a surface. *Analytical chemistry*, 74(3):504–509, 2002.

[6] G. Raschke, S. Kowarik, T. Franzl, C. Sönnichsen, T. A. Klar, J. Feldmann, A. Nichtl, and K. Kürzinger. Biomolecular Recognition Based on Single Gold Nanoparticle Light Scattering. *Nano Letters*, 3(7):935–938, July 2003. ISSN 1530-6984. doi:10.1021/nl034223+.

[7] E. Katz and I. Willner. Integrated nanoparticle–biomolecule hybrid systems: synthesis, properties, and applications. *Angewandte Chemie International Edition*, 43 (45):6042–6108, 2004.

[8] N. Nath and A. Chilkoti. Label-Free Biosensing by Surface Plasmon Resonance of Nanoparticles on Glass: Optimization of Nanoparticle Size. *Analytical Chemistry*, 76 (18):5370–5378, September 2004. ISSN 0003-2700. doi:10.1021/ac049741z.

[9] M. E. Stewart, N. H. Mack, V. Malyarchuk, J. A. Soares, T.-W. Lee, S. K. Gray, R. G. Nuzzo, and J. A. Rogers. Quantitative multispectral biosensing and 1d imaging

using quasi-3d plasmonic crystals. *Proceedings of the National Academy of Sciences*, 103(46):17143–17148, 2006.

[10] T. Arai, P. K. R. Kumar, C. Rockstuhl, K. Awazu, and J. Tominaga. An optical biosensor based on localized surface plasmon resonance of silver nanostructured films. *Journal of Optics A: Pure and Applied Optics*, 9(7):699, 2007.

[11] C.-D. Chen, S.-F. Cheng, L.-K. Chau, and C. C. Wang. Sensing capability of the localized surface plasmon resonance of gold nanorods. *Biosensors and Bioelectronics*, 22(6):926–932, 2007.

[12] S. M. Marinakos, S. Chen, and A. Chilkoti. Plasmonic detection of a model analyte in serum by a gold nanorod sensor. *Analytical chemistry*, 79(14):5278–5283, 2007.

[13] Y. Wang, W. Qian, Y. Tan, and S. Ding. A label-free biosensor based on gold nanoshell monolayers for monitoring biomolecular interactions in diluted whole blood. *Biosensors and Bioelectronics*, 23(7):1166–1170, February 2008. ISSN 0956-5663. doi:10.1016/j.bios.2007.10.020.

[14] S. Chen, M. Svedendahl, M. Käll, L. Gunnarsson, and A. Dmitriev. Ultrahigh sensitivity made simple: nanoplasmonic label-free biosensing with an extremely low limit-of-detection for bacterial and cancer diagnostics. *Nanotechnology*, 20(43):434015, 2009. ISSN 0957-4484. doi:10.1088/0957-4484/20/43/434015.

[15] A. B. Dahlin, S. Chen, M. P. Jonsson, L. Gunnarsson, M. Kall, and F. Höök. High-resolution microspectroscopy of plasmonic nanostructures for miniaturized biosensing. *Analytical chemistry*, 81(16):6572–6580, 2009.

[16] F. J. Hernandez, S. K. Dondapati, V. C. Ozalp, A. Pinto, C. K. O'Sullivan, T. A. Klar, and I. Katakis. Label free optical sensor for Avidin based on single gold nanoparticles functionalized with aptamers. *Journal of Biophotonics*, 2(4):227–231, April 2009. ISSN 1864063X, 18640648. doi:10.1002/jbio.200910006.

[17] H. M. Hiep, H. Yoshikawa, M. Saito, and E. Tamiya. An interference localized surface plasmon resonance biosensor based on the photonic structure of Au nanoparticles and SiO2/Si multilayers. *ACS nano*, 3(2):446–452, 2009.

[18] H. M. Kim, S. M. Jin, S. K. Lee, M.-G. Kim, and Y.-B. Shin. Detection of Biomolecular Binding Through Enhancement of Localized Surface Plasmon Resonance (LSPR) by Gold Nanoparticles. *Sensors*, 9(4):2334–2344, March 2009. ISSN 1424-8220. doi:10.3390/s90402334.

[19] W.-S. Liao, X. Chen, T. Yang, E. T. Castellana, J. Chen, and P. S. Cremer. Benchtop chemistry for the rapid prototyping of label-free biosensors: Transmission localized surface plasmon resonance platforms. *Biointerphases*, 4(4):80–85, 2009.

[20] J. McPhillips, A. Murphy, M. P. Jonsson, W. R. Hendren, R. Atkinson, F. Höök, A. V. Zayats, and R. J. Pollard. High-Performance Biosensing Using Arrays of Plasmonic Nanotubes. *ACS Nano*, 4(4):2210–2216, April 2010. ISSN 1936-0851. doi:10.1021/nn9015828.

[21] K. M. Mayer and J. H. Hafner. Localized Surface Plasmon Resonance Sensors. *Chemical Reviews*, 111(6):3828–3857, June 2011. ISSN 0009-2665. doi:10.1021/cr100313v.

[22] M. Svedendahl, R. Verre, and M. Käll. Refractometric biosensing based on optical phase flips in sparse and short-range-ordered nanoplasmonic layers. *Light: Science & Applications*, 3(11):e220, November 2014. doi:10.1038/lsa.2014.101.

[23] H.-H. Jeong, A. G. Mark, M. Alarcón-Correa, I. Kim, P. Oswald, T.-C. Lee, and P. Fischer. Dispersion and shape engineered plasmonic nanosensors. *Nature Communications*, 7:11331, April 2016. ISSN 2041-1723. doi:10.1038/ncomms11331.

[24] M. P. Lambert, A. K. Barlow, B. A. Chromy, C. Edwards, R. Freed, M. Liosatos, T. E. Morgan, I. Rozovsky, B. Trommer, K. L. Viola, and others. Diffusible, nonfibrillar ligands derived from Aβ1–42 are potent central nervous system neurotoxins. *Proceedings of the National Academy of Sciences*, 95(11):6448–6453, 1998.

[25] J. Hardy and D. J. Selkoe. The Amyloid Hypothesis of Alzheimer's Disease: Progress and Problems on the Road to Therapeutics. *Science*, 297(5580):353–356, July 2002. ISSN 0036-8075, 1095-9203. doi:10.1126/science.1072994.

[26] W. L. Klein. Aβ toxicity in Alzheimer's disease: globular oligomers (ADDLs) as new vaccine and drug targets. *Neurochemistry International*, 41(5):345–352, November 2002. ISSN 0197-0186. doi:10.1016/S0197-0186(02)00050-5.

[27] D. J. Selkoe and J. Hardy. The search for an amyloid solution-Response. *Science*, 298(5595):963–964, 2002.

[28] D. M. Walsh, I. Klyubin, J. V. Fadeeva, W. K. Cullen, R. Anwyl, M. S. Wolfe, M. J. Rowan, and D. J. Selkoe. Naturally secreted oligomers of amyloid β protein potently inhibit hippocampal long-term potentiation in vivo. *Nature*, 416(6880): 535–539, 2002.

[29] Y. Gong, L. Chang, K. L. Viola, P. N. Lacor, M. P. Lambert, C. E. Finch, G. A. Krafft, and W. L. Klein. Alzheimer's disease-affected brain: presence of oligomeric Aβ ligands (ADDLs) suggests a molecular basis for reversible memory loss. *Proceedings of the National Academy of Sciences*, 100(18):10417–10422, 2003.

[30] G. A. Krafft and W. L. Klein. ADDLs and the signaling web that leads to Alzheimer's disease. *Neuropharmacology*, 59(4–5):230–242, September 2010. ISSN 0028-3908. doi:10.1016/j.neuropharm.2010.07.012.

[31] A. J. Haes, W. P. Hall, L. Chang, W. L. Klein, and R. P. Van Duyne. A localized surface plasmon resonance biosensor: First steps toward an assay for Alzheimer's disease. *Nano Letters*, 4(6):1029–1034, 2004.

[32] A. J. Haes, L. Chang, W. L. Klein, and R. P. Van Duyne. Detection of a biomarker for Alzheimer's disease from synthetic and clinical samples using a nanoscale optical biosensor. *Journal of the American Chemical Society*, 127(7):2264–2271, 2005.

[33] D. G. Georganopoulou, L. Chang, J.-M. Nam, C. S. Thaxton, E. J. Mufson, W. L. Klein, and C. A. Mirkin. Nanoparticle-based detection in cerebral spinal fluid of a soluble pathogenic biomarker for Alzheimer's disease. *Proceedings of the National Academy of Sciences of the United States of America*, 102(7):2273–2276, February 2005. ISSN 0027-8424, 1091-6490. doi:10.1073/pnas.0409336102.

[34] J. Zhao, X. Zhang, C. R. Yonzon, A. J. Haes, and R. P. Van Duyne. Localized surface plasmon resonance biosensors. *Nanomedicine*, 1(2):219–228, 2006.

[35] V. Crivianu-Gaita and M. Thompson. Aptamers, antibody scFv, and antibody Fab' fragments: An overview and comparison of three of the most versatile biosensor biorecognition elements. *Biosensors and Bioelectronics*, 85:32–45, November 2016. ISSN 0956-5663. doi:10.1016/j.bios.2016.04.091.

[36] A. B. Dahlin, J. O. Tegenfeldt, and F. Höök. Improving the Instrumental Resolution

of Sensors Based on Localized Surface Plasmon Resonance. *Analytical Chemistry*, 78 (13):4416–4423, July 2006. ISSN 0003-2700. doi:10.1021/ac0601967.

[37] A. Curry, G. Nusz, A. Chilkoti, and A. Wax. Analysis of total uncertainty in spectral peak measurements for plasmonic nanoparticle-based biosensors. *Applied Optics*, 46 (10):1931–1939, April 2007. ISSN 1539-4522. doi:10.1364/AO.46.001931.

[38] R. J. Meier. On art and science in curve-fitting vibrational spectra. *Vibrational Spectroscopy*, 39(2):266–269, 2005.

[39] G. J. Nusz, A. C. Curry, S. M. Marinakos, A. Wax, and A. Chilkoti. Rational Selection of Gold Nanorod Geometry for Label-Free Plasmonic Biosensors. *ACS Nano*, 3(4):795–806, April 2009. ISSN 1936-0851, 1936-086X. doi:10.1021/nn8006465.

[40] J. Becker, A. Trügler, A. Jakab, U. Hohenester, and C. Sönnichsen. The Optimal Aspect Ratio of Gold Nanorods for Plasmonic Bio-sensing. *Plasmonics*, 5(2):161–167, March 2010. ISSN 1557-1955, 1557-1963. doi:10.1007/s11468-010-9130-2.

[41] E. Pertreux, A. Lombardi, I. Florea, M. Spuch-Calvar, S. Gómez-Graña, D. Ihiawakrim, C. Hirlimann, O. Ersen, J. Majimel, M. Tréguer-Delapierre, M. Hettich, P. Maioli, A. Crut, F. Vallée, and N. D. Fatti. Surface Plasmon Resonance of an Individual Nano-object on an Absorbing Substrate: Quantitative Effects of Distance and 3d Orientation. *Advanced Optical Materials*, pages n/a–n/a, December 2015. ISSN 2195-1071. doi:10.1002/adom.201500548.

[42] S. M. E. Peters, M. A. Verheijen, M. W. J. Prins, and P. Zijlstra. Strong reduction of spectral heterogeneity in gold bipyramids for single-particle and single-molecule plasmon sensing. *Nanotechnology*, 27(2):024001, January 2016. ISSN 0957-4484, 1361-6528. doi:10.1088/0957-4484/27/2/024001.

[43] K. Johansen, R. Stålberg, I. Lundström, and B. Liedberg. Surface plasmon resonance: instrumental resolution using photo diode arrays. *Measurement Science and Technology*, 11(11):1630, 2000. ISSN 0957-0233. doi:10.1088/0957-0233/11/11/313.

[44] G. G. Nenninger, M. Piliarik, and J. Homola. Data analysis for optical sensors based on spectroscopy of surface plasmons. *Measurement Science and Technology*, 13(12): 2038–2046, December 2002. ISSN 0957-0233. doi:10.1088/0957-0233/13/12/332.

[45] C. Thirstrup and W. Zong. Data analysis for surface plasmon resonance sensors using dynamic baseline algorithm. *Sensors and Actuators B: Chemical*, 106(2):796–802, May 2005. ISSN 0925-4005. doi:10.1016/j.snb.2004.09.032.

[46] K. L. Göeken, V. Subramaniam, and R. Gill. Enhancing spectral shifts of plasmon-coupled noble metal nanoparticles for sensing applications. *Phys. Chem. Chem. Phys.*, 17(1):422–427, 2015. ISSN 1463-9076, 1463-9084. doi:10.1039/C4CP03739A.

[47] I. Ament, J. Prasad, A. Henkel, S. Schmachtel, and C. Sönnichsen. Single Unlabeled Protein Detection on Individual Plasmonic Nanoparticles. *Nano Letters*, 12(2):1092–1095, February 2012. ISSN 1530-6984, 1530-6992. doi:10.1021/nl204496g.

[48] M. A. Beuwer, M. W. J. Prins, and P. Zijlstra. Stochastic Protein Interactions Monitored by Hundreds of Single-Molecule Plasmonic Biosensors. *Nano Letters*, 15(5): 3507–3511, May 2015. ISSN 1530-6984, 1530-6992. doi:10.1021/acs.nanolett.5b00872.

[49] S. Hong, T. Kang, D. Choi, Y. Choi, and L. P. Lee. Self-Assembled Three-Dimensional Nanocrown Array. *ACS Nano*, 6(7):5803–5808, July 2012. ISSN 1936-0851. doi:10.1021/nn204967k.

[50] E. Martinsson, B. Sepulveda, P. Chen, A. Elfwing, B. Liedberg, and D. Aili. Optimizing the refractive index sensitivity of plasmonically coupled gold nanoparticles. *Plasmonics*, 9(4):773–780, 2014.

[51] J. Prasad, I. Zins, R. Branscheid, J. Becker, A. H. R. Koch, G. Fytas, U. Kolb, and C. Sönnichsen. Plasmonic Core–Satellite Assemblies as Highly Sensitive Refractive Index Sensors. *The Journal of Physical Chemistry C*, 119(10):5577–5582, March 2015. ISSN 1932-7447, 1932-7455. doi:10.1021/jp510985n.

[52] M. Pellarin, J. Ramade, J. M. Rye, C. Bonnet, M. Broyer, M.-A. Lebeault, J. Lermé, S. Marguet, J. R. Navarro, and E. Cottancin. Fano Transparency in Rounded Nanocube Dimers Induced by Gap Plasmon Coupling. *ACS Nano*, 10(12):11266–11279, December 2016. ISSN 1936-0851, 1936-086X. doi:10.1021/acsnano.6b06406.

[53] D. Manchon, J. Lermé, T. Zhang, A. Mosset, C. Jamois, C. Bonnet, J.-M. Rye, A. Belarouci, M. Broyer, M. Pellarin, and E. Cottancin. Plasmonic coupling with most of the transition metals: a new family of broad band and near infrared nanoantennas. *Nanoscale*, 7(3):1181–1192, November 2014. ISSN 2040-3364, 2040-3372. doi:10.1039/C4NR05383D.

[54] T. Endo, K. Kerman, N. Nagatani, H. M. Hiepa, D.-K. Kim, Y. Yonezawa, K. Nakano, and E. Tamiya. Multiple label-free detection of antigen-antibody reaction using localized surface plasmon resonance-based core-shell structured nanoparticle layer nanochip. *Analytical Chemistry*, 78(18):6465–6475, 2006.

[55] J. N. Anker, W. P. Hall, O. Lyandres, N. C. Shah, J. Zhao, and R. P. Van Duyne. Biosensing with plasmonic nanosensors. *Nature Materials*, 7(6):442–453, June 2008. ISSN 1476-1122. doi:10.1038/nmat2162.

[56] C. E. Berger, T. A. Beumer, R. P. Kooyman, and J. Greve. Surface plasmon resonance multisensing. *Analytical Chemistry*, 70(4):703–706, 1998.

[57] T. Sannomiya and J. Voeroes. Single plasmonic nanoparticles for biosensing. *Trends in Biotechnology*, 29(7):343–351, July 2011. ISSN 0167-7799. doi:10.1016/j.tibtech.2011.03.003. WOS:000292675700005.

[58] C. Rosman, J. Prasad, A. Neiser, A. Henkel, J. Edgar, and C. Sönnichsen. Multiplexed Plasmon Sensor for Rapid Label-Free Analyte Detection. *Nano Letters*, 13 (7):3243–3247, July 2013. ISSN 1530-6984. doi:10.1021/nl401354f.

[59] C. Yu and J. Irudayaraj. Multiplex biosensor using gold nanorods. *Analytical chemistry*, 79(2):572–579, 2007.

[60] C. Yu, H. Nakshatri, and J. Irudayaraj. Identity Profiling of Cell Surface Markers by Multiplex Gold Nanorod Probes. *Nano Letters*, 7(8):2300–2306, August 2007. ISSN 1530-6984. doi:10.1021/nl070894m.

[61] C. Wang and J. Irudayaraj. Gold Nanorod Probes for the Detection of Multiple Pathogens. *Small*, 4(12):2204–2208, December 2008. ISSN 16136810, 16136829. doi:10.1002/smll.200800309.

[62] C. R. Yonzon, E. Jeoung, S. Zou, G. C. Schatz, M. Mrksich, and R. P. Van Duyne. A comparative analysis of localized and propagating surface plasmon resonance sensors: the binding of concanavalin A to a monosaccharide functionalized self-assembled monolayer. *Journal of the American Chemical Society*, 126(39):12669–12676, 2004.

[63] J. M. Bingham, K. A. Willets, N. C. Shah, D. Q. Andrews, and R. P. Van Duyne.

Localized surface plasmon resonance imaging: simultaneous single nanoparticle spectroscopy and diffusional dynamics. *The Journal of Physical Chemistry C*, 113(39): 16839–16842, 2009.

[64] S. S. Aćimović, M. A. Ortega, V. Sanz, J. Berthelot, J. L. Garcia-Cordero, J. Renger, S. J. Maerkl, M. P. Kreuzer, and R. Quidant. LSPR Chip for Parallel, Rapid, and Sensitive Detection of Cancer Markers in Serum. *Nano Letters*, 14(5):2636–2641, May 2014. ISSN 1530-6984. doi:10.1021/nl500574n.

[65] L. Xie, X. Yan, and Y. Du. An aptamer based wall-less LSPR array chip for label-free and high throughput detection of biomolecules. *Biosensors and Bioelectronics*, 53: 58–64, March 2014. ISSN 0956-5663. doi:10.1016/j.bios.2013.09.031.

[66] S. Nedev, A. S. Urban, A. A. Lutich, and J. Feldmann. Optical Force Stamping Lithography. *Nano Letters*, 11(11):5066–5070, November 2011. ISSN 1530-6984. doi:10.1021/nl203214n.

[67] D.-K. Kim, S. M. Yoo, T. J. Park, H. Yoshikawa, E. Tamiya, J. Y. Park, and S. Y. Lee. Plasmonic Properties of the Multispot Copper-Capped Nanoparticle Array Chip and Its Application to Optical Biosensors for Pathogen Detection of Multiplex DNAs. *Analytical Chemistry*, 83(16):6215–6222, August 2011. ISSN 0003-2700, 1520-6882. doi:10.1021/ac2007762.

[68] O. Avci, N. L. Unlu, A. Y. Ozkumur, and M. S. Unlu. Interferometric Reflectance Imaging Sensor (IRIS)-A Platform Technology for Multiplexed Diagnostics and Digital Detection. *Sensors*, 15(7):17649–17665, July 2015. ISSN 1424-8220. doi:10.3390/s150717649. WOS:000361788200144.

[69] Y. Cui, M. T. Björk, J. A. Liddle, C. Sönnichsen, B. Boussert, and A. P. Alivisatos. Integration of Colloidal Nanocrystals into Lithographically Patterned Devices. *Nano Letters*, 4(6):1093–1098, June 2004. ISSN 1530-6984. doi:10.1021/nl049488i.

Appendices

Appendix A

Effects Of Further Mesh Refinement

A quick study was performed to check if the discrepancies between finite element method (FEM) and generalized Mie theory (GMT) in the interband region of figure 1.12 of section 1.3.1.3 were possibly due to mesh size effects given that the accuracy of the FEM model is expected to decrease with the ratio of wavelength to mesh size. Figure A.1 shows that there is no effect in this case.

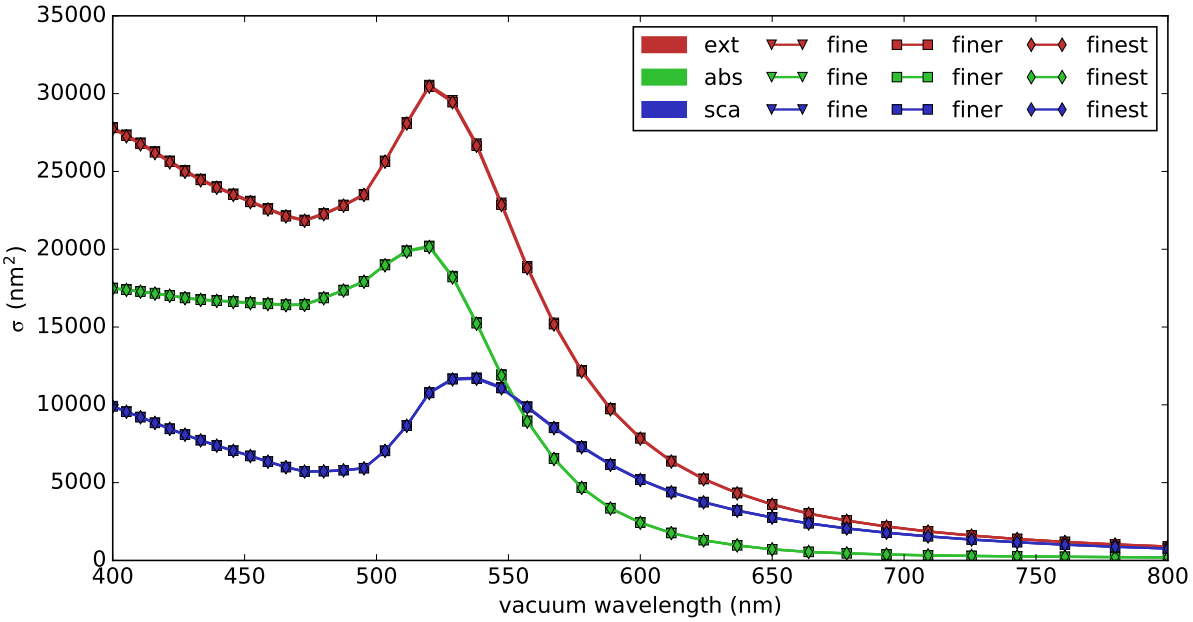

Figure A.1: Effects of mesh refinement on calculated cross sections using FEM. The model is of a gold nanosphere of radius 50 nm in air ($n = 1$) at a distance of 2 nm above a glass substrate ($n = 1.5$). No significant changes are observed with finer meshes. [GMT and FEM calculations]

Appendix B

Oscillating Mirror Characterization

An oscillating mirror was purchased from THORLABS (model GVS011 TSH 38077-X) for the liquid spatial modulation spectroscopy (LSMS) setup to offload the spatial modulation from the stage to the beam in anticipation of heavier sample holders. To characterize the positional response of the mirror at different frequencies and amplitudes, the Gaussian beam of a HeNe laser was profiled using a razor blade mounted on a micrometrically adjustable carriage (figure B.1, with a static mirror). The beam was focused with a lens onto a photodiode and the carriage was gradually advanced to cut the beam with the razorblade. The photodiode signal S_{diode} is therefore proportional to the integral of the cut beam intensity profile. By measuring the signal at different positions, the data points can therefore be used to fit the parameters of the function

$$S_{\text{diode}} = a \operatorname{erf}\left(\frac{x-b}{c}\right) + d \tag{B.1}$$

where

$$\operatorname{erf}(y) = \int_0^y \exp\left(-t^2\right)\, dt$$

Fitting the measured points to this function yielded the values in table B.1. The measured points along with the calculated curve are shown in figure B.2.

Once these parameters were determined, a LabView Virtual Instrument (VI) was created to control the mirror and measure the reported angular position of the mirror controller along with the signal from the photodiode. The mirror was introduced into the optical path before the razor blade and the position of the blade was centered in the path of the

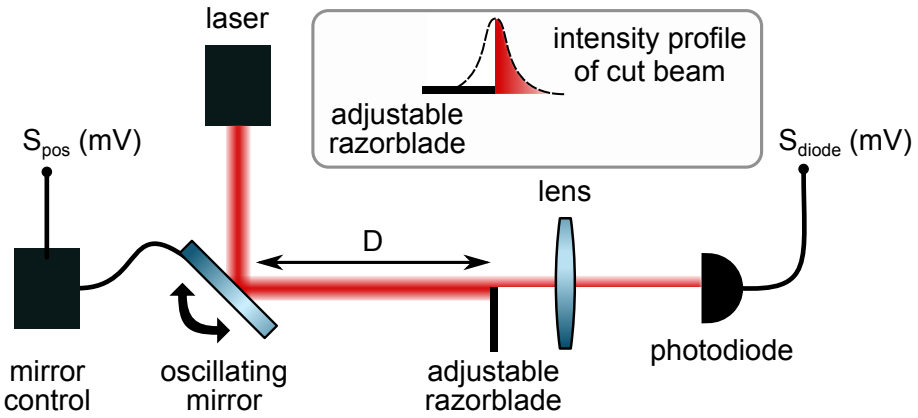

Figure B.1: Schematic overview of the experimental setup for the mirror calibration.

a	8.003 mV
b	12.40 mm
c	0.5977 mm
d	8.005 mV

Table B.1: Error function parameters determined by fitting the razor-blade-profiled HeNe laser beam signal to (B.1).

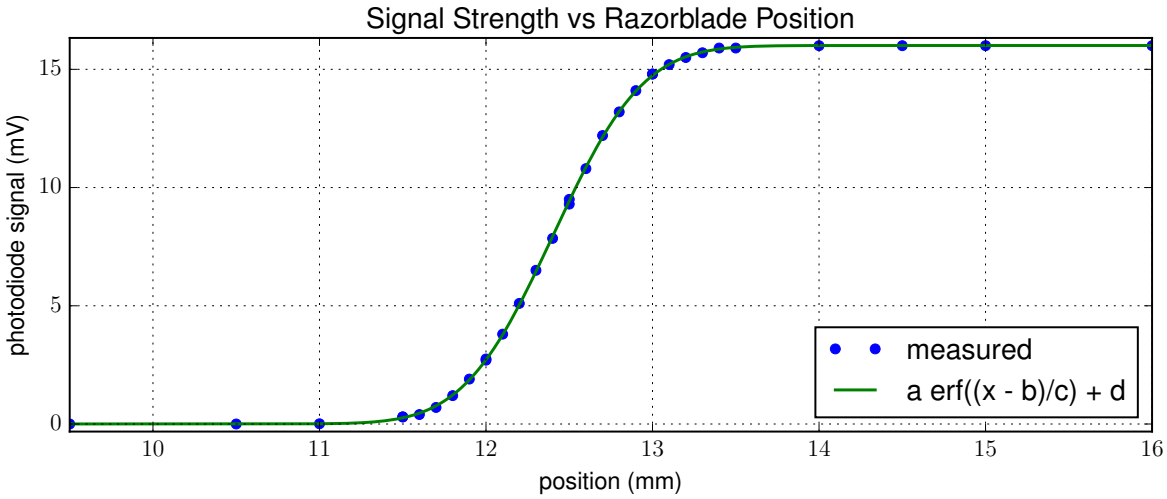

Figure B.2: Measured signal and fit function.

beam. Referring to (B.1), We denote $x' = x - b$ as the offset of the beam at the position of the razor. For small displacements, the change in S_{diode} is approximately linear:

$$
\begin{aligned}
S_{\text{diode}}\big(x'\big) &\approx S_{\text{diode}}(0) + \left.\frac{\mathrm{d}\big(S_{\text{diode}}(y)\big)}{\mathrm{d}y}\right|_{y=0} x' \\
&= d + \left.\frac{\mathrm{d}\Big(a\,\mathrm{erf}\big(\frac{y}{c}\big) + d\Big)}{\mathrm{d}y}\right|_{y=0} x' \\
&= d + \frac{a}{c}x'
\end{aligned}
\tag{B.2}
$$

Solving for the offset yields

$$
x' = \frac{c(S_{\text{diode}} - d)}{a} \tag{B.3}
$$

The offset may also be calculated from the angular position signal S_{pos} of the mirror control as

$$
x' = D\tan\Big(2\big(S_{\text{pos}}r_{\text{a}} + \alpha\big)\Big) \approx 2D\big(S_{\text{pos}}r_{\text{a}} + \alpha\big) \tag{B.4}
$$

where D is the distance to the razorblade (figure B.1), r_{a} is the ratio of radians per volt, and α is the angular offset, and the small-angle approximation has been used ($\tan(y) \approx y$). The factor of 2 arises from the reflection on the mirror.

When the mirror oscillates, both S_{diode} and S_{pos} will be sinusoidal:

$$
S_{\text{diode}} = A_{\text{diode}}\sin(2\pi ft + \phi_{\text{diode}}) + B_{\text{diode}} \tag{B.5}
$$

$$
S_{\text{pos}} = A_{\text{pos}}\sin\big(2\pi ft + \phi_{\text{pos}}\big) + B_{\text{pos}} \tag{B.6}
$$

where the frequency f must be the same in the steady-state regime. A_{diode}, A_{pos}, B_{diode} and B_{pos} can be experimentally determined by analyzing the signals from the diode and mirror controller. Equating (B.3) and (B.4) and substituting B.5 and B.6, respectively, we have

$$\frac{c\big(A_{\text{diode}}\sin(2\pi ft+\phi_{\text{diode}})+B_{\text{diode}}-d\big)}{a}=2D\Big(\Big(A_{\text{pos}}\sin\big(2\pi ft+\phi_{\text{pos}}\big)+B_{\text{pos}}\Big)r_{\text{a}}+\alpha\Big) \tag{B.7}$$

from which we may equate time-dependent and time-independent parts

$$\frac{c}{a}A_{\text{diode}}\sin(2\pi ft+\phi_{\text{diode}})=2Dr_{\text{a}}A_{\text{pos}}\sin\big(2\pi ft+\phi_{\text{pos}}\big) \tag{B.8}$$

$$\frac{c}{a}(B_{\text{diode}}-d))=2D\big(B_{\text{pos}}r_{\text{a}}+\alpha\big) \tag{B.9}$$

The amplitudes and phase offsets of (B.8) must be equal (this was nevertheless checked, data not shown), from which we may deduce an equation for r_{a}:

$$r_{\text{a}}=\frac{cA_{\text{diode}}}{2DaA_{\text{pos}}} \tag{B.10}$$

which can be used to check the ratio of the real angle to the reported position. From (B.9) we may also deduce the angular offset:

$$\alpha=\frac{c}{2Da}(B_{\text{diode}}-d)-B_{\text{pos}}r_{\text{a}} \tag{B.11}$$

The VI was then used to apply a sinusoidally varying voltage to the mirror from 1 mV to 20 mV over a range of frequencies from 200 Hz to 4600 Hz to determine the mirror's dynamic response. Some of the results are shown in figure B.3. The dynamic response varies roughly linearly with the applied voltage for a given frequency but decreases with increasing frequency. The angle factor r_{a} was found to be constant while the angular offset α was found to vary between runs. In all tests, the controller's reported position was found to be in agreement with the angular position and thus reliable under all amplitudes and frequencies.

For LSMS applications (and SMS in general), the real amplitude must be known and the angular offset must be 0° to ensure proper optical alignment and symmetric oscillation on the sample plane. To overcome the random offset and non-linear amplitude response of the mirror with increasing frequency, a VI was written to implement a feedback loop that would gradually adjust both the amplitude and the offset of the applied oscillating voltage at a the target frequency until the controller reported the correct angular amplitude with no offset, thus assuring that the real oscillation on the sample is as intended. This was then

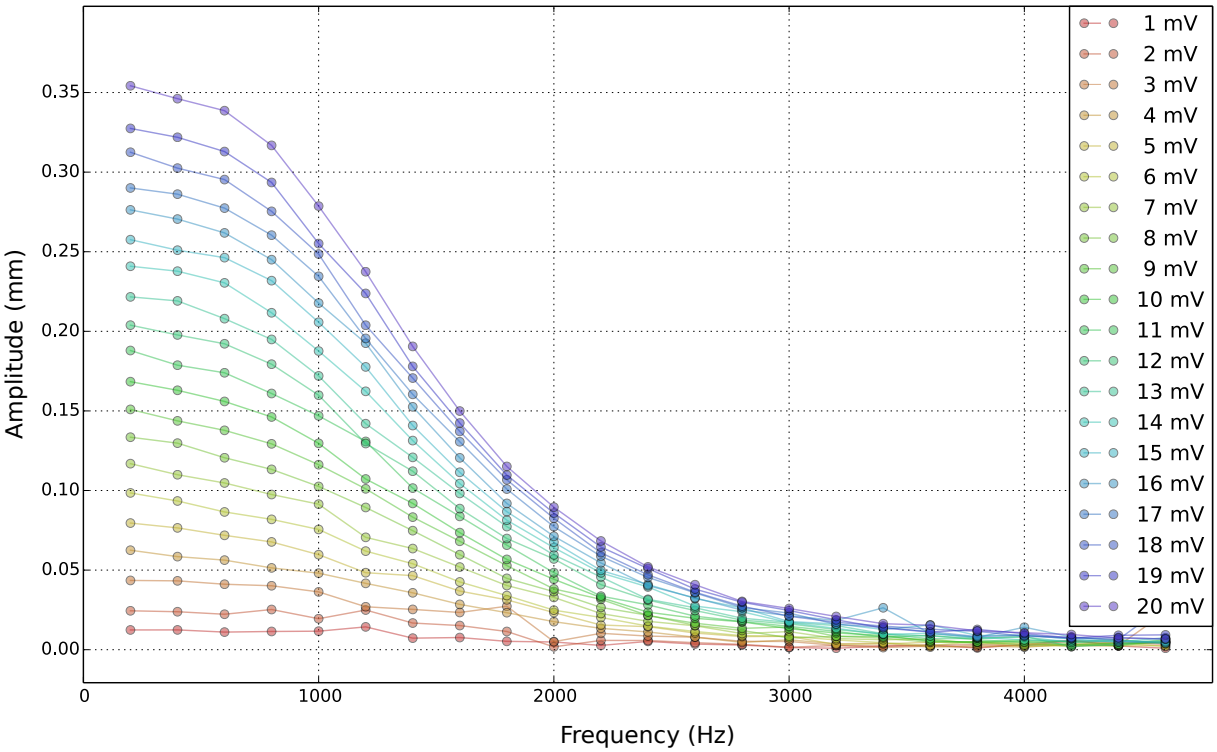

Figure B.3: Response of the mirror under different driving frequencies and amplitudes as measured by the photodiode signal.

integrated into the mirror subclass used by Multi-Instrument Controller and Automator (MICA) to control the LSMS setup.

Appendix C

MICA: Multi-Instrument Controller And Automator

Contents

C.1 Introduction

Multi-Instrument Controller and Automator (MICA) is the interface software written to control the LSMS setup described in section 2.2. It was designed to enabled versatile automation for all types of workflows. The most common use in this work has been to map new samples with automatic object detection and spectra acquisition. Other workflow examples include the automatic remapping of a sample over a predefined range of wavelengths with automatic spectra acquisition (see section D) or the automatic acquisition of object profiles at multiple wavelengths (figures 2.25 and 2.26).

Although MICA was written to control the LSMS setup, it is instrument-agnostic and extensible through an object-oriented design. Each instrument is controlled via a subclass

that encapsulates that instrument. MICA can be used with any setup for any application (not just SMS) by creating a few relatively simple subclasses to manage the different instruments of the setup. For example, for the LSMS setup, subclasses were created for the stage, the lock-in amplifiers, the oscillating mirror and the spectrometers. This approach allows new instruments to be easily integrated into an existing setup without modification of the main interface software.

C.2 Control And Signal Abstraction

To manage completely different instruments through a common interface, MICA abstracts each instrument's controls and signals. Due to LabVIEW's lack of type polymorphism, this was achieved by converting all controls and signals to *double* data types. The consequence of this approach is that MICA is essentially an application to map points in a real m-dimensional control space to images in a real n-dimensional signal space. A measurement is thus simply a mapping of a subset of the control space to the signal space. This is effected through loops that may be nested to an arbitrary level to scan any number of controls in any order.

Consider, for example, the simple case of a 3-dimensional control space that consists of a stage with translation controls x and y and a spectrometer with a wavelength control λ, and a 2-dimensional signal space that consists of the DC and X signals. To create a map of the sample at a fixed wavelength, λ is held constant and x and y are scanned in a nested loop. To measure a spectrum, x and y are held constant while λ is scanned.

Despite this abstraction, each instrument subclass provides a method to open a custom interface for that instrument. These interfaces are accessible via the MICA frontend and can be used to configure aspects of the instrument that can not be managed via the abstracted control space.

C.3 Presets

The user can define so-called "presets" via the MICA interface to launch preconfigured measurements such as sample mapping and spectra acquisition. Presets enable the user to extensively automate complex workflows. They can be created via the interface and saved to XML files for later reuse. They consist of the following components:

Static Controls: A 2-tuple list of control names and values that should be configured once before the measurement starts, such as lock-in amplifier settings.

Static Signals: A 1-tuple list of signal names that should be measured once at the start of the measurement. These will be saved to a separate file in the output directory and can be used to verify the state of the experimental setup after the measurement has been made. For example, throughout this work, all settings of the lock-in amplifiers as well as the oscillation parameters were systematically saved for all measurements.

Dynamic Controls: A 3-tuple list of control names, scan modes and lists of values that should be scanned to perform the measurements. The dynamic controls list is converted to a series of nested loops with the first element as the outer loop and each subsequent element nested within the previous one. This allows the user to fully control the order of measurements.

The list values associated with each control is also arbitrary. The MICA interface provides controls to quickly insert ranges with either a fixed number of points or with a fixed step size. The order in which these values is scanned in nested loops can also be configured via the scan mode parameter. For example, a sample can be mapped by sweeping one axis back and forth as the other is gradually incremented. Multiple controls can also be varied within the same loop. For example, two spectrometers can be scanned simultaneously to measure spectra along different optical pathways at the same time.

Dynamic Signals: The 1-tuple list of signals to measure at each control point in the scan space of the dynamic controls. Each signal point is appended to the open measurement file to ensure that no data is lost.

Output Parameters & Metadata: Parameters that allow the user to give each preset a unique identifier and provide a description of the measurement that will be written to the output directory along with the measured data for future reference. The user can also configure "bases" for the preset here. Bases are used to avoid repetition in presets. They are simply other presets that will be merged into the preset that lists them as a base. For example, a common set of static controls to configure the lock-in amplifier, such as phase, harmonic and sensitivity settings, can be grouped in a base preset's static controls. Other presets can then specify this base instead of including all of these controls in its own list of static controls. This also allows common controls to be managed in one location. Updating a base preset will effect all presets that use it‘. Bases are loaded recursively and can be nested to any depth.

Selectors: Selectors provides the core functionality of MICA's automation capability. While the dynamic controls can be used to scan any number of controls in any order, the loops are fixed when the measurement is started. Selectors allow the user to design workflows that launch new measurements based on previous measurements. They work by loading a preset and updating it with information from the current measurement. For example, a preset to measure a spectrum will specify a range of wavelengths in its dynamic controls. Another preset that maps a sample can use the spectrum preset to automatically study objects. To do this, immediately after the sample has been mapped, the mapping preset uses a selector to inspect

the measured data and determine which points correspond to objects. The selector then loads the spectrum preset and inserts the coordinates of the mapped objects into the spectrum preset's static controls, then enqueues the modified preset in a preset queue. For each object, a modified spectrum preset will be run that moves the stage to the object's location and then measures its spectrum.

The modified preset may itself contain other selectors to nest such actions. For example, a wide-area map of the sample can detect objects and launch presets that locally remap each object to account for sample drift. The local map preset can then launch a spectrum preset to measure the object's spectrum based on the location of the object in the recent local map. Each preset may also specify multiple selectors. For example, a mapping preset could use one selector to measure the spectrum of detected objects while using another selector to acquire signal profiles of the objects along a given axis.

All selectors are implemented as a subclass of a common selector class. A user can therefore define their own selectors as required by their intended workflow. Each selector may accept user-defined parameters via a selector-specific configuration file. For example, object tracking has been performed using a selector that identifies extrema of the measured data (either maxima or minima). The custom parameter file can be used to set upper and lower thresholds for the detection of extrema, including configurable exclusion zones around points that lie outside of the target range.

Static Control Overrides: A 2-tuple list of control names that should override other static controls, including those loaded via the base presets and selectors. This is useful for quickly modifying a few parameters from a previous measurement. For example, the static control overrides could be used to change the oscillation amplitude or frequency during automatic mapping and spectra acquisition.

Presets can be queued via the MICA interface to perform multiple separate measurements. The user can add presets to the queue while MICA is processing the queue. As each preset is processed, additional presets generated by the selectors are inserted into the queue. These can also be loaded on the interface via the preset queue manager and modified. The entire preset queue can also be saved to an XML file and reloaded later.

C.4 Real-time Interactive Measurements

The setup can also be used for real-time measurements in multiple ways. Each instrument can be controlled via its custom interface provided by the associated subclass. A common interface is provided to adjust all controls and view all signals for quick measurements, with either intermittent or continuous monitoring. Signals can also be continuously visually via rolling charts.

One of the consequences of the control and signal abstraction discussed above is that measurements can be made over arbitrary controls using a graphing interface. For example, the stage's x and y controls can be linked to an interactive 2D graph and the X/DC signal can be displayed as the graph data. The graph cursor can then be dragged to create a map in real time. The choice of controls is arbitrary. The x axis could just as well be linked to the wavelength λ, which would allow the graph to map signal profiles along the y axis at different wavelengths. The MICA interface provides interactive 1D and 2D graphs with a number of features such as automatic line and area scanning that may be performed in order or randomly. Data acquired through these real-time measurements can be saved to disk or stored in memory and managed via the main interface.

C.5 Data Visualization And Analysis

MICA provides tools for visualizing data as 1D and 2D graphs. The 1D graph viewer allows the user to display multiple sets of data on a single graph. Each data set can be named and stored in memory and then quickly reloaded later. The displayed data set can also be saved to disk in a single file. For example, this is useful for identifying objects of interest and then saving them for further analysis with other software. Ongoing measurements launched via presets can also be visualized in real-time, for example to observe a spectrum acquisition.

The 2D graph viewer provides cursors that can be used to measure distances and visualize cutplanes along each axis. This is useful for viewing the profiles of NPs in sample maps, for example. Annotation files such as those generated by the extremum selector can be loaded to mark detected objects. There is also functionality for showing a brief statistical analysis of the measured data such as its average value and distribution.

C.6 Standardized Output

MICA saves data in a simple CSV-style file format to facilitate post-processing. Modular LabView Virtual Instruments (VIs) are provided to ensure that output is consistent when generated by different components of the software and these should be used when developing new components.

When a preset is run, it will create a new subdirectory in the user-configured output directory. The name of the created directory will be the current date in ISO format along with the preset identifier. Duplicate names are detected and a numerical suffix is automatically added to avoid overwriting existing data. All files generated by the preset (e.g. static signals, dynamic signals, user notes, selected extrema) are saved within that

directory. If the preset launches other presets, each one of those will created its own subdirectory in the parent preset's output directory. All of the data is thus nested in a fixed hierarchy and can be processed automatically via scripts later.

C.7 Postprocessing Tools

A Python module has been created to work with the data generated by MICA. The module provides a class for loading and manipulating the generated data along with numerous other functions such as those for reconstructing maps and displaying annotations. A suite of command-line tools that use this module has been written and can be used to e.g. generate annotated maps and graphs, extract data, correlate objects between different maps, subtract background signals and generate full reports to examine the collected output of automated measurements. This module and the associated tools have been used to visualize the experimental data throughout this work.

Appendix D

Independence Of Spectra On Tracking Wavelength

Multi-Instrument Controller and Automator (MICA)'s automatic tracking (section C) uses local maps of objects to determine the optimal position for spectra acquisition. At $2f$, the optimal position should be the center of the object for all wavelengths. To confirm that measured spectra were independent of the tracking wavelength, MICA was used to map a gold sphere of 120 nm on a glass substrate in air every 25 nm between 470 nm and 670 nm. The brightest spot on each map was then selected as the position for the spectrum and the spectrum was measured before continuing with the next map. All measurements were made using the "G" Plan Apochromatic (GAPO) objective (discussed in chapter 2) and a mirror oscillation of 400 nm at 186 Hz.

The maps and spectra are shown in figure D.1. Despite the variations in the response and the appearance of a second object towards longer wavelengths, MICA successfully tracked the center of the object in each map and the resulting spectra showed no significant dependence on the tracking wavelength. The variation in signal strength may be attributed to minor changes in the focalization over the course of the measurements. Nevertheless, the spectral position of the localized surface plasmon resonance (LSPR) peak remained stable.

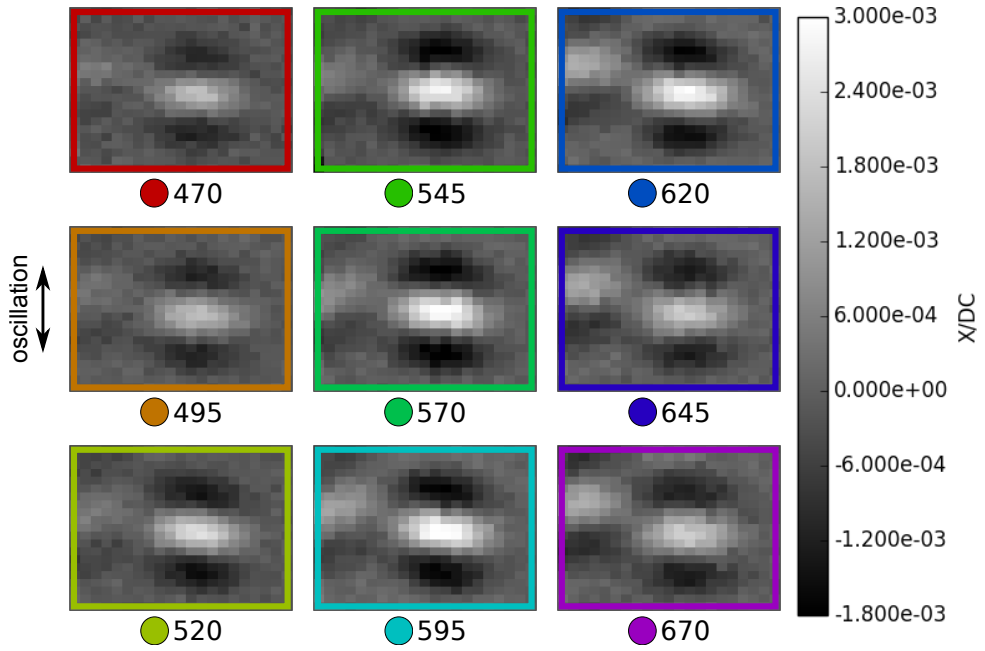

(a) maps

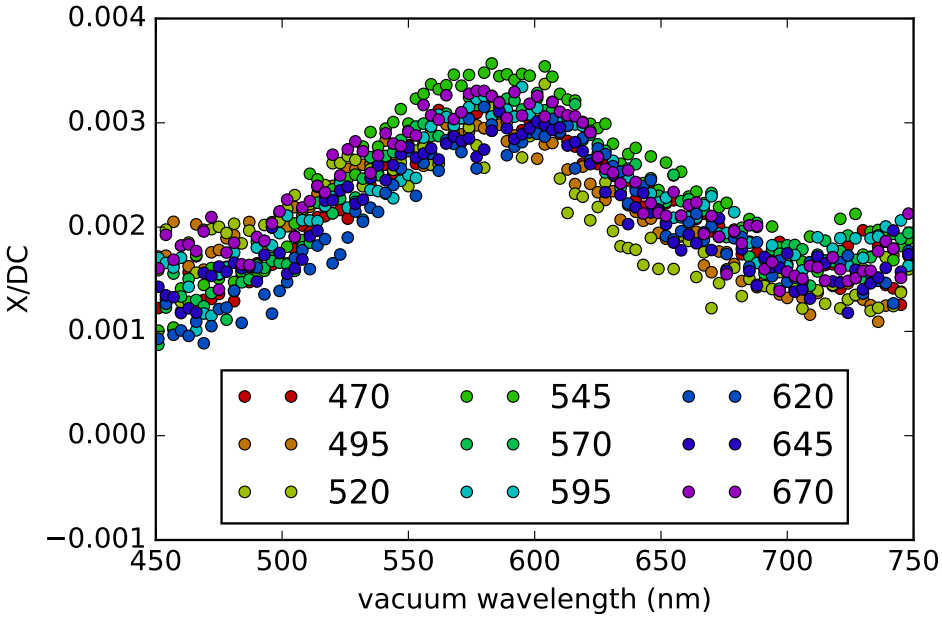

(b) spectra

Figure D.1: Using MICA, a gold sphere of 120 nm on a glass substrate in air was tracked using local maps at wavelengths ranging from 470 nm to 670 nm with a step size of 25 nm. Each map was automatically analyzed to determine the optimal point to acquire a spectrum and the spectrum was then measured. The resulting spectra were independent of the mapping wavelength. The maps are shown with the same z-scale for comparison. The region is approximately 3 µm × 4 µm.

Appendix E

About Figures Of Merit

Contents

The utility of a figure of merit (FOM) for a plasmonic probe is that it provides an indication of the probe's suitability for a sensing application. A high FOM should indicate that the probe will generate a reliably measurable result in the presence of the sensing target. Although the FOM defined by Sherry et al. [1] (FOM = m/Γ, equation 3.3 on page 130) has become the most common in the literature, it makes certain implicit assumptions and may not be the best definition for sensing applications. In this appendix, these assumptions will be briefly explored along with some alternative ways to evaluate plasmonic nanoprobes.

E.1 Different Noise And Sensing Regimes

Let us begin by considering in a general way the three sources of noise that one encounters when making a measurement[2]:

1. Signal noise, which stems from Poissonian photon statistics (e.g. shot noise).
2. Instrument noise due to imperfections in the setup (e.g. drifts in the optical alignment).

3. Uncorrelated background noise (σ_{B}) (e.g. a source of photons that produces more photons than the object under investigation).

Bobroff [3] provides a detailed analysis of the general case in which there is both signal and background noise. He arrives at theoretical limits for the determination of the signal position and shows that it is possible to measure the location with greater precision than the sample interval with a modest signal-to-noise ratio (SNR). The details of the analysis are beyond the scope of this work. We limit our consideration to the development by Unger and Kreiter [2], who focus on plasmonic biosensing applications. The authors first define a FOM as

$$\mathrm{FOM}_{\mathrm{Unger}} \propto \frac{\Delta\omega_{\mathrm{lspr}}}{\Delta\omega_{\mathrm{un}}} \tag{E.1}$$

where $\Delta\omega_{\mathrm{lspr}}$ is the shift of the localized surface plasmon resonance (LSPR) frequency and $\Delta\omega_{\mathrm{un}}$ is the uncertainty in the measurement of the shift. They also identify the signal strength S as

$$S = PTI\sigma t \tag{E.2}$$

where I is the irradiance of the illumination source, T is the cumulative transmittance of the entire optical setup, P is the detector sensitivity, σ is either the scattering (σ_{sca}) or extinction (σ_{ext}) cross-section of the probe (depending on the experiment), and t is the measuring time. Finally, they derive an analytical expression for $\Delta\omega_{\mathrm{lspr}}$ through perturbation theory and arrive at the approximation

$$\Delta\omega_{\mathrm{lspr}} = -\omega\frac{\Delta n}{n}C \tag{E.3}$$

where C is the confinement factor that takes into account the electric field around the resonator and its sensing volume. From these expressions, $\mathrm{FOM}_{\mathrm{Unger}}$ may be expressed for bulk sensing in the signal noise regime, i.e. under conditions in which the signal noise dominates, as

$$\mathrm{FOM}^{\mathrm{SN}}_{\mathrm{Unger,bulk}} \propto \underbrace{\frac{\Delta n}{n}}_{\text{analyte}} \cdot \underbrace{\frac{\sqrt{PTIt}}{f}}_{\text{setup}} \cdot \underbrace{\frac{\omega_{\mathrm{lspr}}C\sqrt{\sigma}}{\Gamma}}_{\text{resonator}} \tag{E.4}$$

where "SN" indicates the signal noise regime and we see that the three terms on the

right-hand side (RHS) depend on the analyte, the setup, and the resonator, in that order. Γ here is the full width at half maximum (FWHM) as in the FOM defined by Sherry et al. [1]. The final term is the one to consider when choosing or optimizing a probe for a given setup and experiment. The ideal probe should have a narrow line width to minimize Γ, strong localization of the field to the sensing volume (the bulk in this case) to maximize C, and a large relevant cross-section.

Further analysis of the other regimes leads to a general expression for the FOM of the probe for bulk refractive index (RI) changes:

$$\mathrm{FOM}_{\mathrm{Unger,bulk}} = \frac{\omega_{\mathrm{lspr}}}{\Gamma} C \sigma^{\alpha} \tag{E.5}$$

where α is 0 in the setup noise regime, 0.5 in the signal noise regime as above, and 1 in the background noise regime. If the sensitivity is expressed in angular frequency as $m = \frac{\mathrm{d}\omega_{\mathrm{lspr}}}{\mathrm{d}n}$, then from (E.5) we find $m = -\omega_{\mathrm{lspr}} C/n$. This is equal to $\frac{1}{n}\mathrm{FOM}_{\mathrm{Unger,bulk}}$ in the setup noise regime where $\alpha = 0$.

Because it is a function of the sensing volume, the confinement factor C depends on the geometry of the analyte under investigation. Unger and Kreiter [2] consider three sensing applications: changes in the bulk RI (bulk sensing), the adhesion of a thin uniform layer on the resonator (layer sensing), and the presence of a spherical volume near the resonator (object sensing).

For layer sensing, the FOM should take into account the local field around the probe. For very thin layers, the field does not vary strongly perpendicularly to the surface and the FOM is expected to be a linear function of the layer thickness d[2]. (E.5) may then be normalized as

$$\mathrm{FOM}_{\mathrm{Unger,layer}} = \frac{\omega_{\mathrm{lspr}}}{\Gamma} \frac{C}{d} \sigma^{\alpha} = \frac{\omega_{\mathrm{lspr}}}{\Gamma} C_{\mathrm{layer}} \sigma^{\alpha} \tag{E.6}$$

where $C_{\mathrm{L}} = C/d$. For a layer of thickness d, $\Delta\omega_{\mathrm{lspr}}$ may be expressed as[1][6–14]

$$\Delta\omega_{\mathrm{lspr}} = m\Delta n\Big(1 - \exp\big(-2d/l_{\mathrm{d}}\big)\Big) \tag{E.7}$$

where l_{d} is the effective decay length of the field. For thin layers ($d \ll 1$), from (3.3) the layer sensitivity becomes $2md/l_{\mathrm{d}}$ where m is the bulk sensitivity. A form analogous to the bulk FOM can be recovered by defining $m_{\mathrm{L}} = 2m/l_{\mathrm{d}}$, which, by identification, is equal to $\mathrm{FOM}_{\mathrm{Unger,layer}}/n$ with $\alpha = 0$ and thus corresponds to the layer sensing FOM in

[1] An equivalent expression in which the factor of 2 is subsumed into l_{d} also appears in the literature[4, 5].

the instrument noise regime. In this regime, probes with local fields that are strongly confined near the probe's surface will have greater FOMs for layer sensing. Such probes will have a poor comparable FOM for bulk sensing. This shows that ideal probes for one regime may be unsuitable for another regime.

For object sensing, no simple expressions are available. For very small objects, FOM is expected to be linear in r^3 where r is the radius of the object. The FOM can therefore be normalized by division with r^3[2]:

$$\mathrm{FOM}_{\mathrm{Unger,object}} = \frac{\omega_{\mathrm{lspr}}}{\Gamma}\frac{C}{r^3}\sigma^{\alpha} = \frac{\omega_{\mathrm{lspr}}}{\Gamma}C_{\mathrm{object}}\sigma^{\alpha} \tag{E.8}$$

Without a detailed analysis, a normalized analogue of (3.3) cannot be given for this regime. Nevertheless, the key point is that for object sensing, the FOM will be improved by strong confinement of the field to the sensing volume and that a single probe may exhibit different FOMs for different sensing regimes.

The cross-section σ and the confinement factor C will vary with the probe size. Within the quasi-static approximation[2], probe size dependencies can be derived for the different confinement factors in the different sensing regimes[2]. A table of the scaling factors of FOM with regard to probe size are presented in figure E.1.

	bulk	layers	particles
	FOM $\propto C_{\mathrm{bulk}} \propto {r_{\mathrm{mp}}}^{0}$	FOM $\propto C_{\mathrm{layer}} \propto {r_{\mathrm{mp}}}^{-1}$	FOM $\propto C_{\mathrm{S}} \propto {r_{\mathrm{mp}}}^{-3}$
instrument noise FOM $\propto \sigma^0 \propto {r_{\mathrm{mp}}}^0({r_{\mathrm{mp}}}^0)$	${r_{\mathrm{mp}}}^{0}$	${r_{\mathrm{mp}}}^{-1}$	${r_{\mathrm{mp}}}^{-3}$
signal noise FOM $\propto \sigma^{0.5} \propto {r_{\mathrm{mp}}}^{1.5}({r_{\mathrm{mp}}}^3)$	${r_{\mathrm{mp}}}^{1.5}({r_{\mathrm{mp}}}^3)$	${r_{\mathrm{mp}}}^{0.5}({r_{\mathrm{mp}}}^2)$	${r_{\mathrm{mp}}}^{-1.5}({r_{\mathrm{mp}}}^0)$
background noise FOM $\propto \sigma^1 \propto {r_{\mathrm{mp}}}^3({r_{\mathrm{mp}}}^6)$	${r_{\mathrm{mp}}}^3({r_{\mathrm{mp}}}^6)$	${r_{\mathrm{mp}}}^2({r_{\mathrm{mp}}}^5)$	${r_{\mathrm{mp}}}^0({r_{\mathrm{mp}}}^3)$

[a] In each entry, absorption and extinction cross sections are considered, the latter are given in brackets.

Table E.1: Dependence of the FOM on probe size for different noise and analyte regimes in the quasi-static approximation. The footnote should read "absorption and scattering" or "extinction and scattering". The erratum is in the original article. $C_{\mathrm{S}} = C_{\mathrm{object}}$. Source: Unger and Kreiter [2]

Within the quasi-static approximation, the table shows that the FOM's dependence on the probe size depends entirely on the noise regime and sensing target. For the instrument noise regime, α is 0 in (E.5) and the FOM is independent of the considered cross-section σ. It nevertheless depends on the probe size through the scaling of the confinement factor C. For bulk sensing, C does not vary with the probe size whereas it varies inversely with the probe size for layer sensing and with r^{-3} for object sensing. For the signal and background noise regimes, both bulk and layer sensing FOMs increase with increasing

[2]See equations 1.32 (σ_{sca}) and 1.33 (σ_{ext}) for the expression of the cross-sections in the quasi-static approximation.

probe size whereas for object sensing they either decrease with or are independent of the object size, depending on the regime and the relevant cross-section.

This consideration of the different noise regimes assumes that a single noise source is dominant. In real applications, multiple noise sources may be important and the regime will be mixed. Furthermore, the discussion above is simplified through the quasi-static approximation and fails to account for shape effects of the object, which may in turn also depend on the probe size. The dominant source of noise is expected to be a function of the probe size and optimization of the FOM will likely involve a compromise near the transition between different noise regimes[2]. This highlights the fact that the common FOM is not an indicator of probe suitability under all conditions.

In each case, FWHM remains a parameter to minimize for all sensing applications. This may be done by minimizing the different terms that contribute to it. For a metallic nano-object (MNO) on a substrate, the FWHM is given as[15]

$$\Gamma = \Gamma_0 + \Gamma_r + \gamma_s + \Gamma_{ads} + \Gamma_{sub} \tag{E.9}$$

where Γ_0 is the Landau damping, Γ_r is the radiative damping, γ_s is the quantum confinement damping, Γ_{ads} is the damping due to adsorbed molecules, and Γ_{sub} is the damping due to the substrate. Which of these can be minimized depends on the available parameters of the intended application.

For example, sensing applications rely on the adsorption of species on the LSPR probe for functionalization and targeted detection. This will increase Γ_{ads} FOM. For objects such as nanorods that display increased sensitivities at specific regions of their surface due to hotspots[16, 17], restricting adsorption to these areas may reduce Γ_{ads} without decreasing sensing potential. To test this, site-directed functionalization has been reported for nanorods[18, 19]. In these studies, the tips of nanorods were selectively functionalized by first passivating the nanorods' surface with cetyltrimethylammonium bromide (CTAB). The CTAB forms a thicker layer on the cylindrical sides of the nanorods compared to the tips due to the tips' curvature. This forms a protective layer that favors functionalization at the more readily accessible tips of the nanorod. When the CTAB is removed, only the tips will be subjected to additional interface damping due to the functionalizing molecules.

E.2 Intensity Shifts Instead Of Position Shifts

Because the definition of FOM above depends on the FWHM, the definition is limited to objects with line shapes for which a meaningful FWHM can be defined (e.g. Lorentzian line shapes). For objects or metamaterials with complex spectra, Becker et al. [20] define

an unrelated FOM to overcome this limitation:

$$\mathrm{FOM}^* = \frac{\left(\frac{\mathrm{d}I}{\mathrm{d}n}\right)}{I} \tag{E.10}$$

where I is the intensity measured at λ_{lspr}. FOM* is thus defined by the relative change in intensity at a given wavelength rather than the shift in the peak. This definition leads to slightly different predictions compared to FOM. For example, a numerical study to determine the optimal aspect ratio of gold nanorods sensing applications found that FOM predicts 4.3 while FOM* predicts 4.2[20, 21]. Although close, the difference is expected to be significant at the limit of detection.

The authors have also defined a related FOM for layer sensing:

$$\mathrm{FOM}^*_{\mathrm{layer}} = \frac{\left(\frac{\mathrm{d}I}{\mathrm{d}l}\right)}{I} \tag{E.11}$$

where l is the layer thickness surrounding the probe. As $\mathrm{FOM}_{\mathrm{Unger,layer}}$ above, $\mathrm{FOM}^*_{\mathrm{layer}}$ also fails to consider local variations of the near-field around the object.

E.3 Alternatives To FOM

Given the importance of shape-dependent field confinement for layer and object sensing. some authors have remarked on the insignificance of the commonly used FOMs in the literature for sensing applications[5, 14, 22]. Some attempts have been made to overcome this by explicitly accounting for sensing and analyte volumes in a custom FOM. For example, Nusz et al. [23] have defined the molecular detection limit MDL, the smallest number of bound molecules measurable by the system:

$$\mathrm{MDL} = \frac{V_{\mathrm{S}}\sqrt{U^2_{\mathrm{system}} + U^2_{\mathrm{fit}}}}{V_{\mathrm{A}}\Delta n \exp\left(-2r/l_{\mathrm{d}}\right)3m} \tag{E.12}$$

where V_{S} is the sensing volume, V_{A} is the analyte volume, Δn is the difference in the RI between the analyte and the surrounding medium, U_{system} is the uncertainty in the physical detection of the LSPR peak, U_{fit} is the uncertainty in the fitting of the LSPR peak, m is the bulk RI sensitivity as above, r is the distance from the particle surface to the analyte, and l_{d} is the decay length of the electric field as above. Nusz et al. have also

defined the dynamic range of a probe as the maximum number of molecules that can be detected by the probe.

While these definitions are more oriented towards real sensing results, they are also more difficult to define as they rely on a precise model of the probe and analyte. There is thus no universal FOM that can readily be used to compare the multitude of probes that exist. The aim of all of the reported FOMs is to compare different probes and predict their performance in a given application. Their utility will depend on how closely the conditions under which they were determined matches those of the intended assay. While they provide good overall guidelines, the development of exact models will ultimately provide better predictors of performance.

Such development is an active area of research. Recent work by Zalyubovskiy et al. [24] have used perturbation theory to determine that there is a hard limit for LSPR probe sensitivity, independent of the probe's shape or arrangement. This limit is due to the confinement of the sensing volume which they describe through a "fill factor", f, the maximum value of which is 1 in their formalism. The model also shows that $m \propto \lambda_{\text{lspr}}$, which is in agreement with previous calculations and findings in the literature[21, 25]

Even more recent work by Yang et al. [26] has developed a perturbation-based model to accurately predict shifts in a wide range of nanoparticle (NP) shapes and sizes beyond the quasi-static approximation. The core of the work relies on recent theoretical developments by Sauvan et al. [27] and [28] to describe the coupling between dissipative nanoresonators and dipole emitters. These works use what Yang et al. call "rigorous" normalization through $\vec{E} \cdot \vec{E}$ instead of $\vec{E} \cdot \vec{E}^*$. This model predicts both the real and imaginary components of $\Delta\omega_{\text{lspr}}$ and thus provide access to phase information. The authors cite this as a strong advantage of this approach compared to other recent work such as that of Zhang and Martin [29], which is restricted to the real component of the shift within the quasi-static approximation.

As these models continue to advance, we will develop new tools for the rational selection and design of plasmonic probes for all types of applications. Of course, experimental results will remain the ultimate benchmark of a probe's performance.

References

[1] L. J. Sherry, S.-H. Chang, G. C. Schatz, R. P. Van Duyne, B. J. Wiley, and Y. Xia. Localized Surface Plasmon Resonance Spectroscopy of Single Silver Nanocubes. *Nano Letters*, 5(10):2034–2038, October 2005. ISSN 1530-6984. doi:10.1021/nl0515753.

[2] A. Unger and M. Kreiter. Analyzing the Performance of Plasmonic Resonators for Dielectric Sensing. *The Journal of Physical Chemistry C*, 113(28):12243–12251, July 2009. ISSN 1932-7447. doi:10.1021/jp9027047.

[3] N. Bobroff. Position measurement with a resolution and noise-limited instrument. *Review of Scientific Instruments*, 57(6):1152–1157, June 1986. ISSN 0034-6748, 1089-7623. doi:10.1063/1.1138619.

[4] M. D. Malinsky, K. L. Kelly, G. C. Schatz, and R. P. Van Duyne. Chain length dependence and sensing capabilities of the localized surface plasmon resonance of silver nanoparticles chemically modified with alkanethiol self-assembled monolayers. *Journal of the American Chemical Society*, 123(7):1471–1482, 2001.

[5] O. Kedem, A. Vaskevich, and I. Rubinstein. Critical Issues in Localized Plasnnon Sensing. *Journal of Physical Chemistry C*, 118(16):8227–8244, April 2014. ISSN 1932-7447. doi:10.1021/jp409954s. WOS:000335114200001.

[6] D. J. Campbell, B. R. Herr, J. C. Hulteen, R. P. Van Duyne, and C. A. Mirkin. Ion-Gated Electron Transfer in Self-Assembled Monolayer Films. *Journal of the American Chemical Society*, 118(42):10211–10219, January 1996. ISSN 0002-7863. doi:10.1021/ja961873p.

[7] L. S. Jung, C. T. Campbell, T. M. Chinowsky, M. N. Mar, and S. S. Yee. Quantitative Interpretation of the Response of Surface Plasmon Resonance Sensors to Adsorbed Films. *Langmuir*, 14(19):5636–5648, September 1998. ISSN 0743-7463, 1520-5827. doi:10.1021/la971228b.

[8] A. J. Haes and R. P. Van Duyne. A Nanoscale Optical Biosensor: Sensitivity and Selectivity of an Approach Based on the Localized Surface Plasmon Resonance Spectroscopy of Triangular Silver Nanoparticles. *Journal of the American Chemical Society*, 124(35):10596–10604, September 2002. ISSN 0002-7863, 1520-5126. doi:10.1021/ja020393x.

[9] J. C. Riboh, A. J. Haes, A. D. McFarland, C. Ranjit Yonzon, and R. P. Van Duyne. A Nanoscale Optical Biosensor: Real-Time Immunoassay in Physiological Buffer Enabled by Improved Nanoparticle Adhesion. *The Journal of Physical Chemistry B*, 107(8):1772–1780, February 2003. ISSN 1520-6106. doi:10.1021/jp022130v.

[10] J. Zhao, X. Zhang, C. R. Yonzon, A. J. Haes, and R. P. Van Duyne. Localized surface plasmon resonance biosensors. *Nanomedicine*, 1(2):219–228, 2006.

[11] K. A. Willets and R. P. Van Duyne. Localized Surface Plasmon Resonance Spectroscopy and Sensing. *Annual Review of Physical Chemistry*, 58(1):267–297, May 2007. ISSN 0066-426X, 1545-1593. doi:10.1146/annurev.physchem.58.032806.104607.

[12] J. N. Anker, W. P. Hall, O. Lyandres, N. C. Shah, J. Zhao, and R. P. Van Duyne. Biosensing with plasmonic nanosensors. *Nature Materials*, 7(6):442–453, June 2008. ISSN 1476-1122. doi:10.1038/nmat2162.

[13] S. Chen, M. Svedendahl, M. Käll, L. Gunnarsson, and A. Dmitriev. Ultrahigh sensitivity made simple: nanoplasmonic label-free biosensing with an extremely low limit-of-detection for bacterial and cancer diagnostics. *Nanotechnology*, 20(43):434015, 2009. ISSN 0957-4484. doi:10.1088/0957-4484/20/43/434015.

[14] M. Svedendahl, S. Chen, A. Dmitriev, and M. Käll. Refractometric Sensing Using Propagating versus Localized Surface Plasmons: A Direct Comparison. *Nano Letters*, 9(12):4428–4433, December 2009. ISSN 1530-6984. doi:10.1021/nl902721z.

[15] E. Pertreux, A. Lombardi, I. Florea, M. Spuch-Calvar, S. Gómez-Graña, D. Ihiawakrim, C. Hirlimann, O. Ersen, J. Majimel, M. Tréguer-Delapierre, M. Hettich,

P. Maioli, A. Crut, F. Vallée, and N. D. Fatti. Surface Plasmon Resonance of an Individual Nano-object on an Absorbing Substrate: Quantitative Effects of Distance and 3d Orientation. *Advanced Optical Materials*, pages n/a–n/a, December 2015. ISSN 2195-1071. doi:10.1002/adom.201500548.

[16] M. Liu, P. Guyot-Sionnest, T.-W. Lee, and S. K. Gray. Optical properties of rodlike and bipyramidal gold nanoparticles from three-dimensional computations. *Physical Review B*, 76(23):235428, December 2007. doi:10.1103/PhysRevB.76.235428.

[17] I. Ament, J. Prasad, A. Henkel, S. Schmachtel, and C. Sönnichsen. Single Unlabeled Protein Detection on Individual Plasmonic Nanoparticles. *Nano Letters*, 12(2):1092–1095, February 2012. ISSN 1530-6984, 1530-6992. doi:10.1021/nl204496g.

[18] P. Pramod, S. T. S. Joseph, and K. G. Thomas. Preferential End Functionalization of Au Nanorods through Electrostatic Interactions. *Journal of the American Chemical Society*, 129(21):6712–6713, May 2007. ISSN 0002-7863. doi:10.1021/ja071536o.

[19] P. Zijlstra, P. M. R. Paulo, K. Yu, Q.-H. Xu, and M. Orrit. Chemical Interface Damping in Single Gold Nanorods and Its Near Elimination by Tip-Specific Functionalization. *Angewandte Chemie International Edition*, 51(33):8352–8355, August 2012. ISSN 14337851. doi:10.1002/anie.201202318.

[20] J. Becker, A. Trügler, A. Jakab, U. Hohenester, and C. Sönnichsen. The Optimal Aspect Ratio of Gold Nanorods for Plasmonic Bio-sensing. *Plasmonics*, 5(2):161–167, March 2010. ISSN 1557-1955, 1557-1963. doi:10.1007/s11468-010-9130-2.

[21] K. M. Mayer and J. H. Hafner. Localized Surface Plasmon Resonance Sensors. *Chemical Reviews*, 111(6):3828–3857, June 2011. ISSN 0009-2665. doi:10.1021/cr100313v.

[22] M. Svedendahl, R. Verre, and M. Käll. Refractometric biosensing based on optical phase flips in sparse and short-range-ordered nanoplasmonic layers. *Light: Science & Applications*, 3(11):e220, November 2014. doi:10.1038/lsa.2014.101.

[23] G. J. Nusz, A. C. Curry, S. M. Marinakos, A. Wax, and A. Chilkoti. Rational Selection of Gold Nanorod Geometry for Label-Free Plasmonic Biosensors. *ACS Nano*, 3(4):795–806, April 2009. ISSN 1936-0851, 1936-086X. doi:10.1021/nn8006465.

[24] S. J. Zalyubovskiy, M. Bogdanova, A. Deinega, Y. Lozovik, A. D. Pris, K. H. An, W. P. Hall, and R. A. Potyrailo. Theoretical limit of localized surface plasmon resonance sensitivity to local refractive index change and its comparison to conventional surface plasmon resonance sensor. *JOSA A*, 29(6):994–1002, 2012.

[25] M. M. Miller and A. A. Lazarides. Sensitivity of Metal Nanoparticle Surface Plasmon Resonance to the Dielectric Environment. *The Journal of Physical Chemistry B*, 109 (46):21556–21565, November 2005. ISSN 1520-6106. doi:10.1021/jp054227y.

[26] J. Yang, H. Giessen, and P. Lalanne. Simple Analytical Expression for the Peak-Frequency Shifts of Plasmonic Resonances for Sensing. *Nano Letters*, 15(5):3439–3444, May 2015. ISSN 1530-6984. doi:10.1021/acs.nanolett.5b00771.

[27] C. Sauvan, J. P. Hugonin, I. S. Maksymov, and P. Lalanne. Theory of the Spontaneous Optical Emission of Nanosize Photonic and Plasmon Resonators. *Physical Review Letters*, 110(23), June 2013. ISSN 0031-9007, 1079-7114. doi:10.1103/PhysRevLett.110.237401.

[28] Q. Bai, M. Perrin, C. Sauvan, J.-P. Hugonin, and P. Lalanne. Efficient and intuitive

method for the analysis of light scattering by a resonant nanostructure. *Optics Express*, 21(22):27371, November 2013. ISSN 1094-4087. doi:10.1364/OE.21.027371.

[29] W. Zhang and O. J. F. Martin. A Universal Law for Plasmon Resonance Shift in Biosensing. *Acs Photonics*, 2(1):144–150, January 2015. ISSN 2330-4022. doi:10.1021/ph500355d. WOS:000348339400021.

Appendix F

Supplementary Figures

Contents

F.1 Refractive Index Of Gold

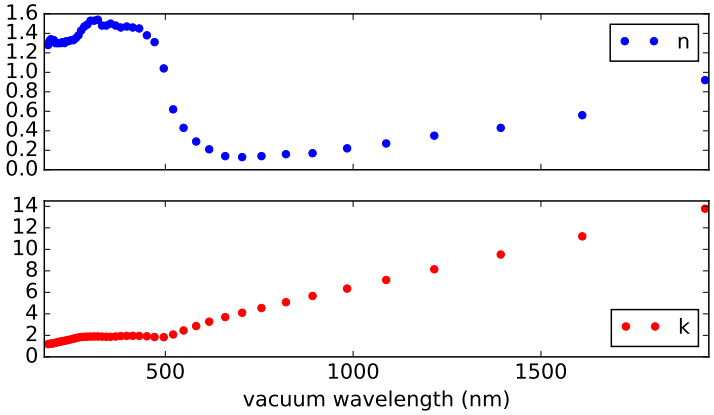

Figure F.1: Real and imaginary components of the refractive index of gold from Johnson and Christy [1]

F.2 Numerical Study Simulations

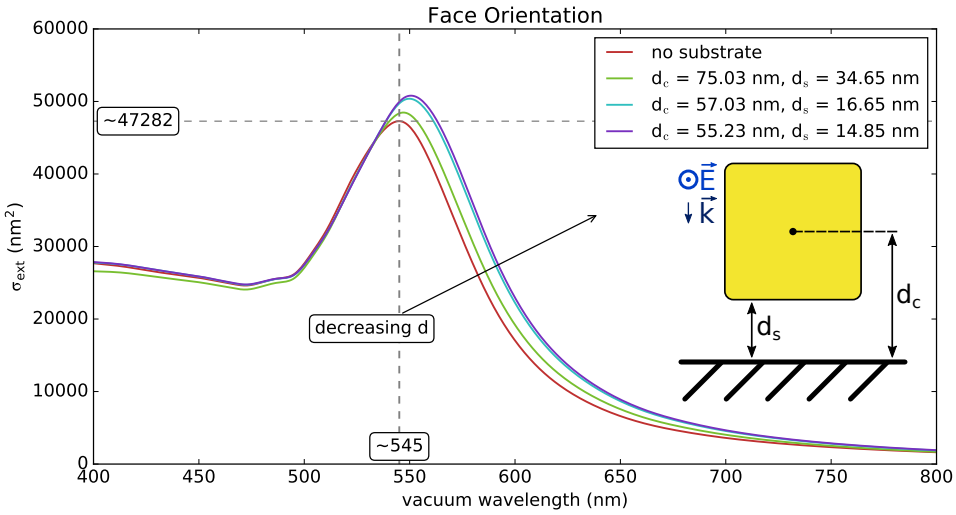

Figure F.2: Extinction cross-section of a rounded gold cube ($l = 80.76\,\text{nm}$, $r = 5\,\text{nm}$) in air ($n = 1$) on its face at varying distance from a glass substrate ($n = 1.5$). Barycenter-to-surface distances are comparable to the edge-oriented cube shown in figure 1.35b on page 73. [FEM calculations]

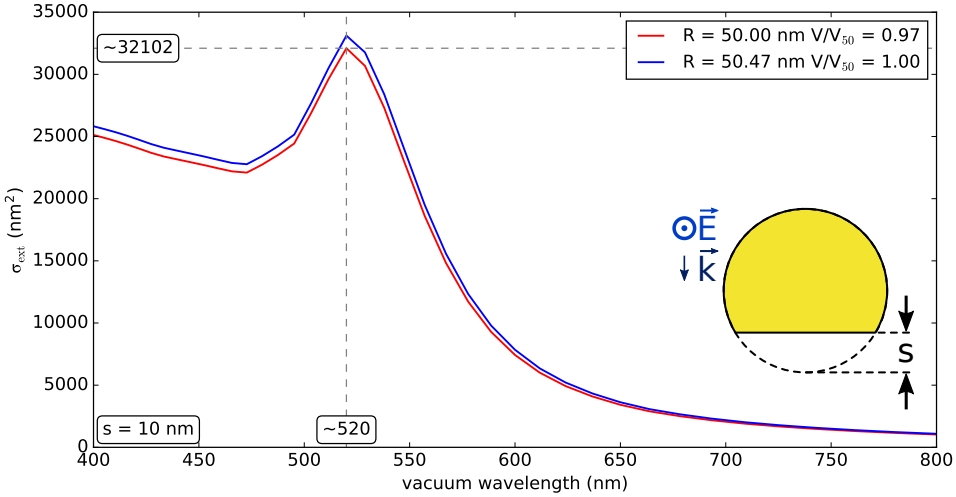

Figure F.3: Extinction cross-sections of a gold sphere in air ($n = 1$) with a slice of thickness $s = 10\,\text{nm}$ removed. In red the radius is held constant at $R = 50\,\text{nm}$ while in blue the radius is increased to keep the volume constant. The responses differ only slightly. [FEM calculations]

F.3 Xenon Lamp Spectral Profile

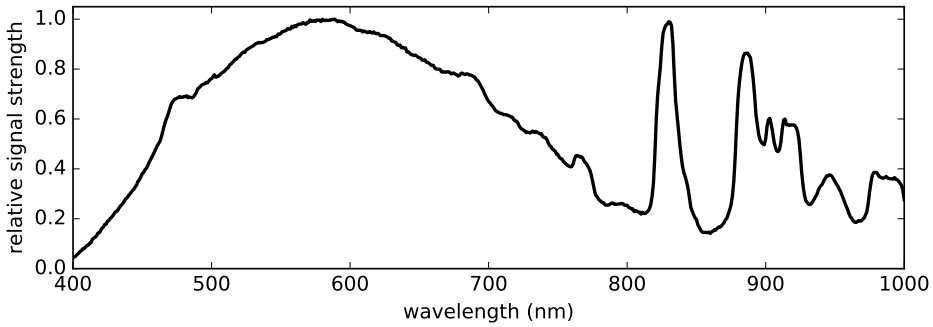

Figure F.4: The spectral intensity profile of the xenon lamp used in the LSMS setup described in section 2.

F.4 Bipyramid Simulations

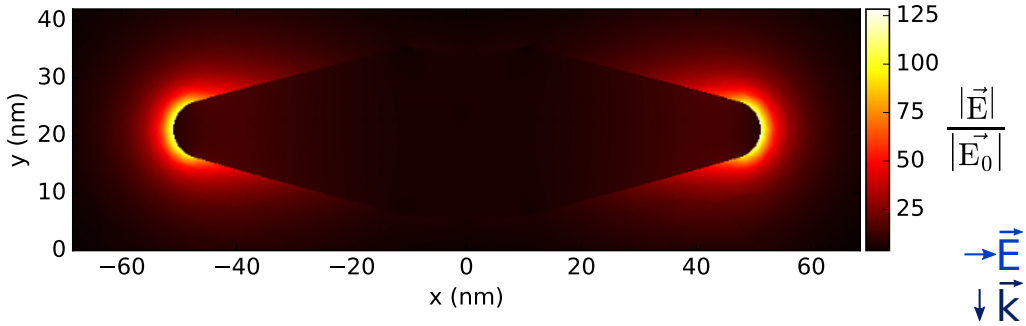

Figure F.5: The relative enhancement of the electric field around a gold BP of length 100 nm and width 30 nm with rounding radius 5 nm at LSPR in air. The incident field is polarized along the longitudinal axis of the object. [FEM calculations]

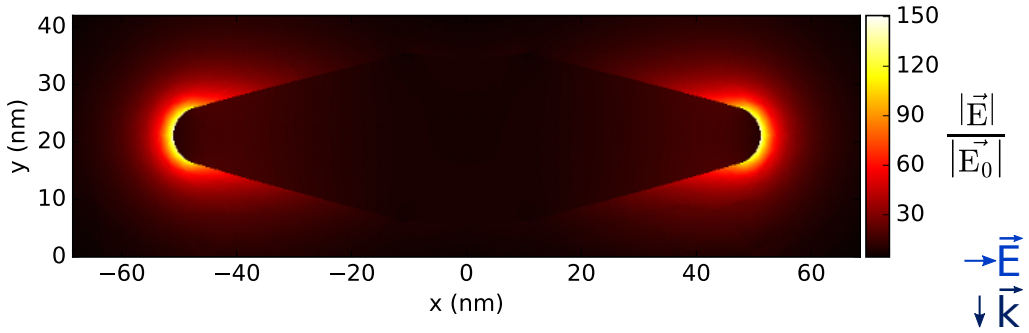

Figure F.6: The relative enhancement of the electric field around a gold BP of length 100 nm and width 30 nm with rounding radius 5 nm at LSPR in water. The incident field is polarized along the longitudinal axis of the object. [FEM calculations]

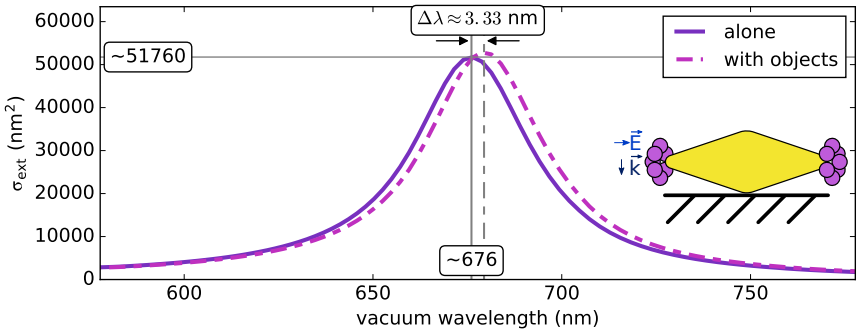

Figure F.7: The equivalent calculation with water replaced by air in the system described in figure 3.11a on page 144. The greater relative change of the effective refractive index n_{eff} induces a greater shift in the LSPR peak. [FEM calculations]

References

[1] P. B. Johnson and R. W. Christy. Optical Constants of the Noble Metals. *Physical Review B*, 6(12):4370–4379, December 1972. doi:10.1103/PhysRevB.6.4370.

Acronyms

ADDL amyloid-derived diffusable ligand.
AFM atomic force microscope.

BP bipyramid.

CCD charge-coupled device.
CSF cerebrospinal fluid.
CT computed tomography.
CTAB cetyltrimethylammonium bromide.
CTAC cetyltrimethylammonium chloride.

DDA discrete dipole approximation.

EM electromagnetic.
ENS de Lyon École Normale Supérieure de Lyon.

FDTD finite-difference time-domain.
FEM finite element method.
FOM figure of merit.
FWHM full width at half maximum.

GAPO "G" Plan Apochromatic.
GMT generalized Mie theory.

HQL hydroxyquinoline.

ILM Institute of Light and Matter.
INL Institut des Nanotechnologies de Lyon.

LC Laboratoire de Chimie.
LFG low-frequency generator.
LOC lab-on-a-chip.
LSMS liquid spatial modulation spectroscopy.
LSPR localized surface plasmon resonance.

MAPO "M" Plan Apochromatic.
MICA Multi-Instrument Controller and Automator.
MNO metallic nano-object.
MRI magnetic resonance imaging.

NA numerical aperture.
NIR near-infrared.
NMR nuclear magnetic resonance.
NP nanoparticle.
NUV near-ultraviolet.

PML perfectly matched layer.
PMM polarization modulation microscopy.
PMMA poly(methyl methacrylate).

RHS right-hand side.
RI refractive index.
RIU refractive index units.
RMS root mean square.

SEM scanning electron microscopy.
SLD superluminescent diode.
SMS spatial modulation spectroscopy.
SNOM scanning near-field optical microscopy.
SNR signal-to-noise ratio.
STM scanning tunneling microscope.

TEM transmission electron microscopy.
T-Matrix Transition Matrix "null-field".

UCBL Université Claude Bernard Lyon 1.
UV ultraviolet.

VI LabView Virtual Instrument.
VSH vector spherical harmonics.

WGM whispering gallery mode.